

Systematic measurements of identified particle spectra in pp, d+Au, and Au+Au collisions at the STAR detector

(STAR Collaboration) Abelev, B. I.; ...; Planinić, Mirko; ...; Poljak, Nikola; ...; Zuo, J. X.

Source / Izvornik: **Physical Review C - Nuclear Physics, 2009, 79**

Journal article, Published version

Rad u časopisu, Objavljena verzija rada (izdavačev PDF)

<https://doi.org/10.1103/PhysRevC.79.034909>

Permanent link / Trajna poveznica: <https://um.nsk.hr/um:nbn:hr:217:293009>

Rights / Prava: [In copyright](#)

Download date / Datum preuzimanja: **2022-08-22**



Repository / Repozitorij:

[Repository of Faculty of Science - University of Zagreb](#)



Systematic measurements of identified particle spectra in pp , $d + \text{Au}$, and $\text{Au} + \text{Au}$ collisions at the STAR detector

B. I. Abelev,⁹ M. M. Aggarwal,³⁰ Z. Ahammed,⁴⁶ B. D. Anderson,¹⁹ D. Arkhipkin,¹³ G. S. Averichev,¹² Y. Bai,²⁸ J. Balewski,²³ O. Barannikova,⁹ L. S. Barnby,² J. Baudot,¹⁷ S. Baumgart,⁵¹ D. R. Beavis,³ R. Bellwied,⁴⁹ F. Benedosso,²⁸ R. R. Betts,⁹ S. Bhardwaj,³⁵ A. Bhasin,¹⁸ A. K. Bhati,³⁰ H. Bichsel,⁴⁸ J. Bielcik,¹¹ J. Bielcikova,¹¹ B. Biritz,⁶ L. C. Bland,³ M. Bombara,² B. E. Bonner,³⁶ M. Botje,²⁸ J. Bouchet,¹⁹ E. Braidot,²⁸ A. V. Brandin,²⁶ E. Bruna,⁵¹ S. Bueltmann,³ T. P. Burton,³ M. Bystersky,¹¹ X. Z. Cai,³⁹ H. Caines,⁵¹ M. Calderón de la Barca Sánchez,⁵ J. Callner,⁹ O. Catu,⁵¹ D. Cebra,⁵ R. Cendejas,⁶ M. C. Cervantes,⁴¹ Z. Chajecki,²⁹ P. Chaloupka,¹¹ S. Chattopadhyay,⁴⁶ H. F. Chen,³⁸ J. H. Chen,³⁹ J. Y. Chen,⁵⁰ J. Cheng,⁴³ M. Cherney,¹⁰ A. Chikanian,⁵¹ K. E. Choi,³⁴ W. Christie,³ S. U. Chung,³ R. F. Clarke,⁴¹ M. J. M. Codrington,⁴¹ J. P. Coffin,¹⁷ T. M. Cormier,⁴⁹ M. R. Cosentino,³⁷ J. G. Cramer,⁴⁸ H. J. Crawford,⁴ D. Das,⁵ S. Dash,¹⁴ M. Daugherty,⁴² C. De Silva,⁴⁹ T. G. Dedovich,¹² M. DePhillips,³ A. A. Derevschikov,³² R. Derradi de Souza,⁷ L. Didenko,³ P. Djawotho,¹⁶ S. M. Dogra,¹⁸ X. Dong,²² J. L. Drachenberg,⁴¹ J. E. Draper,⁵ F. Du,⁵¹ J. C. Dunlop,³ M. R. Dutta Mazumdar,⁴⁶ W. R. Edwards,²² L. G. Efimov,¹² E. Elhalhuli,² M. Elnimr,⁴⁹ V. Emelianov,²⁶ J. Engelage,⁴ G. Eppley,³⁶ B. Erasmus,⁴⁰ M. Estienne,¹⁷ L. Eun,³¹ P. Fachini,³ R. Fatemi,²⁰ J. Fedorisin,¹² A. Feng,⁵⁰ P. Filip,¹³ E. Finch,⁵¹ V. Fine,³ Y. Fisyak,³ C. A. Gagliardi,⁴¹ L. Gaillard,² D. R. Gangadharan,⁶ M. S. Ganti,⁴⁶ E. Garcia-Solis,⁹ V. Ghazikhanian,⁶ P. Ghosh,⁴⁶ Y. N. Gorbunov,¹⁰ A. Gordon,³ O. Grebenyuk,²² D. Grosnick,⁴⁵ B. Grube,³⁴ S. M. Guertin,⁶ K. S. F. F. Guimaraes,³⁷ A. Gupta,¹⁸ N. Gupta,¹⁸ W. Guryn,³ B. Haag,⁵ T. J. Hallman,³ A. Hamed,⁴¹ J. W. Harris,⁵¹ W. He,¹⁶ M. Heinz,⁵¹ S. Heppelmann,³¹ B. Hippolyte,¹⁷ A. Hirsch,³³ E. Hjort,²² A. M. Hoffman,²³ G. W. Hoffmann,⁴² D. J. Hofman,⁹ R. S. Hollis,⁹ H. Z. Huang,⁶ T. J. Humanic,²⁹ G. Igo,⁶ A. Iordanova,⁹ P. Jacobs,²² W. W. Jacobs,¹⁶ P. Jakl,¹¹ F. Jin,³⁹ P. G. Jones,² J. Joseph,¹⁹ E. G. Judd,⁴ S. Kabana,⁴⁰ K. Kajimoto,⁴² K. Kang,⁴³ J. Kapitan,¹¹ M. Kaplan,⁸ D. Keane,¹⁹ A. Kechechyan,¹² D. Kettler,⁴⁸ V. Yu. Khodyrev,³² J. Kiryluk,²² A. Kisiel,²⁹ S. R. Klein,²² A. G. Knospe,⁵¹ A. Kocoloski,²³ D. D. Koetke,⁴⁵ M. Kopytine,¹⁹ L. Kotchenda,²⁶ V. Kouchpil,¹¹ P. Kravtsov,²⁶ V. I. Kravtsov,³² K. Krueger,¹ M. Krus,¹¹ C. Kuhn,¹⁷ L. Kumar,³⁰ P. Kurnadi,⁶ M. A. C. Lamont,³ J. M. Landgraf,³ S. LaPointe,⁴⁹ J. Lauret,³ A. Lebedev,³ R. Lednický,¹³ C.-H. Lee,³⁴ M. J. LeVine,³ C. Li,³⁸ Y. Li,⁴³ G. Lin,⁵¹ X. Lin,⁵⁰ S. J. Lindenbaum,²⁷ M. A. Lisa,²⁹ F. Liu,⁵⁰ H. Liu,⁵ J. Liu,³⁶ L. Liu,⁵⁰ T. Ljubicic,³ W. J. Llope,³⁶ R. S. Longacre,³ W. A. Love,³ Y. Lu,³⁸ T. Ludlam,³ D. Lynn,³ G. L. Ma,³⁹ Y. G. Ma,³⁹ D. P. Mahapatra,¹⁴ R. Majka,⁵¹ O. I. Mall,⁵ L. K. Mangotra,¹⁸ R. Manweiler,⁴⁵ S. Margetis,¹⁹ C. Markert,⁴² H. S. Matis,²² Yu. A. Matulenko,³² T. S. McShane,¹⁰ A. Meschanin,³² J. Millane,²³ M. L. Miller,²³ N. G. Minaev,³² S. Mioduszewski,⁴¹ A. Mischke,²⁸ J. Mitchell,³⁶ B. Mohanty,⁴⁶ L. Molnar,³³ D. A. Morozov,³² M. G. Munhoz,³⁷ B. K. Nandi,¹⁵ C. Nattrass,⁵¹ T. K. Nayak,⁴⁶ J. M. Nelson,² C. Nepali,¹⁹ P. K. Netrakanti,³³ M. J. Ng,⁴ L. V. Nogach,³² S. B. Nurushev,³² G. Odyniec,²² A. Ogawa,³ H. Okada,³ V. Okorokov,²⁶ D. Olson,²² M. Pachr,¹¹ B. S. Page,¹⁶ S. K. Pal,⁴⁶ Y. Pandit,¹⁹ Y. Panebratsev,¹² T. Pawlak,⁴⁷ T. Peitzmann,²⁸ V. Perevoztchikov,³ C. Perkins,⁴ W. Peryt,⁴⁷ S. C. Phatak,¹⁴ M. Planinic,⁵² J. Pluta,⁴⁷ N. Poljak,⁵² A. M. Poskanzer,²² B. V. K. S. Potukuchi,¹⁸ D. Prindle,⁴⁸ C. Pruneau,⁴⁹ N. K. Pruthi,³⁰ J. Putschke,⁵¹ R. Raniwala,³⁵ S. Raniwala,³⁵ R. L. Ray,⁴² R. Reed,⁵ A. Ridiger,²⁶ H. G. Ritter,²² J. B. Roberts,³⁶ O. V. Rogachevskiy,¹² J. L. Romero,⁵ A. Rose,²² C. Roy,⁴⁰ L. Ruan,³ M. J. Russcher,²⁸ V. Rykov,¹⁹ R. Sahoo,⁴⁰ I. Sakrejda,²² T. Sakuma,²³ S. Salur,²² J. Sandweiss,⁵¹ M. Sarsour,⁴¹ J. Schambach,⁴² R. P. Scharenberg,³³ N. Schmitz,²⁴ J. Seger,¹⁰ I. Selyuzhenkov,¹⁶ P. Seyboth,²⁴ A. Shabetai,¹⁷ E. Shalaliev,¹² M. Shao,³⁸ M. Sharma,⁴⁹ S. S. Shi,⁵⁰ X.-H. Shi,³⁹ E. P. Sichtermann,²² F. Simon,²⁴ R. N. Singaraju,⁴⁶ M. J. Skoby,³³ N. Smirnov,⁵¹ R. Snellings,²⁸ P. Sorensen,³ J. Sowinski,¹⁶ H. M. Spinka,¹ B. Srivastava,³³ A. Stadnik,¹² T. D. S. Stanislaus,⁴⁵ D. Staszak,⁶ M. Strikhanov,²⁶ B. Stringfellow,³³ A. A. P. Suaide,³⁷ M. C. Suarez,⁹ N. L. Subba,¹⁹ M. Sumbera,¹¹ X. M. Sun,²² Y. Sun,³⁸ Z. Sun,²¹ B. Surrow,²³ T. J. M. Symons,²² A. Szanto de Toledo,³⁷ J. Takahashi,⁷ A. H. Tang,³ Z. Tang,³⁸ T. Tarnowsky,³³ D. Thein,⁴² J. H. Thomas,²² J. Tian,³⁹ A. R. Timmins,² S. Timoshenko,²⁶ D. Tlusty,¹¹ M. Tokarev,¹² V. N. Tram,²² A. L. Trattner,⁴ S. Trentalange,⁶ R. E. Tribble,⁴¹ O. D. Tsai,⁶ J. Ulery,³³ T. Ullrich,³ D. G. Underwood,¹ G. Van Buren,³ M. van Leeuwen,²⁸ A. M. Vander Molen,²⁵ J. A. Vanfossen Jr.,¹⁹ R. Varma,¹⁵ G. M. S. Vasconcelos,⁷ I. M. Vasilevski,¹³ A. N. Vasiliev,³² F. Videbaek,³ S. E. Vigdor,¹⁶ Y. P. Viyogi,¹⁴ S. Vokal,¹² S. A. Voloshin,⁴⁹ M. Wada,⁴² W. T. Waggoner,¹⁰ F. Wang,³³ G. Wang,⁶ J. S. Wang,²¹ Q. Wang,³³ X. Wang,⁴³ X. L. Wang,³⁸ Y. Wang,⁴³ J. C. Webb,⁴⁵ G. D. Westfall,²⁵ C. Whitten Jr.,⁶ H. Wieman,²² S. W. Wissink,¹⁶ R. Witt,⁴⁴ Y. Wu,⁵⁰ N. Xu,²² Q. H. Xu,²² Y. Xu,³⁸ Z. Xu,³ P. Yepes,³⁶ I.-K. Yoo,³⁴ Q. Yue,⁴³ M. Zawisza,⁴⁷ H. Zbroszczyk,⁴⁷ W. Zhan,²¹ H. Zhang,³ S. Zhang,³⁹ W. M. Zhang,¹⁹ Y. Zhang,³⁸ Z. P. Zhang,³⁸ Y. Zhao,³⁸ C. Zhong,³⁹ J. Zhou,³⁶ R. Zoulkarneev,¹³ Y. Zoulkarneeva,¹³ and J. X. Zuo³⁹

(STAR Collaboration)

¹Argonne National Laboratory, Argonne, Illinois 60439, USA²University of Birmingham, Birmingham, United Kingdom³Brookhaven National Laboratory, Upton, New York 11973, USA⁴University of California, Berkeley, California 94720, USA⁵University of California, Davis, California 95616, USA⁶University of California, Los Angeles, California 90095, USA⁷Universidade Estadual de Campinas, Sao Paulo, Brazil⁸Carnegie Mellon University, Pittsburgh, Pennsylvania 15213, USA⁹University of Illinois at Chicago, Chicago, Illinois 60607, USA

- ¹⁰*Creighton University, Omaha, Nebraska 68178, USA*
¹¹*Nuclear Physics Institute AS CR, CZ-25068 Řež/Prague, Czech Republic*
¹²*Laboratory for High Energy (JINR), Dubna, Russia*
¹³*Particle Physics Laboratory (JINR), Dubna, Russia*
¹⁴*Institute of Physics, Bhubaneswar 751005, India*
¹⁵*Indian Institute of Technology, Mumbai, India*
¹⁶*Indiana University, Bloomington, Indiana 47408, USA*
¹⁷*Institut de Recherches Subatomiques, Strasbourg, France*
¹⁸*University of Jammu, Jammu 180001, India*
¹⁹*Kent State University, Kent, Ohio 44242, USA*
²⁰*University of Kentucky, Lexington, Kentucky, 40506-0055, USA*
²¹*Institute of Modern Physics, Lanzhou, People's Republic of China*
²²*Lawrence Berkeley National Laboratory, Berkeley, California 94720, USA*
²³*Massachusetts Institute of Technology, Cambridge, Massachusetts 02139-4307, USA*
²⁴*Max-Planck-Institut für Physik, Munich, Germany*
²⁵*Michigan State University, East Lansing, Michigan 48824, USA*
²⁶*Moscow Engineering Physics Institute, Moscow, Russia*
²⁷*City College of New York, New York City, New York 10031, USA*
²⁸*NIKHEF and Utrecht University, Amsterdam, The Netherlands*
²⁹*Ohio State University, Columbus, Ohio 43210, USA*
³⁰*Panjab University, Chandigarh 160014, India*
³¹*Pennsylvania State University, University Park, Pennsylvania 16802, USA*
³²*Institute of High Energy Physics, Protvino, Russia*
³³*Purdue University, West Lafayette, Indiana 47907, USA*
³⁴*Pusan National University, Pusan, Republic of Korea*
³⁵*University of Rajasthan, Jaipur 302004, India*
³⁶*Rice University, Houston, Texas 77251, USA*
³⁷*Universidade de Sao Paulo, Sao Paulo, Brazil*
³⁸*University of Science & Technology of China, Hefei 230026, People's Republic of China*
³⁹*Shanghai Institute of Applied Physics, Shanghai 201800, People's Republic of China*
⁴⁰*SUBATECH, Nantes, France*
⁴¹*Texas A&M University, College Station, Texas 77843, USA*
⁴²*University of Texas, Austin, Texas 78712, USA*
⁴³*Tsinghua University, Beijing 100084, People's Republic of China*
⁴⁴*United States Naval Academy, Annapolis, Maryland 21402, USA*
⁴⁵*Valparaiso University, Valparaiso, Indiana 46383, USA*
⁴⁶*Variable Energy Cyclotron Centre, Kolkata 700064, India*
⁴⁷*Warsaw University of Technology, Warsaw, Poland*
⁴⁸*University of Washington, Seattle, Washington 98195, USA*
⁴⁹*Wayne State University, Detroit, Michigan 48201, USA*
⁵⁰*Institute of Particle Physics, CCNU (HZNU), Wuhan 430079, People's Republic of China*
⁵¹*Yale University, New Haven, Connecticut 06520, USA*
⁵²*University of Zagreb, Zagreb, HR-10002, Croatia*
(Received 18 August 2008; published 24 March 2009)

Identified charged-particle spectra of π^\pm , K^\pm , p , and \bar{p} at midrapidity ($|y| < 0.1$) measured by the dE/dx method in the STAR (solenoidal tracker at the BNL Relativistic Heavy Ion Collider) time projection chamber are reported for pp and $d + \text{Au}$ collisions at $\sqrt{s_{NN}} = 200$ GeV and for $\text{Au} + \text{Au}$ collisions at 62.4, 130, and 200 GeV. Average transverse momenta, total particle production, particle yield ratios, strangeness, and baryon production rates are investigated as a function of the collision system and centrality. The transverse momentum spectra are found to be flatter for heavy particles than for light particles in all collision systems; the effect is more prominent for more central collisions. The extracted average transverse momentum of each particle species follows a trend determined by the total charged-particle multiplicity density. The Bjorken energy density estimate is at least several GeV/fm³ for a formation time less than 1 fm/c. A significantly larger net-baryon density and a stronger increase of the net-baryon density with centrality are found in $\text{Au} + \text{Au}$ collisions at 62.4 GeV than at the two higher energies. Antibaryon production relative to total particle multiplicity is found to be constant over centrality, but increases with the collision energy. Strangeness production relative to total particle multiplicity is similar at the three measured RHIC energies. Relative strangeness production increases quickly

with centrality in peripheral Au + Au collisions, to a value about 50% above the pp value, and remains rather constant in more central collisions. Bulk freeze-out properties are extracted from thermal equilibrium model and hydrodynamics-motivated blast-wave model fits to the data. Resonance decays are found to have little effect on the extracted kinetic freeze-out parameters because of the transverse momentum range of our measurements. The extracted chemical freeze-out temperature is constant, independent of collision system or centrality; its value is close to the predicted phase-transition temperature, suggesting that chemical freeze-out happens in the vicinity of hadronization and the chemical freeze-out temperature is universal despite the vastly different initial conditions in the collision systems. The extracted kinetic freeze-out temperature, while similar to the chemical freeze-out temperature in pp , $d + \text{Au}$, and peripheral Au + Au collisions, drops significantly with centrality in Au + Au collisions, whereas the extracted transverse radial flow velocity increases rapidly with centrality. There appears to be a prolonged period of particle elastic scatterings from chemical to kinetic freeze-out in central Au + Au collisions. The bulk properties extracted at chemical and kinetic freeze-out are observed to evolve smoothly over the measured energy range, collision systems, and collision centralities.

DOI: [10.1103/PhysRevC.79.034909](https://doi.org/10.1103/PhysRevC.79.034909)

PACS number(s): 25.75.Nq, 25.75.Dw, 24.85.+p

I. INTRODUCTION

Quantum chromodynamics (QCD) predicts a phase transition at sufficiently high energy density from normal hadronic matter to a deconfined state of quarks and gluons, the quark-gluon plasma (QGP) [1–3]. Such a phase transition may be achievable in ultrarelativistic heavy-ion collisions. Many QGP signatures have been proposed which include rare probes (e.g., direct photon and dilepton production and jet modification) as well as bulk probes (e.g., enhanced strangeness and antibaryon production and strong collective flow) [4]. While rare probes are more robust, they are relatively difficult to measure. On the other hand, signals of QGP that are related to the bulk of the collision are most probably disguised or diluted by other processes such as the final state interaction. Simultaneous observations and systematic studies of multiple QGP signals in the bulk would, however, serve as strong evidence for QGP formation. These bulk properties include strangeness and baryon production rates and collective radial flow. These bulk observables can be studied via transverse momentum (p_\perp) spectra of identified particles in heavy-ion collisions in comparison with nucleon-nucleon and nucleon-nucleus reference systems.

This paper reports results on identified charged pions π^\pm , charged kaons K^\pm , protons p , and antiprotons \bar{p} at low p_\perp at midrapidity [5]. The results are measured by the STAR experiment in pp and $d + \text{Au}$ collisions at a nucleon-nucleon center-of-mass energy of $\sqrt{s_{NN}} = 200$ GeV and in Au + Au collisions at $\sqrt{s_{NN}} = 62.4, 130$, and 200 GeV. The particles are identified by their specific ionization energy loss in the detector material—the dE/dx method. Transverse momentum spectra, average transverse momenta, total particle production, particle yield ratios, and antibaryon and strangeness production rates are presented as a function of the event multiplicity for pp , $d + \text{Au}$, and Au + Au collisions. The paper also presents freeze-out parameters extracted from thermal equilibrium model and hydrodynamics-motivated blast-wave model fits to the data. The paper summarizes low p_\perp results from STAR with dE/dx particle identification, including the previously published data [6].

The paper is organized as follows: Section II describes the solenoidal tracker at RHIC (STAR) detector detector, followed by descriptions of event selection, track quality cuts, and

centrality definitions. Section III presents the dE/dx method for particle identification at low p_\perp . Section IV discusses the backgrounds and corrections applied at the event and track levels. Section V summarizes the systematic uncertainties of the measurements. Section VI presents results on identified particle p_\perp spectra, average $\langle p_\perp \rangle$, particle yields, and ratios. Section VII discusses the systematics of bulk properties extracted from a statistical model and the hydrodynamics-motivated blast-wave model. Section VIII summarizes the paper. Appendix A describes the details of the Glauber model calculations used in this paper. Appendix B discusses in detail the effect of resonance decays on the extracted kinetic freeze-out parameters. Appendix C lists tabulated data of transverse momentum spectra.

II. DETECTOR SETUP AND DATA SAMPLES

A. Detector setup and track reconstruction

Details of the STAR experiment can be found in Ref. [7]. The main detector of the STAR experiment is the time projection chamber (TPC) [8,9]. The cylindrical axis of the TPC is aligned to the beam direction and is referred to as the z direction. The TPC provides the full azimuthal coverage ($0 \leq \phi \leq 2\pi$) and a pseudorapidity coverage of $-1.8 < \eta < 1.8$.

Trigger selection of the experiment is obtained from the zero degree calorimeters (ZDCs) [10], the beam-beam counters (BBCs) [11], and the central trigger barrel (CTB) [12]. The ZDCs are located at ± 18 m along the z direction from the TPC center and measure neutral energy. The scintillator-based BBCs provide the principal relative luminosity measurement in pp data taking. The scintillator CTB surrounds the TPC and measures the charged-particle multiplicity within $|\eta| < 1$. The coincidence of the signals from the ZDCs and the BBCs selects minimum-bias (MB) events in pp and $d + \text{Au}$ collisions. Our minimum-bias pp events correspond to non-singly diffractive (NSD) pp collisions, whose cross section is measured to be 30.0 ± 3.5 mb [13]. The combination of the CTB and ZDC information provides the minimum-bias trigger for Au + Au collisions. In addition, a central trigger is constructed by imposing an upper cut on the ZDC signal

with a modest minimum CTB cut to exclude contamination from very peripheral events; the central trigger corresponds to approximately 12% of the total cross section. The trigger efficiencies are found to be approximately 86% and 95% in pp and $d + \text{Au}$, respectively, and essentially 100% in $\text{Au} + \text{Au}$ collisions.

The TPC is filled with P-10 gas (90% argon and 10% methane). Charged particles interact with the gas atoms while traversing the TPC gas volume and ionize the electrons out of the gas atoms. A drift electric field is provided along the z direction between the TPC central membrane and both ends of the TPC by a negative high voltage on the central membrane. Ionization electrons drift in the electric field toward the TPC ends. The TPC ends are divided into 12 equal-size bisectors and are equipped with read-out pads and front-end electronics. Multiwire proportional chambers (MWPCs) are installed close to the end pads inside the TPC. The drifting electrons avalanche in the high fields at the MWPC anode wires. The positive ions created in the avalanche induce a temporary image charge on the pads measured by a preamplifier/shaper/waveform digitizer system [9,14]. The original track positions (hits) are formed from the signals on each pad row (a row of read-out pads) by the hit reconstruction algorithm. Hits can be reconstructed to a small fraction of a pad width, because the induced charge from an avalanche is shared over several adjacent pads.

The TPC is located inside a magnet, which provides a magnetic field along the z direction for particle momentum measurements. Data are taken at a maximum magnetic field of 0.5 T. Inhomogeneities are on the level of 5×10^{-3} T and are incorporated in track reconstruction [15]. The direction of the magnetic field can be reversed to study systematic effects, which are found to be negligible for the bulk particles presented in this paper.

Track reconstruction starts from the outermost hits in the TPC, projecting inward assuming an initial primary vertex position at the center of the TPC. Hits on the pad rows are searched about the projected positions, and track segments are formed. Particle track momentum is estimated from the curvature of the track segments and the magnetic field strength. The momentum information is in turn used to refine further track projections. Track segments can be connected over short gaps from missed pad-row signals. Tracks are formed from track segments and are allowed to cross the TPC sector boundaries. The reconstructed tracks are called global tracks.

The primary interaction vertex is fit from the global tracks with at least ten hits. The distance of closest approach (d_{ca}) to the fit primary vertex is calculated for each global track. Iterations are made such that global tracks with $d_{\text{ca}} > 3$ cm are excluded from subsequent primary vertex fitting. Tracks with $d_{\text{ca}} < 3$ cm (from the final fit primary vertex position) and at least ten hits are called primary tracks. The primary tracks are refit including the primary vertex to improve particle track momentum determination. The reconstructed transverse momentum resolution is measured to be $\sigma_{\delta p_{\perp}} = 0.01 + p_{\perp}/(200 \text{ GeV}/c)$ [16]. The effect of the momentum resolution is negligible on the measured low p_{\perp} particle spectra reported here and is thus not corrected for. Only primary tracks are used in this analysis.

TABLE I. Summary of data sets, primary vertex cuts, and the number of good events (after cuts) used in the analysis.

Run	Data set	$\sqrt{s_{NN}}$ (GeV)	Year	Trigger	Max. $ z_{\text{vtx}} $	No. of events
I	Au + Au	130	2000	Min. bias	25 cm	2.0 million
I	Au + Au	130	2000	Central	25 cm	2.0 million
II	Au + Au	200	2001	Min. bias	30 cm	2.0 million
II	pp	200	2002	Min. bias	30 cm	3.9 million
III	$d + \text{Au}$	200	2003	Min. bias	50 cm	8.8 million
IV	Au + Au	62.4	2004	Min. bias	30 cm	6.4 million

B. Event selection and track quality cuts

Data sets used in this paper are from pp collisions at 200 GeV from run II, $d + \text{Au}$ collisions at 200 GeV from run III, and $\text{Au} + \text{Au}$ collisions at 62.4 GeV from run IV, at 130 GeV from run I, and at 200 GeV from run II. The pp and $\text{Au} + \text{Au}$ data at 200 GeV from run II have been published in Ref. [17], and the $\text{Au} + \text{Au}$ data for K^{\pm} , p , and \bar{p} at 130 GeV from run I have been published in Refs. [18–20]. These data are incorporated in this paper to provide a systematic overview. The pion spectra from the 130 GeV $\text{Au} + \text{Au}$ data are analyzed in this work. The data sets are summarized in Table I.

The longitudinal, z position of the interaction point is determined on-line by the measured signal time difference in the two ZDCs. A cut of the order of 50 cm on the z position of the interaction point from the TPC center is applied on-line for all data sets (except pp) in order to maximize the amount of useful data for physics analysis, since events with primary vertex far away from the TPC center have a significantly nonuniform acceptance. In off-line data analyses, further cuts are applied on the z position of the reconstructed primary vertex, z_{vtx} , to ensure nearly uniform detector acceptance and avoid multiplicity biases near the edges of the on-line cuts. These off-line cuts are listed in Table I. In addition, the x and y positions of the primary vertex are required to be within ± 3.5 cm of the beam, since the beam pipe diameter is 3 in.

The use of primary tracks significantly reduces contributions from background processes and pileup events in pp data. Tracks can have a maximum of 45 hits. In the analysis, at least 25 hits are required for each track to avoid track splitting effects. Singly charged particles must have a minimum p_{\perp} of 0.15 GeV/ c to exit the TPC in the 0.5 T magnetic field. In this analysis, tracks are required to have $p_{\perp} > 0.2$ GeV/ c . For the identified particle results in this paper, the rapidity region is restricted within $|y| < 0.1$ (i.e., midrapidity). The full 2π azimuthal coverage of the TPC is utilized.

C. Centrality measures

1. Centrality definitions

In $\text{Au} + \text{Au}$ collisions, the measured (uncorrected) charged-particle multiplicity density in the TPC within $|\eta| < 0.5$, $dN_{\text{ch}}^{\text{raw}}/d\eta$, is used for centrality selection. The primary tracks to be counted in the charged-particle multiplicity are required to have at least ten fit points (good primary tracks).

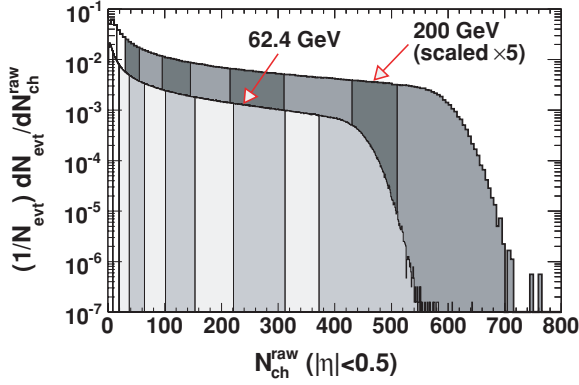


FIG. 1. (Color online) Uncorrected charged-particle multiplicity distribution measured in the TPC in $|\eta| < 0.5$ for Au + Au collisions at 62.4 and 200 GeV. The shaded regions indicate the centrality bins used in the analysis. The 200 GeV data are scaled by a factor of 5 for clarity.

The multiplicity distributions in Au + Au collisions at 62.4 and 200 GeV are shown in Fig. 1. Nine centrality bins are chosen, the same as in Ref. [17]; they correspond to the fraction of the measured total cross section from central to peripheral collisions of 0–5%, 5–10%, 10–20%, 20–30%, 30–40%, 40–50%, 50–60%, 60–70%, and 70–80%. The 80–100% centrality is not used in our analysis because of its significant trigger bias due to vertex inefficiency at low multiplicities and the contamination from electromagnetic interactions.

In $d + \text{Au}$ collisions, centralities are selected based on the charged-particle multiplicity measured in the east (Au-direction) forward time projection chamber (E-FTPC) [21] within the pseudorapidity range of $-3.8 < \eta < -2.8$. To be counted, tracks are required to have at least six hits out of 11 maximum and a $d_{ca} < 3$ cm. Additionally, the transverse momentum is required to not exceed 3 GeV/c because of the reduced momentum resolution and a significant background contamination at high p_\perp [21]. Figure 2(a) shows the measured (uncorrected) E-FTPC charged-particle multiplicity. Three centrality classes are defined, as indicated by the shaded regions, representing 40–100%, 20–40%, and 0–20%

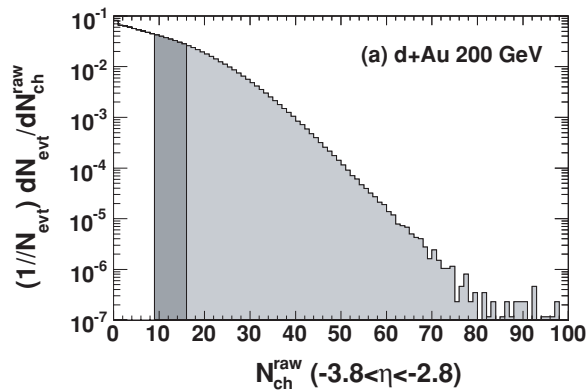


FIG. 2. (a) Uncorrected charged-particle multiplicity distribution measured in the E-FTPC (Au-direction) within $-3.8 < \eta < -2.8$ in $d + \text{Au}$ collisions at 200 GeV. The shaded regions indicate the centrality bins used in the analysis. (b) The TPC midrapidity multiplicity distributions ($|\eta| < 0.5$) for the corresponding E-FTPC selected centrality bins.

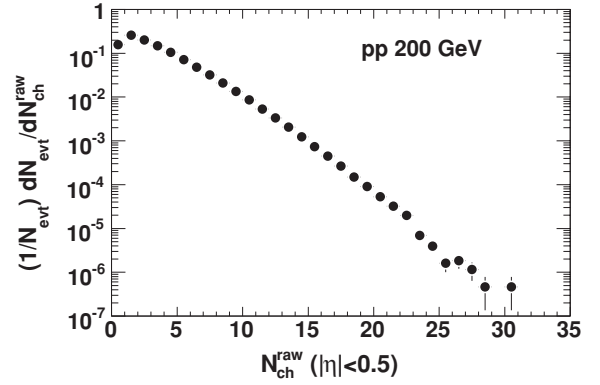


FIG. 3. Uncorrected charged-particle multiplicity distribution measured in the TPC within $|\eta| < 0.5$ in pp collisions at 200 GeV.

of the measured total cross section [22]. The midrapidity multiplicities measured in the TPC for the selected centrality bins are shown in Fig. 2(b). Positive correlation between the TPC multiplicity and the E-FTPC multiplicity is evident, although the correlation is not very strong because of the low multiplicities of $d + \text{Au}$ collisions.

The reason to use the FTPC multiplicity instead of the TPC midrapidity multiplicity for centrality selection is to avoid autocorrelation between centrality and the measurements of charged particles which are made within $|y| < 0.1$ in the TPC. The autocorrelation is not significant for Au + Au collisions because of their large multiplicities. The autocorrelation is significant for pp , and since the FTPC was not ready for data taking in the pp run, only minimum-bias data are presented for pp . For completeness, the uncorrected multiplicity distribution in minimum-bias pp collisions is shown in Fig. 3.

Table II summarizes the centralities for pp , $d + \text{Au}$, and Au + Au collisions.

2. Corrected charged-particle multiplicity

The results in this paper are presented as a function of centrality. As an experimental measure of centrality, the

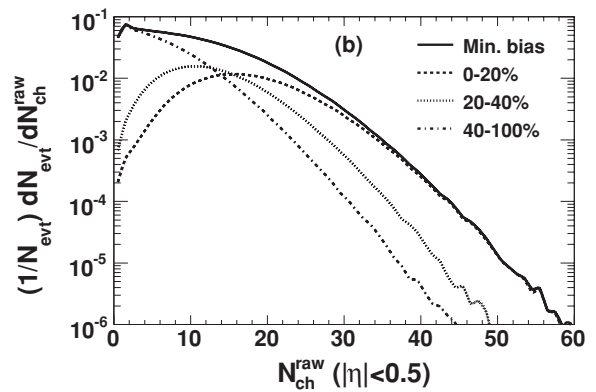


TABLE II. Summary of centralities in pp and $d + \text{Au}$ collisions at 200 GeV and in $\text{Au} + \text{Au}$ collisions at 62.4, 130, and 200 GeV. Our minimum-bias pp data correspond to NSD events with total cross section of 30.0 ± 3.5 mb. [13]. The centrality percentages in other systems are in terms of the measured total cross sections. The uncorrected charged-particle multiplicity $dN_{\text{ch}}^{\text{raw}}/d\eta$ for $d + \text{Au}$ is measured in the E-FTPC within $-3.8 < \eta < -2.8$, and for all other systems in the TPC within $|\eta| < 0.5$. The corrected charged-particle multiplicity $dN_{\text{ch}}/d\eta$ (and the corrected negatively charged-particle multiplicity $dN_{h^-}/d\eta$ for the 130 GeV $\text{Au} + \text{Au}$ data) are from the TPC within $|\eta| < 0.5$. The multiplicity rapidity density dN/dy are from the rapidity slice of $|y| < 0.1$. The 200 GeV pp and $\text{Au} + \text{Au}$ data are from Ref. [17]; the 130 GeV data are from Ref. [23] and this work; and the 200 GeV $d + \text{Au}$ and 62.4 GeV $\text{Au} + \text{Au}$ data are from this work. The Monte Carlo Glauber model is used in the calculation of the impact parameter (b), the number of participant nucleons (N_{part}), the number of binary nucleon-nucleon collisions (N_{coll}), and the overlap area between the colliding nuclei in the transverse plane (S_{\perp}). The nucleon-nucleon cross sections used in the calculations are 36 ± 2 , 39 ± 2 , and 41 ± 2 mb for 62.4, 130, and 200 GeV, respectively. The Glauber model results for $d + \text{Au}$ are from Ref. [24], and for all other systems from this work. The quoted errors are total statistical and systematic uncertainties added in quadrature.

Centrality	$dN_{\text{ch}}^{\text{raw}}/d\eta$		$dN_{\text{ch}}/d\eta$	$dN_{h^-}/d\eta$	dN_{ch}/dy	b (fm)		N_{part}	N_{coll}	S_{\perp} (fm ²)
	Range	Mean				Range	Mean			
<hr/>										
<i>pp</i> 200 GeV										
Min. bias	–	2.4	2.98 ± 0.34		3.40 ± 0.23	–	–	2	1	4.1 ± 0.7
<i>d + Au</i> 200 GeV										
Min. bias	–	10.2	10.2 ± 0.68		11.3 ± 0.7			8.31 ± 0.37	7.51 ± 0.39	
40–100%	0–9	6.2	6.23 ± 0.34		6.98 ± 0.44			5.14 ± 0.44	4.21 ± 0.49	
20–40%	10–16	12.6	14.1 ± 1.0		14.9 ± 0.9			11.2 ± 1.1	10.6 ± 0.8	
0–20%	≥ 17	17.6	19.9 ± 1.6		20.9 ± 1.3			15.7 ± 1.2	15.1 ± 1.3	
<i>Au + Au</i> 200 GeV										
<i>Au + Au</i> ($\sigma_{pp} = 41$ mb)										
70–80%	14–29	22.5	22 ± 2		26.5 ± 1.8	12.3–13.2	12.8 ± 0.3	15.7 ± 2.6	15.0 ± 3.2	17.8 ± 2.2
60–70%	30–55	43.1	45 ± 3		52.1 ± 3.5	11.4–12.3	11.9 ± 0.3	28.8 ± 3.7	32.4 ± 5.5	27.2 ± 2.5
50–60%	56–93	74.8	78 ± 6		90.2 ± 6.0	10.5–11.4	11.0 ± 0.3	49.3 ± 4.7	66.8 ± 9.0	38.8 ± 2.7
40–50%	94–145	120	126 ± 9		146 ± 10	9.33–10.5	9.90 ± 0.23	78.3 ± 5.3	127 ± 13	52.1 ± 2.7
30–40%	146–216	181	195 ± 14		222 ± 15	8.10–9.33	8.73 ± 0.19	117.1 ± 5.2	221 ± 17	67.5 ± 2.9
20–30%	217–311	264	287 ± 20		337 ± 23	6.61–8.10	7.37 ± 0.16	167.6 ± 5.4	365 ± 24	86.1 ± 3.1
10–20%	312–430	370	421 ± 30		484 ± 33	4.66–6.61	5.70 ± 0.14	234.3 ± 4.6	577 ± 36	109.8 ± 3.4
5–10%	431–509	470	558 ± 40		648 ± 44	3.31–4.66	4.03 ± 0.13	298.6 ± 4.1	805 ± 50	133.0 ± 3.5
0–5%	≥ 510	559	691 ± 49		811 ± 56	0–3.31	2.21 ± 0.07	350.6 ± 2.4	1012 ± 59	153.9 ± 4.3
<i>Au + Au</i> 130 GeV										
<i>Au + Au</i> ($\sigma_{pp} = 39$ mb)										
58–85%	11–57	30.8		17.9 ± 1.3	39.5 ± 4.0	11.1–13.4	12.3 ± 0.4	22.6 ± 5.0	24.4 ± 7.0	21.9 ± 3.6
45–58%	57–105	80.3		47.3 ± 3.3	105 ± 8	9.77–11.1	10.5 ± 0.3	61.0 ± 7.8	88 ± 16	43.4 ± 3.8
34–45%	105–163	133		78.9 ± 5.5	177 ± 11	8.50–9.77	9.15 ± 0.28	100.9 ± 8.4	175 ± 22	60.2 ± 3.7
26–34%	163–217	190		115 ± 8	257 ± 18	7.43–8.50	7.99 ± 0.25	141.9 ± 8.4	280 ± 26	75.6 ± 3.9
18–26%	217–286	251		154 ± 11	348 ± 24	6.19–7.43	6.82 ± 0.21	187.7 ± 7.5	411 ± 31	91.9 ± 3.8
11–18%	286–368	327		196 ± 14	460 ± 34	4.83–6.19	5.55 ± 0.18	237.8 ± 6.8	568 ± 39	109.7 ± 3.7
6–11%	368–417	392		236 ± 17	562 ± 35	3.58–4.83	4.23 ± 0.16	289.0 ± 5.4	739 ± 49	127.8 ± 3.7
0–6%	≥ 417	462		290 ± 20	695 ± 45	0–3.58	2.39 ± 0.09	344.3 ± 3.1	945 ± 58	149.5 ± 4.3
<i>Au + Au</i> 62.4 GeV										
<i>Au + Au</i> ($\sigma_{pp} = 36$ mb)										
70–80%	9–19	12.4	13.9 ± 1.1		17.7 ± 1.3	12.3–13.1	12.7 ± 0.3	15.3 ± 2.4	14.1 ± 2.8	16.1 ± 2.0
60–70%	20–37	26.8	29.1 ± 2.2		35.8 ± 2.8	11.4–12.3	11.8 ± 0.3	27.8 ± 3.7	30.0 ± 5.2	24.8 ± 2.4
50–60%	38–64	49.1	53.1 ± 4.2		65.0 ± 5.0	10.4–11.4	10.9 ± 0.2	47.9 ± 4.7	61.2 ± 8.2	35.8 ± 2.6
40–50%	65–101	81.0	87.2 ± 7.1		107 ± 8	9.27–10.4	9.83 ± 0.23	76.3 ± 5.2	115 ± 12	48.7 ± 2.7
30–40%	102–153	125.2	135 ± 11		166 ± 11	8.05–9.27	8.67 ± 0.19	114.3 ± 5.1	199 ± 16	63.6 ± 2.8
20–30%	154–221	184.8	202 ± 17		249 ± 16	6.56–8.05	7.32 ± 0.17	164.1 ± 5.4	325 ± 23	81.6 ± 3.1
10–20%	222–312	263.6	292 ± 25		359 ± 24	4.63–6.56	5.67 ± 0.14	229.8 ± 4.6	511 ± 34	104.6 ± 3.3
5–10%	313–372	340.5	385 ± 33		476 ± 30	3.29–4.63	4.00 ± 0.13	293.9 ± 4.2	710 ± 47	127.2 ± 3.6
0–5%	≥ 373	411.8	472 ± 41		582 ± 38	0–3.29	2.20 ± 0.07	346.5 ± 2.8	891 ± 57	147.5 ± 4.3

corrected charged-particle rapidity density (dN_{ch}/dy) is used. It is obtained from the identified charged-particle spectra (π^{\pm} , K^{\pm} , \bar{p} , and p) as the sum of the individual rapidity densities. The identified charged-particle spectra are either

from prior STAR publications [17–20] or obtained by this work [5]. The charged-particle rapidity densities are listed in Table II for various systems and centralities. The systematic uncertainties on dN_{ch}/dy are discussed in Sec. V B.

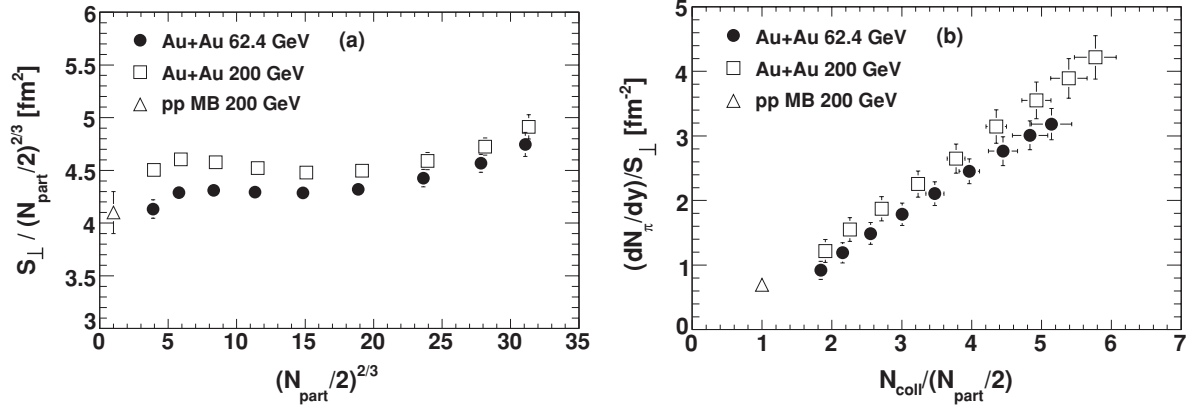


FIG. 4. (a) Ratio of the transverse overlap area S_{\perp} to $(N_{\text{part}}/2)^{2/3}$ vs $(N_{\text{part}}/2)^{2/3}$. (b) Ratio of the charged-pion multiplicity to the transverse overlap area $\frac{dN_{\pi}/dy}{S_{\perp}}$ vs $N_{\text{coll}}/N_{\text{part}}$. Errors shown are total errors, dominated by systematic uncertainties. The systematic uncertainties are correlated between N_{part} , N_{coll} , and S_{\perp} , and are largely canceled in the plotted ratio quantities.

Another commonly used centrality measure is the charged-particle pseudorapidity density, either uncorrected ($dN_{\text{ch}}^{\text{raw}}/d\eta$) or corrected ($dN_{\text{ch}}/d\eta$) for detector losses and tracking efficiency. These quantities are also listed in Table II for reference. The correction is done using reconstruction efficiency of pions obtained from embedding Monte Carlo (see Sec. IV D). This is because the efficiencies at high p_{\perp} are the same for different particle species, and at low p_{\perp} charged particles are dominated by pions. The pseudorapidity multiplicity density data for 130 GeV are from Ref. [25], for pp and Au + Au at 200 GeV from Ref. [17], and for $d + \text{Au}$ at 200 GeV and Au + Au at 62.4 GeV from this work.

3. Glauber model calculations

While the charged-hadron multiplicity is a viable experimental way to characterize centrality, it is sometimes desirable to use other variables directly connected to the collision geometry. Those variables include the number of participant nucleons (N_{part}), the number of nucleon-nucleon binary collisions (N_{coll}), and the ratio of the charged-pion rapidity density to the transverse overlap area of the colliding nuclei ($\frac{dN_{\pi}/dy}{S_{\perp}}$). Many models have studied particle production mechanisms based on these centrality variables. For example, the two-component model [26–28], characterizing particle production by a linear combination of N_{part} and N_{coll} , can describe the multiplicity density well, allowing the extraction of the relative fractions of the two components. The gluon saturation model [29–33] predicts a suppressed multiplicity in heavy-ion collisions relative to the N_{coll} -scaled pp collision multiplicity, with an increased $\langle p_{\perp} \rangle$ for the produced particles. The relevant and perhaps only scale in such a gluon-saturation picture is $\frac{dN_{\pi}/dy}{S_{\perp}}$ [29].

Unfortunately, N_{part} , N_{coll} , and the transverse overlap area S_{\perp} cannot be measured directly from collider experiments, so they have to be extracted from the measured multiplicity distributions via models, such as the Glauber model [34,35]. The essential ingredient is to match the calculated cross

section vs impact parameter ($d\sigma/db$) to the measured cross section vs charged multiplicity ($d\sigma/dN_{\text{ch}}$), exploiting the fact that the average multiplicity should monotonically increase with decreasing impact parameter b . The matching relates the measured N_{ch} to b (and thus N_{part} and N_{coll}).

Two different schemes are used to implement the Glauber model: the optical calculation and the Monte Carlo (MC) calculation. The details of the optical and MC Glauber calculations are described in Appendix A. In this work, the MC Glauber calculation is used except when otherwise noted. The N_{part} , N_{coll} , and S_{\perp} for Au + Au collisions from the MC Glauber model calculation are listed in Table II. For pp collisions, the overlap area S_{\perp} is simply taken as the pp cross section σ_{pp} . For $d + \text{Au}$ collisions, the N_{part} and N_{coll} are calculated using the realistic wave function for the deuteron in Ref. [24].

Figure 4(a) shows the ratio of S_{\perp} to $(N_{\text{part}}/2)^{2/3}$ as a function of $(N_{\text{part}}/2)^{2/3}$. The overlap area S_{\perp} scales with $(N_{\text{part}}/2)^{2/3}$ to a good approximation, and the scaling factor is the proton-proton cross section used in the Glauber calculation, $\sigma_{pp} = 36$ and 41 mb for 62.4 and 200 GeV, respectively. Figure 4(b) shows the ratio of the charged-pion multiplicity to the transverse overlap area $\frac{dN_{\pi}/dy}{S_{\perp}}$ as a function of $\frac{N_{\text{coll}}}{N_{\text{part}}/2}$, the average number of binary collisions per participant nucleon pair. As seen from the figure, the two quantities have monotonic correspondence and have little dependence on beam energy (i.e., on the value of σ_{pp}).

III. PARTICLE IDENTIFICATION BY dE/dx

Charged particles, while traversing the TPC gas volume, interact with the gas atoms and lose energy by ionizing electrons out of the gas atoms. This specific ionization energy loss, called the dE/dx , is a function of the particle momentum magnitude. This property is used for particle identification. This paper focuses on particle identification in the low p_{\perp} region. This section describes the low $p_{\perp} dE/dx$

particle identification method in detail. Extension of particle identification to high p_\perp is possible by the time of flight (TOF) patch [36,37] and by using the relativistic rise of the specific ionization energy loss ($r \, dE/dx$) [16]. The details of the TOF and $r \, dE/dx$ methods are out of the scope of this paper.

The electron ionization process has large fluctuations; the measured dE/dx sample for a given track length follows the Landau distribution. The Landau tail results in a large fluctuation in the average dE/dx . To reduce fluctuation, a truncated mean $\langle dE/dx \rangle$ is used to characterize the ionization energy loss of charged particles. In this analysis, the truncated mean $\langle dE/dx \rangle$ is calculated from the lowest 70% of the measured dE/dx values of the hits for each track. The resolution of the obtained $\langle dE/dx \rangle$ depends on the track length and particle momentum. For a minimum ionizing pion at momentum $p = 0.5$ GeV/c with long track length (45 hits), the resolution is measured to be 8–9% in central Au + Au collisions. The resolution is better in pp , $d + \text{Au}$, and peripheral Au + Au collisions because of less cluster overlapping.

The ionization energy loss by charged particles in material is given by the Bethe-Bloch formula [38] and for thin material by the more precise Bichsel formula [39]. At low momentum, ionization energy loss is approximately inversely proportional to the particle velocity squared. With the measured particle momentum and $\langle dE/dx \rangle$, the particle type can be determined by comparing the measurements against the Bethe-Bloch expectation. Figure 5(a) shows the measured $\langle dE/dx \rangle$ vs momentum magnitude for particles in $|\eta| < 0.1$. Various bands, corresponding to different mass particles, are clearly separated at low p_\perp . At modest p_\perp , the bands start to overlap: e^\pm and K^\pm merge at ~ 0.5 GeV/c, K^\pm and π^\pm merge at ~ 0.75 GeV/c, and p (\bar{p}) and π^\pm merge at ~ 1.2 GeV/c. However, particles can still be *statistically* identified by a fitting procedure to deconvolute the overlapped distribution into several components. The separation of the dE/dx bands depends on the pseudorapidity region and decreases toward higher rapidities. To obtain maximal

separation, we only concentrate on the midrapidity region of $|y| < 0.1$.

Since the $\langle dE/dx \rangle$ distribution for a fixed particle type is not Gaussian [40], a new variable is useful in order to have a proper deconvolution into Gaussians. It is shown [40] that a better Gaussian variable, for a given particle type, is the z variable, defined as

$$z_i = \ln \left(\frac{\langle dE/dx \rangle}{\langle dE/dx \rangle_i^{\text{BB}}} \right), \quad (1)$$

where $\langle dE/dx \rangle_i^{\text{BB}}$ is the Bethe-Bloch (Bichsel [39]) expectation of $\langle dE/dx \rangle$ for the given particle type i ($i = \pi, K, p$). In this analysis, $\langle dE/dx \rangle_i^{\text{BB}}$ is parametrized as

$$\langle dE/dx \rangle_i^{\text{BB}} = A_i \left(1 + \frac{m_i^2}{p_{\text{mag}}^2} \right), \quad (2)$$

where m_i is the particle rest mass and p_{mag} is the particle momentum magnitude. This parametrization is found to describe the data well, with the normalization factor A_i determined from data. The expected value of z_i for the particle in study is around 0. The z_K variable is shown for K^- in Fig. 5(b), where the kaon band is situated around 0.

The z_i distribution is constructed for a given particle type in a given p_\perp bin within $|y| < 0.1$. Figure 6 shows the z_π and z_K distributions, each for two p_\perp bins. The distributions show a multi-Gaussian structure. To extract the raw particle yield for a given particle type, a multi-Gaussian fit is applied to the z_i distribution as superimposed in Fig. 6. The parameters of the multi-Gaussian fit are the centroids, widths, and amplitudes for π^\pm , e^\pm , K^\pm , \bar{p} , and p . The positive and negative particle z_i distributions are fit simultaneously. The particle and antiparticle centroids and widths are kept the same. The centroid of the particle type in study is not fixed at zero but treated as a free parameter, because the parametrization by Eq. (2) is only approximate. For the large p_\perp bins where the $\langle dE/dx \rangle$ bands merge, the Gaussian widths

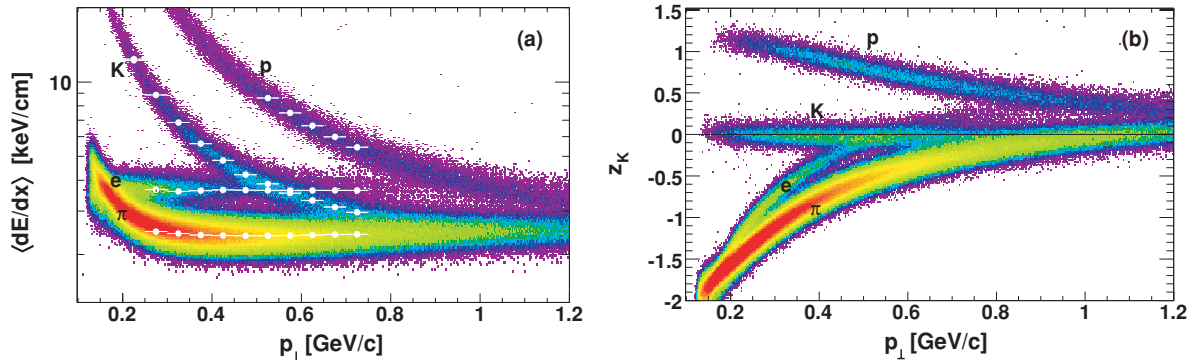


FIG. 5. (Color online) (a) Truncated $\langle dE/dx \rangle$ of specific ionization energy loss of π^- , e^- , K^- , and \bar{p} as a function of p_\perp for particles in $|\eta| < 0.1$ measured in 200 GeV minimum-bias pp collisions by the STAR-TPC. The Gaussian centroids for π^- , e^- , K^- and \bar{p} fit to the kaon z_K distributions are shown with circles. (b) z_K variable for kaon vs p_\perp in 200 GeV minimum-bias pp collisions. Particles are restricted in $|y_K| < 0.1$ where the kaon mass is used in the rapidity calculation. In this narrow rapidity (or pseudorapidity) slice, p_\perp is approximately equal to p_{mag} .

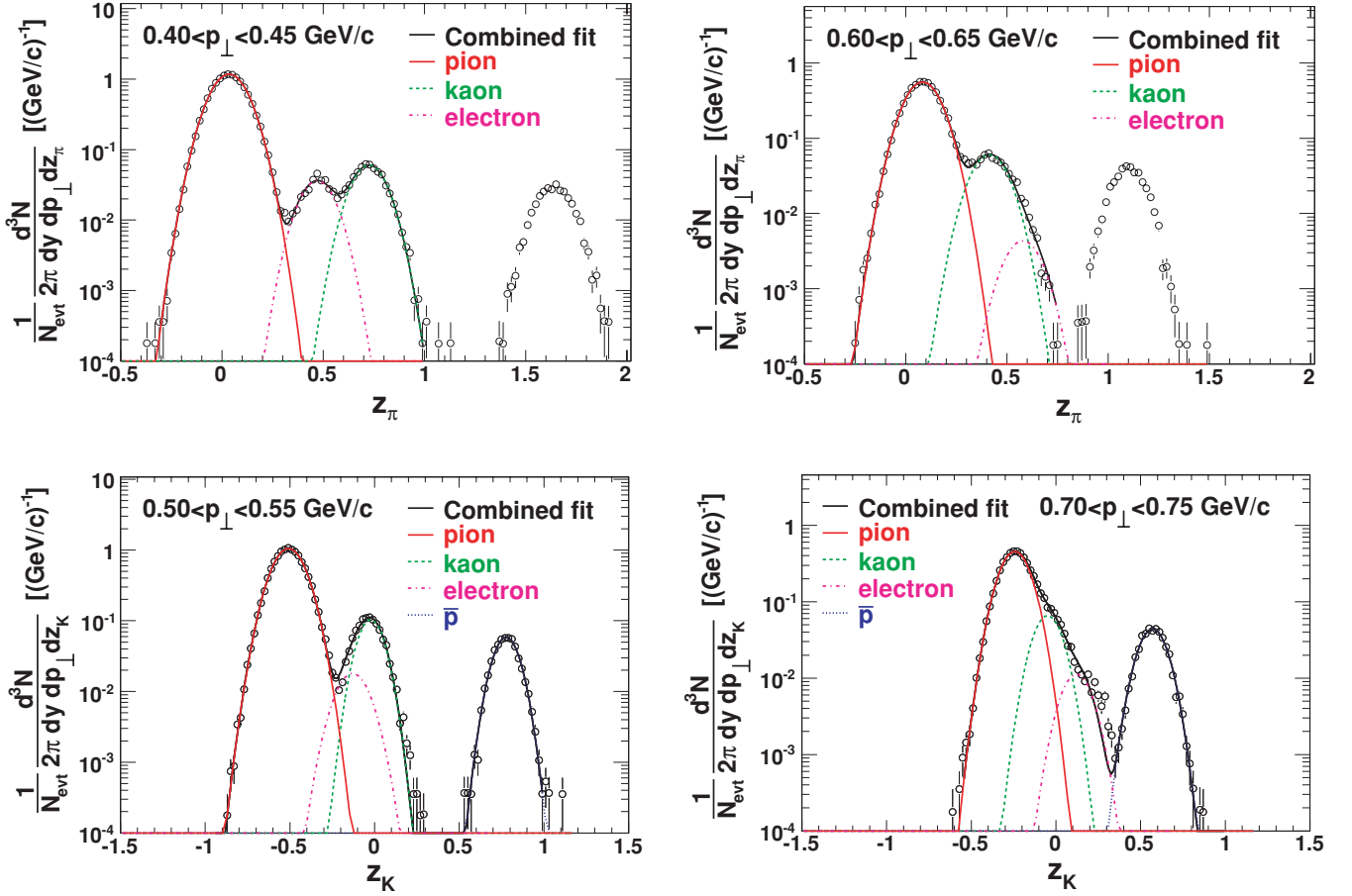


FIG. 6. (Color online) Distributions of z_π for π^- (upper panels) and z_K for K^- (lower panels) in 200 GeV minimum-bias pp collisions. Four p_\perp bins are shown. Errors shown are statistical only. The curves represent the Gaussian fits to the z_π and z_K distributions, with individual particle peaks plotted separately.

for all three particle species are kept the same. The fit centroids of π^- , e^- , K^- , and \bar{p} , where K^- is the particle type in study, are superimposed on Fig. 5(a) as a function of p_\perp . The kaon z_K fit centroid is very close to zero, affirming the good description of $\langle dE/dx \rangle_K^{\text{BB}}$ by Eq. (2) at low p_\perp .

The particle yield extracted from the fit to the corresponding z distribution is the raw yield. The fit yields for the other particle peaks cannot be used, because the rapidity calculation is incorrect for those particle types. Thus, the same procedure is repeated for each particle type separately.

As shown in Fig. 5, particle identification as a function of momentum magnitude is limited because of the merging of the dE/dx bands at large p_\perp . Pions can be identified in the momentum range of 0.2–0.7 GeV/c, kaons 0.2–0.7 GeV/c, and (anti)protons 0.35–1.2 GeV/c. Kaon identification is particularly difficult, because electrons are merged into the kaon band above $p_\perp > 0.5$ GeV/c. To extract the kaon yield at relatively large p_\perp , electron contributions are interpolated to the dE/dx overlapping p_\perp range and are then fixed. The uncertainties in the estimation of electron contaminations are the main source of systematic uncertainties on the extracted kaon yields at large p_\perp , as discussed in Sec. V.

IV. CORRECTIONS AND BACKGROUNDS

A. Monte Carlo embedding technique

The correction factors are obtained by the multistep embedding MC technique. First, simulated tracks are blended into real events at the raw data level. Real data events to be used in the embedding are sampled over the entire data-taking period in order to have proper representation of the whole data set used in the analysis. MC tracks are simulated with primary vertex position taken from the real events. The MC track kinematics are taken from flat distributions in η and p_\perp . The flat p_\perp distribution is used in order to have similar statistics in different p_\perp bins. The number of embedded MC tracks is of the order of 5% of the measured multiplicity in real events. The tracks are propagated through the full simulation of the STAR detector and geometry using GEANT with a realistic simulation of the STAR-TPC response. The simulation starts with the initial ionization of the TPC gas by charged particles, followed by electron transport and multiplication in the drift field, and finally the induced signal on the TPC read-out pads and the response of the read-out electronics. All physical processes (hadronic interaction, decay, multiple scattering, etc.) are turned on in the GEANT simulation. The obtained raw

data pixel information for the simulated particles are added to the existing information of the real data. Detector effects such as the saturation of ADC channels are taken into account. The format of the resulting combined events is identical to that of the real raw data events.

Second, the mixed events are treated just as real data and are processed through the full reconstruction chain. Clusters and hits are formed from the pixel information; tracks are reconstructed from the hits.

Third, an association map is created between the input MC tracks and the reconstructed tracks of the mixed event. The association is made by matching hits by proximity.¹ For each MC hit from GEANT, a search for reconstructed hits from the embedded event is performed with a window of ± 6 mm in x , y , and z [25]. The window size is chosen based on the hit resolution and the typical occupancy of the TPC in central Au + Au collisions. If a reconstructed hit is found in the search window, the MC hit is marked as matched. The MC track is considered to be reconstructed if more than ten of its hits are matched to a single reconstructed track in the embedded event. Multiple associations are allowed, but the probability is small of having a single MC track matched with two or more reconstructed tracks or vice versa. From the multiple associations, the effects of track splitting (two reconstructed tracks matched to one MC track) and track merging (two MC tracks matched to a single reconstructed track) can be studied. The reconstruction efficiency is obtained by the ratio of the number of matched MC tracks to the number of input MC tracks. The reconstruction efficiency contains the net effect of tracking efficiency, detector acceptance, decays, and interaction losses.

The most critical quality assurance is to make sure that the MC simulation reproduces the characteristics of the real data. This is carried out by comparing various distributions from real data and from embedding MC; see Figs. 7–9.

Figure 7 shows the longitudinal and transverse hit residuals for matched MC tracks from embedding and for real data tracks. The hit residuals are compared as a function of the dip angle (the angle between the particle momentum and the z direction), the crossing angle (the angle between the particle momentum and the TPC pad-row direction [8,9]), and the hit z position. Good agreement is found, as seen from Fig. 7. The observed differences are small relative to the typical TPC occupancy and do not affect the obtained reconstruction efficiency.

Figure 8 shows the d_{ca} distributions of kaons reconstructed from matched MC kaon tracks and kaon candidates from real data. Kaon candidates are selected from real data by applying a tight dE/dx cut of $\pm 0.5\sigma$ around the kaon Bethe-Bloch curve. Kaons are used because they contain minimal weak decay contributions and other background so that their d_{ca} distributions give a good assessment of the quality of the embedding data. Good agreement is found between embedding MC and real data.

¹Another possible matching algorithm is the identity (ID) truth method, where the track ID information is propagated to the reconstructed hits.

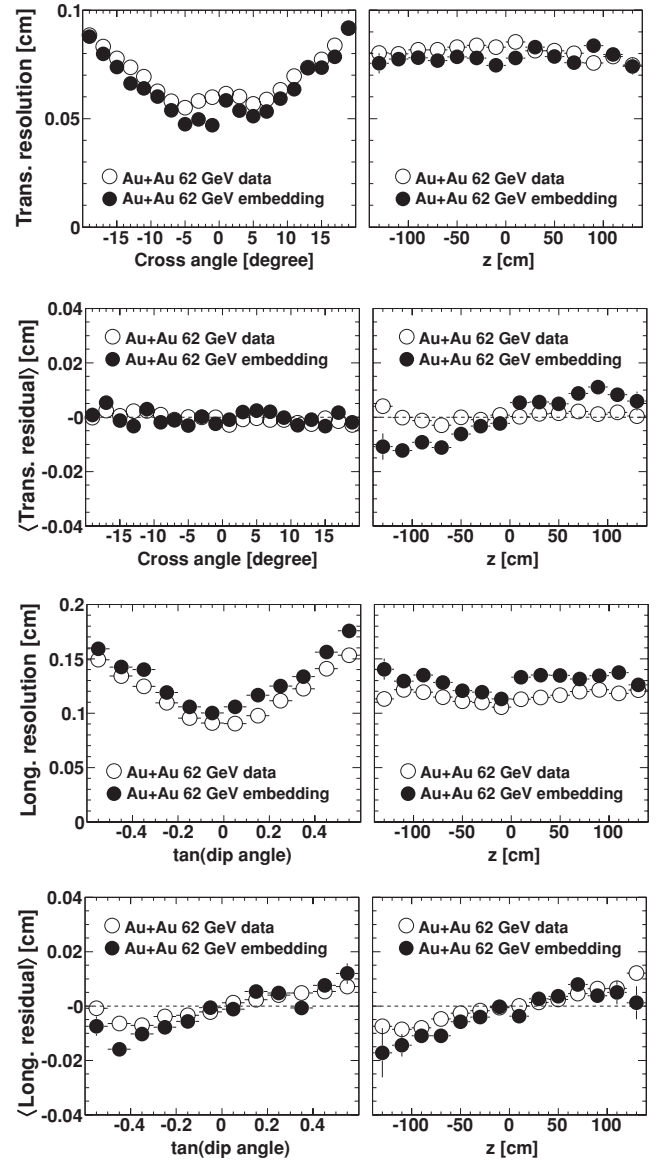


FIG. 7. Hit resolution and mean hit residual as a function of the track crossing angle at the hit position, the track dip angle, and the hit z coordinate. The data are an enriched K^+ sample (via dE/dx cut) within $|y| < 1$ and $0.4 < p_{\perp} < 0.5$ GeV/ c in 62.4 GeV Au + Au collisions. Errors shown are statistical only.

Figure 9 shows a comparison of the number of hits distributions between reconstructed pions from MC embedding and pion candidates from real data. Pion candidates are selected by applying a dE/dx cut of $|z_{\pi}| < 0.3$. Good agreement is found. The small differences found at large number of hits do not affect the calculated reconstruction efficiency, because the cut on the number of hits is 25, which is significantly below the peak of the hit distribution.

B. Energy loss correction

Low momentum particles lose significant amounts of energy while traversing the detector material [38]. The track

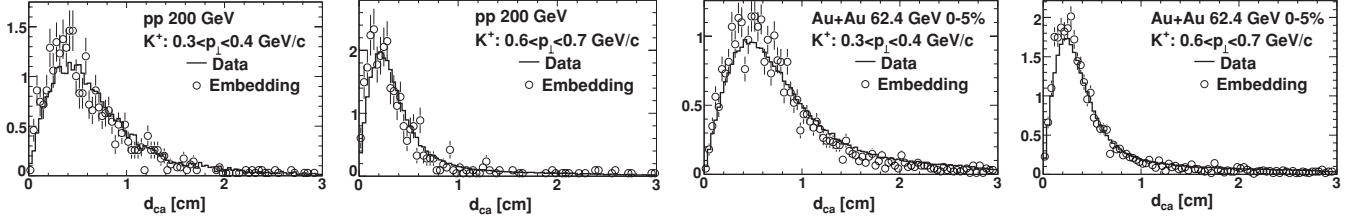


FIG. 8. Comparison of d_{ca} distributions between K^+ candidates from real data and K^+ from MC embedding. Two p_{\perp} bins are shown for 200 GeV pp collisions and for 62.4 GeV 5% central Au + Au collisions, respectively. Kaon candidates are selected from data by a dE/dx cut of $\pm 0.5\sigma$ from the Bethe-Bloch expected values. Errors shown are statistical only. The distributions have been normalized to unit area to only compare the shapes.

reconstruction algorithm takes into account the Coulomb scattering and the energy loss, while assuming pion mass for each particle. A correction for the energy loss in the momenta of the heavier particles (K^{\pm} , p , and \bar{p}) is needed. The correction is obtained from embedding MC. Figure 10 shows the difference between the measured transverse momentum and the MC input transverse momentum, $p_{\perp}^{\text{meas}} - p_{\perp}^{\text{MC}}$, vs the measured momentum magnitude, p^{meas} , for particles within $|y| < 0.1$. The profile can be parametrized to provide the correction function for the measured momentum:

$$p_{\perp} - p_{\perp}^{\text{meas}} = \delta_0 + \delta \left(1 + \frac{m^2}{(p^{\text{meas}})^2} \right)^{\alpha}. \quad (3)$$

Here m is the mass of the particle, and δ_0 , δ , and α are the fit parameters. The fit values are $\delta_0 = 0.006(0.013)$ GeV/c, $\delta = -0.0038(-0.0081)$ GeV/c, and $\alpha = 1.10(1.03)$ for K^{\pm} (p and \bar{p}), respectively.

The energy loss correction shows little centrality dependence as expected. It only depends on the detector geometry of a given run. Although the silicon strip detector [41] was installed in STAR after the 200 GeV pp and Au + Au runs, there is no observable change in the magnitude of the correction for the subsequent 200 GeV $d + Au$ and 62.4 GeV Au + Au runs. We have also investigated energy loss in different rapidity windows to assess possible systematic effects. No evidence for rapidity dependence of the energy loss is found; the energy loss correction is observed to be the same for symmetric rapidity cuts within $|y| < 0.5$.

The energy loss correction is applied off-line to all tracks using the correction formula for the given particle type of interest (i.e., the particle type being analyzed with the z_i distribution). For all the results presented in this paper, the corrected p_{\perp} is used.

C. Vertex inefficiency and fake vertex

Several labels are used in this section to refer to tracks used for different purposes: global tracks, *good* global tracks, primary tracks, *good* primary tracks, and primary tracks used in the particle spectra analysis. They are listed in Table III with the corresponding definitions and cuts.

In high-multiplicity Au + Au collisions, the primary vertex can be determined accurately. In pp and $d + Au$ collisions, where charged-particle multiplicity is low, the vertex-finding algorithm (an already improved and better-tuned version [11] than the one used for Au + Au data) occasionally fails to find a primary vertex. In addition, at high luminosity, the vertex finder can fail as a result of the confusion from pileup events, and, in some cases, it provides a wrong reconstructed vertex.

To study the pileup effect, two simulated sets of pp events are mixed at the raw data level, and the combined set is reconstructed by the full reconstruction chain. The first set is considered the real event, and the other set is used as the pileup background event. The pileup level is varied from 0 to 100%, where 100% means each real event has a pileup event in it. (The real pp data from run II have a much smaller rate than this.) The reconstructed numbers of good global tracks and good primary tracks of the mixed event are examined as a function of the pileup level. The number of good primary tracks, N_{prim} , is found to be independent of the degree of pileup level. The number of good global tracks, N_{glob} , increases with increasing pileup level. Therefore, N_{prim} is chosen to characterize the vertex-finding efficiency. This is also desirable because only the number of primary tracks represents the true event of interest.

The vertex-finding efficiencies in pp and $d + Au$ collisions are studied by HIJING MC events [42] embedded into abort-gap events (events triggered and reconstructed at empty bunch

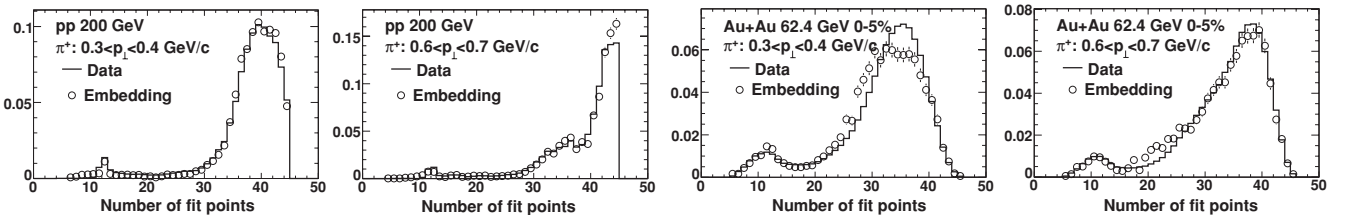


FIG. 9. Comparison of distributions of the number of fit points between π^- candidates from real data and π^- from MC embedding. Two p_{\perp} bins are shown for 200 GeV pp collisions and for 62.4 GeV 5% central Au + Au collisions. Pion candidates are selected by a dE/dx cut of $|z_{\pi}| < 0.3$. Errors shown are statistical only. The distributions have been normalized to unit area to only compare the shapes.

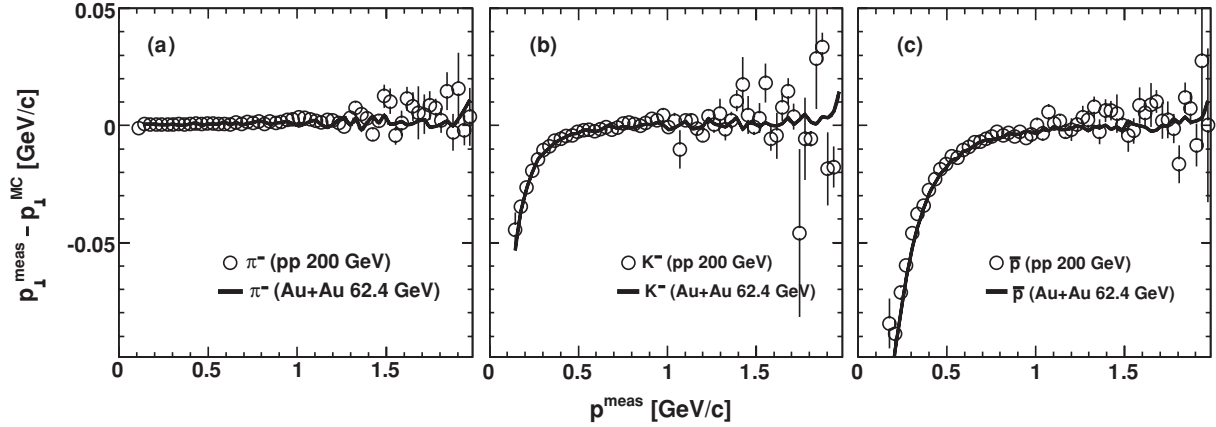


FIG. 10. Energy loss effect for (a) π^\pm , (b) K^\pm , and (c) p and \bar{p} at midrapidity ($|y| < 0.1$) as a function of particle momentum magnitude in 200 GeV pp and 62.4 GeV central 0–5% Au + Au collisions. Only negative particles are shown; energy loss for particles and antiparticles are the same. Errors shown are statistical only. The pion energy loss is already corrected by the track reconstruction algorithm.

crossings). The abort-gap events represent the background in the real collision environment. The embedded event is subsequently reconstructed by the full reconstruction chain. In every MC event, there is a well-defined primary vertex. With the embedded event reconstructed and the MC information in hand, the vertex-finding efficiency can be obtained. The overall vertex-finding efficiency $\epsilon_{\text{vtx}}(N_{\text{glob}})$ is determined as the ratio of the number of reconstructed events with the correct vertex position (within 2 cm of the input MC event vertex) to the number of input MC events. The obtained $\epsilon_{\text{vtx}}(N_{\text{glob}})$ is shown in Fig. 11(a). The vertex-finding efficiency here is expressed in terms of N_{glob} because the number of primary tracks cannot be readily obtained; those MC events that fail the vertex-finding program do not have primary tracks defined.

A reconstructed vertex that is farther than 2 cm (three-dimensional distance) from that of the input MC event is considered as a fake vertex. The fake vertex rate $\delta_{\text{fake}}(N_{\text{glob}})$ is obtained by the ratio of the number of fake vertex events to the number of input MC events. The obtained $\delta_{\text{fake}}(N_{\text{glob}})$ is also shown in Fig. 11(a).

The extracted vertex-finding efficiency and fake vertex rate are expressed as a function of N_{glob} . However, as mentioned earlier, the number of good primary tracks should be used as the variable, because it is not affected by pileup. To use N_{prim} as the variable, a map of N_{prim} vs N_{glob} is used: for each N_{prim} bin, the vertex-finding efficiency and the fake vertex rate are obtained by convoluting $\epsilon_{\text{vtx}}(N_{\text{glob}})$ and $\delta_{\text{fake}}(N_{\text{glob}})$, respectively. The obtained $\epsilon_{\text{vtx}}(N_{\text{prim}})$ and $\delta_{\text{fake}}(N_{\text{prim}})$ are shown in Fig. 11(b).

The vertex-finding efficiency and the fake vertex rate are corrected by weighting the particles in each event by the factor

$$[\epsilon_{\text{vtx}}(N_{\text{prim}}) + \delta_{\text{fake}}(N_{\text{prim}})]^{-1}. \quad (4)$$

Each event is weighted by the same factor when counting events for normalization. The overall correction factor is found to be nearly one for the two central bins of $d + \text{Au}$ collisions, so the correction is only applied to the peripheral bin of $d + \text{Au}$ collisions and minimum-bias pp collisions.

From the MC study, the particle spectra from fake vertex events are extracted and compared with those from good events (with a correctly reconstructed vertex). It is found that particles from the fake vertex events have somewhat harder p_\perp spectra than those in good events, presumably because of the wrongly assigned primary vertex position in final track fitting and because higher p_\perp particles are assigned larger weight in the vertex-fitting algorithm [11]. Figure 12 shows the ratio of the charged-hadron p_\perp spectrum in good vertex events to that in all events with a reconstructed vertex (i.e., sum of good and fake vertex events) for minimum-bias pp and $d + \text{Au}$ collisions. The spectra are normalized per event before the ratio is taken. This ratio is parametrized, and the parametrization, $\epsilon_{\text{fake}}(p_\perp)$, is multiplied with all p_\perp spectra to correct for the p_\perp -dependent effect of the fake vertex events. The correction is found to be rather insensitive to the particle type, so a single correction function is applied to all particle species. Again the correction is found to be negligible in the two central bins of $d + \text{Au}$ collisions, so it is only applied to the peripheral bin of $d + \text{Au}$ collisions and minimum-bias pp collisions.

D. Tracking efficiency

The raw spectra are corrected for detector acceptance and tracking efficiency which are obtained from the MC embedding method. Figures 13 and 14 show the obtained efficiency, the product of tracking efficiency and detector acceptance, for minimum-bias pp and $d + \text{Au}$ collisions and for peripheral and central Au + Au collisions, respectively. All efficiencies are expressed as a function of the input MC p_\perp . The p_\perp dependences are the same in pp and $d + \text{Au}$ collisions

TABLE III. Various track definitions and the corresponding cuts.

Track definition	d_{ca} cut	Min. number of hits
Global	—	10
Good global	—	15
Primary	$d_{\text{ca}} < 3$ cm	10
Good primary	$d_{\text{ca}} < 3$ cm	15
Used in analysis	$d_{\text{ca}} < 3$ cm	25

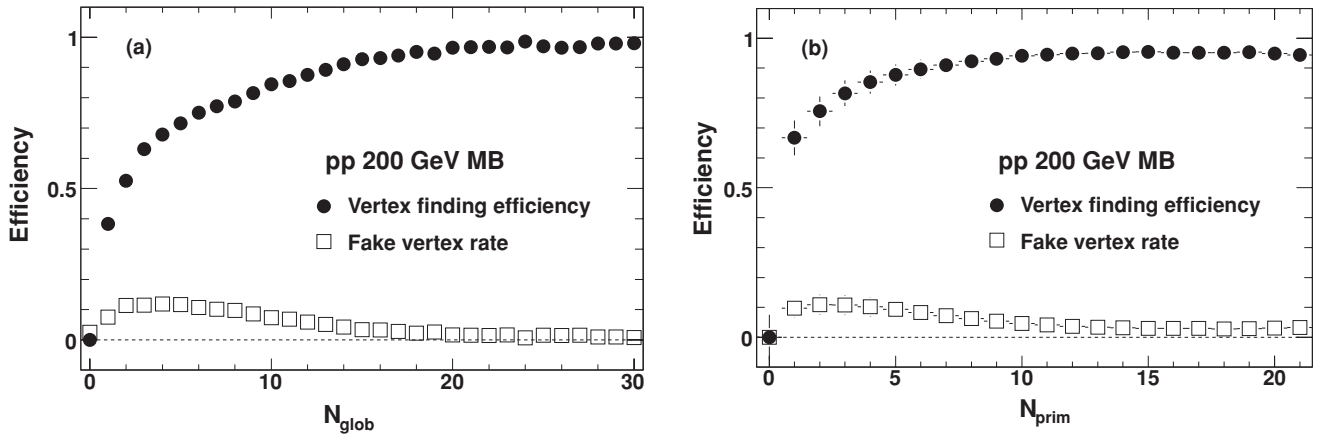


FIG. 11. Vertex-finding efficiency ϵ_{vtx} and fake vertex rate δ_{fake} as a function of the number of (a) good global tracks and (b) good primary tracks. Errors shown or smaller than the point size are statistical only.

and similar in Au + Au collisions. The pion efficiency is independent of p_{\perp} for $p_{\perp} > 0.2$ GeV/c, but falls steeply at lower p_{\perp} because particles below $p_{\perp} = 0.15$ GeV/c cannot traverse the entire TPC due to their large track curvature inside the solenoidal magnetic field. The efficiency for protons and antiprotons is flat above $p_{\perp} \sim 0.35$ GeV/c. At lower p_{\perp} , the efficiency drops steeply because of the large multiple scattering effect due to the large (anti)proton mass. The kaon efficiency shown in Figs. 13 and 14 increases smoothly with p_{\perp} and already includes decay loss (which decreases with increasing p_{\perp}). The significantly smaller kaon efficiency at small momentum than that of pions is caused by the large loss of kaons due to decays.

In pp and $d + \text{Au}$ collisions, the difference between the efficiencies for the different multiplicity bins is negligible because the multiplicities are low, and the different occupancies have no effect on the track reconstruction performance. In Au + Au collisions, the particle multiplicity (hence the TPC occupancy) is high, resulting in the different reconstruction efficiency magnitudes in peripheral and central Au + Au collisions as seen in Fig. 14. The change in the efficiency from peripheral

to central collisions at 62.4 GeV is smooth and of the order of 15–20%. However, this is still a relatively small variation; the 5% embedded multiplicity used in the embedding MC simulation, which biases the embedded events toward higher multiplicity and TPC occupancy, has negligible effect on the calculated reconstruction efficiency for each centrality bin.

The curves superimposed in Figs. 13 and 14 are parametrizations to the efficiencies. Table IV lists the fit

TABLE IV. Parametrizations to π^- , K^- , \bar{p} , and p efficiencies for 200 GeV minimum-bias $d + \text{Au}$ data and five centrality bins of 62.4 GeV Au + Au data.

	$d + \text{Au}$	$\text{Au} + \text{Au}$				
	min. bias	70–80%	50–60%	30–40%	10–20%	0–5%
$\pi^-: P_0 \exp[-(P_1/p_{\perp})^{P_2}]$						
P_0	0.856	0.840	0.818	0.809	0.781	0.759
P_1	0.075	0.129	0.111	0.109	0.097	0.070
P_2	1.668	4.661	3.631	3.224	2.310	1.373
$K^-: P_0 \exp[-(P_1/p_{\perp})^{P_2}] + P_3 p_{\perp}$						
P_0	0.527	0.608	0.585	0.503	0.494	0.450
P_1	0.241	0.238	0.234	0.231	0.229	0.229
P_2	3.496	2.425	3.034	3.968	3.492	3.925
P_3	0.160	0.099	0.085	0.152	0.139	0.149
$\bar{p}: (P_0 \exp[-(P_1/p_{\perp})^{P_2}] + P_3 p_{\perp}) \exp[(P_4/p_{\perp})^{P_5}]$						
P_0	0.830	0.317	0.233	0.227	0.245	0.246
P_1	0.295	0.303	0.303	0.300	0.305	0.301
P_2	7.005	19.473	13.480	11.183	15.567	13.054
P_3	−0.029	−0.004	0.028	0.041	0.026	0.039
P_4	0 fixed	10.156	4.160	2.031	1.895	0.889
P_5	0 fixed	0.006	0.104	0.153	0.107	0.160
$p: (P_0 \exp[-(P_1/p_{\perp})^{P_2}] + P_3 p_{\perp}) \exp[(P_4/p_{\perp})^{P_5}]$						
P_0	0.921	0.189	0.201	0.193	0.187	0.221
P_1	0.291	0.306	0.310	0.303	0.308	0.307
P_2	7.819	10.643	16.825	9.565	12.826	14.488
P_3	−0.057	0.023	0.026	0.041	0.042	0.033
P_4	0 fixed	15.212	9.331	3.585	3.380	1.944
P_5	0 fixed	0.131	0.127	0.194	0.194	0.181

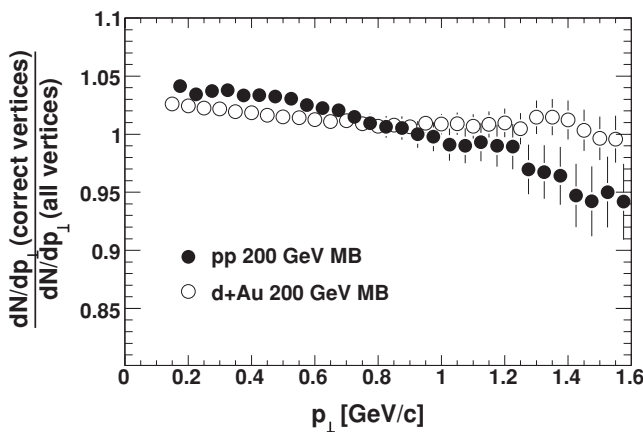


FIG. 12. p_{\perp} dependent correction to particle spectra due to fake vertex events, $\epsilon_{\text{fake}}(p_{\perp})$, in 200 GeV minimum-bias pp and $d + \text{Au}$ collisions. Errors shown are statistical only.

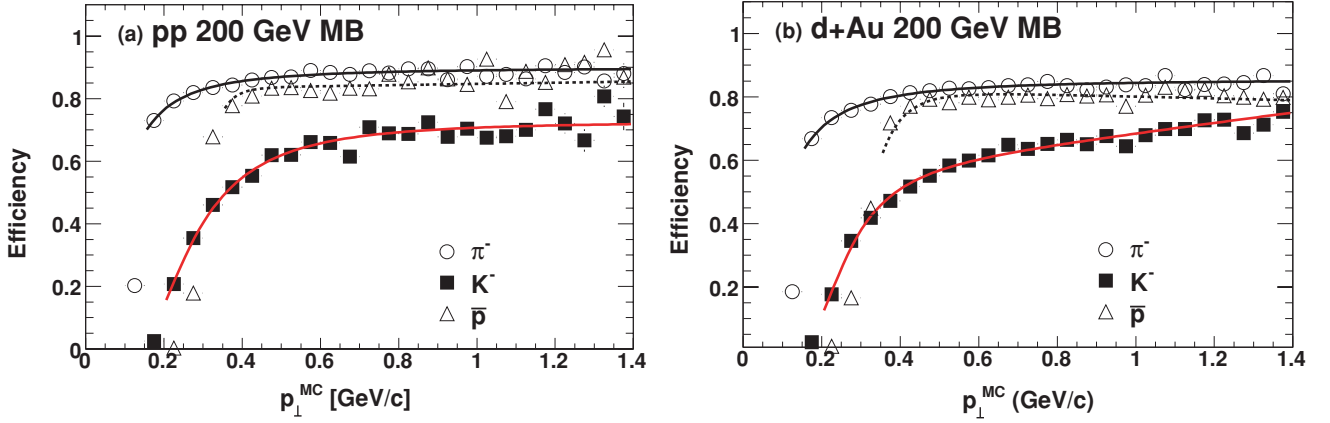


FIG. 13. (Color online) Efficiency (product of tracking efficiency and detector acceptance) of π^- , K^- , and \bar{p} in (a) pp and (b) $d + Au$ collisions at 200 GeV as a function of input MC p_\perp . Errors shown are binomial errors. The curves are parametrizations to the efficiency data and are used for corrections in the analysis.

parameters for 200 GeV minimum-bias $d + Au$ data and five centrality bins of 62.4 GeV $Au + Au$ data. The fit parameters for π^- , K^- , \bar{p} , and p are tabulated. The fit parameters for π^+ and π^- are similar, and also for K^+ and K^- . These parametrizations are used in the analysis for efficiency corrections.

E. Proton background correction

The proton sample contains background protons knocked out from the beam pipe and the detector materials by interactions of produced hadrons in these materials [43]. Most of these protons have large d_{ca} and are not reconstructed as primary particles. However, some of these background protons have small d_{ca} and are therefore included in the primary track sample, and a correction is needed.

Figure 15 shows the d_{ca} distributions of protons and antiprotons for two selected p_\perp bins in 200 GeV $d + Au$ and 62.4 GeV central $Au + Au$ collisions. The protons and antiprotons are selected by a dE/dx cut of $|z_p| < 0.3$, where z_p is given by Eq. (1). The long, nearly flat d_{ca} tail in the

proton distribution comes mainly from knock-out background protons. The effect is large at low p_\perp and significantly diminished at high p_\perp (note the logarithm scale for the high- p_\perp data). Antiprotons do not have knock-out background; the flat d_{ca} tail is absent from their d_{ca} distributions.

To correct for the knock-out background protons, the d_{ca} dependence at $d_{ca} < 3$ cm is needed for the knock-out protons. Based on MC simulation studies, we found the following functional form to describe the background protons well [20]:

$$p_{bkgd}(d_{ca}) \propto [1 - \exp(-d_{ca}/d_0)]^\alpha. \quad (5)$$

Assuming that the shape of the background-subtracted proton d_{ca} distribution is identical to that for the antiproton d_{ca} distribution, the proton data can be fit by

$$p(d_{ca}) = \bar{p}(d_{ca})/r_{\bar{p}/p} + A \cdot p_{bkgd}(d_{ca}), \quad (6)$$

where the magnitude of the background protons A , the parameter d_0 , the exponent α , and the antiproton-to-proton ratio $r_{\bar{p}/p}$ are free parameters. This assumption is, however, not strictly valid because the weak decay contributions to the proton and antiproton samples are in principle different, and

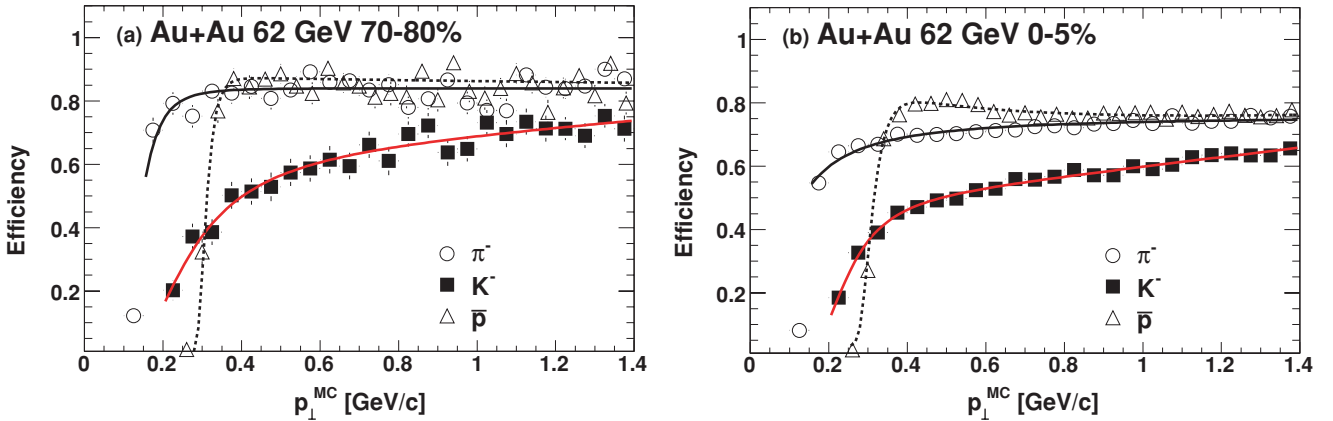


FIG. 14. (Color online) Efficiency (product of tracking efficiency and detector acceptance) of π^- , K^- , and \bar{p} in (a) 70–80% peripheral $Au + Au$ and (b) 0–5% central $Au + Au$ collisions at 62.4 GeV as a function of input MC p_\perp . Errors shown are binomial errors. The curves are parametrizations to the efficiency data and are used for corrections in the analysis.

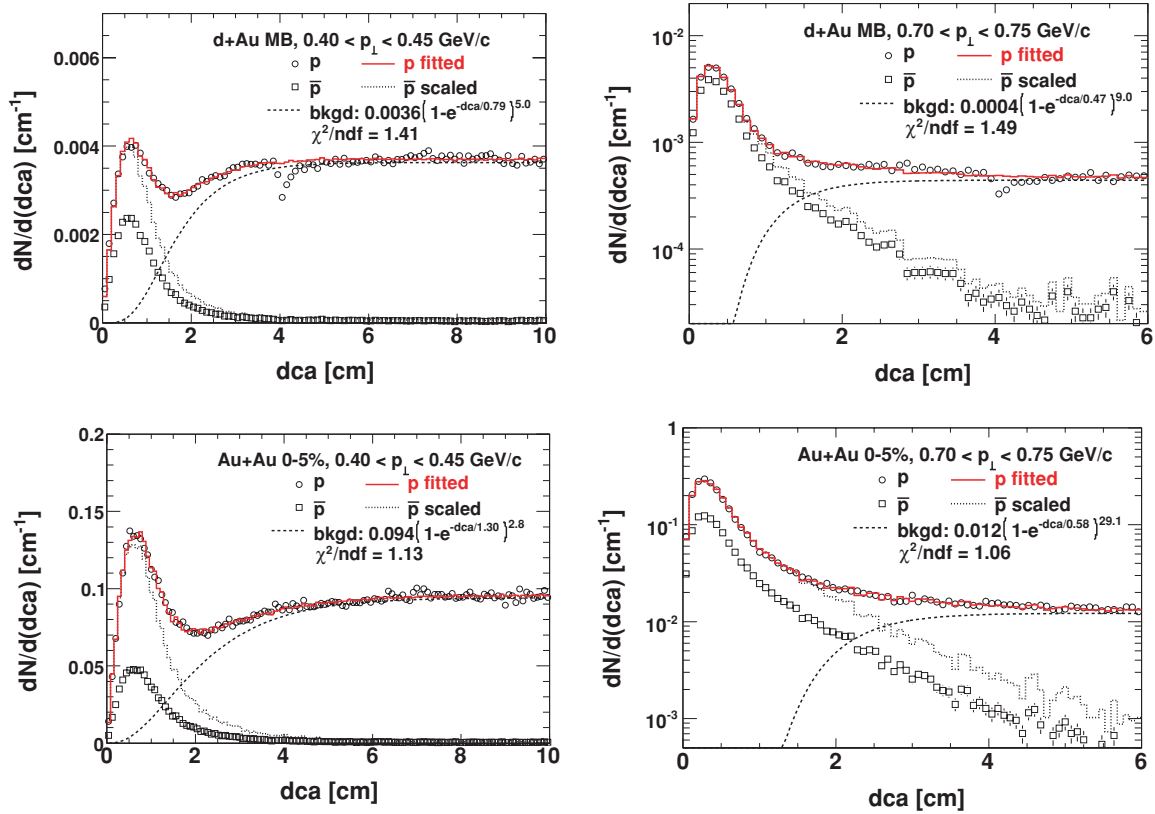


FIG. 15. (Color online) d_{ca} distributions of protons and antiprotons for $0.40 < p_{\perp} < 0.45$ GeV/c and $0.70 < p_{\perp} < 0.75$ GeV/c in 200 GeV minimum-bias $d + Au$ (upper panels) and 62.4 GeV 0–5% central Au + Au collisions (lower panels). Errors shown are statistical only. The dashed curve is the fit proton background; the dotted histogram is the \bar{p} distribution scaled up by the fit p/\bar{p} ratio; and the solid histogram is the fit p distribution by Eq. (6). The range $3.2 < d_{ca} < 5$ cm is excluded from the fit for the $d + Au$ data. Note the logarithm scale of the right panels.

the d_{ca} distribution of the weak decay products differs from that of the primordial protons and antiprotons. However, the measured $\bar{\Lambda}/\Lambda$ ratio is close to the \bar{p}/p ratio [44], and the difference in d_{ca} distributions between protons and antiprotons arising from weak decay contaminations is small. The effect of slightly different proton and antiproton d_{ca} distributions on the extracted background proton fraction is estimated and is within the systematic uncertainty discussed in Sec. V.

The d_{ca} distributions of protons and antiprotons are fit with Eq. (6) in each p_{\perp} and centrality bin. The d_{ca} distributions up to 10 cm are included in the fit for the Au + Au data. The proton d_{ca} distributions in $d + Au$ collisions, however, have a peculiar dip at $d_{ca} \approx 4$ cm, as seen in Fig. 15. We think this dip is related to effects of the beam pipe (whose diameter is 3 in.) and a specific algorithm of the vertex finder in low-multiplicity collisions; however, its exact cause is still under investigation. Because of the dip in the $d + Au$ data, we fit the d_{ca} distributions up to 10 cm but exclude the region $3.2 < d_{ca} < 5$ cm from the fit. The fit results are shown in Fig. 15. The dashed curve is the fit proton background. The dotted curve is the \bar{p} distribution scaled up by the fit p/\bar{p} ratio. The solid histogram is the fit of Eq. (6) to the proton distribution. The fit qualities are good. It is found that the fit power exponent α is larger than 1, indicating that the background protons die off faster than the simple $1 - \exp(-d_{ca}/d_0)$ form at small d_{ca} . The α value is large at

high p_{\perp} ; there is practically no background at high p_{\perp} at small d_{ca} .

Table V lists the fraction of knock-out background protons out of the total measured proton sample within $d_{ca} < 3$ cm

TABLE V. Fraction of proton background out of total measured proton sample as a function of p_{\perp} . Minimum-bias $d + Au$ collisions at 200 GeV and three centrality bins of Au + Au collisions at 62.4 GeV are listed. The errors are systematic uncertainties.

p_{\perp} (GeV/c)	$d + Au$ 200 GeV Min. bias	Au + Au 62.4 GeV		
		70–80%	30–40%	0–5%
0.425	0.49 ± 0.07	0.32 ± 0.09	0.36 ± 0.08	0.36 ± 0.08
0.475	0.47 ± 0.04	0.29 ± 0.06	0.29 ± 0.06	0.29 ± 0.05
0.525	0.41 ± 0.04	0.26 ± 0.05	0.22 ± 0.04	0.23 ± 0.04
0.575	0.36 ± 0.04	0.18 ± 0.05	0.15 ± 0.03	0.16 ± 0.03
0.625	0.28 ± 0.04	0.12 ± 0.05	0.12 ± 0.03	0.11 ± 0.02
0.675	0.23 ± 0.04	0.09 ± 0.05	0.08 ± 0.02	0.07 ± 0.02
0.725	0.17 ± 0.04	0.06 ± 0.05	0.05 ± 0.02	0.04 ± 0.01
0.775	0.12 ± 0.05	0.05 ± 0.05	0.04 ± 0.02	0.03 ± 0.01
0.825	0.10 ± 0.05	0.03 ± 0.03	0.02 ± 0.01	0.02 ± 0.01
0.875	0.06 ± 0.04	0.03 ± 0.03	0.02 ± 0.01	0.02 ± 0.01
0.925	0.06 ± 0.04	0.02 ± 0.02	0.01 ± 0.01	0.01 ± 0.01
0.975	0.04 ± 0.04	0.02 ± 0.02	0.01 ± 0.01	0.01 ± 0.01

as a function of p_{\perp} in minimum-bias $d + \text{Au}$ and three selected centrality bins of $\text{Au} + \text{Au}$ data. The fraction of knock-out background protons depends on a number of factors, including the amount of detector material, analysis cuts, the total particle multiplicity produced in the collisions, and their kinetic energies. Since the ratio of proton multiplicity to total particle multiplicity varies somewhat with centrality, and the particle kinematics change with centrality, the background fraction varies slightly with centrality.

For pp data [17] and $\text{Au} + \text{Au}$ data at 130 [20] and 200 GeV [17], the background protons are corrected in a similar way. The fraction of background protons are similar in all collision systems.

F. Pion background correction

The pion spectra are corrected for feed-downs from weak decays, muon contamination, and background pions produced in the detector materials. The corrections are obtained from MC simulations of HIJING events, with the STAR geometry and a realistic description of the detector response. The simulated events are reconstructed in the same way as for real data. The weak-decay daughter pions are mainly from K_S^0 and Λ and are identified by the parent particle information accessible from the simulation. The pion decay muons can be misidentified as primordial pions because of the similar masses of muon and pion. This contamination is obtained from MC by identifying the decay, which is also accessible from the simulation. The obtained weak-decay pion background and muon contamination are shown in Fig. 16 as a function of p_{\perp} . The total background rate, which is dominated by these two sources, is also shown.

The pion background fraction is independent of event multiplicity in 200 GeV pp and $d + \text{Au}$ collisions; therefore, a single correction is applied. In 62.4 GeV $\text{Au} + \text{Au}$ collisions, the multiplicity dependence of the pion background is weak (within 1.5% over the entire centrality range); a single, averaged correction is applied to all centralities, similar to the approach in Ref. [17].

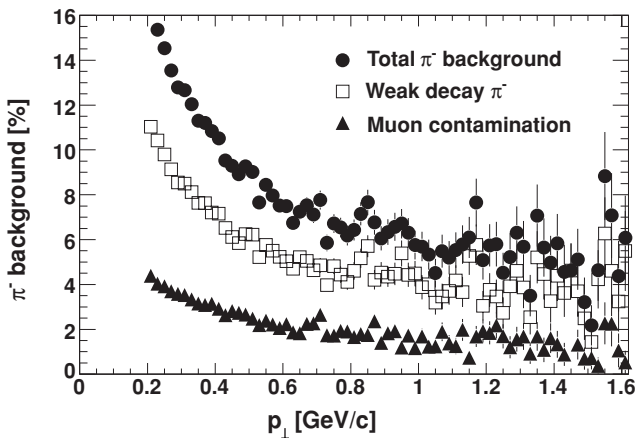


FIG. 16. Pion background fraction from weak decays (Λ , K_S^0) and μ^\pm contamination as a function of p_{\perp} in minimum-bias $d + \text{Au}$ collisions at 200 GeV. Errors shown are statistical only.

V. SYSTEMATIC UNCERTAINTIES

A. On transverse momentum spectra

The point-to-point systematic uncertainties on the spectra are estimated by varying event and track selection and analysis cuts and by assessing sample purity from the dE/dx measurement. In addition, the Gaussian fit ranges are varied to estimate the systematic uncertainty on the extracted raw spectra. The estimated uncertainties are less than 4% for π^\pm , p , and \bar{p} . Those for K^\pm are less than 12% for p_{\perp} bins with significant overlap in dE/dx with e^\pm or π^\pm , and less than 4% for other bins. These point-to-point systematic errors are similar for pp , $d + \text{Au}$, and $\text{Au} + \text{Au}$ collisions. The point-to-point systematic errors are combined with statistical errors in quadrature in the plotted spectra in Figs. 18–21. The combined errors are treated as random errors and are included in the fitting of the spectra.

For proton spectra, an additional systematic error is estimated due to background subtraction. The estimated uncertainty at $p_{\perp} = 0.45\text{--}0.50$ GeV/c is about 8% and drops rapidly with p_{\perp} [20,45] (see Table V). The p_{\perp} dependence of background contribution varies somewhat with centrality, presumably due to the combined effect of the rapid change in the proton p_{\perp} spectral shape with centrality and little change in that of the pion. The proton background uncertainties for pp and $d + \text{Au}$ collisions are similar. The systematic uncertainties on the pion spectra due to background correction are negligible.

A correlated overall systematic uncertainty of 5% is estimated for all spectra and is dominated by uncertainties in the MC determination of reconstruction efficiencies. This systematic uncertainty is estimated by varying parameters in the MC simulation.

B. On dN/dy

The particle yield measured at midrapidity ($|y| < 0.1$) for each identified particle spectrum is calculated from the measured p_{\perp} range and extrapolated to the unmeasured regions with various parametrizations. For kaons and protons, the extrapolation is done by the hydrodynamics-motivated blast-wave model fit (described in Sec. VII). Our default blast-wave fit does not include resonance decays (the effect of which is studied in detail in Appendix B). The fit is done to all six spectra of π^\pm , K^\pm , p , and \bar{p} simultaneously. However, because the low p_{\perp} regions of the pion spectra are affected by resonance decays, the $p_{\perp} < 0.5$ GeV/c parts of the pion spectra are excluded from the blast-wave fit. Instead, the Bose-Einstein distribution

$$\frac{dN}{m_{\perp} dm_{\perp}} \propto 1/[\exp(m_{\perp}/T_{\text{BE}}) - 1] \quad (7)$$

is found to describe the pion spectra well and is employed to extrapolate the pion spectra, with T_{BE} a fit parameter. The point-to-point systematic errors on the spectra are included in the fits.

Table VI shows the fractional yields of dN/dy extrapolated to the unmeasured p_{\perp} regions. The systematic uncertainties on the extrapolated yields are estimated by comparing the

TABLE VI. Fraction of measured and extrapolated yield for negatively charged particles for selected collision systems and centralities. For extrapolation, Bose-Einstein fit is used for pions and blast-wave fit is used for kaons and (anti)protons.

System	Measured dN/dy	Extrapolated dN/dy	
		Low p_{\perp}	High p_{\perp}
π^{-} , measured range $p_{\perp} = 0.2\text{--}0.7$ GeV/c			
$d + \text{Au}$ min. bias	59%	30%	11%
Au + Au 70–80%	58%	32%	10%
Au + Au 30–40%	58%	28%	14%
Au + Au 0–5%	58%	28%	14%
K^{-} , measured range $p_{\perp} = 0.2\text{--}0.75$ GeV/c			
$d + \text{Au}$ min. bias	60%	12%	28%
K , measured range $p_{\perp} = 0.25\text{--}0.75$ GeV/c			
Au + Au 70–80%	58%	21%	21%
Au + Au 30–40%	56%	15%	29%
Au + Au 0–5%	54%	13%	33%
\overline{p} , measured range $p_{\perp} = 0.4\text{--}1.10$ GeV/c			
$d + \text{Au}$ min. bias	53%	21%	26%
\overline{p} , measured range $p_{\perp} = 0.35\text{--}1.15$ GeV/c			
Au + Au 70–80%	65%	21%	14%
Au + Au 30–40%	64%	12%	24%
Au + Au 0–5%	60%	9%	31%

extrapolation with those using other fit functions. Those fit functions are

$$\begin{aligned}
 p_{\perp} \text{ exponential: } \frac{dN}{p_{\perp} dp_{\perp}} &\propto \exp(-p_{\perp}/T_{p_{\perp}}), \\
 p_{\perp} \text{ Gaussian: } \frac{dN}{p_{\perp} dp_{\perp}} &\propto \exp(-p_{\perp}^2/T_{p_{\perp}}^2), \\
 p_{\perp}^3 \text{ exponential: } \frac{dN}{p_{\perp} dp_{\perp}} &\propto \exp(-p_{\perp}^3/T_{p_{\perp}}^3), \\
 m_{\perp} \text{ exponential: } \frac{dN}{m_{\perp} dm_{\perp}} &\propto \exp(-m_{\perp}/T_{m_{\perp}}), \\
 \text{Boltzmann: } \frac{dN}{m_{\perp} dm_{\perp}} &\propto m_T \exp(-m_{\perp}/T_B),
 \end{aligned} \quad (8)$$

where $T_{p_{\perp}}$, $T_{m_{\perp}}$, and T_B are fit parameters. The fit functions used for pion dN/dy systematic uncertainty assessment are the blast-wave function and the p_{\perp} exponential. Those used for kaons are the m_{\perp} exponential and the Boltzmann function. Those used for proton and antiproton are the p_{\perp} Gaussian and p_{\perp}^3 exponential; also used for $\text{Au} + \text{Au}$ 20–80% centrality bins and for $d + \text{Au}$ collisions are the Boltzmann function, the m_{\perp} exponential, and the p_{\perp} exponential.

The systematic uncertainties on the extrapolated total particle yields are dominated by the uncertainties in the extrapolation, which are estimated to be of the order of 15% of the extrapolated part of the integrated yields for pions and kaons, and 15–40% for antiprotons and protons depending on centrality. The 5% overall MC uncertainty is added in quadrature. For protons, the p_{\perp} -dependent systematic uncertainty on background subtraction leads to an overall systematic uncertainty in the yields. This systematic uncer-

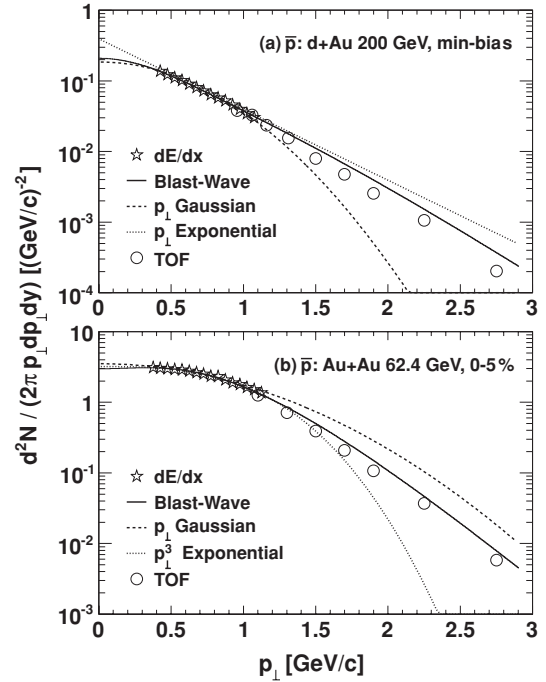


FIG. 17. Midrapidity identified antiproton spectra in (a) 200 GeV minimum-bias $d + \text{Au}$ and (b) 62.4 GeV central $\text{Au} + \text{Au}$ collisions measured by dE/dx together with those by TOF [46,47]. The dE/dx data are from $|y| < 0.1$ and the TOF data are from $|y| < 0.5$. The curves are various fits to the dE/dx data for extrapolation. The quadratic sum of statistical errors and point-to-point systematic errors are plotted, but are smaller than the point size.

tainty is estimated and included in quadrature in the total systematic uncertainties on dN/dy .

Identified particle spectra in pp and $d + \text{Au}$ collisions at 200 GeV and $\text{Au} + \text{Au}$ collisions at 62.4 GeV are measured at relatively high p_{\perp} by the TOF detector in STAR [46,47]. In the overlap region in p_{\perp} , the TOF measurements and the TPC measurements reported here are consistent within systematic uncertainties. The TOF measurement is a good systematic check on our extrapolation. As an example, Fig. 17 shows the measured antiproton spectra by dE/dx in $d + \text{Au}$ and central $\text{Au} + \text{Au}$ collisions and their various parametrizations, together with the TOF measurements. The TOF measurements are well within the range of the extrapolations. Blast-wave fits are also performed including the large p_{\perp} ranges from TOF [46,47] and the spectra obtained by the extended particle identification method ($r dE/dx$) [16]. The blast-wave fit parameters thus obtained are consistent with our results within the systematic uncertainties. To keep consistency and fair comparisons of the various data sets, only the TPC measurements are studied here, since TOF was only installed as a prototype test for a full TOF system and was absent in many collision systems reported here.

The total charged-particle density dN_{ch}/dy , calculated from the sum of the individual dN/dy yields of π^{\pm} , K^{\pm} , p , and \bar{p} , is used as one of the centrality measures in this paper. The systematic uncertainties on dN_{ch}/dy are calculated

assuming that the extrapolation uncertainties are completely correlated between particles and antiparticles and completely uncorrelated between different particle species. In addition, the efficiency uncertainty is common for all particle species, and the proton background uncertainty is uncorrelated with the rest.

C. On particle ratios and $\langle p_\perp \rangle$

Systematic uncertainties on particle yield ratios come from those on the extrapolated total yields, estimated as above. The efficiency uncertainties are canceled in the ratios. The extrapolation uncertainties are canceled to a large degree in the antiparticle-to-particle ratios; a common systematic uncertainty of 2%, 3%, and 5% is assigned to π^-/π^+ , K^-/K^+ , and \bar{p}/p , respectively [17]. The extrapolation uncertainties are treated as uncorrelated in the unlike particle ratios (K^-/π^- , \bar{p}/π^- , p/π^- , etc.). The uncertainty due to proton background subtraction is added in quadrature for the ratios involved with the proton yield.

The average transverse momentum $\langle p_\perp \rangle$ is extracted from the measured spectra and the extrapolations (blast-wave model fits for kaons and protons and Bose-Einstein function for pions as described above). Systematic uncertainties on $\langle p_\perp \rangle$ are also estimated by using the various functional forms mentioned before for extrapolation of the spectra. For protons, an additional systematic uncertainty on $\langle p_\perp \rangle$ due to the p_\perp -dependent proton background subtraction is estimated and included in quadrature in the total systematic uncertainties.

D. On chemical freeze-out parameters

Chemical freeze-out parameters (chemical freeze-out temperature T_{chem} , baryon and strangeness chemical potentials μ_B and μ_S , and strangeness suppression factor γ_S) are extracted from the measured particle ratios obtained from the six particle spectra within the framework of a statistical model. The systematic uncertainties on the particle ratios are included in the statistical model fit and are treated as independent. These uncertainties propagate to the systematic uncertainties on the chemical freeze-out parameters.

Our measured protons are inclusive of all protons from primordial Σ^+ and Λ (and Σ^0 -decay Λ) decays, and likewise for the antiparticles. To assess the systematic uncertainties on the fit chemical freeze-out parameters, we vary the detection probability of weak-decay (anti)protons from 100% to 50%. The chemical freeze-out temperature thus obtained is larger by about 8 MeV and is included in the systematic uncertainty estimate. The effects on baryon and strangeness chemical potentials are negligible. Because of the decay kinematics, Λ 's from Ξ and Ω decays mostly follow the parent direction [44], and the decay protons from most of those decay Λ 's are reconstructed as primordial protons in the STAR TPC; likewise for the antiparticles. In our statistical model fit, we assume 50% of the (anti)protons from multistep decays are included in our measured primary (anti)proton samples. To assess the systematic uncertainty due to the multistep decay products, we include either all the multistep decay (anti)protons or none of them in the statistical model fit. We found that this systematic uncertainty is small.

The other source of systematic uncertainty is due to the relatively limited set of particle ratios used in this analysis. While the T_{chem} , μ_B , and μ_S should be well constrained because of the high statistics data for pions, kaons, and (anti)protons, the *ad hoc* strangeness suppression factor γ_S is not well constrained, because the single-strangeness K^\pm are the only strangeness species used in this work. STAR has measured a variety of strange and multistrange particles, including $K^{*\pm}$, K_S^0 , Λ and $\bar{\Lambda}$, Λ_{1520} , Ξ and $\bar{\Xi}$, and Ω and $\bar{\Omega}$ at 130 [44,48–50] and 200 GeV [51–53]. The chemical freeze-out parameters have also been studied by particle ratios including these particles [50]. It is found that the extracted chemical freeze-out temperature and baryon and strangeness chemical potentials are similar to those obtained from this work using the limited set of particle ratios. However, the γ_S parameter differs: in central Au + Au collisions, $\gamma_S \sim 0.9$ from this work and ~ 1.0 from the fit including the extended list of strange and multistrange particles [50]. This difference gives a reasonable estimate of the systematic uncertainty on γ_S .

E. On kinetic freeze-out parameters

The kinetic freeze-out parameters are extracted from the simultaneous blast-wave parametrization of the measured particle spectra. The kinetic freeze-out temperature T_{kin} , the average transverse radial flow velocity $\langle \beta \rangle$, and the flow velocity profile exponent n are treated as free parameters. The point-to-point systematic errors on the spectra are included in the blast-wave fit. The p_\perp -dependent systematic uncertainty due to proton background correction is taken into account in evaluating the systematic uncertainties of the blast-wave parameters.

The measured pions contain large contributions from resonance decays; the contributions vary with the pion p_\perp . Our default blast-wave fit does not include resonance decays. To reduce the systematic uncertainty due to resonance decays, the low p_\perp part ($p_\perp < 0.5$ GeV/c) of the pion spectra is excluded from the blast-wave fit. The remaining systematic uncertainty is estimated by varying the p_\perp range of the pion spectra included in the blast-wave fit. The resonance decay effect on the blast-wave fit is also thoroughly studied in Appendix B. Comparisons between the blast-wave parameters obtained including or excluding resonance decays also give a good estimate of the systematic uncertainties.

Because of the large mass of (anti)protons and kaons, the (anti)proton and kaon spectra constrain the transverse flow velocity well. Thus the systematic uncertainties on the kinetic freeze-out parameters are also assessed by excluding the K^\pm spectra, the p spectrum, or the \bar{p} spectrum from the blast-wave fit.

While the spectra are mainly determined by T_{kin} and $\langle \beta \rangle$, the shape of the flow velocity profile also has some effect on the spectra because of the nonlinearity in the dependence of the spectral shape on the flow velocity. However, the effect is fairly weak, as indicated by the large fitting errors on the velocity profile exponent n for some of the spectra. Nevertheless, to assess the systematic uncertainty from this effect, we fit the spectra by fixing n to unity. The fit qualities are significantly degraded for some of the spectra. However, we use the changes

in the fit parameters as our conservative estimates of the systematic uncertainties due to the flow velocity profile used.

We note that the blast-wave model assumes a simple picture of local particle sources of a common temperature in a transverse radial velocity field to describe the flattening of particle transverse spectra. The extracted kinetic freeze-out parameters are within the framework of this picture. However, it is possible that other effects may also contribute to the spectra flattening: semihard scattering may even be the main contributor in pp collisions [54]; the possible effect of statistical global energy and momentum conservation on particle spectra was recently studied in Ref. [55]. Such effects are not included in our systematic uncertainties on the extracted values of the kinetic freeze-out parameters.

VI. RESULTS AND DISCUSSIONS

In this section, results on identified π^\pm , K^\pm , p , and \bar{p} in $d + \text{Au}$ collisions at 200 GeV and $\text{Au} + \text{Au}$ collisions at 62.4 GeV [5] are presented and discussed. The results are measured at midrapidity in the range $|y| < 0.1$. The charged-pion spectra in

$\text{Au} + \text{Au}$ collisions at 130 GeV are also presented. The results are discussed together with previously published identified π^\pm , K^\pm , p , and \bar{p} results in pp and $\text{Au} + \text{Au}$ collisions at 200 GeV [17] and charged kaon [18] and (anti)proton results [20] at 130 GeV.

The identified particle spectra are presented first, followed by the average transverse momenta $\langle p_\perp \rangle$, the integrated particle multiplicity densities dN/dy and ratios, and baryon and strangeness production rates. The $\langle p_\perp \rangle$ and dN/dy are extracted from the measured spectra and the extrapolations from the blast-wave model fits for kaons and protons and the Bose-Einstein function for pions. To have the same procedure to obtain dN/dy and $\langle p_\perp \rangle$, the identified particle spectra from 130 GeV $\text{Au} + \text{Au}$ collisions are fit by the blast-wave model parametrization in this work. The extracted $\langle p_\perp \rangle$ and dN/dy are listed in Tables VII and VIII, respectively. The quoted errors are the quadratic sum of statistical and systematic uncertainties and are dominated by the latter. Since the systematic uncertainties on particle ratios cannot be readily obtained from the individual particle dN/dy yields, Table IX lists particle ratios together with the total uncertainties.

TABLE VII. Extrapolated average transverse momenta, $\langle p_\perp \rangle$ in GeV/c, of identified particles for various collision systems and centralities. Quoted errors are the quadratic sum of statistical and systematic uncertainties, and are dominated by the latter.

System	Centrality	π^-	π^+	K^-	K^+	\bar{p}	p
pp 200 GeV	Min. bias	0.348 ± 0.018	0.348 ± 0.018	0.517 ± 0.030	0.517 ± 0.030	0.683 ± 0.041	0.686 ± 0.041
	Min. bias	0.367 ± 0.027	0.369 ± 0.027	0.599 ± 0.068	0.599 ± 0.068	0.847 ± 0.090	0.847 ± 0.093
$d + \text{Au}$ 200 GeV	40–100%	0.359 ± 0.024	0.364 ± 0.025	0.582 ± 0.071	0.582 ± 0.071	0.816 ± 0.085	0.817 ± 0.087
	20–40%	0.363 ± 0.031	0.370 ± 0.031	0.623 ± 0.085	0.623 ± 0.085	0.896 ± 0.112	0.895 ± 0.116
	0–20%	0.378 ± 0.028	0.378 ± 0.028	0.607 ± 0.061	0.607 ± 0.061	0.855 ± 0.081	0.855 ± 0.085
	70–80%	0.363 ± 0.018	0.367 ± 0.018	0.550 ± 0.035	0.553 ± 0.035	0.746 ± 0.049	0.749 ± 0.049
	60–70%	0.377 ± 0.019	0.377 ± 0.019	0.583 ± 0.033	0.583 ± 0.033	0.814 ± 0.047	0.817 ± 0.047
$\text{Au} + \text{Au}$ 200 GeV	50–60%	0.389 ± 0.020	0.389 ± 0.020	0.609 ± 0.036	0.608 ± 0.036	0.863 ± 0.052	0.864 ± 0.052
	40–50%	0.395 ± 0.020	0.395 ± 0.020	0.619 ± 0.037	0.619 ± 0.037	0.895 ± 0.055	0.897 ± 0.055
	30–40%	0.402 ± 0.021	0.404 ± 0.021	0.643 ± 0.042	0.643 ± 0.042	0.939 ± 0.062	0.939 ± 0.062
	20–30%	0.408 ± 0.021	0.411 ± 0.021	0.668 ± 0.047	0.668 ± 0.047	0.989 ± 0.071	0.989 ± 0.071
	10–20%	0.416 ± 0.021	0.421 ± 0.021	0.680 ± 0.055	0.681 ± 0.055	1.017 ± 0.082	1.017 ± 0.082
	5–10%	0.418 ± 0.021	0.422 ± 0.021	0.704 ± 0.064	0.703 ± 0.064	1.070 ± 0.098	1.071 ± 0.098
	0–5%	0.422 ± 0.022	0.427 ± 0.022	0.719 ± 0.074	0.720 ± 0.074	1.103 ± 0.114	1.104 ± 0.110
	58–85%	0.355 ± 0.036	0.351 ± 0.035	0.559 ± 0.020	0.560 ± 0.020	0.745 ± 0.030	0.745 ± 0.030
	45–58%	0.366 ± 0.020	0.360 ± 0.020	0.576 ± 0.030	0.571 ± 0.030	0.808 ± 0.054	0.808 ± 0.054
	34–45%	0.375 ± 0.014	0.375 ± 0.014	0.598 ± 0.048	0.604 ± 0.048	0.869 ± 0.053	0.871 ± 0.053
$\text{Au} + \text{Au}$ 130 GeV	26–34%	0.382 ± 0.020	0.383 ± 0.020	0.628 ± 0.049	0.633 ± 0.049	0.925 ± 0.066	0.926 ± 0.066
	18–26%	0.386 ± 0.020	0.388 ± 0.020	0.644 ± 0.046	0.640 ± 0.046	0.942 ± 0.067	0.944 ± 0.067
	11–18%	0.391 ± 0.023	0.395 ± 0.023	0.650 ± 0.036	0.649 ± 0.036	0.949 ± 0.085	0.949 ± 0.085
	6–11%	0.390 ± 0.011	0.393 ± 0.011	0.640 ± 0.034	0.642 ± 0.034	0.965 ± 0.078	0.966 ± 0.078
	0–6%	0.404 ± 0.013	0.404 ± 0.013	0.667 ± 0.030	0.666 ± 0.030	1.002 ± 0.087	1.003 ± 0.087
	70–80%	0.357 ± 0.021	0.356 ± 0.021	0.529 ± 0.023	0.531 ± 0.023	0.702 ± 0.044	0.706 ± 0.045
	60–70%	0.372 ± 0.019	0.364 ± 0.019	0.542 ± 0.015	0.542 ± 0.015	0.728 ± 0.028	0.729 ± 0.031
	50–60%	0.381 ± 0.018	0.379 ± 0.018	0.560 ± 0.022	0.560 ± 0.022	0.759 ± 0.042	0.761 ± 0.046
$\text{Au} + \text{Au}$ 62.4 GeV	40–50%	0.385 ± 0.017	0.385 ± 0.017	0.584 ± 0.020	0.583 ± 0.020	0.812 ± 0.042	0.814 ± 0.049
	30–40%	0.395 ± 0.015	0.394 ± 0.015	0.607 ± 0.021	0.607 ± 0.021	0.864 ± 0.053	0.864 ± 0.061
	20–30%	0.400 ± 0.012	0.403 ± 0.013	0.629 ± 0.023	0.629 ± 0.023	0.913 ± 0.060	0.910 ± 0.070
	10–20%	0.402 ± 0.014	0.402 ± 0.014	0.636 ± 0.029	0.636 ± 0.029	0.928 ± 0.031	0.925 ± 0.050
	5–10%	0.404 ± 0.010	0.407 ± 0.011	0.644 ± 0.027	0.643 ± 0.027	0.950 ± 0.040	0.948 ± 0.059
	0–5%	0.403 ± 0.011	0.406 ± 0.011	0.645 ± 0.029	0.646 ± 0.029	0.959 ± 0.060	0.956 ± 0.075

TABLE VIII. Integrated multiplicity rapidity density, dN/dy , of identified particles and net-protons for various collision systems and centralities. Quoted errors are the quadratic sum of statistical and systematic uncertainties, and are dominated by the latter.

System	Centrality	π^-	π^+	K^-	K^+	\bar{p}	p	$p - \bar{p}$
pp 200 GeV	Min. bias	1.42 ± 0.11	1.44 ± 0.11	0.145 ± 0.013	0.150 ± 0.013	0.113 ± 0.010	0.138 ± 0.012	0.025 ± 0.004
$d + \text{Au}$ 200 GeV	Min. bias	4.63 ± 0.31	4.62 ± 0.31	0.582 ± 0.052	0.595 ± 0.054	0.412 ± 0.053	0.500 ± 0.069	0.088 ± 0.029
	40–100%	2.89 ± 0.20	2.87 ± 0.21	0.348 ± 0.032	0.356 ± 0.033	0.236 ± 0.030	0.281 ± 0.039	0.045 ± 0.018
	20–40%	6.06 ± 0.41	6.01 ± 0.41	0.783 ± 0.085	0.803 ± 0.087	0.569 ± 0.082	0.72 ± 0.11	0.154 ± 0.050
	0–20%	8.42 ± 0.57	8.49 ± 0.58	1.09 ± 0.09	1.11 ± 0.10	0.793 ± 0.087	0.95 ± 0.11	0.159 ± 0.049
	70–80%	10.9 ± 0.8	10.8 ± 0.8	1.38 ± 0.13	1.41 ± 0.13	0.915 ± 0.081	1.09 ± 0.10	0.170 ± 0.030
$\text{Au} + \text{Au}$ 200 GeV	60–70%	21.1 ± 1.6	21.1 ± 1.6	2.89 ± 0.26	2.98 ± 0.27	1.84 ± 0.16	2.20 ± 0.20	0.361 ± 0.061
	50–60%	36.3 ± 2.8	36.2 ± 2.7	5.19 ± 0.47	5.40 ± 0.49	3.16 ± 0.29	3.88 ± 0.35	0.72 ± 0.11
	40–50%	58.9 ± 4.5	58.7 ± 4.5	8.37 ± 0.78	8.69 ± 0.81	4.93 ± 0.46	6.17 ± 0.57	1.24 ± 0.18
	30–40%	89.6 ± 6.8	89.2 ± 6.8	13.2 ± 1.3	13.6 ± 1.3	7.46 ± 0.72	9.30 ± 0.89	1.85 ± 0.30
	20–30%	136 ± 10	135 ± 10	19.7 ± 2.0	20.5 ± 2.0	11.2 ± 1.1	14.4 ± 1.4	3.22 ± 0.51
	10–20%	196 ± 15	194 ± 15	28.7 ± 3.1	30.0 ± 3.2	15.7 ± 1.7	20.1 ± 2.2	4.42 ± 0.77
	5–10%	261 ± 20	257 ± 20	39.8 ± 4.6	40.8 ± 4.7	21.4 ± 2.5	28.2 ± 3.3	6.8 ± 1.3
	0–5%	327 ± 25	322 ± 25	49.5 ± 6.2	51.3 ± 6.5	26.7 ± 3.4	34.7 ± 4.4	8.0 ± 1.8
	58–85%	16.0 ± 2.1	16.0 ± 1.9	2.23 ± 0.14	2.31 ± 0.15	1.31 ± 0.09	1.65 ± 0.11	0.347 ± 0.040
	45–58%	42.4 ± 3.5	42.2 ± 3.5	5.81 ± 0.41	6.83 ± 0.48	3.33 ± 0.30	4.38 ± 0.39	1.05 ± 0.14
$\text{Au} + \text{Au}$ 130 GeV	34–45%	70.9 ± 4.9	71.8 ± 5.0	10.1 ± 0.9	11.2 ± 1.0	5.51 ± 0.45	7.35 ± 0.60	1.85 ± 0.20
	26–34%	104 ± 8	103 ± 8	15.0 ± 1.3	16.4 ± 1.4	8.02 ± 0.81	10.9 ± 1.1	2.91 ± 0.35
	18–26%	140 ± 11	140 ± 11	20.5 ± 1.8	22.3 ± 1.9	10.5 ± 1.0	14.4 ± 1.3	3.94 ± 0.41
	11–18%	187 ± 16	186 ± 16	26.6 ± 1.9	29.0 ± 2.1	12.8 ± 1.6	17.9 ± 2.2	5.09 ± 0.70
	6–11%	228 ± 16	228 ± 16	33.1 ± 2.4	35.6 ± 2.6	15.7 ± 1.6	21.9 ± 2.3	6.25 ± 0.75
	0–6%	280 ± 20	278 ± 20	42.7 ± 2.8	46.3 ± 3.0	20.0 ± 2.2	28.2 ± 3.1	8.24 ± 0.93
$\text{Au} + \text{Au}$ 62.4 GeV	70–80%	7.43 ± 0.62	7.34 ± 0.62	0.813 ± 0.055	0.868 ± 0.058	0.464 ± 0.047	0.745 ± 0.086	0.280 ± 0.050
	60–70%	14.7 ± 1.3	14.8 ± 1.3	1.74 ± 0.12	1.95 ± 0.13	0.960 ± 0.059	1.60 ± 0.12	0.639 ± 0.078
	50–60%	26.8 ± 2.4	26.5 ± 2.3	3.31 ± 0.23	3.64 ± 0.25	1.68 ± 0.12	2.98 ± 0.22	1.30 ± 0.11
	40–50%	43.7 ± 3.5	43.2 ± 3.5	5.68 ± 0.39	6.62 ± 0.46	2.77 ± 0.19	5.07 ± 0.36	2.30 ± 0.19
	30–40%	67.4 ± 5.2	66.5 ± 5.1	8.89 ± 0.62	10.4 ± 0.7	4.27 ± 0.35	8.08 ± 0.67	3.81 ± 0.33
	20–30%	101 ± 7	98.9 ± 6.9	14.0 ± 1.0	15.9 ± 1.1	6.39 ± 0.55	12.2 ± 1.1	5.86 ± 0.52
	10–20%	146 ± 11	144 ± 11	19.8 ± 1.4	23.0 ± 1.6	8.77 ± 0.78	17.8 ± 1.6	9.07 ± 0.85
	5–10%	192 ± 13	191 ± 13	27.2 ± 1.9	31.2 ± 2.2	11.4 ± 1.1	23.8 ± 2.4	12.4 ± 1.3
	0–5%	237 ± 17	233 ± 17	32.4 ± 2.3	37.6 ± 2.7	13.6 ± 1.7	29.0 ± 3.8	15.4 ± 2.1

A. Transverse momentum spectra

Figure 18 shows the centrality-dependent and minimum-bias π^\pm , K^\pm , p , and \bar{p} spectra in $d + \text{Au}$ collisions at 200 GeV. The minimum-bias spectra are obtained from the cross-section weighted sum of the corresponding spectra in each centrality bin. The minimum-bias $d + \text{Au}$ spectra are in good agreement with the previously published results [46]. Spectra from different centralities are similar.

Figure 19 shows the centrality dependence of the π^\pm , K^\pm , p , and \bar{p} spectra measured in $\text{Au} + \text{Au}$ collisions at 62.4 GeV. Pion spectral shapes are similar in all centrality bins. Kaon and (anti)proton spectra show a significant flattening with increasing centrality with the effect being stronger for proton.

Figure 20 shows the centrality-dependent pion spectra measured in $\text{Au} + \text{Au}$ collisions at 130 GeV. All spectra are parallel, indicating no significant centrality dependence of the shape. The kaon spectra at 130 GeV are published in Ref. [18], and the proton and antiproton spectra are published in Ref. [19].

Spectra results from pp and $\text{Au} + \text{Au}$ collisions at 200 GeV are published in Ref. [17]. Spectra shapes from 62.4, 130, and 200 GeV $\text{Au} + \text{Au}$ collisions are all similar. Hardening of the spectra is more pronounced with increasing centrality and increasing particle mass at all three energies.

Figure 21 compares pion, kaon, and antiproton spectra in pp , $d + \text{Au}$, and $\text{Au} + \text{Au}$ collisions. The pp , $d + \text{Au}$, and peripheral $\text{Au} + \text{Au}$ spectra are similar in shape. The central $\text{Au} + \text{Au}$ spectra of kaons and (anti)protons are significantly flatter.

B. Average transverse momenta

The spectra shape can be quantified by the average transverse momentum $\langle p_\perp \rangle$. In Fig. 22, the evolution of $\langle p_\perp \rangle$ is shown as a function of the charged-particle multiplicity. The pion $\langle p_\perp \rangle$ increases slightly with centrality in $\text{Au} + \text{Au}$ collisions. For kaons, protons, and antiprotons, the $\langle p_\perp \rangle$ increases significantly with centrality. No obvious centrality dependence is observed for $d + \text{Au}$ collisions.

TABLE IX. Particle dN/dy ratios for various collision systems and centralities. Quoted errors are the quadratic sum of statistical and systematic uncertainties, and are dominated by the latter (except some of the antiparticle-to-particle ratios).

System	Centrality	π^-/π^+	K^-/K^+	\bar{p}/p	K^-/π^-	\bar{p}/π^-	K^+/π^+	p/π^+
pp 200 GeV	Min. bias	0.988 ± 0.043	0.967 ± 0.040	0.819 ± 0.047	0.102 ± 0.008	0.080 ± 0.006	0.104 ± 0.008	0.096 ± 0.008
	Min. bias	1.003 ± 0.031	0.979 ± 0.036	0.824 ± 0.061	0.126 ± 0.011	0.089 ± 0.011	0.129 ± 0.011	0.108 ± 0.015
$d + Au$ 200 GeV	40–100%	1.008 ± 0.042	0.977 ± 0.037	0.841 ± 0.067	0.120 ± 0.011	0.082 ± 0.010	0.124 ± 0.012	0.098 ± 0.014
	20–40%	1.007 ± 0.035	0.976 ± 0.041	0.787 ± 0.064	0.129 ± 0.014	0.094 ± 0.013	0.134 ± 0.014	0.120 ± 0.018
	0–20%	0.993 ± 0.035	0.982 ± 0.036	0.833 ± 0.058	0.130 ± 0.011	0.094 ± 0.010	0.131 ± 0.011	0.112 ± 0.013
	70–80%	1.003 ± 0.044	0.981 ± 0.049	0.843 ± 0.048	0.127 ± 0.010	0.084 ± 0.007	0.130 ± 0.011	0.100 ± 0.008
$Au + Au$ 200 GeV	60–70%	1.003 ± 0.043	0.971 ± 0.040	0.836 ± 0.047	0.137 ± 0.011	0.087 ± 0.007	0.141 ± 0.011	0.104 ± 0.008
	50–60%	1.002 ± 0.044	0.961 ± 0.040	0.815 ± 0.047	0.143 ± 0.011	0.087 ± 0.007	0.149 ± 0.012	0.107 ± 0.009
	40–50%	1.003 ± 0.044	0.963 ± 0.039	0.799 ± 0.046	0.142 ± 0.012	0.084 ± 0.007	0.148 ± 0.012	0.105 ± 0.009
	30–40%	1.005 ± 0.045	0.969 ± 0.040	0.801 ± 0.047	0.147 ± 0.013	0.083 ± 0.007	0.152 ± 0.013	0.104 ± 0.009
	20–30%	1.008 ± 0.046	0.961 ± 0.039	0.777 ± 0.047	0.145 ± 0.013	0.082 ± 0.008	0.152 ± 0.014	0.107 ± 0.010
	10–20%	1.012 ± 0.049	0.959 ± 0.041	0.780 ± 0.048	0.147 ± 0.015	0.080 ± 0.008	0.155 ± 0.016	0.104 ± 0.011
	5–10%	1.014 ± 0.050	0.975 ± 0.046	0.759 ± 0.051	0.153 ± 0.017	0.082 ± 0.009	0.159 ± 0.017	0.110 ± 0.012
	0–5%	1.015 ± 0.051	0.965 ± 0.048	0.769 ± 0.055	0.151 ± 0.018	0.082 ± 0.010	0.159 ± 0.019	0.108 ± 0.013
	58–85%	0.996 ± 0.066	0.963 ± 0.050	0.790 ± 0.043	0.140 ± 0.018	0.082 ± 0.010	0.144 ± 0.016	0.103 ± 0.012
	45–58%	1.004 ± 0.040	0.850 ± 0.047	0.760 ± 0.043	0.137 ± 0.011	0.078 ± 0.008	0.162 ± 0.013	0.104 ± 0.010
$Au + Au$ 130 GeV	34–45%	0.988 ± 0.037	0.900 ± 0.044	0.749 ± 0.040	0.142 ± 0.013	0.078 ± 0.006	0.156 ± 0.014	0.102 ± 0.008
	26–34%	1.003 ± 0.039	0.912 ± 0.045	0.734 ± 0.039	0.145 ± 0.014	0.077 ± 0.008	0.159 ± 0.015	0.106 ± 0.011
	18–26%	1.002 ± 0.037	0.920 ± 0.045	0.727 ± 0.038	0.146 ± 0.014	0.075 ± 0.007	0.159 ± 0.015	0.103 ± 0.010
	11–18%	1.003 ± 0.037	0.915 ± 0.046	0.716 ± 0.039	0.142 ± 0.012	0.069 ± 0.009	0.156 ± 0.013	0.096 ± 0.013
	6–11%	1.003 ± 0.043	0.929 ± 0.045	0.715 ± 0.039	0.145 ± 0.010	0.069 ± 0.007	0.156 ± 0.011	0.096 ± 0.010
	0–6%	1.008 ± 0.029	0.923 ± 0.037	0.708 ± 0.036	0.153 ± 0.010	0.071 ± 0.008	0.167 ± 0.011	0.101 ± 0.011
	70–80%	1.012 ± 0.031	0.936 ± 0.036	0.623 ± 0.047	0.109 ± 0.009	0.063 ± 0.007	0.118 ± 0.010	0.101 ± 0.013
	60–70%	0.990 ± 0.031	0.894 ± 0.037	0.600 ± 0.039	0.119 ± 0.010	0.065 ± 0.005	0.132 ± 0.011	0.108 ± 0.010
$Au + Au$ 62.4 GeV	50–60%	1.011 ± 0.032	0.907 ± 0.038	0.563 ± 0.031	0.123 ± 0.011	0.063 ± 0.006	0.137 ± 0.012	0.113 ± 0.010
	40–50%	1.012 ± 0.032	0.858 ± 0.036	0.546 ± 0.030	0.130 ± 0.010	0.063 ± 0.005	0.153 ± 0.012	0.117 ± 0.009
	30–40%	1.014 ± 0.033	0.854 ± 0.036	0.529 ± 0.028	0.132 ± 0.010	0.063 ± 0.006	0.156 ± 0.012	0.121 ± 0.011
	20–30%	1.023 ± 0.034	0.883 ± 0.036	0.522 ± 0.027	0.138 ± 0.010	0.063 ± 0.005	0.160 ± 0.011	0.124 ± 0.011
	10–20%	1.013 ± 0.033	0.862 ± 0.037	0.492 ± 0.026	0.136 ± 0.010	0.060 ± 0.006	0.160 ± 0.012	0.124 ± 0.012
	5–10%	1.007 ± 0.033	0.870 ± 0.036	0.481 ± 0.026	0.141 ± 0.010	0.060 ± 0.006	0.164 ± 0.011	0.125 ± 0.012
	0–5%	1.018 ± 0.033	0.860 ± 0.035	0.469 ± 0.026	0.137 ± 0.010	0.057 ± 0.007	0.162 ± 0.012	0.125 ± 0.016

One interesting observation is that the $\langle p_\perp \rangle$ in central $d + Au$ collisions is larger than that in peripheral $Au + Au$ collisions. This can be due to jets, k_\perp broadening, and multiple scattering [56]. These effects can be stronger in $d + Au$ collisions than in peripheral $Au + Au$ collisions, because nucleons in the deuteron suffer multiple collisions traversing the incoming Au nucleus in central $d + Au$ collisions, while peripheral $Au + Au$ collisions are close to simple superposition of multiple pp collisions. In fact, the $\langle p_\perp \rangle$ in peripheral $Au + Au$ collisions is similar to that in pp .

On the other hand, the $\langle p_\perp \rangle$ in central $d + Au$ collisions is smaller than that in central $Au + Au$ collisions. Central $d + Au$ collisions likely have larger effects from initial state multiple scattering and k_\perp broadening. Although jet contribution is larger in central $Au + Au$ than in $d + Au$, it is likely softened due to jet energy loss in central $Au + Au$ collisions. Consequently, jet contribution to the flattening of the low p_\perp spectra in $Au + Au$ collisions may not be much larger than that in $d + Au$ collisions. The larger $\langle p_\perp \rangle$ in central $Au + Au$ collisions cannot be only due to the effects already present

in $d + Au$ collisions, as random-walk models argue [56], but it is also due to other effects including transverse radial flow, caused by thermodynamic pressure, and the remaining contributions from (semi-)hard scatterings. Transverse radial flow suggested by these data will be discussed in more detail in Sec. VII.

For $Au + Au$ collisions, $\langle p_\perp \rangle$ increases significantly with increasing centrality. The trends are similar at 62.4, 130, and 200 GeV, and the $\langle p_\perp \rangle$ values qualitatively agree with each other at the same dN_{ch}/dy . This suggests that the kinetic freeze-out properties in $Au + Au$ collisions are rather energy independent for the measured collision energies.

In the color glass condensate (gluon saturation) picture, small x gluons overlap and recombine, reducing the total number of gluons and increasing their transverse energy [29,30]. These gluons hadronize into mostly soft hadrons. Thus, a lower particle multiplicity and larger $\langle p_\perp \rangle$ is predicted. In the gluon saturation picture, the only relevant scale is $\frac{dN_\pi/dy}{S_\perp}$, and the $\langle p_\perp \rangle$ is predicted to scale with $\sqrt{\frac{dN_\pi/dy}{S_\perp}}$ [29,30]. In

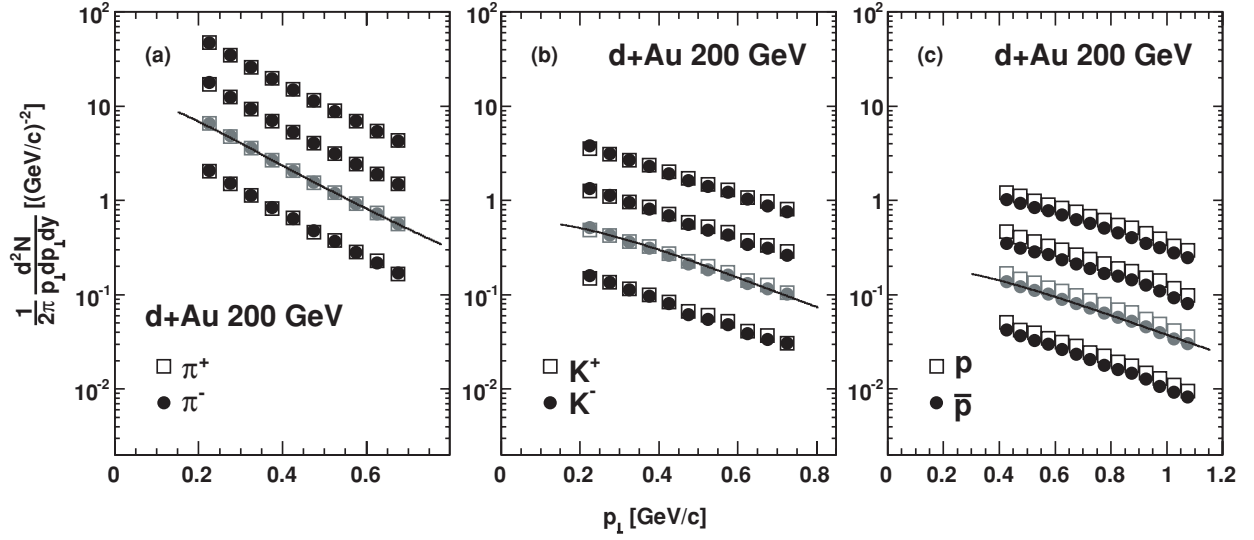


FIG. 18. Midrapidity ($|y| < 0.1$) identified particle spectra in $d + \text{Au}$ collisions at 200 GeV. The p and \bar{p} spectra are inclusive, including weak decay products. Spectra are plotted for three centrality bins and for minimum-bias events. Spectra from top to bottom are for 0–20% scaled by 4, 20–40% scaled by 2, minimum bias not scaled, and 40–100% scaled by 1/2. Errors plotted are statistical and point-to-point systematic errors added in quadrature, but are smaller than the point size. The curves are the blast-wave model fits to the minimum-bias data; the normalizations of the curves are fixed by the corresponding negative particle spectra.

Fig. 22(b), the $\langle p_\perp \rangle$ is shown as a function of $\sqrt{dN_\pi/dS_\perp dy}$ for minimum-bias pp and for $\text{Au} + \text{Au}$ collisions of the various centralities. A linear dependence of the $\langle p_\perp \rangle$ on $\sqrt{dN_\pi/dS_\perp dy}$ is observed for all three particle species, as shown by the lines in Fig. 22. It is interesting to note that the slope, characterizing the rate of increase in the $\langle p_\perp \rangle$, is a factor of 2 larger for \bar{p} than for kaons which is in turn is a factor of 2 larger than for pions. The intercepts of the linear fits for \bar{p} and kaons are the same, but are larger than that for pions.

C. Total particle production

The total particle multiplicity reflects the total entropy generated in the collision system. There has been renewed interest in total particle production as its centrality dependence could distinguish between different models of particle production [57]. Models based on the assumption of final-state gluon saturation advocate a decrease of the charged-particle multiplicities per participant nucleon with increasing centrality. For example, the EKRT model [58] parametrizes

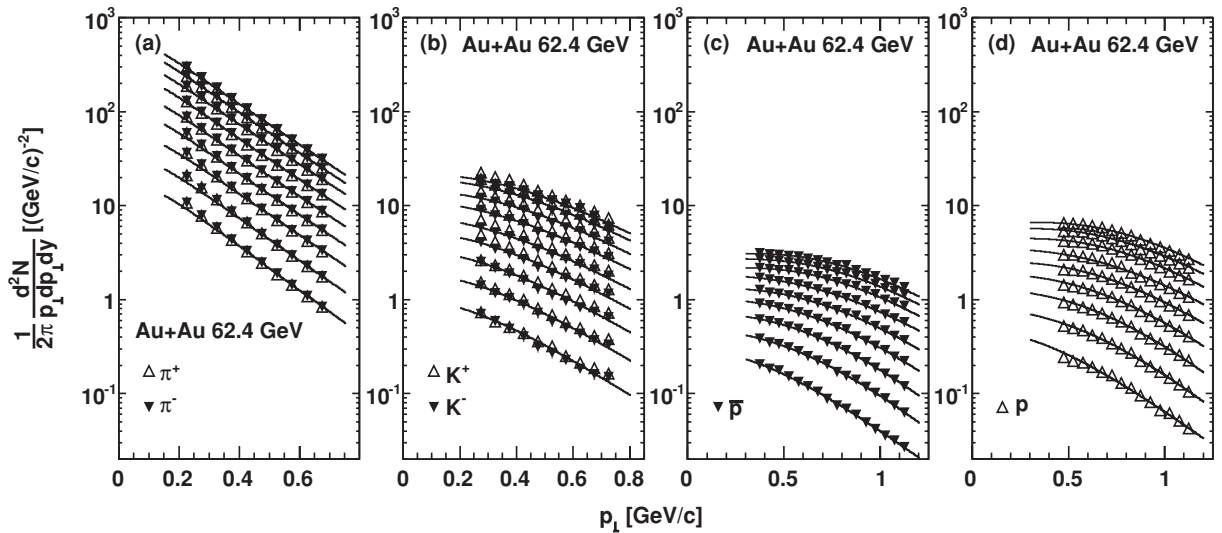


FIG. 19. Midrapidity ($|y| < 0.1$) identified particle spectra in $\text{Au} + \text{Au}$ collisions at 62.4 GeV. The p and \bar{p} spectra are inclusive, including weak decay products. Spectra are plotted for nine centrality bins, from top to bottom, 0–5%, 5–10%, 10–20%, 20–30%, 30–40%, 40–50%, 50–60%, 60–70%, and 70–80%. Errors plotted are statistical and point-to-point systematic errors added in quadrature, but are smaller than the point size. The curves are the blast-wave model fits to the spectra; the normalizations of the curves in (a) and (b) are fixed by the corresponding negative particle spectra.

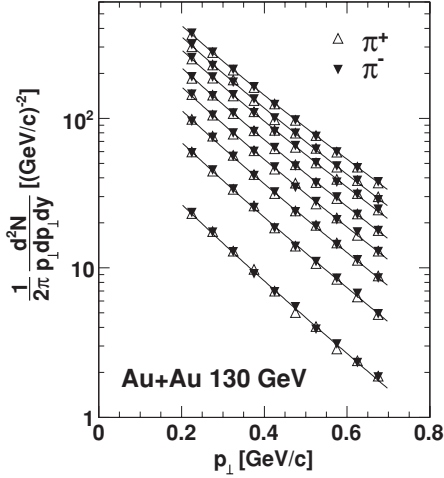


FIG. 20. Midrapidity ($|y| < 0.1$) identified pion spectra in Au + Au collisions at 130 GeV. Spectra are plotted for eight centrality bins, from top to bottom, 0–6%, 6–11%, 11–18%, 18–26%, 26–34%, 34–45%, 45–58%, and 58–85%. Errors plotted are statistical and point-to-point systematic errors added in quadrature, but they are smaller than the data point size. The curves are the Bose-Einstein fits to the spectra; the normalizations of the curves are fixed by the corresponding negative particle spectra.

the multiplicity rapidity density as

$$\left. \frac{dN_{\text{ch}}}{d\eta} \right|_{b=0} = C \frac{2}{3} 1.16 \left(\frac{N_{\text{part}}}{2} \right)^{0.92} (\sqrt{s})^{0.40}. \quad (9)$$

Models based on initial state gluon saturation (e.g., the color glass condensate model [59,60]) or pQCD inspired models (e.g., the HIJING [42,61] or the soft/hard scattering model used in Ref. [29]) predict an increase of the rapidity density per participant nucleon with centrality. In both the HIJING and the soft/hard models, particle production arises from two major

contributions: (a) a soft component scaling with the number of participants N_{part} and (b) a hard component from minijet production, which is directly proportional to the number of binary collisions N_{coll} and the average inclusive jet cross section. Reference [29] expresses these two components as

$$dN_{\text{ch}}/d\eta = (1 - x_{\text{hard}})n_{pp} \frac{N_{\text{part}}}{2} + x_{\text{hard}}n_{pp}N_{\text{coll}}, \quad (10)$$

where x_{hard} is the fraction of hard collisions. The basic assumption here is that the average particle multiplicity produced per hard process in heavy-ion collisions is identical to that in pp collisions. In Eq. (10), n_{pp} is the charged-particle pseudorapidity density in NSD pp interactions. We have measured n_{pp} in pp collisions only at 200 GeV. To apply the two-component model to data at other energies, we use a parametrization from $p\bar{p}$ measurements [62–65] by

$$n_{pp} = (2.5 \pm 1.0) - (0.25 \pm 0.19) \ln(s) + (0.023 \pm 0.008) \ln^2(s), \quad (11)$$

where s is the squared center-of-mass energy in GeV^2 . The parametrized value of $n_{pp} = 2.43$ at 200 GeV differs from our measurement in pp collisions because of the numerical difference between our measured NSD cross section of 30.0 ± 3.5 mb [13] and the measurement in Ref. [66] of 35 ± 1 mb.

In the following, we call Eqs. (9) and (10) the EKRT and K-N parametrizations, respectively, and use them to study the discrimination power of our data against the two opposing models of particle production. Unfortunately, neither N_{part} nor N_{coll} can be directly measured in the experiment. They can only be derived by calculating the nuclear overlap integral with the help of the Glauber model. However, two different implementations of the Glauber calculation, the optical and the MC Glauber calculations, lead to different values of N_{part} and N_{coll} with rather large uncertainties for peripheral collisions (for details, see Appendix A).

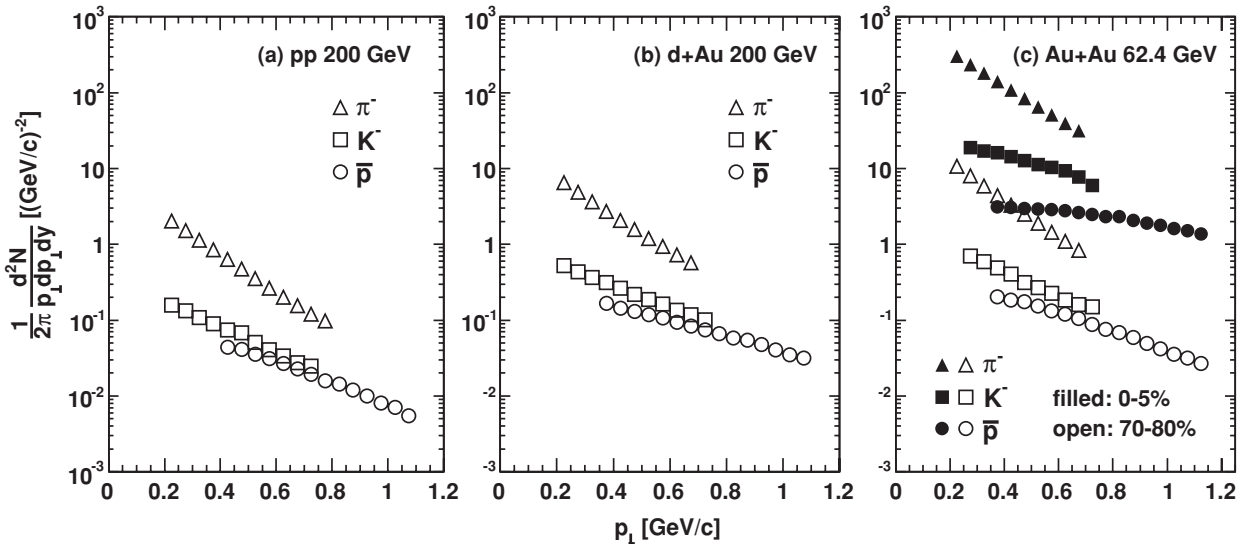


FIG. 21. Comparisons of π^- , K^- , and \bar{p} transverse momentum spectra for (a) minimum-bias pp collisions at 200 GeV, (b) minimum-bias $d + \text{Au}$ collisions at 200 GeV, and (c) Au + Au collisions at 62.4 GeV. Two centralities are shown: 0–5% central collisions (filled symbols) and 70–80% peripheral collisions (open symbols). Errors are statistical and point-to-point systematic errors added in quadrature.

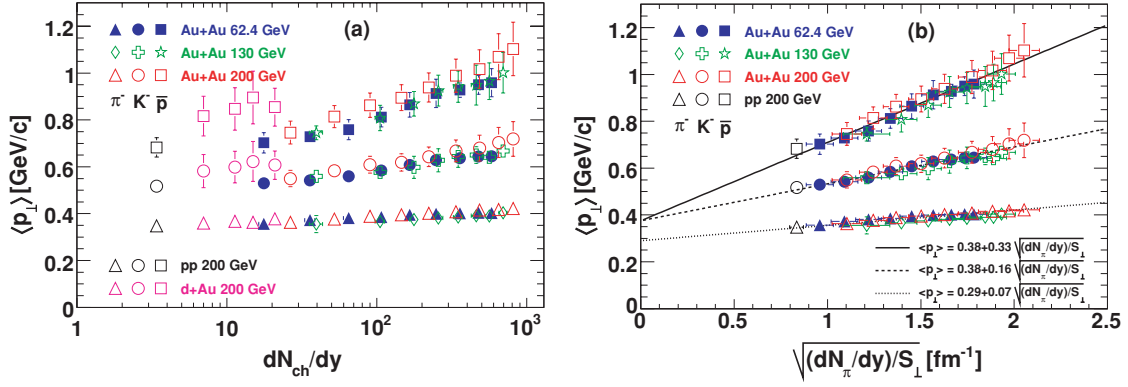


FIG. 22. (Color online) Average transverse momenta as a function of (a) dN_{ch}/dy and (b) $\sqrt{dN_{\pi}/dy}/S_{\perp 1}$ for Au + Au collisions at 62.4, 130, and 200 GeV. The minimum-bias pp data are also shown. The $d + Au$ data are shown in panel (a). Errors shown are systematic errors and statistical errors added in quadrature.

Figure 23 shows the pseudorapidity multiplicity density per participant pair, $\frac{dN_{ch}/d\eta}{N_{part}/2}$, vs the number of participants N_{part} for Au + Au collisions at 62.4 and 200 GeV, where we have used N_{part} and N_{coll} from the optical Glauber calculation in panel (a) and the MC Glauber calculation in the panel (b). The $dN_{ch}/d\eta$ data are from Table II. In both panels, the vertical error bars represent the quadratic sum of the systematic uncertainties on $dN_{ch}/d\eta$ and N_{part} . The latter dominates the uncertainties for peripheral collisions.

As seen in Fig. 23(a) (using the optical Glauber calculation), we observe no significant change in charged-hadron production as a function of centrality within the large uncertainties (mainly from the optical Glauber calculations). Superimposed for comparison are the EKRT and K-N parametrizations in the dashed and solid curves, respectively. The EKRT parametrization is obtained from the best fit to the data by Eq. (9), treating C as the single fit parameter. The K-N parametrization is obtained from the best fit to the data by Eq. (10), treating n_{pp} as fixed from Eq. (11) and x_{hard} as the single fit parameter. Neither our data nor the EKRT

parametrization seem to approach the parametrized n_{pp} by Eq. (11) in the limit of $N_{part} = 2$. The K-N parametrization recovers n_{pp} for $N_{part} = 2$ by construction of the model. Both models do a modest job in describing the data.

When using the MC Glauber model to evaluate N_{part} and N_{coll} as done in Fig. 23(b), our data clearly exhibit a centrality dependence rising from the most peripheral to the most central collisions, by about $(50 \pm 20)\%$ and $(40 \pm 20)\%$ for 62.4 and 200 GeV, respectively. The data are fit by Eq. (9) treating C as the single fit parameter. The obtained EKRT parametrizations (dashed curves) clearly fail to describe our data because of the opposite centrality dependence. The fit χ^2/ndf is printed on the plot and is fairly large, especially considering that the systematic uncertainties are included in the fit as random errors. On the other hand, shown in the solid curves are the K-N parametrizations obtained from fitting Eq. (10) to the data fixing n_{pp} by Eq. (11) and treating x_{hard} as the single fit parameter. As can be seen, the K-N parametrization fits the data better. We obtain the fit fraction of hard collisions to be $x_{hard} = (7.8 \pm 1.3)\%$ and $(12.8 \pm 1.3)\%$ for Au + Au collisions at

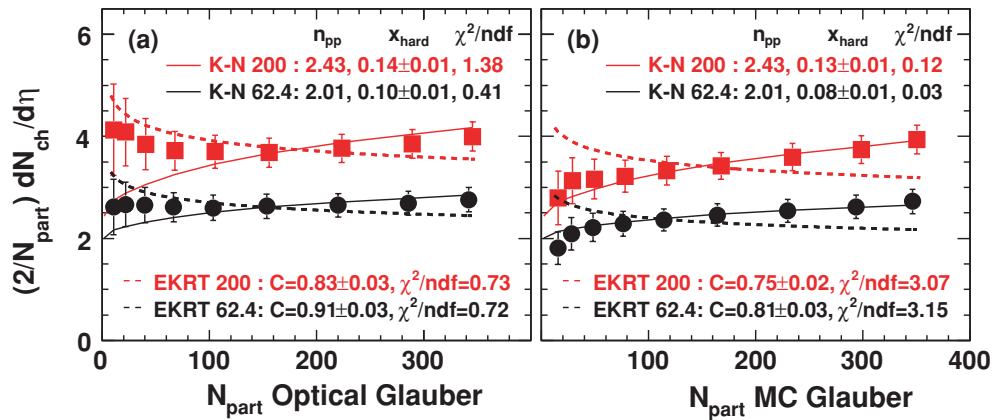


FIG. 23. (Color online) Pseudorapidity multiplicity density per participant nucleon pair $\frac{dN_{ch}/d\eta}{N_{part}/2}$ vs the number of participants N_{part} , with N_{part} calculated from (a) the optical Glauber model and (b) the MC Glauber model. Data are presented for Au + Au collisions at 62.4 GeV (black dots) and 200 GeV (red squares). The vertical errors are total uncertainties including uncertainties on N_{part} . The uncertainties on N_{part} (horizontal error bars) are smaller than the data point size. The solid curves are the K-N fit by Eq. (10) where x_{hard} is a fit parameter and n_{pp} is fixed from Eq. (11). The dashed curves are the EKRT fit by Eq. (9) where C is a fit parameter.

62.4 and 200 GeV, respectively. We may evaluate the fraction of produced particles originating from hard collisions, within the framework of the K-N two-component model, as

$$F_{\text{hard}} = \frac{x_{\text{hard}} n_{pp} N_{\text{coll}}}{dN_{\text{ch}}/d\eta}, \quad (12)$$

yielding $F_{\text{hard}} = (30 \pm 5)\%$ and $(46 \pm 5)\%$ for the top 5% central Au + Au collisions at 62.4 and 200 GeV, respectively.

In our K-N two-component model study, we used the charged-particle multiplicity from NSD pp interactions in Eq. (11) and the Glauber model results calculated with the total pp cross section. This is because singly diffractive nucleon-nucleon interactions also contribute to the total charged-particle multiplicities in Au + Au collisions. If we use instead the Glauber data of $\sigma_{pp} = 36$ mb from Table II for 200 GeV, we obtain $x_{\text{hard}} = (15 \pm 2)\%$.

It should be noted that the K-N two-component model assumes the same average particle multiplicity per hard process in pp and Au + Au collisions. This assumption is likely invalid, because jet-medium interactions induce a larger average multiplicity per hard process in Au + Au collisions with a softer energy distribution [67]. The size of this effect is dependent on centrality. This relative increase in particle multiplicity from hard processes would result in an overestimate of the fraction of hard component, especially for pp collisions. A two-component model study based on the multiplicity dependence of transverse rapidity spectra from pp collisions, assuming most of the charged particles are pions, has revealed a significantly smaller fraction of hard component [54]. It remains an open question as to how realistic the simple K-N two-component model is for heavy-ion collisions. An improved two-component model would be to use the total transverse energy instead of the total particle multiplicity, as the total transverse energy likely remains the same with jet modification processes. However, such a model would need as input the total transverse energy in inelastic pp collisions, which is not well measured.

It is worth noting that the normalized pseudorapidity density $\frac{dN_{\text{ch}}/d\eta}{N_{\text{part}}/2}$ in the EKRT parametrization has only the overall scale C as a free parameter. The centrality dependence is fixed by $N_{\text{part}}^{0.92}$. In the K-N parametrization, on the other hand, the overall scale is fixed by n_{pp} , while the centrality dependence changes with the free parameter x_{hard} . However, the n_{pp} value is obtained from parametrization to elementary collision data and thus is designed to describe the overall scale of the heavy-ion data. As shown in Fig. 23, as a result of the uncertainties from the Glauber calculations, we cannot explicitly rule out either of the models. However, recent developments in analyzing the small systems (Cu + Cu) indicate that the MC Glauber model is preferred, albeit with its own caveats as mentioned before. This in turn favors the two-component model and initial state gluon saturation [68] over the EKRT model.

D. Bjorken energy density estimate

The central rapidity region is approximately boost invariant [17]. Under boost invariance, the energy density of the central

rapidity region in the collision zone at formation time τ can be estimated by the Bjorken energy density [2]

$$\epsilon_{Bj} = \frac{dE_{\perp}}{dy} \frac{1}{S_{\perp} \tau}, \quad (13)$$

where E_{\perp} is the total transverse energy, and S_{\perp} is the transverse overlap area of the colliding nuclei. Since we do not measure transverse energy, but only charged-particle transverse momenta, we use the approximation

$$\frac{d\langle E_{\perp} \rangle}{dy} \approx \frac{3}{2} \left(\langle m_{\perp} \rangle \frac{dN}{dy} \right)_{\pi^{\pm}} + 2 \left(\langle m_{\perp} \rangle \frac{dN}{dy} \right)_{K^{\pm}, p, \bar{p}}. \quad (14)$$

Here, we calculate $\langle m_{\perp} \rangle = \sqrt{\langle p_{\perp} \rangle^2 + m^2}$ from the π^{\pm} , K^{\pm} , p , and \bar{p} average transverse momenta presented in this work and in Refs. [17–20]. The factors 3/2 and 2 compensate for the neutral particles. Isospin effects are estimated to be less than 2% and are neglected. Propagation of systematic uncertainties is done in the same way as for the total dN_{ch}/dy discussed in Sec. VB, i.e., the extrapolation uncertainties are correlated between particle and antiparticle and uncorrelated between different particle species, and the overall reconstruction efficiency is correlated for all particle species. The uncertainties on the $\langle p_{\perp} \rangle$ are not included because they come from extrapolation of the spectra, similar to those on the dN_{ch}/dy , and are already applied to the dN_{ch}/dy .

Figure 24 shows the product of the Bjorken energy density and the formation time as a function of N_{part} . For the top 5% central collisions, $\epsilon_{Bj} \times \tau = 3.7 \pm 0.3$ GeV/fm² at collision energy 62.4 GeV, 4.4 ± 0.3 at 130 GeV (not shown), and 5.2 ± 0.4 at 200 GeV. Our 130 GeV value is in good agreement with the value $\epsilon_{Bj} \times \tau = 4.6$ GeV/fm² quoted in Ref. [69] for the most central 2% inelastic collisions. These estimated Bjorken energy densities are at least several GeV/fm³ with a formation time $\tau < 1$ fm/c. They well exceed the phase transition energy density of 1 GeV/fm³ predicted by lattice QCD [3].

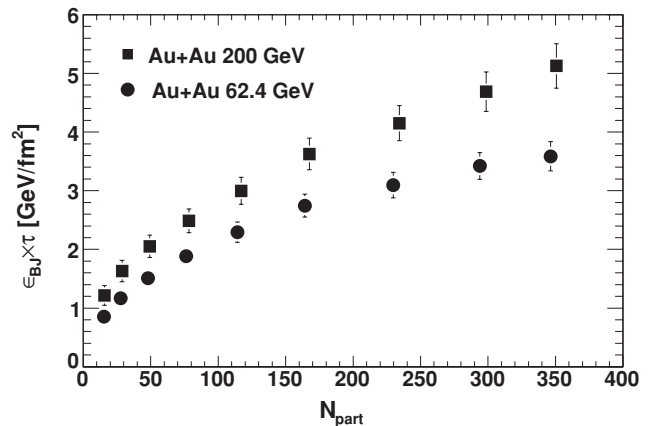


FIG. 24. Estimate of the product of the Bjorken energy density and the formation time ($\epsilon_{Bj} \times \tau$) as a function of centrality N_{part} . Errors shown are the quadratic sum of statistical and systematic uncertainties.

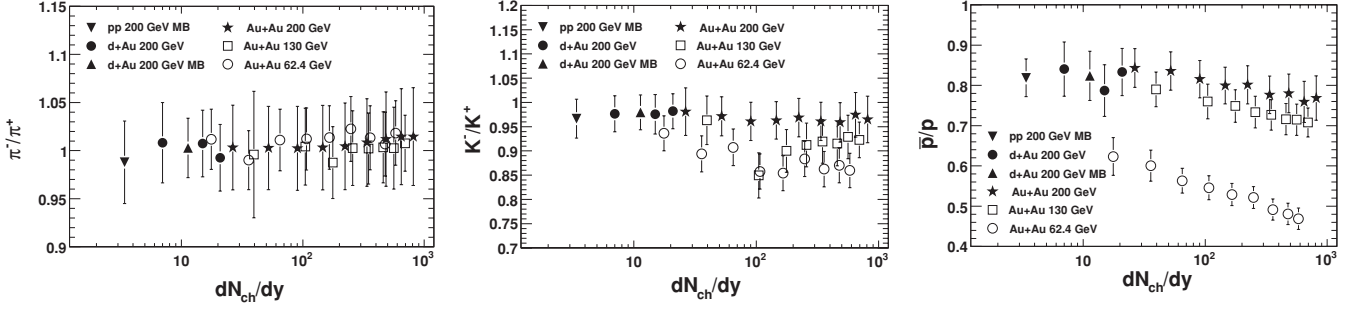


FIG. 25. Antiparticle-to-particle ratios as a function of dN_{ch}/dy for pp and $d + Au$ collisions at 200 GeV and $Au + Au$ collisions at 62.4, 130, and 200 GeV. Errors shown are the quadratic sum of statistical and systematic uncertainties.

At the top CERN Super Proton Synchrotron (SPS) energy, the formation time is traditionally taken as $\tau = 1$ fm/c resulting in $\epsilon_{Bj} = 3.2$ GeV/fm³ for central Pb + Pb collisions [70]. At RHIC, the choice of τ is still a matter of debate. While Ref. [71] uses $\tau = 0.6$ fm/c for their hydrodynamic model ($\sqrt{s_{NN}} = 200$ GeV), Ref. [72] uses $\tau = 0.2$ fm/c, evaluated from the energy loss of high $p_{\perp}\pi^0$ in $\sqrt{s_{NN}} = 130$ GeV $Au + Au$ collisions. Because of these uncertainties in τ , the Bjorken energy density estimate should be taken with caution, in addition to the assumptions of Bjorken longitudinal boost invariance and formation of a thermalized central region at an initial time τ . It should be noted that due to final state interactions, measured (final) total transverse energies are expected to be less than initial ones [73].

E. Antiparticle-to-particle ratios

Relative particle production can be studied by particle ratios of the integrated dN/dy yields. Figure 25 shows the antiparticle-to-particle ratios (π^-/π^+ , K^-/K^+ , and \bar{p}/p) as a function of the charged-particle multiplicity in pp , $d + Au$ at 200 GeV and $Au + Au$ collisions at 62.4, 130, and 200 GeV. The 200 GeV and some of the 130 GeV data have been presented before [17,45,49]. The π^-/π^+ ratio is approximately unity for all measured collision systems and collision energies. The ratios are independent of multiplicity and centrality. Similar behavior has been observed at lower collision energies as well.

The K^-/K^+ ratios are close to unity in pp , $d + Au$, and $Au + Au$ collisions at 200 GeV. The ratio decreases slightly from the 200 GeV to the 62.4 GeV $Au + Au$ data. This may be due to the increasing net baryon density in the collision zone, which leads to differences in associated production of kaons. There appears to be a decreasing trend with centrality in the 62.4 GeV data, presumably due to a significant increase in the net baryon density.

The \bar{p}/p ratio appears to be independent of multiplicity in pp and $d + Au$ collisions at 200 GeV. The ratio in peripheral $Au + Au$ at 200 GeV is similar to that in pp and $d + Au$ collisions at the same energy. A slight decrease is observed with increasing centrality in $Au + Au$ collisions at 200 and 130 GeV. The ratio is significantly lower at 62.4 and shows a considerable drop with increasing centrality. The drop of the

\bar{p}/p ratio with increasing centrality is consistent with larger baryon stopping in central collisions.

Figure 26 shows the K^-/K^+ ratio vs the \bar{p}/p ratio, together with results from other energies [74–79]. Both ratios are affected by the net baryon content; they show a strong correlation as seen in Fig. 26. This can be simply understood in the chemical equilibrium model where particle ratios are governed by only a few parameters. This aspect will be discussed in Sec. VII. It is worth noting that at low energies, the absorption of antiprotons in the baryon-rich environment plays a vital role.

F. Baryon production and transport

The antiproton is the lightest antibaryon. Most high-mass antibaryons decay into antiprotons. The \bar{p}/π^- ratio, therefore,

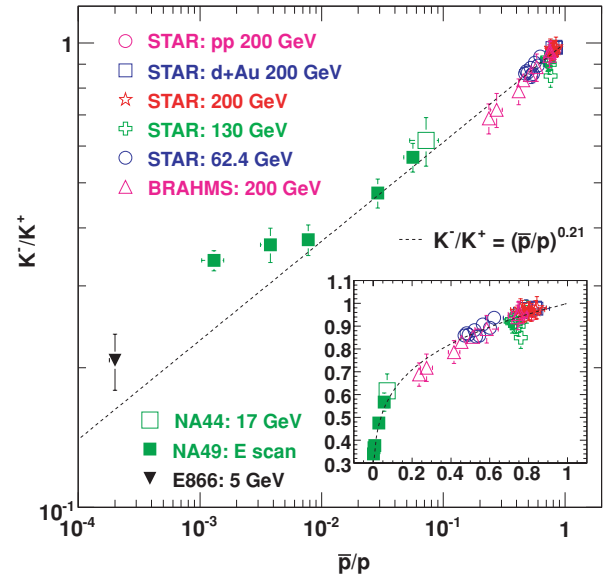


FIG. 26. (Color online) Ratio of charged kaons vs that of antiprotons to protons at various energies. Errors shown are the quadratic sum of statistical and systematic uncertainties. The line is a power-law fit to the data except for the AGS data point (the inverse solid triangle) and the two lowest energy SPS data points (solid squares), which have significant baryon absorption effect. The insert is a linear plot.

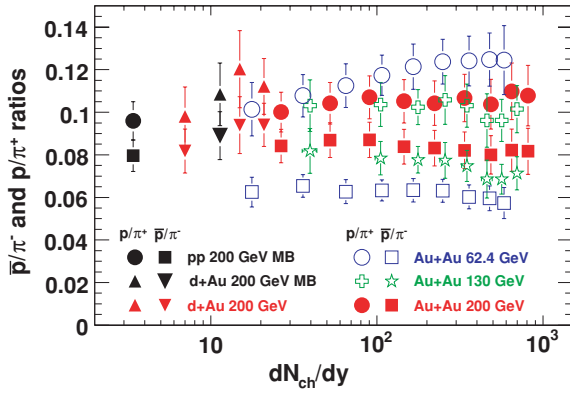


FIG. 27. (Color online) p/π^+ and \bar{p}/π^- ratios as a function of the charged-particle multiplicity in pp , $d + \text{Au}$, and $\text{Au} + \text{Au}$ collisions. Errors shown are the quadratic sum of statistical and systematic uncertainties.

characterizes well antibaryon production relative to total particle multiplicity. As mentioned earlier, the inclusive \bar{p} yield reported here is the sum of the primordial \bar{p} yield and the weak-decay contributions. Because all decay (anti)protons are measured in the data sample, the weak-decay contribution can be estimated as $0.64(\bar{\Lambda} + \bar{\Sigma}^0 + \bar{\Xi} + \bar{\Omega}^+) + 0.52\bar{\Sigma}^-$. With the assumption of isospin symmetry with $\bar{n} \approx \bar{p}$ and $\bar{\Sigma}^0 \approx \bar{\Sigma}^+ \approx \bar{\Sigma}^-$, one may estimate the total antibaryon rapidity density to be approximately twice the measured antiproton rapidity density [19], and the total net-baryon density to be approximately twice the total net-proton density. The assumption of isospin symmetry is fairly good for $\text{Au} + \text{Au}$ collisions and should be good for pp collisions at high energy because of the efficient charge exchange reactions that convert between protons and neutrons [80].

Figure 27 shows the \bar{p}/π^- ratio as a function of event multiplicity in pp , $d + \text{Au}$, and $\text{Au} + \text{Au}$ collisions. The ratio at 200 GeV is found to be independent of centrality and is the same for pp , $d + \text{Au}$, and $\text{Au} + \text{Au}$ collisions within the experimental uncertainties. The values of the \bar{p}/π^- ratio at 62.4 GeV are lower than those at 200 GeV at all centralities, indicating the significant effect of collision energy on the production of heavy particles even at these high energies. Although the net-baryon density increases with centrality, especially at 62.4 GeV with narrower rapidity gap between the beams, the \bar{p}/π^- ratio does not seem to be affected much by the net-baryon density, suggesting that antibaryon absorption is not a significant effect at these energies. At the lower BNL Alternating Gradient Synchrotron (AGS) and SPS energies, the \bar{p}/π^- has a much stronger decreasing trend with increasing centrality [81]; baryon stopping and the effect of net-baryon density are much stronger at low energies.

It has been argued that production of antibaryons, due to their large masses, is sensitive to energy density. An increased antibaryon production relative to total entropy with increasing centrality at the same collision energy could indicate formation of high energy density, or QGP in central collisions. On the hadronic level, at high pion density, multiple-pion fusion into

baryon-antibaryon pairs could contribute significantly to the antibaryon yield [82]. Such an increase with centrality is not observed in data, but it could be canceled by the effect of positive net-baryon density, resulting in antibaryon absorption. On the other hand, antibaryon production does increase with the collision energy. However, this cannot be taken as evidence of QGP formation, as antibaryon production is very sensitive to the available energy for production because of their large mass. Indeed, antibaryon production in elementary collisions is found to be a sensitive function of the collision energy.

Figure 27 also shows the p/π^+ ratio as a function of the charged-particle multiplicity. The p/π^+ ratio is found to be constant over centrality at 130 and 200 GeV and shows an increasing trend with centrality at 62.4 GeV. The p/π^+ ratio is found to be the same in pp , $d + \text{Au}$, and $\text{Au} + \text{Au}$ collisions at 200 GeV within our experimental uncertainties. Unlike antibaryons, baryons come from two sources: pair production together with antibaryons and transport from the initial colliding nuclei at beam rapidities. The latter can be obtained from the difference between baryon and antibaryon yields. Figure 27 indicates a finite net-baryon number is present at midrapidity in all collisions. A finite baryon number has been transported over ~ 3 – 5.4 units of rapidity in these collisions. How baryons are transported over many units of rapidity has been a long-standing theoretical issue [83–85]. Baryon transport occurs very early in the collision and affects the subsequent evolution of the collision system. Further understanding of baryon transport can shed more light on the evolution of heavy-ion collisions.

Figure 28 shows the ratio of the number of net-protons ($p - \bar{p}$) to half the number of participant nucleons, i.e., the approximate probability of each incoming nucleon to be transported to midrapidity, as a function of N_{part} . The probability is nonzero even in pp collisions at 200 GeV. Compared with pp , the probability is larger in central heavy-ion collisions at the same energy by a factor of ~ 2 . The probability of baryon transport to midrapidity is larger in

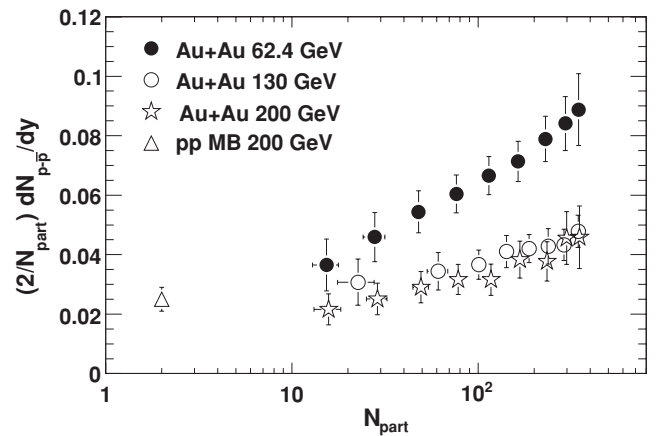


FIG. 28. Ratio of midrapidity net-protons to half the number of participants vs the number of participants in pp collisions at 200 GeV and in $\text{Au} + \text{Au}$ collisions at 62.4, 130, and 200 GeV. Errors shown are the quadratic sum of statistical and systematic uncertainties.

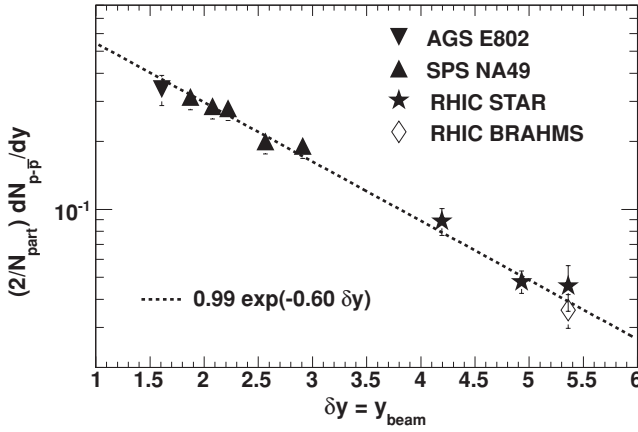


FIG. 29. Ratio of midrapidity inclusive net-protons to half the number of participants in central heavy-ion collisions as a function of the rapidity shift. The AGS data are from Refs. [75,86], SPS data from Refs. [87–89], and BRAHMS data from Ref. [90]. The published SPS data have already been corrected for weak decays, the size of which is of the order 20–25% [88], so we have added 25% to the published net-proton yields to obtain the inclusive ones. Errors shown are total statistical and systematic uncertainties. The dashed line is an exponential fit to the data.

the lower 62.4 GeV collisions, owing to the smaller beam rapidity.

Our data demonstrate that baryon-antibaryon pair production and baryon stopping are two independent processes: the baryon-antibaryon pair production rate does not depend on the collision centrality and increases with the collision energy, whereas the baryon stopping increases with the collision centrality and decreases with the collision energy. The net-baryon density due to baryon stopping may have an effect on the final observed yield of antibaryons because of absorption. However, this effect does not seem to be significant at our measured energies.

Proton and antiproton production has been measured in heavy-ion collisions at lower energies. Figure 29 shows the ratio of midrapidity inclusive net-proton density to half of the number of participants in central Au + Au collisions as a function of the beam rapidity (i.e., the rapidity shift suffered by those net-protons). The measured NA49 data have been corrected for weak decays, which is dominated by weak-decay protons, the size of which is of the order of 20–25% [88]. To obtain the inclusive net-proton yield, we multiplied the measured NA49 data by a factor of 1.25. All other data are inclusive measurements already including weak-decay products. The ratio (or the approximate probability of each nucleon to be transported to midrapidity) drops rapidly with increasing rapidity shift. The dashed line is an exponential fit to the data, yielding $\frac{dN_{p-\bar{p}}/dy}{N_{\text{part}}/2} = 0.99 \exp(-0.60\delta y)$.

One may view the net-proton density vs rapidity shift, obtained from central collisions at different energies, as a “measure” of the rapidity distribution of net-protons in central Au + Au collisions at the top RHIC energy. Since the net-protons shown in Fig. 29 contain equal contributions from

the two colliding nuclei, the net-proton rapidity distribution in Au + Au collisions at the top RHIC energy is the data points in Fig. 29 multiplied by a factor varying between 1/2 and 1. At small $\delta y \sim 0$, the net-proton density should be close to 1/2 of those shown in Fig. 29, and at large δy (i.e., nearly midrapidity), the factor should be close to 1. Assuming an exponential variation in this factor between 1/2 and 1, i.e., a net-proton rapidity distribution of $\frac{dN_{p-\bar{p}}/dy}{N_{\text{part}}/2} = 2^{\delta y/5.36-1} \times 0.99 \exp(-0.60\delta y) = 0.50 \exp(-0.47\delta y)$ in 200 GeV Au + Au collisions (where 5.36 is the beam rapidity for 100 GeV beams), we estimate a rapidity shift of $\langle \delta y \rangle = 1/0.47 \approx 2.1$. It is interesting to note that the integral of the above rapidity distribution between 0 and 5.36 comes out to be rather close to unity as required by proper normalization. Clearly the exponential form we used is a simplification. BRAHMS has measured the rapidity distribution of net-protons in the range $0 < y < 3$ in central Au + Au collisions at 200 GeV and used a more sophisticated functional form to estimate the average rapidity shift to be approximately 2.06 ± 0.16 [90].

G. Strangeness production

Strangeness has a special place in heavy-ion physics. Enhanced production of strangeness has long been predicted as a prominent signature of QGP formation. In a hadron gas, strangeness has to be produced via strange hadron pairs, which requires a large energy; whereas in QGP, it can be produced via a strange quark-antiquark pair, which is energetically favored [91–93]. Elementary pp collisions, where QGP formation is unlikely, are important as a reference: an enhanced strangeness production in heavy-ion collisions relative to pp could signal QGP formation. However, other processes can also enhance strangeness production as shown by many studies [94,95]. Although not a sufficient signature for QGP formation, strangeness enhancement is a necessary condition which QGP formation requires.

Strangeness production and the K/π ratios have been intensively studied in heavy-ion collisions at the AGS [76,96–98] and the SPS [77,99–105], and in elementary interactions of pp [106,107] and $\bar{p}p$ [108,109], prior to RHIC [17,18,110]. Figure 30(a) compiles the K/π ratios in pp collisions and central heavy-ion collisions as a function of the collision energy $\sqrt{s_{NN}}$. The 200 GeV pp and Au + Au data are from Ref. [17], and the Au + Au data at 62.4 and 130 GeV are from this work. The K/π ratio was already studied in Ref. [18], but there the pion yield was not measured but estimated from negatively charged hadrons, kaons, and antiprotons. In this work, the measured pion yield is used to obtain the K/π ratio. The other data in Fig. 30 are taken from Refs. [106–109] for pp collisions and Refs. [17,76,77,96–105] for central heavy-ion collisions, as also compiled in Ref. [18].

One obvious feature in Fig. 30(a) is that the K^-/π^- ratio in heavy-ion collisions steadily increases with $\sqrt{s_{NN}}$, while K^+/π^+ sharply increases at low energies. The addition of the

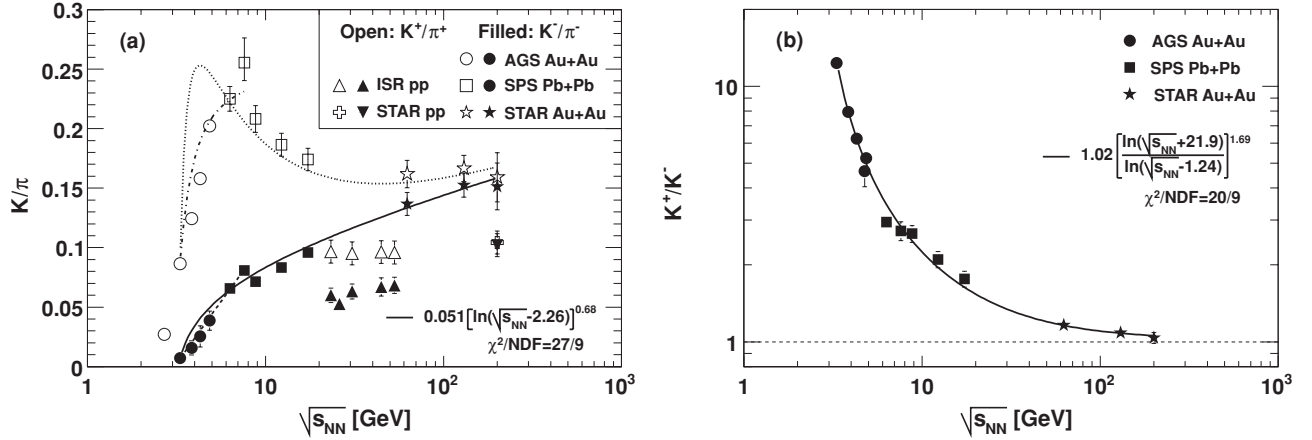


FIG. 30. (a) K^+/π^+ and K^-/π^- ratios as a function of the collision energy in pp [106–109] and central heavy-ion collisions. (b) K^+/K^- ratio as a function of the collision energy in central heavy-ion collisions. The heavy-ion data not covered in this work are taken from Refs. [17,76,77,96–105]. The error bars on the heavy-ion data are the quadratic sum of statistical and systematic uncertainties and are statistical only on the elementary collision data. The curves going through the heavy-ion K^-/π^- and K^+/K^- data are phenomenological fits. The curves going through the heavy-ion K^+/π^+ data are the product of the fit curves. See text for details.

K^+/π^+ measurements at RHIC energies clearly demonstrates that K^+/π^+ drops at high energies. A maximum K^+/π^+ value is reached at about $\sqrt{s_{NN}} \approx 10$ GeV. This behavior of K^+/π^+ can be partially attributed to the net-baryon density, which changes significantly with $\sqrt{s_{NN}}$, as noted previously [111–113]. It is instructive to consider the two possible kaon production mechanisms: pair production of K and \bar{K} , which is sensitive to $\sqrt{s_{NN}}$, and the associated production of K (\bar{K}) with a hyperon (antihyperon), which is sensitive to the baryon (antibaryon) density.² The excess of K over \bar{K} is due to the finite net-baryon density. To visualize the relative contributions from these two mechanisms, Fig. 30(b) shows the ratio of K^+/K^- as function of $\sqrt{s_{NN}}$ in central heavy-ion collisions. The ratio sharply drops with energy, demonstrating the transition from associated production of K^+ dominant at low energies to the dominance of equal production of K^+ and K^- via either pair production of K^+K^- or associated production of K^+ (K^-) with hyperon (antihyperon) at high energies. The K^+/K^- dependence on $\sqrt{s_{NN}}$ is relatively smooth and can be fit reasonably well by the functional form shown in the figure. On the other hand, the rate of symmetric production of K^+ and K^- increases with $\sqrt{s_{NN}}$, as seen in the K^-/π^- ratio in Fig. 30(a). We fit the K^-/π^- ratio by the functional form shown in the figure as the solid curve. The curve describes the data points well except at low $\sqrt{s_{NN}}$, where the K^-/π^- ratio can be better described by a linear increase in $\log(\sqrt{s_{NN}})$, as shown by the dashed line. The product of the curve in Fig. 30(b) and the solid curve (dashed line) in Fig. 30(a) yields the dotted (dash-dotted) curve in Fig. 30(a). It suggests that the smooth dropping of K^+/K^- with $\sqrt{s_{NN}}$ in Fig. 30(b) and the seemingly smooth increase of K^-/π^- with $\sqrt{s_{NN}}$ can generate a maximum in K^+/π^+ at $\sqrt{s_{NN}} \sim$

10 GeV. In fact, model studies [112,113] have indeed shown a maximum in the K^+/π^+ excitation function. However, the maximum peak from model studies is broad and smooth, not as sharp as Fig. 30(a) shows.

NA49 first observed the sharp maximum peak structure in the K^+/π^+ ratio [77] and referred to it as the “horn.” They attribute the horn to a phase transition between hadrons and the QGP, because ordinary physics (involving production rate and baryon density) does not seem to explain the data. The smooth dependence of the K^+/K^- ratio on $\sqrt{s_{NN}}$ indicates that the horn is not K^+/π^+ specific but is also present in the K^-/π^- ratio as can be seen in Fig. 30(a). To shed light on the horn, more precise measurements are needed for which the RHIC energy scan program should help.

Figure 30(a) indicates that the enhancement in K^-/π^- from elementary pp to central heavy-ion collisions is about 50% and is similar at the SPS and RHIC, while that in K^+/π^+ is larger at lower energies because of the large net-baryon density in heavy-ion collisions. The increase in K/π ratios from pp to central heavy-ion collisions has been argued as being due to canonical suppression of strangeness production in small-volume pp collisions [114–117]. Although the increase in the K/π ratios from pp to central heavy-ion collisions cannot be readily taken as evidence for QGP formation, it is interesting to study how and where the increase happens as a function of centrality. Figure 31 shows the K^-/π^- ratio as a function of the charged-hadron multiplicity in pp , $d + \text{Au}$, and $\text{Au} + \text{Au}$ collisions at RHIC energies. The K^+/π^+ ratio shows similar dependence on centrality. The K^-/π^- ratio appears to increase approximately linearly with $\log(dN_{ch}/dy)$.

Experiments at the AGS and SPS have also studied the centrality dependence of kaon production in heavy-ion collisions. Figure 32 shows those results as a function of the number of participants N_{part} together with our results at RHIC. The K^-/π^- ratio increases with N_{part} within the

²These mechanisms also apply at the quark level.

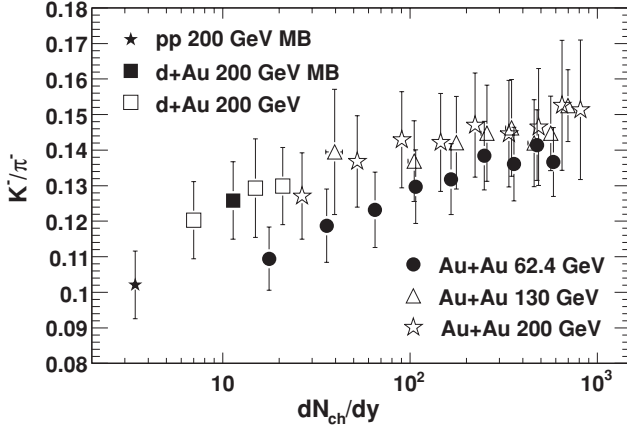


FIG. 31. K^-/π^- ratio as a function of the charged-particle rapidity density in pp , $d + \text{Au}$, and $\text{Au} + \text{Au}$ collisions at RHIC. Errors shown are the quadratic sum of statistical and systematic uncertainties.

same collision system.³ The increase happens rather quickly at RHIC, restricted to very peripheral collisions; little variation with centrality is found from medium-central to central collisions. At lower energies, the K^-/π^- ratio increases steadily with N_{part} . However, at the same value of N_{part} , the ratio differs in different systems at similar energies as shown in Refs. [76,101], indicating that N_{part} is not an appropriate variable to describe K^-/π^- . This has been noted and emphasized before in Refs. [76,101].

Neither charged-hadron multiplicity nor the number of participants can satisfactorily describe the systematics of the K^-/π^- ratio. It is desirable to search for a quantity that better describes the systematics. We first note that strangeness

³Systematic uncertainties on the K/π ratio are largely correlated. The 130 GeV data may miss a very peripheral but crucial data point.

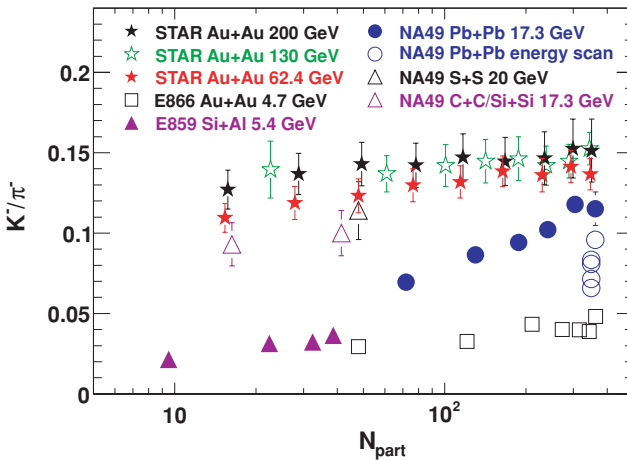


FIG. 32. (Color online) K^-/π^- ratio as a function of the number of participants N_{part} in heavy-ion collisions at the AGS [76,97], SPS [77,100–105], and RHIC. Errors shown are the quadratic sum of statistical and systematic uncertainties for the RHIC data, and only statistical for the AGS and SPS data.

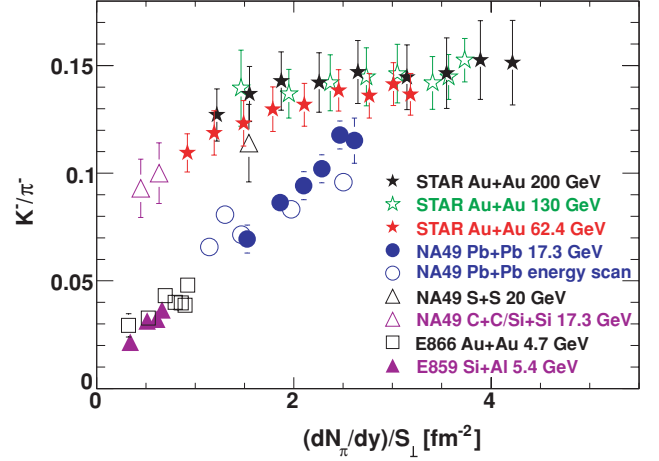


FIG. 33. (Color online) K^-/π^- ratio as a function of $\frac{dN_\pi/dy}{S_\perp}$ in heavy-ion collisions at the AGS [76,97], SPS [77,100–105], and RHIC. Errors shown are the quadratic sum of statistical and systematic uncertainties for the RHIC data, and statistical only for the AGS and SPS data.

production may be enhanced as a result of the fast and energetically favorable process of gluon-gluon fusion into strange quark-antiquark pairs, and therefore it may be sensitive to the initial gluon density. Indeed, it has been argued that particle production at RHIC (and perhaps at SPS) is dominated by the gluon saturation region [118,119]. At high energies, the only relevant quantity in the gluon saturation picture is $\frac{dN_\pi/dy}{S_\perp}$, which is approximately proportional to the number of nucleon-nucleon collisions per participant, as mentioned earlier. Motivated by these considerations, Fig. 33 shows the K^-/π^- ratio as a function of $\frac{dN_\pi/dy}{S_\perp}$. It is interesting to note that the K^-/π^- ratio linearly increases with $\frac{dN_\pi/dy}{S_\perp}$ in the AGS and SPS energy regime. The RHIC data show a different behavior: the K^-/π^- ratio increases from pp to peripheral $\text{Au} + \text{Au}$ collisions but quickly saturates in medium-central to central collisions.

In the gluon saturation picture, it is possible that the initial gluon density is saturated at RHIC energies [119]. As the saturation scale becomes large, the difference between kaon and pion masses becomes less important, resulting in a roughly constant K^-/π^- . Gluon saturation may already be relevant in central Pb + Pb collisions at the top SPS energy [119]. Gluon saturation should be irrelevant at AGS energies, as gluons can be distinguished longitudinally, and quark contribution to particle production is significant. However, the fact that Si + Al and Au + Au data are on top of each other in Fig. 33 indicates that $\frac{dN_\pi/dy}{S_\perp}$ may be the relevant quantity for K^-/π^- at the AGS, although the interpretation may be different from that at high energies.

VII. FREEZE-OUT PROPERTIES

In this section, particle ratios are used in the context of a thermal equilibrium model [120–123] to extract chemical freeze-out properties. The extracted blast-wave model fit parameters are investigated to learn about the kinetic freeze-out properties. The systematics of the chemical and kinetic

freeze-out properties extracted from data within the model frameworks are studied, and implications of these results in terms of the system created in heavy-ion collisions are discussed.

A. Chemical freeze-out properties

In the chemical equilibrium model, particle abundance in a thermal system of volume V is governed by only a few parameters,

$$N_i/V = \frac{g_i}{(2\pi)^3} \gamma_S \int \frac{1}{\exp\left(\frac{E_i - \mu_B B_i - \mu_S S_i}{T_{\text{chem}}}\right) \pm 1} d^3p, \quad (15)$$

where N_i is the abundance of particle species i , g_i is the spin degeneracy, B_i and S_i are the baryon number and strangeness

number, respectively, E_i is the particle energy, and the integral is over the whole momentum space. The model parameters are the chemical freeze-out temperature (the temperature of the system) T_{chem} , the baryon and strangeness chemical potentials μ_B and μ_S , respectively, and the *ad hoc* strangeness suppression factor γ_S .

The measured particle abundance ratios are fit by the chemical equilibrium model. The ratios included in the fit are π^-/π^+ , K^-/K^+ , \bar{p}/p , K^-/π^- , and \bar{p}/π^- . The fit is performed for each collision system and each multiplicity or centrality class. The extracted chemical freeze-out parameters are summarized in Table X. The 200 GeV pp and Au + Au results are from Ref. [17].

Figure 34(a) shows the extracted baryon and strangeness chemical potentials as a function of the charged-particle

TABLE X. Chemical and kinetic freeze-out properties in pp and $d + \text{Au}$ collisions at 200 GeV, and Au + Au collisions at 62.4, 130, and 200 GeV. Quoted errors are the total statistical and systematic uncertainties. The 200 GeV pp and Au + Au data are from Ref. [17].

System	Centrality	Chemical properties					Kinetic properties			
		T_{chem} (MeV)	μ_B (MeV)	μ_S (MeV)	γ_S	χ^2/ndf	T_{kin} (MeV)	$\langle\beta\rangle$	n	χ^2/ndf
pp 200 GeV	Min. bias	157.5 ± 3.6	8.9 ± 3.8	2.3 ± 3.6	0.56 ± 0.04	0.81	127 ± 13	0.244 ± 0.081	4.3 ± 1.7	1.18
	Min. bias	164^{+11}_{-8}	16.5 ± 6.5	3.3 ± 3.6	0.69 ± 0.07	0.013	112 ± 26	0.407 ± 0.033	1.9 ± 0.9	0.89
$d + \text{Au}$ 200 GeV	40–100%	159^{+10}_{-7}	14.4 ± 6.7	2.5 ± 3.6	0.66 ± 0.07	0.051	112 ± 24	0.377 ± 0.031	2.2 ± 1.3	1.55
	20–40%	168^{+14}_{-10}	21.0 ± 7.6	4.2 ± 4.1	0.71 ± 0.08	0.068	107 ± 33	0.428 ± 0.067	1.9 ± 0.9	1.32
	0–20%	167^{+12}_{-7}	15.8 ± 6.3	3.2 ± 3.6	0.71 ± 0.07	0.069	116 ± 21	0.420 ± 0.030	1.6 ± 0.7	0.72
	70–80%	157.9 ± 3.9	14.1 ± 4.2	2.8 ± 2.6	0.70 ± 0.06	0.51	129 ± 14	0.358 ± 0.084	1.50 ± 0.28	0.70
Au-Au 200 GeV	60–70%	158.7 ± 4.1	15.3 ± 4.2	2.3 ± 2.6	0.76 ± 0.06	0.51	118 ± 13	0.405 ± 0.071	1.57 ± 0.11	0.42
	50–60%	158.8 ± 4.1	17.7 ± 4.2	2.1 ± 2.6	0.81 ± 0.07	0.35	115 ± 12	0.456 ± 0.071	1.16 ± 0.08	0.45
	40–50%	155.8 ± 4.0	18.9 ± 4.2	2.7 ± 2.6	0.80 ± 0.07	0.17	108 ± 12	0.499 ± 0.071	0.98 ± 0.06	0.48
	30–40%	156.5 ± 4.2	18.6 ± 4.2	3.1 ± 2.6	0.83 ± 0.07	0.04	109 ± 11	0.514 ± 0.061	0.90 ± 0.05	0.45
	20–30%	156.7 ± 4.8	21.3 ± 4.2	3.2 ± 2.6	0.82 ± 0.08	0.03	102 ± 11	0.539 ± 0.061	0.90 ± 0.04	0.37
	10–20%	155.1 ± 4.8	21.0 ± 4.2	3.0 ± 2.6	0.83 ± 0.09	0.02	99 ± 12	0.560 ± 0.061	0.80 ± 0.03	0.36
	5–10%	156.5 ± 5.3	22.8 ± 4.5	4.9 ± 2.6	0.86 ± 0.10	0.02	91 ± 12	0.577 ± 0.051	0.86 ± 0.02	0.51
	0–5%	159.3 ± 5.8	21.9 ± 4.5	3.9 ± 2.6	0.86 ± 0.11	0.03	89 ± 12	0.592 ± 0.051	0.82 ± 0.02	0.25
	58–85%	159^{+11}_{-7}	19.9 ± 4.9	3.0 ± 4.3	0.78 ± 0.11	0.004	136 ± 32	0.400 ± 0.027	0.0 ± 10.1	0.96
	45–58%	158^{+10}_{-6}	26.2 ± 5.2	-5.9 ± 4.6	0.82 ± 0.08	0.015	113 ± 16	0.465 ± 0.010	0.6 ± 0.5	0.78
Au + Au 130 GeV	34–45%	158^{+9}_{-5}	25.8 ± 4.8	-1.0 ± 4.1	0.83 ± 0.09	0.153	103 ± 11	0.502 ± 0.013	0.8 ± 0.3	1.01
	26–34%	158^{+10}_{-6}	27.1 ± 4.9	0.6 ± 4.1	0.84 ± 0.09	0.006	103 ± 16	0.526 ± 0.017	0.8 ± 0.3	0.81
	18–26%	156^{+10}_{-6}	27.4 ± 4.7	1.5 ± 4.0	0.85 ± 0.09	0.005	103 ± 15	0.531 ± 0.017	0.8 ± 0.2	0.81
	11–18%	153^{+9}_{-6}	27.9 ± 4.8	1.5 ± 4.0	0.83 ± 0.08	0.012	106 ± 20	0.538 ± 0.023	0.7 ± 0.4	0.52
	6–11%	153^{+9}_{-5}	27.7 ± 4.7	2.7 ± 3.8	0.84 ± 0.07	0.005	93 ± 12	0.558 ± 0.019	0.7 ± 0.3	0.70
	0–6%	154^{+10}_{-6}	29.0 ± 4.6	2.4 ± 3.3	0.89 ± 0.07	0.136	96 ± 8	0.567 ± 0.020	0.7 ± 0.3	0.67
	70–80%	154^{+8}_{-6}	37.7 ± 6.5	6.6 ± 3.5	0.62 ± 0.06	0.244	130 ± 15	0.306 ± 0.065	2.1 ± 1.8	0.93
	60–70%	156^{+8}_{-5}	42.5 ± 5.8	4.0 ± 3.6	0.69 ± 0.07	0.178	130 ± 15	0.389 ± 0.019	0.4 ± 0.9	0.55
	50–60%	155^{+8}_{-5}	47.0 ± 5.1	6.7 ± 3.5	0.71 ± 0.07	0.197	129 ± 16	0.426 ± 0.021	0.0 ± 9.8	0.59
	40–50%	156^{+9}_{-5}	51.3 ± 5.2	3.2 ± 3.6	0.78 ± 0.07	0.237	120 ± 13	0.459 ± 0.009	0.6 ± 0.5	0.54
Au + Au 62.4 GeV	30–40%	157^{+9}_{-5}	54.2 ± 5.2	3.6 ± 3.6	0.79 ± 0.07	0.275	113 ± 12	0.494 ± 0.008	0.6 ± 0.4	0.45
	20–30%	157^{+9}_{-5}	54.5 ± 5.2	6.6 ± 3.4	0.82 ± 0.07	0.715	105 ± 10	0.517 ± 0.020	0.8 ± 0.3	0.52
	10–20%	156^{+9}_{-5}	59.4 ± 5.4	6.2 ± 3.5	0.82 ± 0.07	0.261	105 ± 14	0.535 ± 0.017	0.6 ± 0.4	0.52
	5–10%	155^{+9}_{-5}	61.0 ± 5.7	7.4 ± 3.5	0.85 ± 0.07	0.066	100 ± 12	0.546 ± 0.019	0.7 ± 0.3	0.77
	0–5%	154^{+10}_{-7}	62.7 ± 6.0	7.1 ± 3.5	0.82 ± 0.07	0.480	99 ± 10	0.554 ± 0.018	0.6 ± 0.4	0.75

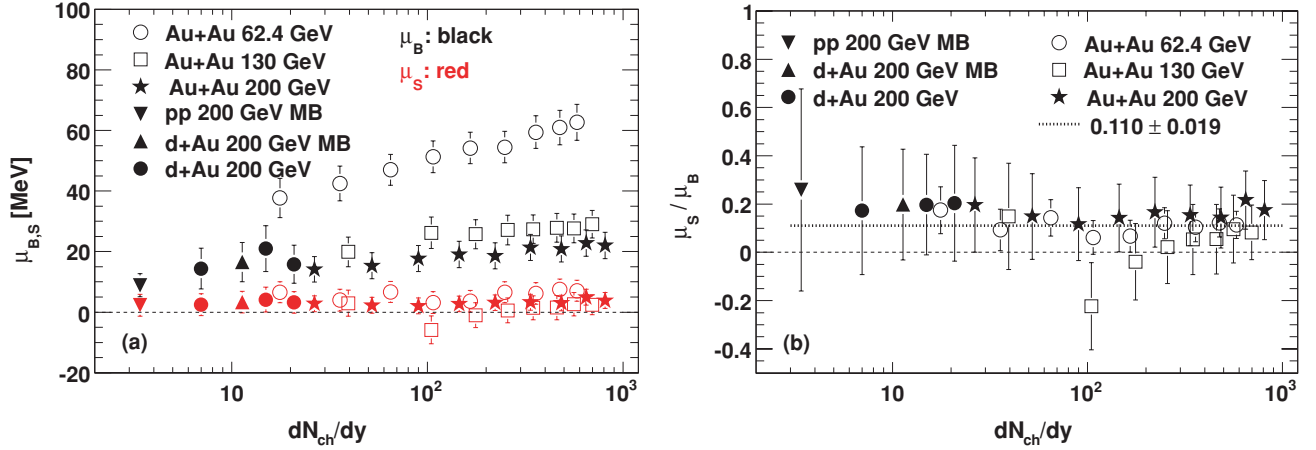


FIG. 34. (Color online) (a) Baryon (μ_B) and strangeness (μ_S) chemical potentials extracted from chemical equilibrium model fits to pp and $d + Au$ data at 200 GeV, and Au + Au data at 62.4, 130, and 200 GeV. (b) Ratio μ_S/μ_B of the extracted chemical potentials. Errors shown are the total statistical and systematic errors. The 200 GeV pp and Au + Au fit results are from Ref. [17].

multiplicity in pp and $d + Au$ at 200 GeV and in Au + Au collisions at 62.4, 130, and 200 GeV. The baryon chemical potential increases with centrality in heavy-ion collisions, especially at 62.4 GeV. This is already indicated by the \bar{p}/p ratio in Fig. 25. The strangeness chemical potential is small and close to zero. It is mainly reflected in the K/π and K^-/K^+ ratios. As already shown in Fig. 26, the K^-/K^+ ratio is correlated with the \bar{p}/p ratio by a universal curve. In the chemical equilibrium picture without considering resonance decays, these ratios are simply equal to $K^-/K^+ = \exp[(-2\mu_B/3 + 2\mu_S)/T_{chem}]$ and $\bar{p}/p = \exp(-2\mu_B/T_{chem})$, respectively. Weak decays and resonance decays complicate the situation, but the effects of decays are small for the K^-/K^+ and \bar{p}/p ratios. A power-law fit to all data points in Fig. 26 (except the AGS data point and the two lowest SPS data points) yields $K^-/K^+ \propto (\bar{p}/p)^{0.21}$. This gives $\mu_S/\mu_B \approx 0.12$ in the chemical equilibrium picture. We show in Fig. 34(b) the ratio of the extracted μ_S to μ_B . A fit to a constant indeed shows $\mu_S/\mu_B = 0.110 \pm 0.019$. Analyses of chemical freeze-out parameters in heavy-ion collisions at other energies indicate a similar relationship [124]. The strong correlation between μ_S and μ_B should not come as a surprise, as the (anti)hyperons couple these two parameters naturally. However, the same relationship holding for different energies is not expected *a priori*.

Figure 35 shows the extracted strangeness suppression factor γ_S as a function of the charged-particle multiplicity. The γ_S in pp , $d + Au$, and peripheral Au + Au collisions is significantly smaller than unity, suggesting that strangeness production is strongly suppressed in these collisions. The γ_S factor increases with centrality, reaching a value in central Au + Au collisions that is not much smaller than unity. This suggests that strangeness production in central collisions is no longer strongly suppressed; strangeness is nearly chemically equilibrated with the light flavors.

The extracted chemical freeze-out temperature is shown in Fig. 36. A striking feature is that the chemical freeze-out

temperature is independent of collision system or centrality. In each system investigated, the extracted chemical freeze-out temperature is $T_{chem} \approx 156$ MeV, which is close to the lattice QCD calculation of the cross-over temperature between the deconfined phase and the hadronic phase for three flavors (154 ± 8 MeV) [125]. On the other hand, the initial conditions in Au + Au collisions of different centralities (and at different energies) are very different. In other words, systems starting off with different initial conditions always evolve toward a “universal” condition at chemical freeze-out, independent of the initial conditions [17]. The proximity of the fit T_{chem} and the predicted phase-transition temperature strongly suggests that chemical freeze-out happens at the phase-transition boundary, or hadronization. Indeed, hadronization should be universal.

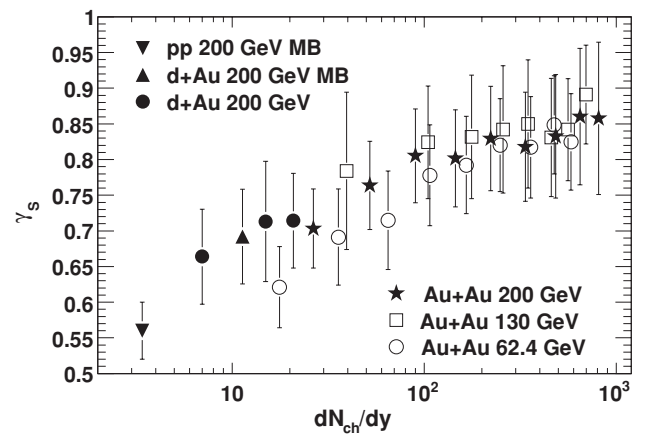


FIG. 35. Strangeness suppression factor extracted from chemical equilibrium model fit to pp and $d + Au$ data at 200 GeV, and Au + Au data at 62.4, 130, and 200 GeV. Errors shown are the total statistical and systematic uncertainties. The 200 GeV pp and Au + Au fit results are from Ref. [17].

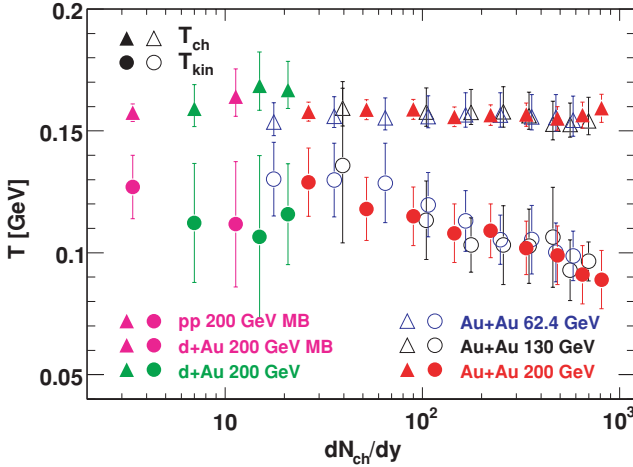


FIG. 36. (Color online) Chemical and kinetic freeze-out temperatures as a function of the charged-hadron multiplicity. Errors shown are the total statistical and systematic uncertainties. The 200 GeV pp and Au + Au data are from Ref. [17].

The success of the chemical equilibrium model in describing the data should not be readily taken as a proof of chemical equilibrium of each individual collision [126]. In pp (and other elementary) collisions, the compositions of most particles are described well by the chemical equilibrium model but with the *ad hoc* strangeness suppression factor significantly smaller than unity. This has been argued as due, in part, to canonical suppression from conservation of strangeness in small volumes [114,115,126]. Canonical suppression appears to explain elementary e^+e^- data, while additional suppression seems needed to account for strangeness production in pp collisions. The apparent success of the chemical equilibrium model in describing elementary collisions, despite the strangeness suppression factor, in all likelihood suggests that particle production in these collisions is a statistical process, and the chemical temperature is a parameter governing the statistical production processes [126].

On the other hand, the stringent constraints of conservation laws are largely lifted in heavy-ion collisions as they only need to be satisfied globally over a large volume. As a result, particle ensembles can be treated in a grand canonical framework. The chemical equilibrium model can describe the abundances of all stable hadrons. The *ad hoc* strangeness suppression factor extracted from central heavy-ion collisions is close to unity, implying that strangeness is as equally equilibrated as light quarks. Moreover, many experimental results indicate that the medium created at RHIC is strongly interacting [6], which will naturally lead to thermalization. Thus the success of the chemical equilibrium model may indeed suggest that the individual Au + Au collisions are largely thermalized.

B. Kinetic freeze-out properties

The measured p_\perp spectral shape flattens significantly with increasing particle mass in central Au + Au collisions. This suggests the presence of a collective transverse radial flow field, although other physics mechanisms such as (semi)hard

scatterings also contribute. As shown in Figs. 18 and 19, the spectra are well described by the hydrodynamics-motivated blast-wave model [127–133]. The blast-wave model makes the simple assumption that particles are locally thermalized at a kinetic freeze-out temperature and are moving with a common collective transverse radial flow velocity field. The common flow velocity field results in a larger transverse momentum of heavier particles, leading to the change in the observed spectral shape with increasing particle mass.

Assuming a hard-sphere uniform density particle source with a kinetic freeze-out temperature T_{kin} and a transverse radial flow velocity β , the particle transverse momentum spectral shape is given by [127]

$$\frac{dN}{p_\perp dp_\perp} \propto \int_0^R r dr m_\perp I_0 \left(\frac{p_\perp \sinh \rho}{T_{\text{kin}}} \right) K_1 \left(\frac{m_\perp \cosh \rho}{T_{\text{kin}}} \right), \quad (16)$$

where $\rho = \tanh^{-1} \beta$, and I_0 and K_1 are the modified Bessel functions. We use a flow velocity profile of the form

$$\beta = \beta_S (r/R)^n, \quad (17)$$

where β_S is the surface velocity and r/R is the relative radial position in the thermal source. The choice of the value of R bears no effect in the model.

Six particle spectra (π^\pm , K^\pm , p , and \bar{p}) of a given centrality bin are fit simultaneously with the blast-wave model. The free parameters are the kinetic freeze-out temperature T_{kin} , the average transverse flow velocity $\langle \beta \rangle = \frac{2}{2+n} \beta_S$, and the exponent of the assumed flow velocity profile n . The low momentum parts of the pion spectra ($p_\perp < 0.5$ GeV/c) are excluded from the fit because of significant contributions from resonance decays.

The blast-wave fit results for Au + Au collisions are listed in Table X. The χ^2/ndf is smaller than unity because the point-to-point systematic errors, which are included in the fit and dominate over statistical ones, are estimated on the conservative side and might not be completely random. If the χ^2/ndf is scaled such that the minimum is unity, then somewhat smaller statistical errors on the fit parameters are obtained.

Figure 36 shows the extracted kinetic freeze-out temperature as a function of the event multiplicity for pp and $d + \text{Au}$ collisions at 200 GeV and for Au + Au collisions at 62.4, 130, and 200 GeV, together with the chemical freeze-out temperature. As opposed to T_{chem} , the kinetic freeze-out temperature T_{kin} shows a notable decreasing trend with centrality in Au + Au collisions. The T_{kin} values from pp and $d + \text{Au}$ collisions are similar to those in peripheral Au + Au, although the systematic uncertainties are large.

Figure 37 shows the extracted average transverse radial flow velocity $\langle \beta \rangle$ as a function of the event multiplicity. The $\langle \beta \rangle$ increases dramatically with increasing centrality in Au + Au collisions. The effect of the $\langle \beta \rangle$ increase on the transverse spectra is significantly stronger than the counter effect of the T_{kin} drop. The combination of the π , K , p , and \bar{p} spectra favors an increase of $\langle \beta \rangle$ with centrality rather than a similar increase in T_{kin} .

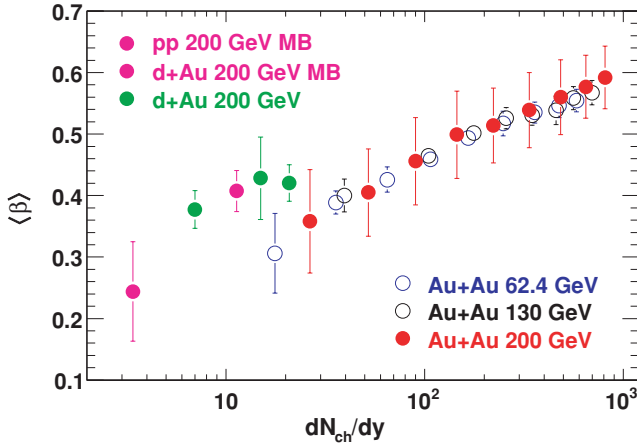


FIG. 37. (Color online) Average transverse radial flow velocity extracted from blast-wave model fit to pp and $d + \text{Au}$ at 200 GeV, and to $\text{Au} + \text{Au}$ collisions at 62.4, 130, and 200 GeV as a function of the charged-hadron multiplicity. Errors shown are the total statistical and systematic uncertainties. The 200 GeV pp and $\text{Au} + \text{Au}$ data are from Ref. [17].

To have the same base for comparison, the pp and $d + \text{Au}$ data are also fit by the blast-wave model. The fit results are listed in Table X and shown as a function of the event multiplicity in Figs. 36 and 37 together with the $\text{Au} + \text{Au}$ results. The model is found to give a fairly good description of the measured π^\pm , K^\pm , p , and \bar{p} spectra. Surprisingly, the fit average flow velocities from pp and $d + \text{Au}$ collisions are not small and certainly not zero as one would naively expect. This should not be taken as proof that there is collective flow in pp and $d + \text{Au}$ collisions, because hard scatterings and jet production, generating relatively more high p_\perp hadrons, can mimic collective flow and give rise to the extracted finite $\langle\beta\rangle$ [54]. In $d + \text{Au}$ collisions, there is an additional effect of initial state scattering, which broadens the transverse momentum of the colliding constituents and hence the produced hadrons in the final state. Meanwhile, statistical global energy and momentum conservation can deplete large momentum particles shown in recent studies [55], and the effect can be large in low multiplicity collisions. In the same framework, large initial energy fluctuation available for midrapidity particle production tends to harden the transverse spectrum [51,134]. The interplay between these effects, as well as the relevance of statistical global energy and momentum conservation in high energy collisions, needs further quantitative studies.

In $\text{Au} + \text{Au}$ collisions, the contribution from hard (and semihard) scatterings is larger than in pp collisions because hard scatterings scale with the number of binary nucleon-nucleon collisions, while soft processes scale with the number of participant nucleons. From the two-component model study in Sec. VIC, the hard-scattering contribution in pp collisions at 200 GeV is 13%, while in the top 5% central $\text{Au} + \text{Au}$ collisions it is 46%, a factor of 3.5 times that in pp . From the blast-wave model with a linear flow velocity profile, the increase in average $\langle p_\perp \rangle$ or $\langle m_\perp \rangle$ due to radial flow velocity $\langle\beta\rangle$

is approximately proportional to $\langle\beta\rangle^3$. Assuming the apparent finite flow velocity extracted from pp data, $\langle\beta\rangle_{pp} = 0.24 \pm 0.08$, is solely due to the energy excess of produced particles from hard processes over soft processes, and assuming the particle production from hard processes is identical in pp and central $\text{Au} + \text{Au}$ collisions, then the hard processes in central $\text{Au} + \text{Au}$ collisions would generate an apparent flow velocity of $3.5^{1/3} \langle\beta\rangle_{pp} = 0.36$. However, the extracted flow velocity from the blast-wave model for central $\text{Au} + \text{Au}$ collisions is significantly larger, $\langle\beta\rangle_{AA} = 0.59 \pm 0.05$. One may take the additional excess in central $\text{Au} + \text{Au}$ collisions as the effect of collective transverse radial flow and estimate the collective flow velocity in central $\text{Au} + \text{Au}$ collisions by $\langle\beta\rangle_{\text{flow}} \sim \sqrt[3]{\langle\beta\rangle_{AA}^3 - 3.5 \langle\beta\rangle_{pp}^3} = 0.54 \pm 0.08$. As discussed in Sec. VIC, the Kharzeev-Nardi two-component model likely overestimates the fraction of the hard component in pp collisions. However, using the hard-component fraction obtained from Ref. [54], with the same assumptions as stated above, the estimate of the collective flow velocity in central $\text{Au} + \text{Au}$ collisions is not significantly altered. We note, however, that the preceding estimate is simplistic. The full understanding of the effects on transverse spectra from radial flow, (semi)hard scatterings, interactions between (semi)hard scatterings and the medium [67,135,136], and the interplay between these effects will need rigorous study, which is outside the scope of this paper. It should be understood that the extracted values of the radial flow velocity in this paper are under the framework of the blast-wave model.

Despite the different physical processes, the extracted T_{kin} and $\langle\beta\rangle$ evolve smoothly from pp to central heavy-ion collisions. In pp and peripheral $\text{Au} + \text{Au}$ collisions, the kinetic freeze-out temperature is close to the chemical freeze-out temperature. As the multiplicity increases the T_{kin} decreases and the $\langle\beta\rangle$ increases. This trend continues through $d + \text{Au}$ and $\text{Au} + \text{Au}$ collisions.

The extracted kinetic freeze-out temperature and the radial flow velocity are similar for $\text{Au} + \text{Au}$ collisions at the three measured energies. As shown by Figs. 36 and 37, the magnitudes of the freeze-out parameters extracted from $\text{Au} + \text{Au}$ collisions seem to be correlated only with the charged-particle multiplicity dN_{ch}/dy . This may suggest that the expansion rates, both before and after chemical freeze-out, are determined by the total event multiplicity, or the initial energy density as expressed through the energy density estimate in Eq. (13). In other words, a higher initial energy density results in a larger expansion rate and longer expansion time, yielding a larger flow velocity and lower kinetic freeze-out temperature.

The blast-wave fit so far treated all particles as primordial, ignoring resonance decays which are contained in the measured inclusive spectra. To assess the effect of resonance decays on the extracted kinetic freeze-out parameters, we extended the blast-wave model to include resonance decays as described in detail in Appendix B. We found that the thus extracted kinetic freeze-out parameters agree with those obtained without including resonances within systematic uncertainties. This is because the resonance decay contributions are relatively p_\perp independent within the p_\perp

ranges of our measurements. In addition, our study including short-lived resonances lends support to the picture of regeneration of short-lived resonances [48,51,137,138] during a relatively long time span from chemical to kinetic freeze-out.

C. Excitation functions

The thermal model has been very successful in describing heavy-ion collisions and elementary particle collisions over a wide range of collision energies. Heavy-ion data from many energies have also been successfully fit by the blast-wave model. We compile results from some of these previous investigations [120–123,126,139–143], together with RHIC data, to study the excitation functions of the extracted chemical and kinetic freeze-out parameters. We note that the thermal model studies in Refs. [120–122] do not include γ_S as a free parameter; strangeness is treated as equilibrated with light flavors, i.e., $\gamma_S = 1$.

Figure 38 shows the baryon chemical potential extracted from chemical equilibrium model fits to central heavy-ion (Au + Au/Pb + Pb) data at various energies. The extracted μ_B falls monotonically from low to high energies. There are fewer net-baryons at midrapidity at higher energy, because fewer baryons can transport over the larger rapidity gap.

Figure 39 shows the evolution of the extracted chemical (open symbols) and kinetic (filled symbols) freeze-out temperatures as a function of the collision energy in central heavy-ion collisions. The extracted T_{chem} rapidly rises at the GSI heavy-ion synchrotron (SIS) and AGS energy range and saturates at SPS and RHIC energies. In other words, central heavy-ion collisions at high energies can be characterized by a unique, energy-independent chemical freeze-out temperature. The value of T_{chem} is close to the phase-transition temperature predicted by lattice QCD. This suggests the collision system at high energies decouples chemically at the phase boundary.

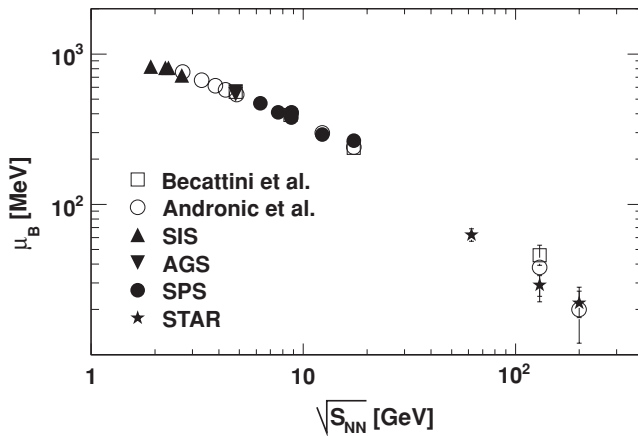


FIG. 38. Baryon chemical potential extracted for central heavy-ion collisions as a function of the collision energy. STAR 62.4 and 130 GeV data are from this work; the 200 GeV data are from Ref. [17]. Other data are from SIS [140,141], AGS [120,122,126,142], SPS [121,122,126,139,142], and compilation by Refs. [143,144]. Errors shown are the total statistical and systematic errors.

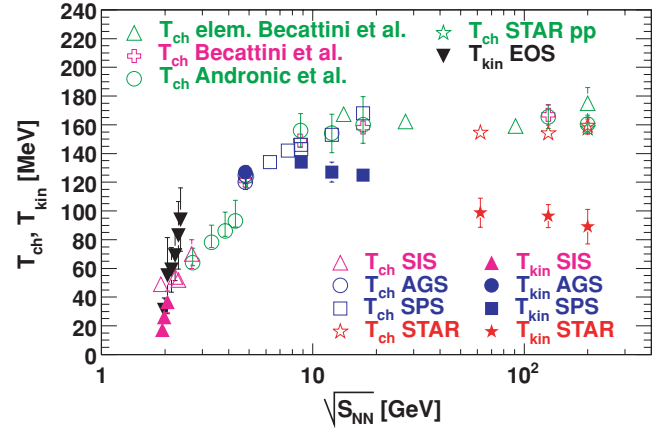


FIG. 39. (Color online) Extracted chemical (open symbols) and kinetic (filled symbols) freeze-out temperatures for central heavy-ion collisions as a function of the collision energy. The STAR 62.4 and 130 GeV data are from this work; the STAR 200 GeV data are from Ref. [17]. The other kinetic freeze-out results are from FOPI [145], EOS [146], E866 [147], and NA49 [148] experiments. The other chemical freeze-out data are from SIS [140,141], AGS [120,122,126,142], and SPS [121,122,126,139,142] and compilation by Refs. [143,144]. Errors shown are the total statistical and systematic errors.

On the other hand, the extracted kinetic freeze-out temperature rises at SIS and AGS energies and decreases at higher energies, especially at RHIC energies. At low energies, the extracted T_{kin} is similar to T_{chem} . This suggests that kinetic freeze-out happens relatively quickly after or concurrently with chemical freeze-out. The two measured temperatures begin to separate at a collision energy around $\sqrt{s_{NN}} = 10$ GeV, above which T_{kin} decreases with increasing energy, while T_{chem} remains relatively constant. This suggests a prolonging of the period between chemical and kinetic freeze-outs, during which the particles scatter elastically, building up additional collective motion in the system while it undergoes further expansion and cooling.

Figure 40 shows the evolution of the extracted average flow velocity as a function of the collision energy. The extracted $\langle \beta \rangle$ steeply increases from SIS to AGS energies, and continues to increase at a lower rate at higher energies. Collective flow is an integral of all collective flow contributions over the entire evolution of the collision system. Part of it comes from the early stage of the collisions before chemical freeze-out, built up by the high pressure in the core of the collision zone. After chemical freeze-out, particles continue to interact elastically in central collisions, building up further transverse radial flow. This late-stage transverse expansion cools down the system and results in a lower kinetic freeze-out temperature in central collisions as discussed above. One should note that the extracted average flow velocity can be generated by different underlying physics at very low (SIS, AGS) and high (SPS, RHIC) incident energies.

It is valuable to study collective radial flow at chemical freeze-out, as it comes from the early stage of the collision and hence is more sensitive to the initial condition than the final

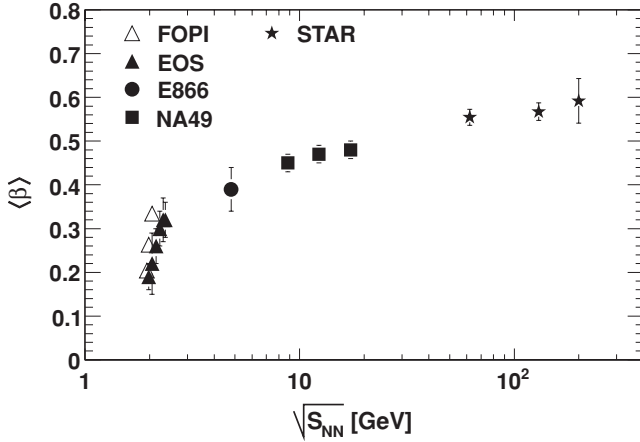


FIG. 40. Average transverse radial flow velocity extracted from the blast-wave model for central heavy-ion collisions as a function of the collision energy. The STAR 62.4 and 130 GeV data are from this work, and the STAR 200 GeV pp and Au + Au data from Ref. [17]. The other data are from FOPI [145], EOS [146], E866 [147], and NA49 [148] experiments. Errors shown are the total statistical and systematic errors.

measured radial flow. The radial flow at chemical freeze-out may be assessed by analyzing p_{\perp} spectra of particles with small hadronic interaction cross sections; some rare particles such as ϕ , Ξ , and Ω must develop most of their flow early (perhaps prehadronization), because their interaction cross sections are much lower than for the common π , K , p , and \bar{p} . It is found that the extracted radial flow for these rare particles is substantial in central heavy-ion collisions at RHIC, perhaps suggesting strong partonic flow in these collisions [50,149].

Figure 41 shows the chemical freeze-out temperature vs baryon chemical potential extracted from chemical equilibrium model fits to central Au + Au data. Low energy data points (SIS, AGS, SPS) are from the chemical equilibrium model fits [122,139–141,143,144] and references

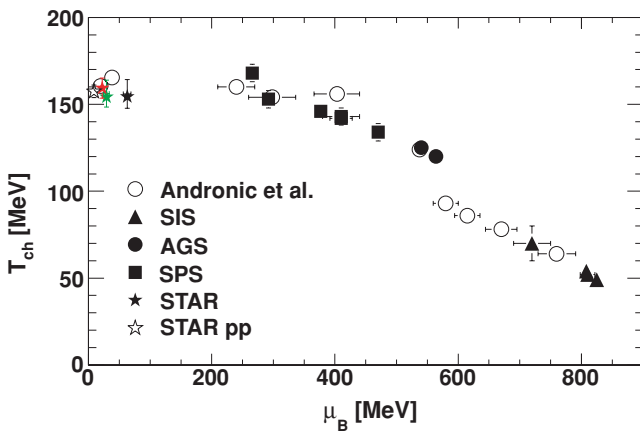


FIG. 41. (Color online) Phase diagram plot of chemical freeze-out temperature vs baryon chemical potential extracted from chemical equilibrium models. Low energy data are from Refs. [120–122,126,139–142] and compilations in Refs. [143,144]. Errors shown are the total statistical and systematic errors.

therein. At RHIC energies, the chemical freeze-out points appear to be in the vicinity of the hadron-QGP phase transition (hadronization) predicted by lattice gauge theory [150,151].

VIII. SUMMARY

Charged particles of π^{\pm} , K^{\pm} , p , and \bar{p} are identified by the specific ionization energy loss (dE/dx) method in STAR at low transverse momenta and midrapidity ($|y| < 0.1$) in pp and $d + Au$ collisions at $\sqrt{s_{NN}} = 200$ GeV and in Au + Au collisions at 62.4, 130, and 200 GeV. Transverse momentum spectra of the identified particles are reported. Spectra of heavy particles are flatter than those of light particles in all collision systems. This effect becomes more prominent in more central Au + Au collisions. In pp and $d + Au$ collisions, processes such as semihard scattering and k_{\perp} broadening should play an important role. In central Au + Au collisions, the flattening of the spectra is likely dominated by collective transverse radial flow, developed because of the large pressure buildup in the early stage of heavy-ion collisions.

The transverse momentum spectra are extrapolated to the unmeasured regions by the hydrodynamics-motivated blast-wave model parametrization for kaons, protons, and antiprotons and by the Bose-Einstein function for pions. The total integrated particle yields are reported. The Bjorken energy density estimated from the total transverse energy is at least several GeV/fm³ at a formation time of less than 1 fm/c. The extrapolated $\langle p_{\perp} \rangle$ increases with particle mass in each collision system and increases with centrality for each particle species. The $\langle p_{\perp} \rangle$ systematics are similar for the three measured energies at RHIC and appear to be strongly correlated with the total particle multiplicity density or the ratio of the multiplicity density over the transverse overlap area of the colliding nuclei.

Ratios of the integrated particle yields are presented and discussed. While rather independent of centrality for 130 and 200 GeV, the \bar{p}/p ratio drops significantly with centrality in 62.4 GeV Au + Au collisions. This indicates a more significant net-baryon content at midrapidity in Au + Au collisions at 62.4 GeV. On the other hand, antibaryon production relative to the total particle multiplicity, while lower at the lower energy, is independent of centrality for all three collision energies at RHIC, despite the increasing net-baryon density at the low 62.4 GeV energy.

Strangeness production relative to the total particle multiplicity is similar at the different RHIC energies. The effect of collision energy on the production rate is significantly smaller on strangeness production than on antibaryon production. Relative strangeness production increases quickly with centrality in peripheral Au + Au collisions and remains the same above medium-central collisions at RHIC. The increase in relative strangeness production in central Au + Au collisions from pp is approximately 50%.

The particle yield ratios are fit in the framework of the thermal equilibrium model. The extracted chemical freeze-out temperature is the same in pp , $d + Au$, and Au + Au collisions at all measured energies at RHIC and shows little

centrality dependence in Au + Au collisions. The extracted value of chemical freeze-out temperature is close to the lattice QCD predicted phase-transition temperature between hadronic matter and the quark-gluon plasma, suggesting that chemical freeze-out happens in the vicinity of the phase boundary shortly after hadronization. The extracted strangeness suppression factor is substantially below unity in pp , $d + \text{Au}$, and peripheral Au + Au collisions; strangeness production is significantly suppressed in these collisions. The strangeness suppression factor in medium-central to central Au + Au collisions is not much below unity; the strangeness and light flavor are nearly equilibrated, which may suggest a fundamental change from peripheral to central collisions.

The extracted kinetic freeze-out temperature from the blast-wave fit to the transverse momentum spectra, on the other hand, decreases from pp and $d + \text{Au}$ to central Au + Au collisions. At the same time, the extracted collective flow velocity increases significantly with increasing centrality. While the apparent finite flow velocity fit in pp and $d + \text{Au}$ collisions may be due to semihard scatterings and jets, the extracted large flow velocity in central Au + Au collisions is likely dominated by collective transverse radial flow. The significant difference between the extracted chemical and kinetic freeze-out temperatures suggests the presence of an elastic rescattering phase between the two freeze-outs. The variations of the extracted freeze-out properties are smooth from pp and $d + \text{Au}$ to Au + Au collisions and over the measured energies for the Au + Au collision system; the trends seem to be tied to the event multiplicity. Resonance decays are found to have little effect on the extracted kinetic freeze-out parameters because the resonance decay products have similar kinematics as the primordial particles in our measured transverse momentum ranges. The study including different contributions from short-lived resonances lends support to the regeneration picture of those resonances with a long time span from chemical to kinetic freeze-out.

The identified particle spectra at RHIC energies and the equilibrium model studies presented here suggest that the collision systems chemically decouple at a universal temperature, independent of the vastly different initial conditions at different centralities. The apparent different collective flow strengths in the final state of nonperipheral heavy-ion collisions likely are dominated by transverse radial flow and stem out of the different amount of pressure build-up at the initial stage. Part of the collective flow in central collisions appears to be built up after chemical freeze-out, during which the collision zone undergoes further expansion and cooling through particle elastic scatterings, resulting in a lower kinetic decoupling temperature in more central collisions.

ACKNOWLEDGMENTS

We thank the RHIC Operations Group and RCF at BNL, the NERSC Center at LBNL, and the resources provided by the Open Science Grid consortium for their support. This work was supported in part by the Offices of NP and HEP within the US

DOE Office of Science, the US NSF, the Sloan Foundation, the DFG Excellence Cluster EXC153 of Germany, CNRS/IN2P3, RA, RPL, and EMN of France, STFC and EPSRC of the United Kingdom, FAPESP of Brazil, the Russian Ministry of Sci. and Tech., the NNSFC, CAS, MoST, and MoE of China, IRP and GA of the Czech Republic, FOM of the Netherlands, DAE, DST, and CSIR of the Government of India, Swiss NSF, the Polish State Committee for Scientific Research, and the Korea Sci. & Eng. Foundation.

APPENDIX A: GLAUBER MODEL

To describe heavy-ion collisions, geometric quantities are often used, such as the number of participant nucleons N_{part} , the number of nucleon-nucleon binary collisions N_{coll} , and the transverse overlap area of the colliding nuclei S_{\perp} . Unfortunately these quantities cannot be measured directly from experiments.⁴ Their values can only be derived by mapping the measured data, such as the dN/dN_{ch} distribution, to the corresponding distribution obtained from phenomenological calculations, thus relating N_{part} , N_{coll} , and S_{\perp} to the measured dN/dN_{ch} distribution. These types of calculations are generally called Glauber model calculations and come in two implementation schemes: the *optical* and the *Monte Carlo* Glauber calculations.

The optical model is based on an analytic consideration of continuously overlapping nuclei [29,152–154]. The MC approach is based on a computer simulation of billiard-ball-like colliding nucleons [68,155–159]. Figure 42 shows the differential cross sections vs b of minimum-bias Au + Au collisions at 200 GeV calculated by the optical and MC Glauber models. As seen from the figure, the differential cross sections agree between the two calculations except at large impact parameters or in very peripheral collisions. The disagreement in very peripheral collisions is understood because the optical

⁴An exception is that in fixed target experiments, the number of participants can be experimentally measured by zero degree calorimeters.

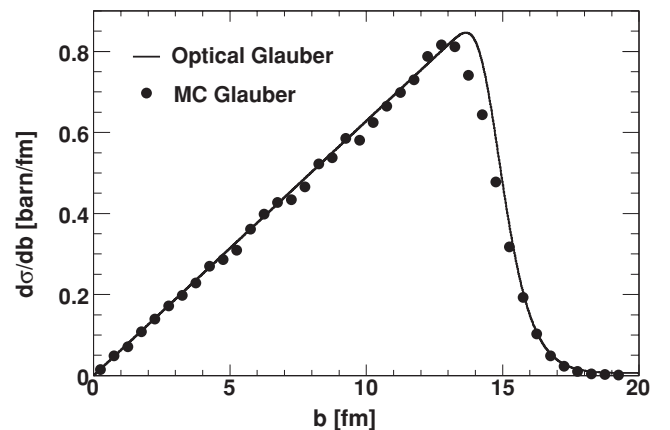


FIG. 42. Differential cross sections obtained from the optical and MC Glauber calculations for Au + Au collisions at 200 GeV. Statistical errors are smaller than the point size.

TABLE XI. Optical Glauber model results corresponding to the centrality bins used in the 62.4, 130, and 200 GeV Au + Au data. The quoted errors are systematic uncertainties.

Centrality	b range (fm)	b (fm)	N_{part}	N_{coll}
Au + Au 200 GeV ($\sigma_{pp} = 41$ mb)				
90–100%	14.3–15.7	$14.8^{+1.1}_{-0.5}$	$1.43^{+0.73}_{-0.64}$	$1.02^{+0.57}_{-0.47}$
80–90%	13.4–14.3	13.8 ± 0.4	$4.5^{+1.3}_{-1.1}$	$3.7^{+1.2}_{-1.0}$
70–80%	12.5–13.4	13.0 ± 0.3	$10.7^{+2.2}_{-2.0}$	$10.0^{+2.7}_{-2.3}$
60–70%	11.6–12.5	12.1 ± 0.3	$22.0^{+3.3}_{-3.1}$	$25.1^{+5.3}_{-4.8}$
50–60%	10.6–11.6	11.1 ± 0.3	40.6 ± 4.3	$56.2^{+9.1}_{-8.6}$
40–50%	9.48–10.6	10.0 ± 0.3	67.8 ± 5.0	113 ± 14
30–40%	8.21–9.48	8.86 ± 0.23	105.4 ± 5.3	206 ± 19
20–30%	6.70–8.21	7.48 ± 0.19	155.9 ± 5.1	351 ± 26
10–20%	4.74–6.70	5.78 ± 0.15	223.6 ± 4.2	571 ± 36
5–10%	3.35–4.74	4.08 ± 0.11	$289.6^{+2.9}_{-3.1}$	807 ± 48
0–5%	0–3.35	2.23 ± 0.06	$345.8^{+1.8}_{-2.0}$	1027 ± 61
Au + Au 130 GeV ($\sigma_{pp} = 39$ mb)				
85–100%	13.6–15.2	$14.3^{+1.0}_{-0.5}$	$2.7^{+1.7}_{-1.3}$	$2.0^{+1.4}_{-1.0}$
58–85%	11.3–13.6	12.5 ± 0.4	$17.0^{+4.6}_{-3.9}$	$18.6^{+6.6}_{-5.2}$
45–58%	9.92–11.3	10.6 ± 0.4	$51.8^{+7.6}_{-7.0}$	76^{+16}_{-14}
34–45%	8.62–9.92	9.29 ± 0.31	$89.7^{+8.4}_{-8.0}$	161 ± 23
26–34%	7.54–8.62	8.10 ± 0.27	$131.0^{+8.3}_{-8.1}$	268 ± 28
18–26%	6.28–7.54	6.93 ± 0.23	175.7 ± 7.6	398 ± 33
11–18%	4.91–6.28	5.62 ± 0.19	228.2 ± 6.3	564 ± 39
6–11%	3.62–4.91	4.30 ± 0.14	280.0 ± 4.7	740 ± 47
0–6%	0–3.62	2.42 ± 0.08	339.3 ± 2.6	958 ± 59
Au + Au 62.4 GeV ($\sigma_{pp} = 36$ mb)				
90–100%	14.2–15.6	$14.7^{+1.0}_{-0.5}$	$1.47^{+0.73}_{-0.64}$	$1.02^{+0.56}_{-0.46}$
80–90%	13.3–14.2	$13.7^{+0.4}_{-0.3}$	$4.6^{+1.2}_{-1.1}$	$3.6^{+1.2}_{-1.0}$
70–80%	12.5–13.3	12.9 ± 0.3	$10.6^{+2.2}_{-1.9}$	$9.7^{+2.5}_{-2.2}$
60–70%	11.5–12.5	12.0 ± 0.3	$21.8^{+3.3}_{-3.1}$	$23.6^{+4.9}_{-4.4}$
50–60%	10.5–11.5	11.0 ± 0.3	$40.0^{+4.3}_{-4.1}$	$52.0^{+8.2}_{-7.7}$
40–50%	9.42–10.5	9.98 ± 0.26	66.8 ± 4.9	103 ± 12
30–40%	8.15–9.42	8.80 ± 0.22	103.8 ± 5.2	186 ± 17
20–30%	6.66–8.15	7.43 ± 0.19	153.5 ± 5.0	314 ± 24
10–20%	4.71–6.66	5.74 ± 0.15	$220.4^{+4.1}_{-4.3}$	506 ± 34
5–10%	3.33–4.71	4.06 ± 0.10	$285.9^{+3.1}_{-3.3}$	712 ± 46
0–5%	0–3.33	2.22 ± 0.06	342.2 ± 2.3	903 ± 59

approach loses its validity in these collisions. Because of this disagreement, the integrated total cross sections differ between the optical and MC calculations by about 5%.

To relate Glauber calculations to experimental measurements, one first obtains the impact parameter range corresponding to the measured centrality bin using the differential cross section, such as the ones shown in Fig. 42. The average N_{part} and N_{coll} values are then calculated in the Glauber model for the impact parameter range. Table XI lists the N_{part} and N_{coll} values obtained from the optical Glauber calculations for our multiplicity classes in 62.4, 130, and 200 GeV Au + Au collisions. The MC Glauber results are already listed in Table II in the main text. As seen from the tables, different implementations of the Glauber model lead to slightly different values for N_{part} and N_{coll} , as has been noted

before in Ref. [158]. The results are different for nonperipheral collisions, even though the differential cross sections match between the two Glauber calculations. This is because the impact parameter ranges corresponding to the same measured centrality bin differ slightly due to the different total cross sections. The disagreement in the Glauber results is more significant in peripheral collisions for the reasons noted above. Thus, any results reported in terms of Glauber quantities must be carefully interpreted based upon specifics of the underlying calculations.

In the following, we will briefly describe the optical and MC Glauber calculations.

A. Optical Glauber model

For our optical Glauber calculation, we start by assuming a spherically symmetric Woods-Saxon density profile,

$$\rho(r) = \frac{\rho_0}{1 + \exp(\frac{r-r_0}{a})}, \quad (\text{A1})$$

with the parameter $a = 0.535 \pm 0.027$ fm as experimentally measured in e -Au scattering and reported in Refs. [160,161]. From the same publication, we extracted the value for r_0 , but increased it from 6.38 fm to 6.5 ± 0.1 fm to approximate the effect of the neutron skin. The normalization factor $\rho_0 = 0.161$ fm $^{-3}$ is fixed by $\int_0^\infty \rho(r) 4\pi r^2 dr = 197$, the total number of nucleons in the Au nucleus.

We concentrate on symmetric Au + Au collisions. Let the beam axis be along \hat{z} . The nuclear thickness density function is given by

$$T_A(\vec{s}) = T_A(s) = \int_{-\infty}^{\infty} \rho(\vec{s}, z) dz, \quad (\text{A2})$$

where \vec{s} is a vector perpendicular to the beam axis \hat{z} , and $s = |\vec{s}|$; $\rho(\vec{s}, z)$ is the nuclear density in the volume element $ds^2 dz$ at (\vec{s}, z) ; and for our spherical nucleus, $\rho(\vec{s}, z) = \rho(s, z) = \rho(\sqrt{s^2 + z^2})$ as given by Eq. (A1).

For a Au + Au collision with impact parameter \vec{b} , the nuclear overlap integral can be calculated as the integral over two density profiles,

$$T_{AA}(b) = \int T_A(\vec{s}) T_A(\vec{s} - \vec{b}) ds^2. \quad (\text{A3})$$

The number of binary nucleon-nucleon collisions is given by

$$N_{\text{coll}}(b) = \sigma_{pp} T_{AA}(b). \quad (\text{A4})$$

Here we assume that the interaction probability is solely given by the proton-proton cross section σ_{pp} , thus neglecting effects like excitation and energy loss. The number of participant nucleons (nucleons suffering at least one collision) is derived from T_A by

$$N_{\text{part}}(b) = 2 \int T_A(\vec{s}) (1 - e^{-\sigma_{pp} T_A(\vec{s} - \vec{b})}) ds^2. \quad (\text{A5})$$

By definition, there is no fluctuation in the optical Glauber model. For a given b , quantities like T_A , T_{AA} , N_{coll} , and

N_{part} are analytically defined. To calculate the cross section, however, one has to invoke the concept of fluctuation. In this sense, Eq. (A4) gives the average number of binary collisions for Au + Au collisions at impact parameter b , and taking Poisson statistics, the probability for no interaction is $e^{-N_{\text{coll}}(b)}$. The differential cross section is thus given by

$$\frac{d\sigma_{AA}}{db} = 2\pi b(1 - e^{-\sigma_{pp}T_{AA}(b)}). \quad (\text{A6})$$

The total hadronic cross section for Au + Au collisions can hence be obtained as

$$\sigma_{AA} = \int_0^\infty db \frac{d\sigma_{AA}}{db}. \quad (\text{A7})$$

The values of σ_{pp} are taken to be $\sigma_{pp} = 36 \pm 2, 39 \pm 2$, and 41 ± 2 mb for 62.4, 130, and 200 GeV, respectively. With these pp cross sections, the corresponding total cross sections for Au + Au are calculated to be approximately $\sigma_{AA} = 7.18, 7.24$, and 7.27 b, respectively.

To relate N_{part} and N_{coll} to the experimental observable N_{ch} , the mean of the total number of charged tracks in our centrality bin, we use Eqs. (A6) and (A7) to obtain the impact parameters corresponding to the fraction of the total geometric cross section for our centrality bin. For a given impact parameter range $b_1 < b < b_2$ for each centrality bin, we then use Eqs. (A6), (A4), and (A5) to calculate the N_{coll} and N_{part} by

$$N_{\text{coll}} = \frac{\int_{b_1}^{b_2} N_{\text{coll}}(b) \frac{d\sigma_{AA}}{db} db}{\int_{b_1}^{b_2} \frac{d\sigma_{AA}}{db} db}, \quad (\text{A8})$$

$$N_{\text{part}} = \frac{\int_{b_1}^{b_2} N_{\text{part}}(b) \frac{d\sigma_{AA}}{db} db}{\int_{b_1}^{b_2} \frac{d\sigma_{AA}}{db} db}. \quad (\text{A9})$$

B. Monte Carlo Glauber model

The MC method simulates a number of independent Au + Au collisions. For each collision, a target and a projectile nucleus are modeled according to the Woods-Saxon nucleon density profile of Eq. (A1). The nucleons are separated by a minimum distance $d_{\text{min}} = 0.4$ fm, which is characteristic of the range of the repulsive nucleon-nucleon force. The target and projectile nuclei are separated by the impact parameter b , with b^2 chosen randomly from a flat distribution. The nucleons follow straight-line trajectories in collisions. A pair of nucleons along the path is determined to “interact” if the nucleons are separated by a transverse distance

$$d \leq \sqrt{\frac{\sigma_{pp}}{\pi}}, \quad (\text{A10})$$

where σ_{pp} is the nucleon-nucleon interaction cross section. The colliding nuclei are considered to have interacted (resulting in an Au + Au event) if at least one pair of nucleons has interacted. Again, the values of σ_{pp} are taken to be $\sigma_{pp} = 36 \pm 2, 39 \pm 2$, and 41 ± 2 mb for 62.4, 130, and 200 GeV, respectively. With these pp cross sections, the corresponding total cross sections for Au + Au are calculated to be approximately $\sigma_{AA} = 6.84, 6.89$, and 6.93 b, respectively.

The normalized differential cross section, $\frac{1}{\sigma_{AA}} \frac{d\sigma_{AA}}{db}$, is obtained from the normalized event distribution. The $\frac{1}{\sigma_{AA}} \frac{d\sigma_{AA}}{db}$ distribution is divided into bins corresponding to the fractions of the measured total cross section of the used centrality bins. The number of participants N_{part} is defined as the total number of nucleons that undergo at least one interaction. The number of binary collisions N_{coll} is defined as the total number of nucleon-nucleon interactions in the collision. The mean values of N_{part} and N_{coll} are determined for each centrality bin in the same way as for the optical Glauber model, by Eqs. (A8) and (A9).

The transverse overlap area S_\perp for pp collisions is taken to be the pp cross section σ_{pp} . To calculate the transverse overlap area between the colliding nuclei of Au + Au collisions, the individual pp interaction cross sections are projected onto the transverse plane. The overlap area in the transverse plane, S_\perp , is then calculated. The overlapping portion of the projected areas from two or more nucleon-nucleon interactions is counted only once. The mean S_\perp , weighted by the differential cross section, is determined in the same manner as in Eqs. (A8) and (A9). Table II lists the obtained S_\perp along with N_{part} and N_{coll} .

C. Uncertainties

The uncertainties on N_{part} , N_{coll} , and S_\perp from both the optical and MC Glauber model calculations are evaluated by varying the Woods-Saxon parameters, the values of σ_{pp} and d_{min} , and by including an uncertainty in the determination of the measured total Au + Au cross section.

- (i) The Woods-Saxon nuclear density profile parameters a and r_0 are varied within their respective uncertainties: $a = 0.535 \pm 0.027$ fm and $r = 6.50 \pm 0.12$ fm.
- (ii) The σ_{pp} values are 36 mb (62.4 GeV), 39 mb (130 GeV), and 41 mb (200 GeV) as default and are varied within an uncertainty of ± 2 mb.
- (iii) The d_{min} value is 0.4 fm as default and is varied between 0.2 and 0.5 fm. This only applies to the MC Glauber calculation.
- (iv) Because of inefficiencies in the online trigger and offline primary vertex reconstruction for peripheral collisions, our measured total (minimum-bias) cross section does not fully account for the total Au + Au hadronic cross section. The measured fractions of the total cross section are determined to be $97 \pm 3\%$ [47,162], $95 \pm 5\%$ [23, 25], and $97 \pm 3\%$ [13,163] for minimum-bias Au + Au collisions at 62.4, 130, and 200 GeV, respectively. These fractions are used in the determination of our Glauber model results, and their uncertainties are included in the quoted uncertainties on the results.

The uncertainties from these sources are determined separately and summed in quadrature in the quoted uncertainties on the Glauber results in Tables II and XI. In peripheral collisions, the uncertainties are dominated by those in the minimum-bias cross-section measurements. In central collisions, the uncertainty in N_{coll} is dominated by the uncertainty in σ_{pp} , while all sources contribute significantly to the uncertainties

in N_{part} and S_{\perp} . The uncertainties on N_{part} , N_{coll} , and S_{\perp} are correlated.

APPENDIX B: RESONANCE EFFECT ON BLAST-WAVE FIT

The blast-wave fit in Sec. VII B treats all particles as primordial, ignoring resonance decays. However, the measured identified inclusive particle spectra contain contributions from resonance decays. The question arises as to whether resonance decays have a significant effect on the extracted kinetic freeze-out parameters. To answer this question, the blast-wave model fit is extended to include resonance decays. The identified particle p_{\perp} spectra measured at midrapidity in minimum-bias pp and in the most central 5% Au + Au collisions at 200 GeV [17] are utilized to study the effect of resonance decays on the extracted kinetic freeze-out parameters [5].

A. Effect of resonance decays

The study is based on the combination of the chemical equilibrium model [120–123] and the blast-wave model by Wiedemann and Heinz [164]. Several changes have been implemented with respect to the original code [164] to provide the same basis for the calculation as in data [17]. The Wiedemann-Heinz blast-wave model uses the same temperature to determine the relative abundances of particles and resonances and to calculate their kinetic distributions. In this study, two distinct freeze-out temperatures are implemented: the chemical freeze-out temperature and the kinetic freeze-out temperature. The relative abundances of particles and resonances are determined by chemical freeze-out parameters and are fixed in our study. We used the following chemical freeze-out parameters: $T_{\text{chem}} = 159$ MeV, $\mu_B = 18$ MeV, $\mu_S = 2.3$ MeV, and $\gamma = 0.62$ for pp collisions at 200 GeV [17,52]; and $T_{\text{chem}} = 160$ MeV, $\mu_B = 24$ MeV, $\mu_S = 1.4$ MeV, and $\gamma = 0.99$ for the top 5% central Au + Au collisions at 200 GeV [17,165]. More particles are included than in Ref. [164]: ρ , ω , η , η' , K^{*0} , $K^{*\pm}$, and ϕ , and Λ , Δ , Σ , Ξ , Λ_{1520} , Σ_{1385} , and Ω . A box flow profile is chosen, similarly to Ref. [17]: $\beta = \beta_S(r/R)^n$, where n is fixed to be 0.82 for Au + Au collisions and set free for pp collisions. A flat rapidity distribution is implemented at midrapidity. This is needed because, although the measured spectra are in $|y| < 0.1$, resonances outside this region can decay into

particles falling within the region. The resonance kinematics are calculated at a given kinetic freeze-out temperature and average flow velocity. The spectra of the decay products are combined with those of the primordial ones. Spin, isospin degeneracies and decay branching ratios are properly taken into account.

The calculated particle spectra are fit to the measured identified particle spectra [17], and the kinetic freeze-out temperature and the transverse flow velocity are extracted for both pp and the 5% central Au + Au collisions. The extracted parameters are summarized in Table XII (the row labeled “100% ρ ”). Figures 43 and 44 show the calculated, best-fit particle spectra of π^- , K^- , and \bar{p} for pp and central Au + Au collisions, respectively. Calculated inclusive pion spectra do not contain weak decay pions, just as in Ref. [17]. Resonance contributions are labeled by the initial resonance particle (e.g., a \bar{p} emerging from the $\bar{\Xi} \rightarrow \bar{\Lambda} \rightarrow \bar{p}$ decays is labeled “ Ξ decay”). Only major resonance decay contributions are shown, but all contributions including minor ones are included in the calculated inclusive spectra. Those minor contributions include η , η' , ϕ , Δ , Σ , Σ_{1385} , and Λ_{1520} decays to pions, Ω and Λ_{1520} decays to kaons, and Ω and Λ_{1520} decays to (anti)protons.

The lower panels of Figs. 43 and 44 show the resonance contributions to the inclusive spectra relative to the primordial ones for pp and central Au + Au collisions, respectively. The inclusive kaon and antiproton spectra do not show significant changes in the spectral shapes compared to the primordial ones for both pp and central Au + Au collisions in the measured p_{\perp} ranges. The shape of the inclusive π spectrum in pp is also similar to the primordial one but is more significantly modified in central Au + Au collisions because of light meson contributions (ρ , ω and η) at both small and large p_{\perp} . The largest contribution is from the ρ meson. The shapes of the modifications are different for pp and central Au + Au because of the significant flattening of the spectra in Au + Au but not in pp . The η and ω mesons are less significant in pp than those in central Au + Au. However, in our measured p_{\perp} range of 0.2–0.7 GeV/c, any modification in the shape of the pion spectrum is still not large, as seen from Fig. 44.

For comparison, the default blast-wave fit with no resonances is also shown in Figs. 43 and 44. These fits are the spectra for the thermal particles with the corresponding fit parameters. As can be seen from Tables X and XII and the figure, blast-wave fits with and without the resonances give similar quality fits to the data. The extracted kinetic

TABLE XII. Extracted kinetic freeze-out parameters and the fit χ^2/ndf from the blast-wave model including resonances for minimum-bias pp and top 5% central Au + Au collisions at 200 GeV. Three cases of treating ρ decays are studied. The flow profile n parameter is fixed to 0.82 for the Au + Au fit and is free for the pp fit. All errors are statistical.

Case	pp Minimum bias				Au + Au top 5%			
	T_{kin} (MeV)	$\langle\beta\rangle$	n	χ^2/ndf	T_{kin} (MeV)	$\langle\beta\rangle$	n	χ^2/ndf
100% ρ	117.8 ± 3.2	0.29 ± 0.01	3.1 ± 0.6	1.1	$77.2^{+0.8}_{-0.9}$	$0.604^{+0.004}_{-0.003}$	0.82 fixed	0.60
0% ρ	121.9 ± 0.9	0.35 ± 0.01	1.2 ± 0.1	4.4	$94.6^{+0.9}_{-1.0}$	$0.603^{+0.004}_{-0.002}$	0.82 fixed	0.37
50% ρ	122.2 ± 1.2	0.35 ± 0.01	1.0 ± 0.3	2.5	$87.4^{+0.9}_{-1.1}$	$0.605^{+0.002}_{-0.002}$	0.82 fixed	0.45

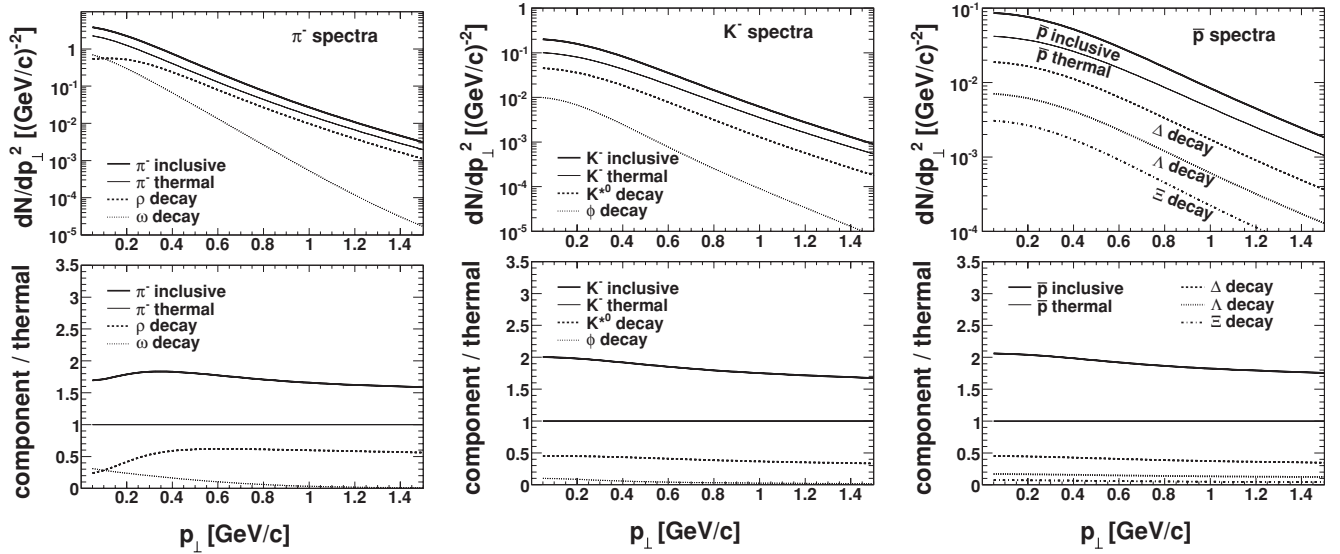


FIG. 43. Upper panels: Calculated π^- , K^- , and \bar{p} transverse momentum spectra from the primordial thermal component and major resonance decay contributions for pp collisions at 200 GeV. The kinetic freeze-out parameters fit to data are used for the thermal calculations [17]. Lower panels: Resonance contributions relative to the thermal spectrum. K^{*-} decay (not shown) has the same contribution to K^- (and K^+) spectra as K^{*0} decay. Σ and Σ_{1385} decays (not shown) contribute to the \bar{p} (and proton) spectra with similar magnitude as Λ decays.

freeze-out temperature and average flow velocity agree within the systematic uncertainties [17]. In other words, resonance decays appear to have no significant effect on the extracted kinetic freeze-out parameters. This is primarily due to the limited p_\perp ranges of the measured data where resonance decay products have more or less the same spectral shapes as the primordial particles have.

It was claimed in Refs. [166–168] that a single freeze-out temperature for chemical and kinetic freeze-out can satisfactorily describe the data. To test this, the spectra are also fit with a single, fixed kinetic freeze-out temperature $T_{\text{kin}} = T_{\text{chem}} = 160$ MeV including resonances. The fit $\langle\beta\rangle$

is $0.520^{+0.001}_{-0.002}$ with $\chi^2/\text{ndf} = 19.6$; the quality of our fit is similar to those in Refs. [166–168]. Based on this fit quality, a single temperature scenario is ruled out by the data, and we are not able to confirm the conclusion in Refs. [166–168].

B. Regeneration of short-lived resonances

The blast-wave model assumes that all particles and resonances decouple at the same T_{kin} and β . Short-lived resonances (e.g., ρ and Δ), as a result of their short lifetimes relative to the system evolution time, decay and are regenerated

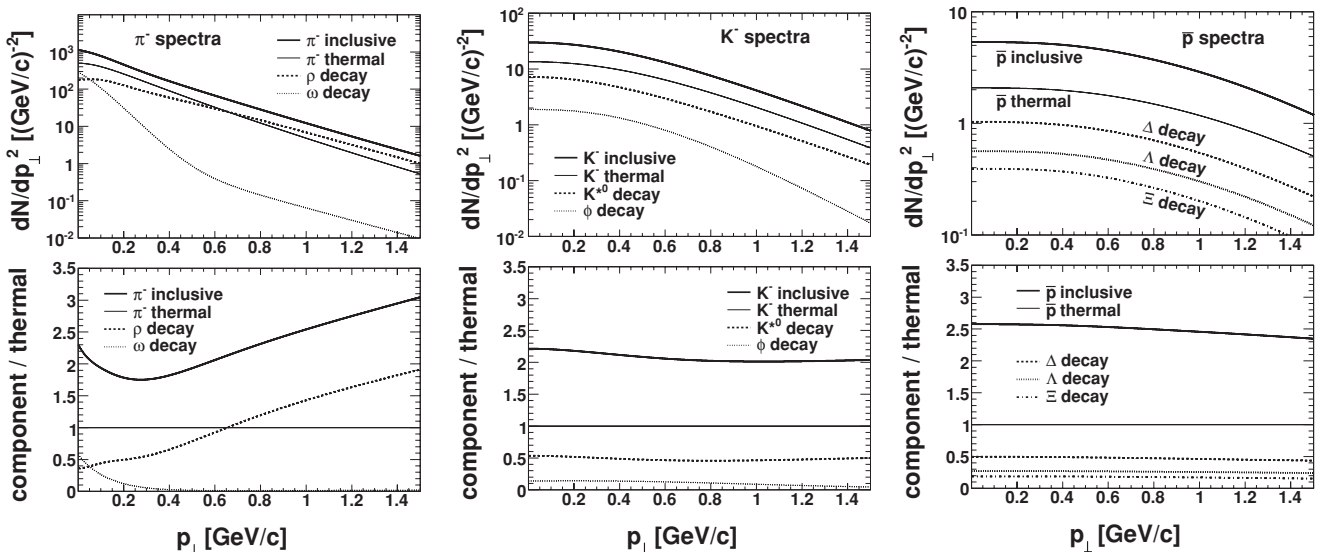


FIG. 44. Same as Fig. 43, but for the top 5% central Au + Au collisions at 200 GeV [17].

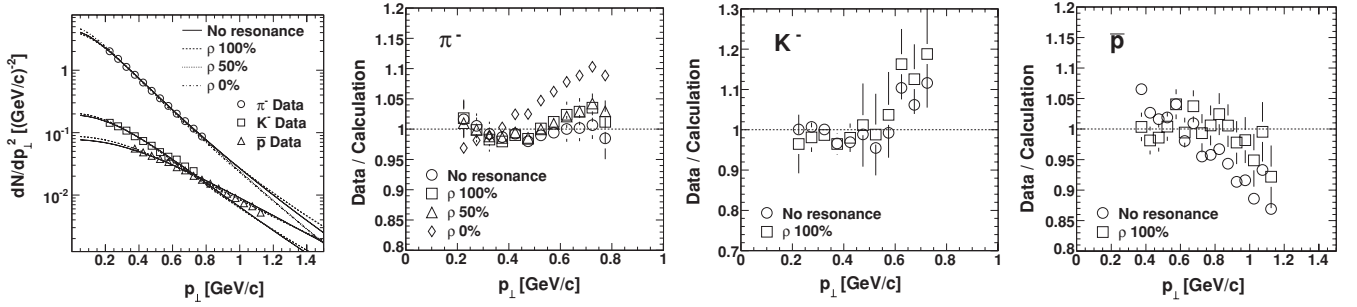


FIG. 45. Left-most panel: Fit of the calculated spectra (curves) to the measured ones (data points) in pp collisions at 200 GeV [17]. Four calculated spectra are shown for π^- (upper curves): three include resonances with different ρ contributions and one excludes resonances. Only two calculated curves are shown for K^- (middle curves) and \bar{p} (lower curves): one includes resonances with 100% ρ and the other excludes resonances. Other panels: Ratios of data spectrum to calculations. Two calculations are shown for K^- and \bar{p} , while four calculations are shown for π^- . Error bars are the quadratic sum of the statistical and point-to-point systematic errors on the data, and are shown for two sets of the data points for π^- and only one set for K^- and \bar{p} .

continuously, hence they might have different flow velocities and temperatures than long-lived resonances (and the bulk itself). Thus, it is reasonable to expect that short-lived resonances do not gain significantly larger flow velocity than the net flow of their decay daughters, as would be naively expected from their large masses.

The ρ meson contributes to the pion spectrum and could alter the inclusive pion spectrum shape significantly. In the default treatment of resonances in the blast-wave parametrization, the ρ acquires p_\perp as given by the kinetic freeze-out temperature and the common transverse flow velocity (with the corresponding ρ mass), and the decay pions are calculated from decay kinematics. To test the validity of the regeneration picture, two additional cases of different ρ contributions are studied. (1) The ρ decay pions have the same p_\perp spectral shape as the primordial pions. This is equivalent to a zero ρ lifetime; the ρ does not have time to interact with the medium and gain its own flow; the flow it has is from that of the resonant pion pair that flow with the medium. In this case, the existence of ρ does not make a difference in the final fit results. This case is referred to as “0% ρ ” below. (2) Half of the ρ contribution is taken as in case (1) and the other half as in the default treatment. This case is referred to as “50% ρ ” below. Since ρ is very efficient at gaining flow compared to the much lighter pions, the default treatment of the blast-wave parametrization gives the largest flow to ρ , and case (1) gives the smallest flow.

Table XII shows the fit results for the two cases, together with the default case of resonance treatment (i.e., the “100% ρ ” case), for both pp and central Au + Au collisions. Figures 45 and 46 show the fits of the calculated inclusive pion spectra to the measured ones for pp and central Au + Au, respectively. Fits are performed to the six measured spectra simultaneously, but only negatively charged particles are shown. The fit results from only the 0% and 50% ρ cases are shown for the pions.

As can be seen from the table and the figures, the models with all three cases of ρ contribution describe the spectra data well. The fit T_{kin} and $\langle\beta\rangle$ values from all three cases agree; they also agree with those obtained without including resonances within systematic uncertainties (shown in Table X). It is interesting to note, however, that for the three ρ cases, the lowest χ^2/ndf is found for the 100% ρ case in pp collisions and for the 0% ρ case in central Au + Au collisions. If taken literally, this could imply that pp collisions favor no regeneration, and central Au + Au collisions favor complete regeneration, hence a long time span between chemical freeze-out and kinetic freeze-out, lending support to the similar observation made by the K^* measurement [48,51].

APPENDIX C: INVARIANT p_\perp SPECTRA DATA TABLES

The transverse momentum spectra of the invariant yield per event are tabulated in Tables XIII–XXXVII.

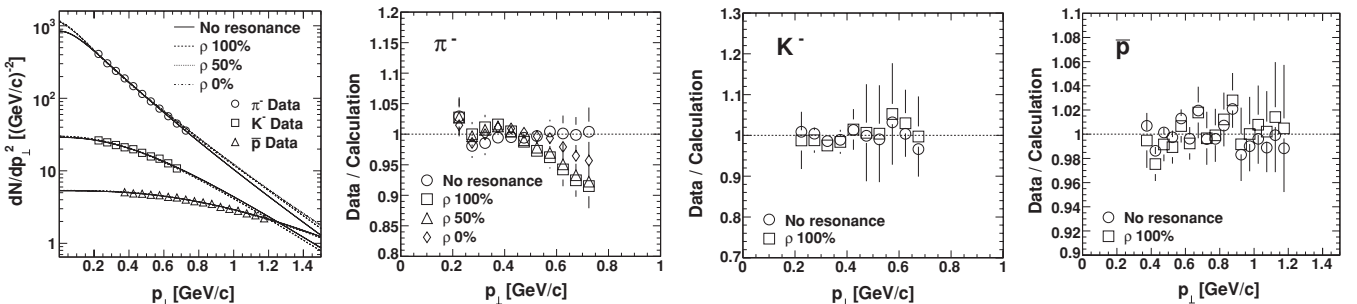


FIG. 46. Same as Fig. 45, but for the top 5% central Au + Au collisions at 200 GeV [17].

TABLE XIII. Identified π^\pm , K^\pm , antiproton, and proton invariant transverse momentum spectra at midrapidity ($|y| < 0.1$) in minimum-bias pp collisions at 200 GeV: $d^2N/(2\pi p_\perp dp_\perp dy)$ $[(\text{GeV}/c)^{-2}]$ vs p_\perp (GeV/c). Errors are the quadratic sum of statistical errors and point-to-point systematic errors. For proton, systematic uncertainties due to proton background subtraction are also included in quadrature. See Sec. V A for other systematic uncertainties. Data were published in Ref. [17].

p_\perp	π^-	π^+	K^-	K^+	\bar{p}	p
0.225	2.02 ± 0.06	2.07 ± 0.06	$(1.43 \pm 0.11) \times 10^{-1}$	$(1.52 \pm 0.11) \times 10^{-1}$		
0.275	1.52 ± 0.03	1.54 ± 0.03	$(1.26 \pm 0.05) \times 10^{-1}$	$(1.30 \pm 0.05) \times 10^{-1}$		
0.325	1.13 ± 0.02	1.14 ± 0.02	$(1.08 \pm 0.02) \times 10^{-1}$	$(1.08 \pm 0.02) \times 10^{-1}$		
0.375	$(8.44 \pm 0.09) \times 10^{-1}$	$(8.57 \pm 0.09) \times 10^{-1}$	$(8.77 \pm 0.24) \times 10^{-2}$	$(9.16 \pm 0.25) \times 10^{-2}$	$(5.54 \pm 0.13) \times 10^{-2}$	
0.425	$(6.35 \pm 0.07) \times 10^{-1}$	$(6.38 \pm 0.07) \times 10^{-1}$	$(7.34 \pm 0.26) \times 10^{-2}$	$(7.47 \pm 0.27) \times 10^{-2}$	$(4.81 \pm 0.11) \times 10^{-2}$	
0.475	$(4.69 \pm 0.05) \times 10^{-1}$	$(4.76 \pm 0.05) \times 10^{-1}$	$(6.17 \pm 0.63) \times 10^{-2}$	$(6.26 \pm 0.64) \times 10^{-2}$	$(4.25 \pm 0.10) \times 10^{-2}$	$(5.07 \pm 0.25) \times 10^{-2}$
0.525	$(3.54 \pm 0.04) \times 10^{-1}$	$(3.59 \pm 0.04) \times 10^{-1}$	$(4.87 \pm 0.50) \times 10^{-2}$	$(5.26 \pm 0.54) \times 10^{-2}$	$(3.77 \pm 0.09) \times 10^{-2}$	$(4.69 \pm 0.19) \times 10^{-2}$
0.575	$(2.67 \pm 0.03) \times 10^{-1}$	$(2.73 \pm 0.03) \times 10^{-1}$	$(4.11 \pm 0.42) \times 10^{-2}$	$(4.41 \pm 0.45) \times 10^{-2}$	$(3.38 \pm 0.08) \times 10^{-2}$	$(4.08 \pm 0.14) \times 10^{-2}$
0.625	$(2.02 \pm 0.04) \times 10^{-1}$	$(2.07 \pm 0.04) \times 10^{-1}$	$(3.70 \pm 0.28) \times 10^{-2}$	$(3.81 \pm 0.28) \times 10^{-2}$	$(2.78 \pm 0.07) \times 10^{-2}$	$(3.42 \pm 0.10) \times 10^{-2}$
0.675	$(1.53 \pm 0.03) \times 10^{-1}$	$(1.55 \pm 0.03) \times 10^{-1}$	$(2.86 \pm 0.22) \times 10^{-2}$	$(3.06 \pm 0.24) \times 10^{-2}$	$(2.49 \pm 0.06) \times 10^{-2}$	$(2.87 \pm 0.07) \times 10^{-2}$
0.725	$(1.16 \pm 0.03) \times 10^{-1}$	$(1.16 \pm 0.03) \times 10^{-1}$	$(2.42 \pm 0.27) \times 10^{-2}$	$(2.49 \pm 0.28) \times 10^{-2}$	$(2.03 \pm 0.06) \times 10^{-2}$	$(2.41 \pm 0.07) \times 10^{-2}$
0.775	$(8.65 \pm 0.30) \times 10^{-2}$	$(8.95 \pm 0.31) \times 10^{-2}$			$(1.75 \pm 0.06) \times 10^{-2}$	$(2.13 \pm 0.06) \times 10^{-2}$
0.825					$(1.52 \pm 0.05) \times 10^{-2}$	$(1.82 \pm 0.05) \times 10^{-2}$
0.875					$(1.27 \pm 0.04) \times 10^{-2}$	$(1.54 \pm 0.05) \times 10^{-2}$
0.925					$(1.05 \pm 0.04) \times 10^{-2}$	$(1.31 \pm 0.04) \times 10^{-2}$
0.975					$(8.95 \pm 0.34) \times 10^{-3}$	$(1.11 \pm 0.04) \times 10^{-2}$
1.025					$(7.36 \pm 0.34) \times 10^{-3}$	$(9.78 \pm 0.40) \times 10^{-3}$
1.075					$(6.59 \pm 0.32) \times 10^{-3}$	$(8.56 \pm 0.37) \times 10^{-3}$
1.125					$(5.21 \pm 0.29) \times 10^{-3}$	$(7.38 \pm 0.38) \times 10^{-3}$

TABLE XIV. Identified π^- invariant transverse momentum spectra at midrapidity ($|y| < 0.1$) in $d + \text{Au}$ collisions at 200 GeV: $d^2N/(2\pi p_\perp dp_\perp dy)$ $[(\text{GeV}/c)^{-2}]$ vs p_\perp (GeV/c). Errors are the quadratic sum of statistical errors and point-to-point systematic errors. See Sec. V A for other systematic uncertainties.

p_\perp	Min. bias	40–100%	20–40%	0–20%
0.225	6.59 ± 0.07	4.16 ± 0.04	8.84 ± 0.09	$(1.16 \pm 0.01) \times 10^1$
0.275	4.84 ± 0.05	3.07 ± 0.03	6.29 ± 0.06	8.70 ± 0.09
0.325	3.60 ± 0.04	2.28 ± 0.02	4.69 ± 0.05	6.51 ± 0.07
0.375	2.69 ± 0.03	1.69 ± 0.02	3.51 ± 0.04	4.89 ± 0.05
0.425	2.05 ± 0.08	1.28 ± 0.05	2.66 ± 0.11	3.74 ± 0.15
0.475	1.56 ± 0.06	$(9.66 \pm 0.39) \times 10^{-1}$	2.04 ± 0.08	2.87 ± 0.12
0.525	1.20 ± 0.05	$(7.31 \pm 0.29) \times 10^{-1}$	1.57 ± 0.06	2.22 ± 0.09
0.575	$(9.27 \pm 0.37) \times 10^{-1}$	$(5.64 \pm 0.23) \times 10^{-1}$	1.21 ± 0.05	1.73 ± 0.07
0.625	$(7.22 \pm 0.43) \times 10^{-1}$	$(4.38 \pm 0.26) \times 10^{-1}$	$(9.45 \pm 0.57) \times 10^{-1}$	1.35 ± 0.08
0.675	$(5.67 \pm 0.17) \times 10^{-1}$	$(3.40 \pm 0.10) \times 10^{-1}$	$(7.43 \pm 0.23) \times 10^{-1}$	1.07 ± 0.03

TABLE XV. Identified π^+ invariant transverse momentum spectra at midrapidity ($|y| < 0.1$) in $d + \text{Au}$ collisions at 200 GeV: $d^2N/(2\pi p_\perp dp_\perp dy)$ $[(\text{GeV}/c)^{-2}]$ vs p_\perp (GeV/c). Errors are the quadratic sum of statistical errors and point-to-point systematic errors. See Sec. V A for other systematic uncertainties.

p_\perp	Min. bias	40–100%	20–40%	0–20%
0.225	6.54 ± 0.07	4.10 ± 0.04	8.53 ± 0.09	$(1.19 \pm 0.01) \times 10^1$
0.275	4.78 ± 0.05	3.00 ± 0.03	6.23 ± 0.06	8.69 ± 0.09
0.325	3.59 ± 0.04	2.27 ± 0.02	4.65 ± 0.05	6.49 ± 0.07
0.375	2.68 ± 0.03	1.65 ± 0.02	3.48 ± 0.04	4.94 ± 0.05
0.425	2.07 ± 0.08	1.31 ± 0.05	2.66 ± 0.11	3.77 ± 0.15
0.475	1.54 ± 0.06	$(9.23 \pm 0.37) \times 10^{-1}$	2.04 ± 0.08	2.90 ± 0.12
0.525	1.22 ± 0.05	$(7.55 \pm 0.30) \times 10^{-1}$	1.58 ± 0.06	2.23 ± 0.09
0.575	$(9.32 \pm 0.37) \times 10^{-1}$	$(5.67 \pm 0.23) \times 10^{-1}$	1.22 ± 0.05	1.74 ± 0.07
0.625	$(7.40 \pm 0.44) \times 10^{-1}$	$(4.60 \pm 0.28) \times 10^{-1}$	$(9.54 \pm 0.57) \times 10^{-1}$	1.37 ± 0.08
0.675	$(5.67 \pm 0.17) \times 10^{-1}$	$(3.32 \pm 0.10) \times 10^{-1}$	$(7.49 \pm 0.23) \times 10^{-1}$	1.09 ± 0.03

TABLE XVI. Identified K^- invariant transverse momentum spectra at midrapidity ($|y| < 0.1$) in $d + \text{Au}$ collisions at 200 GeV: $d^2N/(2\pi p_\perp dp_\perp dy)$ $[(\text{GeV}/c)^{-2}]$ vs p_\perp (GeV/ c). Errors are the quadratic sum of statistical errors and point-to-point systematic errors. See Sec. V A for other systematic uncertainties.

p_\perp	Min. bias	40–100%	20–40%	0–20%
0.225	$(5.15 \pm 0.16) \times 10^{-1}$	$(3.21 \pm 0.11) \times 10^{-1}$	$(6.65 \pm 0.23) \times 10^{-1}$	$(9.47 \pm 0.32) \times 10^{-1}$
0.275	$(4.34 \pm 0.05) \times 10^{-1}$	$(2.73 \pm 0.04) \times 10^{-1}$	$(5.63 \pm 0.09) \times 10^{-1}$	$(7.85 \pm 0.12) \times 10^{-1}$
0.325	$(3.64 \pm 0.08) \times 10^{-1}$	$(2.25 \pm 0.05) \times 10^{-1}$	$(4.75 \pm 0.11) \times 10^{-1}$	$(6.70 \pm 0.15) \times 10^{-1}$
0.375	$(3.13 \pm 0.28) \times 10^{-1}$	$(1.96 \pm 0.18) \times 10^{-1}$	$(4.06 \pm 0.37) \times 10^{-1}$	$(5.75 \pm 0.52) \times 10^{-1}$
0.425	$(2.62 \pm 0.37) \times 10^{-1}$	$(1.61 \pm 0.23) \times 10^{-1}$	$(3.43 \pm 0.48) \times 10^{-1}$	$(4.81 \pm 0.68) \times 10^{-1}$
0.475	$(2.11 \pm 0.23) \times 10^{-1}$	$(1.24 \pm 0.14) \times 10^{-1}$	$(2.76 \pm 0.31) \times 10^{-1}$	$(4.07 \pm 0.45) \times 10^{-1}$
0.525	$(1.85 \pm 0.13) \times 10^{-1}$	$(1.09 \pm 0.08) \times 10^{-1}$	$(2.44 \pm 0.17) \times 10^{-1}$	$(3.52 \pm 0.25) \times 10^{-1}$
0.575	$(1.63 \pm 0.15) \times 10^{-1}$	$(9.63 \pm 0.87) \times 10^{-2}$	$(2.15 \pm 0.20) \times 10^{-1}$	$(3.09 \pm 0.28) \times 10^{-1}$
0.625	$(1.32 \pm 0.07) \times 10^{-1}$	$(7.67 \pm 0.40) \times 10^{-2}$	$(1.72 \pm 0.09) \times 10^{-1}$	$(2.57 \pm 0.13) \times 10^{-1}$
0.675	$(1.16 \pm 0.09) \times 10^{-1}$	$(6.76 \pm 0.55) \times 10^{-2}$	$(1.57 \pm 0.13) \times 10^{-1}$	$(2.21 \pm 0.18) \times 10^{-1}$
0.725	$(1.01 \pm 0.05) \times 10^{-1}$	$(6.16 \pm 0.36) \times 10^{-2}$	$(1.31 \pm 0.08) \times 10^{-1}$	$(1.91 \pm 0.11) \times 10^{-1}$

TABLE XVII. Identified K^+ invariant transverse momentum spectra at midrapidity ($|y| < 0.1$) in $d + \text{Au}$ collisions at 200 GeV: $d^2N/(2\pi p_\perp dp_\perp dy)$ $[(\text{GeV}/c)^{-2}]$ vs p_\perp (GeV/ c). Errors are the quadratic sum of statistical errors and point-to-point systematic errors. See Sec. V A for other systematic uncertainties.

p_\perp	Min. bias	40–100%	20–40%	0–20%
0.225	$(4.84 \pm 0.15) \times 10^{-1}$	$(2.99 \pm 0.10) \times 10^{-1}$	$(6.32 \pm 0.22) \times 10^{-1}$	$(8.93 \pm 0.30) \times 10^{-1}$
0.275	$(4.28 \pm 0.05) \times 10^{-1}$	$(2.71 \pm 0.04) \times 10^{-1}$	$(5.50 \pm 0.09) \times 10^{-1}$	$(7.78 \pm 0.11) \times 10^{-1}$
0.325	$(3.68 \pm 0.08) \times 10^{-1}$	$(2.31 \pm 0.05) \times 10^{-1}$	$(4.83 \pm 0.11) \times 10^{-1}$	$(6.68 \pm 0.15) \times 10^{-1}$
0.375	$(3.24 \pm 0.29) \times 10^{-1}$	$(1.99 \pm 0.18) \times 10^{-1}$	$(4.28 \pm 0.39) \times 10^{-1}$	$(5.94 \pm 0.54) \times 10^{-1}$
0.425	$(2.73 \pm 0.38) \times 10^{-1}$	$(1.68 \pm 0.24) \times 10^{-1}$	$(3.58 \pm 0.50) \times 10^{-1}$	$(5.04 \pm 0.71) \times 10^{-1}$
0.475	$(2.25 \pm 0.25) \times 10^{-1}$	$(1.34 \pm 0.15) \times 10^{-1}$	$(2.95 \pm 0.33) \times 10^{-1}$	$(4.30 \pm 0.47) \times 10^{-1}$
0.525	$(2.00 \pm 0.14) \times 10^{-1}$	$(1.22 \pm 0.09) \times 10^{-1}$	$(2.64 \pm 0.19) \times 10^{-1}$	$(3.72 \pm 0.26) \times 10^{-1}$
0.575	$(1.74 \pm 0.16) \times 10^{-1}$	$(1.05 \pm 0.09) \times 10^{-1}$	$(2.30 \pm 0.21) \times 10^{-1}$	$(3.26 \pm 0.30) \times 10^{-1}$
0.625	$(1.41 \pm 0.07) \times 10^{-1}$	$(8.23 \pm 0.42) \times 10^{-2}$	$(1.88 \pm 0.10) \times 10^{-1}$	$(2.70 \pm 0.14) \times 10^{-1}$
0.675	$(1.27 \pm 0.10) \times 10^{-1}$	$(7.36 \pm 0.60) \times 10^{-2}$	$(1.68 \pm 0.14) \times 10^{-1}$	$(2.45 \pm 0.20) \times 10^{-1}$
0.725	$(1.06 \pm 0.06) \times 10^{-1}$	$(6.11 \pm 0.35) \times 10^{-2}$	$(1.44 \pm 0.08) \times 10^{-1}$	$(2.02 \pm 0.11) \times 10^{-1}$

TABLE XVIII. Identified \bar{p} invariant transverse momentum spectra at midrapidity ($|y| < 0.1$) in $d + \text{Au}$ collisions at 200 GeV: $d^2N/(2\pi p_\perp dp_\perp dy)$ $[(\text{GeV}/c)^{-2}]$ vs p_\perp (GeV/ c). Errors are the quadratic sum of statistical errors and point-to-point systematic errors. See Sec. V A for other systematic uncertainties.

p_\perp	Min. bias	40–100%	20–40%	0–20%
0.425	$(1.37 \pm 0.02) \times 10^{-1}$	$(8.46 \pm 0.12) \times 10^{-2}$	$(1.76 \pm 0.03) \times 10^{-1}$	$(2.55 \pm 0.04) \times 10^{-1}$
0.475	$(1.22 \pm 0.01) \times 10^{-1}$	$(7.39 \pm 0.11) \times 10^{-2}$	$(1.55 \pm 0.02) \times 10^{-1}$	$(2.35 \pm 0.03) \times 10^{-1}$
0.525	$(1.11 \pm 0.01) \times 10^{-1}$	$(6.58 \pm 0.09) \times 10^{-2}$	$(1.43 \pm 0.02) \times 10^{-1}$	$(2.12 \pm 0.03) \times 10^{-1}$
0.575	$(1.01 \pm 0.01) \times 10^{-1}$	$(5.97 \pm 0.09) \times 10^{-2}$	$(1.33 \pm 0.02) \times 10^{-1}$	$(1.93 \pm 0.03) \times 10^{-1}$
0.625	$(9.00 \pm 0.19) \times 10^{-2}$	$(5.27 \pm 0.12) \times 10^{-2}$	$(1.18 \pm 0.03) \times 10^{-1}$	$(1.74 \pm 0.04) \times 10^{-1}$
0.675	$(8.05 \pm 0.17) \times 10^{-2}$	$(4.65 \pm 0.11) \times 10^{-2}$	$(1.06 \pm 0.02) \times 10^{-1}$	$(1.57 \pm 0.04) \times 10^{-1}$
0.725	$(7.22 \pm 0.09) \times 10^{-2}$	$(4.12 \pm 0.06) \times 10^{-2}$	$(9.47 \pm 0.15) \times 10^{-2}$	$(1.43 \pm 0.02) \times 10^{-1}$
0.775	$(6.37 \pm 0.20) \times 10^{-2}$	$(3.60 \pm 0.12) \times 10^{-2}$	$(8.48 \pm 0.27) \times 10^{-2}$	$(1.26 \pm 0.04) \times 10^{-1}$
0.825	$(5.77 \pm 0.29) \times 10^{-2}$	$(3.20 \pm 0.16) \times 10^{-2}$	$(7.88 \pm 0.41) \times 10^{-2}$	$(1.14 \pm 0.06) \times 10^{-1}$
0.875	$(5.21 \pm 0.26) \times 10^{-2}$	$(2.93 \pm 0.15) \times 10^{-2}$	$(7.18 \pm 0.37) \times 10^{-2}$	$(1.01 \pm 0.05) \times 10^{-1}$
0.925	$(4.57 \pm 0.10) \times 10^{-2}$	$(2.55 \pm 0.06) \times 10^{-2}$	$(6.37 \pm 0.15) \times 10^{-2}$	$(8.80 \pm 0.20) \times 10^{-2}$
0.975	$(3.95 \pm 0.08) \times 10^{-2}$	$(2.12 \pm 0.05) \times 10^{-2}$	$(5.47 \pm 0.13) \times 10^{-2}$	$(7.92 \pm 0.19) \times 10^{-2}$
1.025	$(3.43 \pm 0.24) \times 10^{-2}$	$(1.85 \pm 0.13) \times 10^{-2}$	$(4.69 \pm 0.34) \times 10^{-2}$	$(6.90 \pm 0.49) \times 10^{-2}$
1.075	$(3.03 \pm 0.10) \times 10^{-2}$	$(1.64 \pm 0.06) \times 10^{-2}$	$(4.03 \pm 0.14) \times 10^{-2}$	$(6.21 \pm 0.21) \times 10^{-2}$

TABLE XIX. Identified proton invariant transverse momentum spectra at midrapidity ($|y| < 0.1$) in $d + \text{Au}$ collisions at 200 GeV: $d^2N/(2\pi p_\perp dp_\perp dy)$ $[(\text{GeV}/c)^{-2}]$ vs p_\perp (GeV/c). Errors are the quadratic sum of statistical errors and point-to-point systematic errors. See Sec. V A for other systematic uncertainties including those due to proton background subtraction.

p_\perp	Min. bias	40–100%	20–40%	0–20%
0.425	$(1.69 \pm 0.02) \times 10^{-1}$	$(1.03 \pm 0.01) \times 10^{-1}$	$(2.35 \pm 0.03) \times 10^{-1}$	$(3.03 \pm 0.04) \times 10^{-1}$
0.475	$(1.47 \pm 0.02) \times 10^{-1}$	$(8.40 \pm 0.11) \times 10^{-2}$	$(2.04 \pm 0.03) \times 10^{-1}$	$(2.79 \pm 0.03) \times 10^{-1}$
0.525	$(1.34 \pm 0.01) \times 10^{-1}$	$(7.86 \pm 0.10) \times 10^{-2}$	$(1.84 \pm 0.02) \times 10^{-1}$	$(2.48 \pm 0.03) \times 10^{-1}$
0.575	$(1.19 \pm 0.01) \times 10^{-1}$	$(6.87 \pm 0.09) \times 10^{-2}$	$(1.64 \pm 0.02) \times 10^{-1}$	$(2.26 \pm 0.03) \times 10^{-1}$
0.625	$(1.10 \pm 0.02) \times 10^{-1}$	$(6.30 \pm 0.14) \times 10^{-2}$	$(1.51 \pm 0.03) \times 10^{-1}$	$(2.08 \pm 0.04) \times 10^{-1}$
0.675	$(9.87 \pm 0.20) \times 10^{-2}$	$(5.73 \pm 0.13) \times 10^{-2}$	$(1.33 \pm 0.03) \times 10^{-1}$	$(1.89 \pm 0.04) \times 10^{-1}$
0.725	$(8.74 \pm 0.10) \times 10^{-2}$	$(4.91 \pm 0.07) \times 10^{-2}$	$(1.19 \pm 0.02) \times 10^{-1}$	$(1.70 \pm 0.02) \times 10^{-1}$
0.775	$(7.95 \pm 0.24) \times 10^{-2}$	$(4.49 \pm 0.15) \times 10^{-2}$	$(1.08 \pm 0.03) \times 10^{-1}$	$(1.55 \pm 0.05) \times 10^{-1}$
0.825	$(6.98 \pm 0.35) \times 10^{-2}$	$(3.88 \pm 0.20) \times 10^{-2}$	$(9.45 \pm 0.48) \times 10^{-2}$	$(1.38 \pm 0.07) \times 10^{-1}$
0.875	$(6.49 \pm 0.33) \times 10^{-2}$	$(3.54 \pm 0.18) \times 10^{-2}$	$(8.93 \pm 0.46) \times 10^{-2}$	$(1.29 \pm 0.07) \times 10^{-1}$
0.925	$(5.55 \pm 0.12) \times 10^{-2}$	$(2.98 \pm 0.07) \times 10^{-2}$	$(7.57 \pm 0.17) \times 10^{-2}$	$(1.12 \pm 0.02) \times 10^{-1}$
0.975	$(4.93 \pm 0.10) \times 10^{-2}$	$(2.60 \pm 0.06) \times 10^{-2}$	$(7.08 \pm 0.16) \times 10^{-2}$	$(9.78 \pm 0.22) \times 10^{-2}$
1.025	$(4.15 \pm 0.29) \times 10^{-2}$	$(2.21 \pm 0.16) \times 10^{-2}$	$(5.84 \pm 0.42) \times 10^{-2}$	$(8.27 \pm 0.59) \times 10^{-2}$
1.075	$(3.61 \pm 0.12) \times 10^{-2}$	$(1.91 \pm 0.06) \times 10^{-2}$	$(4.90 \pm 0.22) \times 10^{-2}$	$(7.39 \pm 0.24) \times 10^{-2}$

TABLE XX. Identified π^- invariant transverse momentum spectra at midrapidity ($|y| < 0.1$) in $\text{Au} + \text{Au}$ collisions at 62.4 GeV: $d^2N/(2\pi p_\perp dp_\perp dy)$ $[(\text{GeV}/c)^{-2}]$ vs p_\perp (GeV/c). Errors are the quadratic sum of statistical errors and point-to-point systematic errors. See Sec. V A for other systematic uncertainties.

p_{\perp}	70–80%	60–70%	50–60%	40–50%	
0.225	$(1.07 \pm 0.02) \times 10^1$	$(2.02 \pm 0.04) \times 10^1$	$(3.63 \pm 0.07) \times 10^1$	$(5.91 \pm 0.12) \times 10^1$	
0.275	7.93 ± 0.16	$(1.53 \pm 0.03) \times 10^1$	$(2.74 \pm 0.05) \times 10^1$	$(4.45 \pm 0.09) \times 10^1$	
0.325	5.89 ± 0.12	$(1.15 \pm 0.02) \times 10^1$	$(2.08 \pm 0.04) \times 10^1$	$(3.36 \pm 0.07) \times 10^1$	
0.375	4.39 ± 0.05	8.69 ± 0.09	$(1.58 \pm 0.02) \times 10^1$	$(2.57 \pm 0.03) \times 10^1$	
0.425	3.28 ± 0.04	6.59 ± 0.07	$(1.20 \pm 0.01) \times 10^1$	$(1.97 \pm 0.02) \times 10^1$	
0.475	2.49 ± 0.03	5.02 ± 0.05	9.27 ± 0.10	$(1.51 \pm 0.02) \times 10^1$	
0.525	1.89 ± 0.02	3.85 ± 0.04	7.12 ± 0.07	$(1.17 \pm 0.01) \times 10^1$	
0.575	1.44 ± 0.03	2.96 ± 0.06	5.51 ± 0.11	9.08 ± 0.18	
0.625	1.10 ± 0.02	2.28 ± 0.05	4.28 ± 0.09	7.07 ± 0.14	
0.675	$(8.37 \pm 0.26) \times 10^{-1}$	1.77 ± 0.05	3.35 ± 0.10	5.55 ± 0.17	
p_{\perp}	30–40%	20–30%	10–20%	5–10%	0–5%
0.225	$(8.87 \pm 0.18) \times 10^1$	$(1.31 \pm 0.03) \times 10^2$	$(1.88 \pm 0.04) \times 10^2$	$(2.44 \pm 0.05) \times 10^2$	$(3.00 \pm 0.06) \times 10^2$
0.275	$(6.71 \pm 0.13) \times 10^1$	$(1.00 \pm 0.02) \times 10^2$	$(1.44 \pm 0.03) \times 10^2$	$(1.89 \pm 0.04) \times 10^2$	$(2.33 \pm 0.05) \times 10^2$
0.325	$(5.14 \pm 0.10) \times 10^1$	$(7.68 \pm 0.15) \times 10^1$	$(1.10 \pm 0.02) \times 10^2$	$(1.45 \pm 0.03) \times 10^2$	$(1.80 \pm 0.04) \times 10^2$
0.375	$(3.95 \pm 0.04) \times 10^1$	$(5.91 \pm 0.06) \times 10^1$	$(8.48 \pm 0.09) \times 10^1$	$(1.12 \pm 0.01) \times 10^2$	$(1.39 \pm 0.01) \times 10^2$
0.425	$(3.04 \pm 0.03) \times 10^1$	$(4.58 \pm 0.05) \times 10^1$	$(6.57 \pm 0.07) \times 10^1$	$(8.69 \pm 0.09) \times 10^1$	$(1.07 \pm 0.01) \times 10^2$
0.475	$(2.36 \pm 0.02) \times 10^1$	$(3.54 \pm 0.04) \times 10^1$	$(5.10 \pm 0.05) \times 10^1$	$(6.75 \pm 0.07) \times 10^1$	$(8.32 \pm 0.08) \times 10^1$
0.525	$(1.82 \pm 0.02) \times 10^1$	$(2.76 \pm 0.03) \times 10^1$	$(3.98 \pm 0.04) \times 10^1$	$(5.26 \pm 0.05) \times 10^1$	$(6.47 \pm 0.07) \times 10^1$
0.575	$(1.42 \pm 0.03) \times 10^1$	$(2.15 \pm 0.04) \times 10^1$	$(3.11 \pm 0.06) \times 10^1$	$(4.10 \pm 0.08) \times 10^1$	$(5.05 \pm 0.10) \times 10^1$
0.625	$(1.11 \pm 0.02) \times 10^1$	$(1.68 \pm 0.03) \times 10^1$	$(2.44 \pm 0.05) \times 10^1$	$(3.22 \pm 0.06) \times 10^1$	$(3.96 \pm 0.08) \times 10^1$
0.675	8.78 ± 0.26	$(1.33 \pm 0.04) \times 10^1$	$(1.93 \pm 0.06) \times 10^1$	$(2.54 \pm 0.08) \times 10^1$	$(3.14 \pm 0.09) \times 10^1$

TABLE XXI. Identified π^+ invariant transverse momentum spectra at midrapidity ($|y| < 0.1$) in $\text{Au} + \text{Au}$ collisions at 62.4 GeV: $d^2N/(2\pi p_\perp dp_\perp dy)$ $[(\text{GeV}/c)^{-2}]$ vs p_\perp (GeV/c). Errors are the quadratic sum of statistical errors and point-to-point systematic errors. See Sec. V A for other systematic uncertainties.

p_\perp	70–80%	60–70%	50–60%	40–50%
0.225	$(1.07 \pm 0.02) \times 10^1$	$(2.11 \pm 0.04) \times 10^1$	$(3.66 \pm 0.07) \times 10^1$	$(5.89 \pm 0.12) \times 10^1$
0.275	7.79 ± 0.16	$(1.56 \pm 0.03) \times 10^1$	$(2.71 \pm 0.05) \times 10^1$	$(4.37 \pm 0.09) \times 10^1$
0.325	5.81 ± 0.12	$(1.16 \pm 0.02) \times 10^1$	$(2.04 \pm 0.04) \times 10^1$	$(3.31 \pm 0.07) \times 10^1$
0.375	4.32 ± 0.05	8.77 ± 0.09	$(1.56 \pm 0.02) \times 10^1$	$(2.53 \pm 0.03) \times 10^1$

TABLE XXI. (*Continued.*)

p_{\perp}	70–80%	60–70%	50–60%	40–50%	
0.425	3.27 ± 0.04	6.60 ± 0.07	$(1.19 \pm 0.01) \times 10^1$	$(1.95 \pm 0.02) \times 10^1$	
0.475	2.44 ± 0.03	5.04 ± 0.05	9.13 ± 0.09	$(1.50 \pm 0.02) \times 10^1$	
0.525	1.86 ± 0.02	3.81 ± 0.04	7.03 ± 0.07	$(1.15 \pm 0.01) \times 10^1$	
0.575	1.43 ± 0.03	2.93 ± 0.06	5.45 ± 0.11	8.94 ± 0.18	
0.625	1.08 ± 0.02	2.26 ± 0.05	4.21 ± 0.09	6.99 ± 0.14	
0.675	$(8.34 \pm 0.26) \times 10^{-1}$	1.75 ± 0.05	3.26 ± 0.10	5.45 ± 0.16	
p_{\perp}	30–40%	20–30%	10–20%	5–10%	0–5%
0.225	$(8.82 \pm 0.18) \times 10^1$	$(1.28 \pm 0.03) \times 10^2$	$(1.87 \pm 0.04) \times 10^2$	$(2.39 \pm 0.05) \times 10^2$	$(2.95 \pm 0.06) \times 10^2$
0.275	$(6.61 \pm 0.13) \times 10^1$	$(9.70 \pm 0.19) \times 10^1$	$(1.41 \pm 0.03) \times 10^2$	$(1.85 \pm 0.04) \times 10^2$	$(2.27 \pm 0.05) \times 10^2$
0.325	$(5.06 \pm 0.10) \times 10^1$	$(7.44 \pm 0.15) \times 10^1$	$(1.08 \pm 0.02) \times 10^2$	$(1.44 \pm 0.03) \times 10^2$	$(1.75 \pm 0.04) \times 10^2$
0.375	$(3.89 \pm 0.04) \times 10^1$	$(5.77 \pm 0.06) \times 10^1$	$(8.36 \pm 0.08) \times 10^1$	$(1.12 \pm 0.01) \times 10^2$	$(1.36 \pm 0.01) \times 10^2$
0.425	$(3.00 \pm 0.03) \times 10^1$	$(4.47 \pm 0.05) \times 10^1$	$(6.49 \pm 0.07) \times 10^1$	$(8.69 \pm 0.09) \times 10^1$	$(1.05 \pm 0.01) \times 10^2$
0.475	$(2.32 \pm 0.02) \times 10^1$	$(3.47 \pm 0.03) \times 10^1$	$(5.04 \pm 0.05) \times 10^1$	$(6.74 \pm 0.07) \times 10^1$	$(8.21 \pm 0.08) \times 10^1$
0.525	$(1.80 \pm 0.02) \times 10^1$	$(2.71 \pm 0.03) \times 10^1$	$(3.92 \pm 0.04) \times 10^1$	$(5.24 \pm 0.05) \times 10^1$	$(6.38 \pm 0.06) \times 10^1$
0.575	$(1.40 \pm 0.03) \times 10^1$	$(2.11 \pm 0.04) \times 10^1$	$(3.07 \pm 0.06) \times 10^1$	$(4.09 \pm 0.08) \times 10^1$	$(4.99 \pm 0.10) \times 10^1$
0.625	$(1.09 \pm 0.02) \times 10^1$	$(1.66 \pm 0.03) \times 10^1$	$(2.41 \pm 0.05) \times 10^1$	$(3.21 \pm 0.06) \times 10^1$	$(3.90 \pm 0.08) \times 10^1$
0.675	8.66 ± 0.26	$(1.31 \pm 0.04) \times 10^1$	$(1.90 \pm 0.06) \times 10^1$	$(2.53 \pm 0.08) \times 10^1$	$(3.09 \pm 0.09) \times 10^1$

TABLE XXII. Identified K^- invariant transverse momentum spectra at midrapidity ($|y| < 0.1$) in Au + Au collisions at 62.4 GeV: $d^2N/(2\pi p_{\perp} dp_{\perp} dy)$ [(GeV/c) $^{-2}$] vs p_{\perp} (GeV/c). Errors are the quadratic sum of statistical errors and point-to-point systematic errors. See Sec. V A for other systematic uncertainties.

p_{\perp}	70–80%	60–70%	50–60%	40–50%	
0.275	$(7.03 \pm 0.19) \times 10^{-1}$	1.41 ± 0.03	2.51 ± 0.06	4.07 ± 0.09	
0.325	$(5.95 \pm 0.20) \times 10^{-1}$	1.18 ± 0.04	2.18 ± 0.07	3.48 ± 0.11	
0.375	$(4.89 \pm 0.26) \times 10^{-1}$	1.04 ± 0.05	1.91 ± 0.10	3.08 ± 0.16	
0.425	$(4.05 \pm 0.49) \times 10^{-1}$	$(8.79 \pm 1.06) \times 10^{-1}$	1.63 ± 0.20	2.71 ± 0.33	
0.475	$(3.14 \pm 0.38) \times 10^{-1}$	$(7.23 \pm 0.87) \times 10^{-1}$	1.31 ± 0.16	2.24 ± 0.27	
0.525	$(2.70 \pm 0.33) \times 10^{-1}$	$(5.86 \pm 0.71) \times 10^{-1}$	1.13 ± 0.14	1.92 ± 0.23	
0.575	$(2.27 \pm 0.19) \times 10^{-1}$	$(5.04 \pm 0.41) \times 10^{-1}$	$(9.71 \pm 0.78) \times 10^{-1}$	1.70 ± 0.14	
0.625	$(1.83 \pm 0.19) \times 10^{-1}$	$(4.37 \pm 0.44) \times 10^{-1}$	$(8.27 \pm 0.83) \times 10^{-1}$	1.48 ± 0.15	
0.675	$(1.61 \pm 0.20) \times 10^{-1}$	$(3.71 \pm 0.45) \times 10^{-1}$	$(7.48 \pm 0.90) \times 10^{-1}$	1.30 ± 0.16	
0.725	$(1.50 \pm 0.10) \times 10^{-1}$	$(3.30 \pm 0.20) \times 10^{-1}$	$(6.51 \pm 0.36) \times 10^{-1}$	1.16 ± 0.06	
p_{\perp}	30–40%	20–30%	10–20%	5–10%	0–5%
0.275	5.88 ± 0.12	9.01 ± 0.19	$(1.21 \pm 0.02) \times 10^1$	$(1.67 \pm 0.03) \times 10^1$	$(1.89 \pm 0.02) \times 10^1$
0.325	5.19 ± 0.16	7.92 ± 0.24	$(1.10 \pm 0.03) \times 10^1$	$(1.46 \pm 0.04) \times 10^1$	$(1.70 \pm 0.03) \times 10^1$
0.375	4.72 ± 0.24	7.19 ± 0.36	$(1.01 \pm 0.05) \times 10^1$	$(1.35 \pm 0.07) \times 10^1$	$(1.61 \pm 0.14) \times 10^1$
0.425	4.20 ± 0.50	6.37 ± 0.76	9.06 ± 1.09	$(1.20 \pm 0.14) \times 10^1$	$(1.44 \pm 0.20) \times 10^1$
0.475	3.49 ± 0.42	5.27 ± 0.63	7.50 ± 0.90	$(1.06 \pm 0.13) \times 10^1$	$(1.27 \pm 0.14) \times 10^1$
0.525	3.04 ± 0.37	4.59 ± 0.55	6.58 ± 0.79	8.86 ± 1.06	$(1.13 \pm 0.08) \times 10^1$
0.575	2.68 ± 0.22	4.06 ± 0.33	5.84 ± 0.47	8.03 ± 0.64	$(1.04 \pm 0.09) \times 10^1$
0.625	2.37 ± 0.24	3.63 ± 0.36	5.32 ± 0.53	7.21 ± 0.72	9.36 ± 0.47
0.675	2.09 ± 0.25	3.24 ± 0.39	4.68 ± 0.56	6.36 ± 0.77	7.73 ± 0.62
0.725	1.80 ± 0.09	2.84 ± 0.15	4.17 ± 0.22	5.43 ± 0.29	5.94 ± 0.31

TABLE XXIII. Identified K^+ invariant transverse momentum spectra at midrapidity ($|y| < 0.1$) in Au + Au collisions at 62.4 GeV: $d^2N/(2\pi p_{\perp} dp_{\perp} dy)$ [(GeV/c) $^{-2}$] vs p_{\perp} (GeV/c). Errors are the quadratic sum of statistical errors and point-to-point systematic errors. See Sec. V A for other systematic uncertainties.

p_{\perp}	70–80%	60–70%	50–60%	40–50%
0.275	$(7.29 \pm 0.19) \times 10^{-1}$	1.54 ± 0.04	2.63 ± 0.06	4.90 ± 0.10
0.325	$(5.82 \pm 0.19) \times 10^{-1}$	1.31 ± 0.04	2.32 ± 0.07	4.14 ± 0.13
0.375	$(5.07 \pm 0.26) \times 10^{-1}$	1.14 ± 0.06	2.09 ± 0.11	3.63 ± 0.18

TABLE XXIII. (*Continued.*)

p_{\perp}	70–80%	60–70%	50–60%	40–50%	
0.425	$(4.40 \pm 0.53) \times 10^{-1}$	$(9.92 \pm 1.20) \times 10^{-1}$	1.81 ± 0.22	3.13 ± 0.38	
0.475	$(3.58 \pm 0.43) \times 10^{-1}$	$(8.04 \pm 0.97) \times 10^{-1}$	1.53 ± 0.18	2.61 ± 0.31	
0.525	$(3.20 \pm 0.39) \times 10^{-1}$	$(6.89 \pm 0.83) \times 10^{-1}$	1.31 ± 0.16	2.23 ± 0.27	
0.575	$(2.52 \pm 0.21) \times 10^{-1}$	$(5.78 \pm 0.47) \times 10^{-1}$	1.14 ± 0.09	1.93 ± 0.16	
0.625	$(2.13 \pm 0.22) \times 10^{-1}$	$(4.97 \pm 0.50) \times 10^{-1}$	$(9.80 \pm 0.98) \times 10^{-1}$	1.67 ± 0.17	
0.675	$(1.86 \pm 0.23) \times 10^{-1}$	$(4.13 \pm 0.50) \times 10^{-1}$	$(8.52 \pm 1.03) \times 10^{-1}$	1.42 ± 0.17	
0.725	$(1.64 \pm 0.10) \times 10^{-1}$	$(3.78 \pm 0.22) \times 10^{-1}$	$(7.26 \pm 0.39) \times 10^{-1}$	1.28 ± 0.07	
p_{\perp}	30–40%	20–30%	10–20%	5–10%	0–5%
0.275	7.11 ± 0.15	$(1.03 \pm 0.02) \times 10^1$	$(1.43 \pm 0.03) \times 10^1$	$(1.91 \pm 0.04) \times 10^1$	$(2.25 \pm 0.05) \times 10^1$
0.325	6.20 ± 0.19	8.86 ± 0.27	$(1.25 \pm 0.04) \times 10^1$	$(1.67 \pm 0.05) \times 10^1$	$(2.03 \pm 0.06) \times 10^1$
0.375	5.52 ± 0.28	8.02 ± 0.40	$(1.15 \pm 0.06) \times 10^1$	$(1.55 \pm 0.08) \times 10^1$	$(1.88 \pm 0.09) \times 10^1$
0.425	4.85 ± 0.58	7.19 ± 0.86	$(1.04 \pm 0.13) \times 10^1$	$(1.40 \pm 0.17) \times 10^1$	$(1.68 \pm 0.20) \times 10^1$
0.475	4.07 ± 0.49	6.09 ± 0.73	8.97 ± 1.08	$(1.21 \pm 0.14) \times 10^1$	$(1.44 \pm 0.17) \times 10^1$
0.525	3.54 ± 0.42	5.32 ± 0.64	7.86 ± 0.94	$(1.05 \pm 0.13) \times 10^1$	$(1.28 \pm 0.15) \times 10^1$
0.575	3.06 ± 0.25	4.69 ± 0.38	6.95 ± 0.56	9.32 ± 0.75	$(1.14 \pm 0.09) \times 10^1$
0.625	2.65 ± 0.27	4.13 ± 0.41	6.09 ± 0.61	8.25 ± 0.83	$(1.01 \pm 0.10) \times 10^1$
0.675	2.34 ± 0.28	3.61 ± 0.43	5.33 ± 0.64	7.20 ± 0.87	8.71 ± 1.05
0.725	2.02 ± 0.10	3.12 ± 0.16	4.55 ± 0.23	6.27 ± 0.33	7.41 ± 0.38

TABLE XXIV. Identified \bar{p} invariant transverse momentum spectra at midrapidity ($|y| < 0.1$) in Au + Au collisions at 62.4 GeV: $d^2N/(2\pi p_{\perp} dp_{\perp} dy)$ [(GeV/c) $^{-2}$] vs p_{\perp} (GeV/c). Errors are the quadratic sum of statistical errors and point-to-point systematic errors. See Sec. V A for other systematic uncertainties.

p_{\perp}	70–80%	60–70%	50–60%	40–50%	
0.375	$(2.05 \pm 0.04) \times 10^{-1}$	$(3.87 \pm 0.06) \times 10^{-1}$	$(6.19 \pm 0.09) \times 10^{-1}$	$(9.12 \pm 0.12) \times 10^{-1}$	
0.425	$(1.85 \pm 0.04) \times 10^{-1}$	$(3.53 \pm 0.06) \times 10^{-1}$	$(5.93 \pm 0.08) \times 10^{-1}$	$(8.75 \pm 0.11) \times 10^{-1}$	
0.475	$(1.76 \pm 0.03) \times 10^{-1}$	$(3.37 \pm 0.05) \times 10^{-1}$	$(5.59 \pm 0.08) \times 10^{-1}$	$(8.31 \pm 0.11) \times 10^{-1}$	
0.525	$(1.53 \pm 0.03) \times 10^{-1}$	$(3.11 \pm 0.05) \times 10^{-1}$	$(5.18 \pm 0.07) \times 10^{-1}$	$(7.89 \pm 0.10) \times 10^{-1}$	
0.575	$(1.34 \pm 0.03) \times 10^{-1}$	$(2.82 \pm 0.04) \times 10^{-1}$	$(4.87 \pm 0.07) \times 10^{-1}$	$(7.29 \pm 0.09) \times 10^{-1}$	
0.625	$(1.20 \pm 0.03) \times 10^{-1}$	$(2.51 \pm 0.06) \times 10^{-1}$	$(4.37 \pm 0.10) \times 10^{-1}$	$(6.85 \pm 0.15) \times 10^{-1}$	
0.675	$(1.05 \pm 0.03) \times 10^{-1}$	$(2.24 \pm 0.05) \times 10^{-1}$	$(3.96 \pm 0.09) \times 10^{-1}$	$(6.24 \pm 0.13) \times 10^{-1}$	
0.725	$(8.84 \pm 0.24) \times 10^{-2}$	$(2.04 \pm 0.05) \times 10^{-1}$	$(3.54 \pm 0.08) \times 10^{-1}$	$(5.65 \pm 0.12) \times 10^{-1}$	
0.775	$(7.49 \pm 0.21) \times 10^{-2}$	$(1.70 \pm 0.04) \times 10^{-1}$	$(3.16 \pm 0.07) \times 10^{-1}$	$(5.11 \pm 0.11) \times 10^{-1}$	
0.825	$(6.87 \pm 0.19) \times 10^{-2}$	$(1.53 \pm 0.04) \times 10^{-1}$	$(2.92 \pm 0.07) \times 10^{-1}$	$(4.83 \pm 0.10) \times 10^{-1}$	
0.875	$(5.99 \pm 0.22) \times 10^{-2}$	$(1.41 \pm 0.05) \times 10^{-1}$	$(2.42 \pm 0.08) \times 10^{-1}$	$(4.06 \pm 0.13) \times 10^{-1}$	
0.925	$(4.93 \pm 0.18) \times 10^{-2}$	$(1.18 \pm 0.04) \times 10^{-1}$	$(2.15 \pm 0.07) \times 10^{-1}$	$(3.63 \pm 0.11) \times 10^{-1}$	
0.975	$(4.21 \pm 0.16) \times 10^{-2}$	$(1.01 \pm 0.03) \times 10^{-1}$	$(1.88 \pm 0.06) \times 10^{-1}$	$(3.25 \pm 0.10) \times 10^{-1}$	
1.025	$(3.57 \pm 0.14) \times 10^{-2}$	$(8.90 \pm 0.31) \times 10^{-2}$	$(1.62 \pm 0.05) \times 10^{-1}$	$(2.89 \pm 0.09) \times 10^{-1}$	
1.075	$(3.15 \pm 0.15) \times 10^{-2}$	$(7.47 \pm 0.33) \times 10^{-2}$	$(1.41 \pm 0.06) \times 10^{-1}$	$(2.48 \pm 0.10) \times 10^{-1}$	
1.125	$(2.68 \pm 0.14) \times 10^{-2}$	$(6.31 \pm 0.31) \times 10^{-2}$	$(1.20 \pm 0.05) \times 10^{-1}$	$(2.21 \pm 0.10) \times 10^{-1}$	
p_{\perp}	30–40%	20–30%	10–20%	5–10%	0–5%
0.375	1.26 ± 0.02	1.70 ± 0.02	2.17 ± 0.02	2.72 ± 0.03	3.11 ± 0.04
0.425	1.19 ± 0.01	1.64 ± 0.02	2.12 ± 0.02	2.62 ± 0.03	3.04 ± 0.04
0.475	1.16 ± 0.01	1.57 ± 0.02	2.07 ± 0.02	2.60 ± 0.03	2.98 ± 0.03
0.525	1.11 ± 0.01	1.53 ± 0.02	2.05 ± 0.02	2.49 ± 0.03	2.92 ± 0.03
0.575	1.05 ± 0.01	1.45 ± 0.02	1.96 ± 0.02	2.43 ± 0.03	2.87 ± 0.03
0.625	$(9.79 \pm 0.21) \times 10^{-1}$	1.37 ± 0.03	1.86 ± 0.04	2.35 ± 0.05	2.75 ± 0.06
0.675	$(9.20 \pm 0.19) \times 10^{-1}$	1.29 ± 0.03	1.77 ± 0.04	2.23 ± 0.05	2.63 ± 0.05
0.725	$(8.36 \pm 0.18) \times 10^{-1}$	1.20 ± 0.02	1.65 ± 0.03	2.09 ± 0.04	2.50 ± 0.05
0.775	$(7.77 \pm 0.16) \times 10^{-1}$	1.10 ± 0.02	1.53 ± 0.03	1.96 ± 0.04	2.33 ± 0.05
0.825	$(7.12 \pm 0.15) \times 10^{-1}$	1.05 ± 0.02	1.45 ± 0.03	1.89 ± 0.04	2.31 ± 0.05
0.875	$(6.76 \pm 0.21) \times 10^{-1}$	$(9.89 \pm 0.30) \times 10^{-1}$	1.39 ± 0.04	1.80 ± 0.06	2.07 ± 0.06
0.925	$(5.98 \pm 0.18) \times 10^{-1}$	$(8.74 \pm 0.27) \times 10^{-1}$	1.24 ± 0.04	1.65 ± 0.05	1.89 ± 0.06
0.975	$(5.25 \pm 0.16) \times 10^{-1}$	$(7.85 \pm 0.24) \times 10^{-1}$	1.14 ± 0.03	1.47 ± 0.05	1.78 ± 0.05

TABLE XXIV. (*Continued.*)

p_{\perp}	30–40%	20–30%	10–20%	5–10%	0–5%
1.025	$(4.68 \pm 0.15) \times 10^{-1}$	$(6.97 \pm 0.22) \times 10^{-1}$	$(9.97 \pm 0.31) \times 10^{-1}$	1.32 ± 0.04	1.62 ± 0.05
1.075	$(4.11 \pm 0.17) \times 10^{-1}$	$(6.32 \pm 0.26) \times 10^{-1}$	$(9.37 \pm 0.38) \times 10^{-1}$	1.23 ± 0.05	1.51 ± 0.06
1.125	$(3.70 \pm 0.15) \times 10^{-1}$	$(5.77 \pm 0.24) \times 10^{-1}$	$(8.62 \pm 0.35) \times 10^{-1}$	1.15 ± 0.05	1.36 ± 0.05

TABLE XXV. Identified proton invariant transverse momentum spectra at midrapidity ($|y| < 0.1$) in Au + Au collisions at 62.4 GeV: $d^2N/(2\pi p_{\perp} dp_{\perp} dy)$ [(GeV/c) $^{-2}$] vs p_{\perp} (GeV/c). Errors are the quadratic sum of statistical errors and point-to-point systematic errors. See Sec. V A for other systematic uncertainties including those due to proton background subtraction.

p_{\perp}	70–80%	60–70%	50–60%	40–50%
0.425	$(2.66 \pm 0.04) \times 10^{-1}$	$(5.28 \pm 0.06) \times 10^{-1}$	$(9.21 \pm 0.10) \times 10^{-1}$	1.43 ± 0.02
0.475	$(2.45 \pm 0.03) \times 10^{-1}$	$(5.25 \pm 0.06) \times 10^{-1}$	$(9.27 \pm 0.11) \times 10^{-1}$	1.43 ± 0.02
0.525	$(2.21 \pm 0.03) \times 10^{-1}$	$(4.95 \pm 0.06) \times 10^{-1}$	$(8.87 \pm 0.10) \times 10^{-1}$	1.38 ± 0.02
0.575	$(2.12 \pm 0.03) \times 10^{-1}$	$(4.69 \pm 0.06) \times 10^{-1}$	$(8.26 \pm 0.10) \times 10^{-1}$	1.32 ± 0.01
0.625	$(1.92 \pm 0.04) \times 10^{-1}$	$(4.17 \pm 0.09) \times 10^{-1}$	$(7.89 \pm 0.16) \times 10^{-1}$	1.26 ± 0.03
0.675	$(1.70 \pm 0.04) \times 10^{-1}$	$(3.90 \pm 0.08) \times 10^{-1}$	$(7.13 \pm 0.15) \times 10^{-1}$	1.17 ± 0.02
0.725	$(1.56 \pm 0.04) \times 10^{-1}$	$(3.39 \pm 0.07) \times 10^{-1}$	$(6.45 \pm 0.14) \times 10^{-1}$	1.07 ± 0.02
0.775	$(1.30 \pm 0.03) \times 10^{-1}$	$(3.03 \pm 0.07) \times 10^{-1}$	$(5.85 \pm 0.12) \times 10^{-1}$	$(9.65 \pm 0.20) \times 10^{-1}$
0.825	$(1.15 \pm 0.03) \times 10^{-1}$	$(2.72 \pm 0.06) \times 10^{-1}$	$(5.14 \pm 0.11) \times 10^{-1}$	$(8.71 \pm 0.18) \times 10^{-1}$
0.875	$(9.48 \pm 0.32) \times 10^{-2}$	$(2.21 \pm 0.07) \times 10^{-1}$	$(4.33 \pm 0.13) \times 10^{-1}$	$(7.55 \pm 0.23) \times 10^{-1}$
0.925	$(8.13 \pm 0.28) \times 10^{-2}$	$(1.95 \pm 0.06) \times 10^{-1}$	$(3.84 \pm 0.12) \times 10^{-1}$	$(6.71 \pm 0.21) \times 10^{-1}$
0.975	$(6.67 \pm 0.23) \times 10^{-2}$	$(1.69 \pm 0.05) \times 10^{-1}$	$(3.39 \pm 0.11) \times 10^{-1}$	$(5.94 \pm 0.18) \times 10^{-1}$
1.025	$(6.17 \pm 0.22) \times 10^{-2}$	$(1.47 \pm 0.05) \times 10^{-1}$	$(2.96 \pm 0.09) \times 10^{-1}$	$(5.23 \pm 0.16) \times 10^{-1}$
1.075	$(5.11 \pm 0.23) \times 10^{-2}$	$(1.24 \pm 0.05) \times 10^{-1}$	$(2.57 \pm 0.11) \times 10^{-1}$	$(4.62 \pm 0.19) \times 10^{-1}$
1.125	$(4.24 \pm 0.20) \times 10^{-2}$	$(1.05 \pm 0.05) \times 10^{-1}$	$(2.25 \pm 0.09) \times 10^{-1}$	$(4.05 \pm 0.17) \times 10^{-1}$

p_{\perp}	30–40%	20–30%	10–20%	5–10%	0–5%
0.425	2.14 ± 0.02	2.98 ± 0.03	4.22 ± 0.04	5.35 ± 0.06	6.47 ± 0.07
0.475	2.10 ± 0.02	3.00 ± 0.03	4.20 ± 0.04	5.37 ± 0.06	6.50 ± 0.07
0.525	2.07 ± 0.02	2.99 ± 0.03	4.16 ± 0.04	5.38 ± 0.06	6.44 ± 0.07
0.575	2.03 ± 0.02	2.89 ± 0.03	4.08 ± 0.04	5.27 ± 0.06	6.38 ± 0.07
0.625	1.90 ± 0.04	2.78 ± 0.06	3.93 ± 0.08	5.05 ± 0.10	6.09 ± 0.12
0.675	1.78 ± 0.04	2.62 ± 0.05	3.75 ± 0.08	4.80 ± 0.10	5.84 ± 0.12
0.725	1.66 ± 0.03	2.44 ± 0.05	3.49 ± 0.07	4.52 ± 0.09	5.49 ± 0.11
0.775	1.51 ± 0.03	2.25 ± 0.05	3.24 ± 0.07	4.21 ± 0.09	5.11 ± 0.10
0.825	1.37 ± 0.03	1.92 ± 0.04	3.01 ± 0.06	3.90 ± 0.08	4.80 ± 0.10
0.875	1.21 ± 0.04	1.74 ± 0.05	2.69 ± 0.08	3.45 ± 0.10	4.29 ± 0.13
0.925	1.09 ± 0.03	1.59 ± 0.05	2.43 ± 0.07	3.18 ± 0.10	3.90 ± 0.12
0.975	$(9.63 \pm 0.29) \times 10^{-1}$	1.44 ± 0.04	2.20 ± 0.07	2.93 ± 0.09	3.60 ± 0.11
1.025	$(8.63 \pm 0.26) \times 10^{-1}$	1.32 ± 0.04	1.98 ± 0.06	2.66 ± 0.08	3.27 ± 0.10
1.075	$(7.73 \pm 0.31) \times 10^{-1}$	1.17 ± 0.05	1.81 ± 0.07	2.41 ± 0.10	3.00 ± 0.12
1.125	$(6.85 \pm 0.27) \times 10^{-1}$	1.07 ± 0.04	1.63 ± 0.07	2.18 ± 0.09	2.69 ± 0.11

TABLE XXVI. Identified π^- invariant transverse momentum spectra at midrapidity ($|y| < 0.1$) in Au + Au collisions at 130 GeV: $d^2N/(2\pi p_{\perp} dp_{\perp} dy)$ [(GeV/c) $^{-2}$] vs p_{\perp} (GeV/c). Errors are the quadratic sum of statistical errors and point-to-point systematic errors. See Sec. V A for other systematic uncertainties.

p_{\perp}	58–85%	45–58%	34–45%	26–34%
0.225	$(2.34 \pm 0.08) \times 10^1$	$(5.88 \pm 0.16) \times 10^1$	$(9.56 \pm 0.27) \times 10^1$	$(1.45 \pm 0.04) \times 10^2$
0.275	$(1.73 \pm 0.05) \times 10^1$	$(4.52 \pm 0.12) \times 10^1$	$(7.46 \pm 0.18) \times 10^1$	$(1.05 \pm 0.03) \times 10^2$
0.325	$(1.28 \pm 0.03) \times 10^1$	$(3.37 \pm 0.07) \times 10^1$	$(5.56 \pm 0.10) \times 10^1$	$(7.98 \pm 0.14) \times 10^1$
0.375	9.11 ± 0.21	$(2.53 \pm 0.05) \times 10^1$	$(4.13 \pm 0.08) \times 10^1$	$(6.01 \pm 0.11) \times 10^1$
0.425	6.92 ± 0.17	$(1.85 \pm 0.04) \times 10^1$	$(3.22 \pm 0.06) \times 10^1$	$(4.73 \pm 0.09) \times 10^1$
0.475	5.49 ± 0.14	$(1.39 \pm 0.03) \times 10^1$	$(2.37 \pm 0.05) \times 10^1$	$(3.45 \pm 0.07) \times 10^1$

TABLE XXVI. (*Continued.*)

p_{\perp}	58–85%	45–58%	34–45%	26–34%
0.525	3.88 ± 0.11	$(1.10 \pm 0.03) \times 10^1$	$(1.90 \pm 0.04) \times 10^1$	$(2.77 \pm 0.07) \times 10^1$
0.575	3.09 ± 0.11	8.54 ± 0.29	$(1.43 \pm 0.05) \times 10^1$	$(2.09 \pm 0.07) \times 10^1$
0.625	2.32 ± 0.09	6.76 ± 0.24	$(1.13 \pm 0.04) \times 10^1$	$(1.73 \pm 0.06) \times 10^1$
0.675	1.86 ± 0.07	4.92 ± 0.18	8.56 ± 0.24	$(1.29 \pm 0.04) \times 10^1$
p_{\perp}	18–26%	11–18%	6–11%	0–6%
0.225	$(1.90 \pm 0.05) \times 10^2$	$(2.55 \pm 0.06) \times 10^2$	$(3.11 \pm 0.08) \times 10^2$	$(3.71 \pm 0.08) \times 10^2$
0.275	$(1.42 \pm 0.03) \times 10^2$	$(1.89 \pm 0.04) \times 10^2$	$(2.25 \pm 0.07) \times 10^2$	$(2.77 \pm 0.06) \times 10^2$
0.325	$(1.09 \pm 0.02) \times 10^2$	$(1.43 \pm 0.02) \times 10^2$	$(1.75 \pm 0.03) \times 10^2$	$(2.13 \pm 0.02) \times 10^2$
0.375	$(8.16 \pm 0.14) \times 10^1$	$(1.09 \pm 0.02) \times 10^2$	$(1.35 \pm 0.03) \times 10^2$	$(1.62 \pm 0.02) \times 10^2$
0.425	$(6.38 \pm 0.11) \times 10^1$	$(8.15 \pm 0.14) \times 10^1$	$(1.00 \pm 0.02) \times 10^2$	$(1.24 \pm 0.01) \times 10^2$
0.475	$(4.80 \pm 0.09) \times 10^1$	$(6.56 \pm 0.11) \times 10^1$	$(7.96 \pm 0.16) \times 10^1$	$(9.76 \pm 0.11) \times 10^1$
0.525	$(3.69 \pm 0.08) \times 10^1$	$(5.04 \pm 0.11) \times 10^1$	$(6.22 \pm 0.16) \times 10^1$	$(7.57 \pm 0.15) \times 10^1$
0.575	$(2.97 \pm 0.09) \times 10^1$	$(3.74 \pm 0.12) \times 10^1$	$(4.80 \pm 0.17) \times 10^1$	$(5.95 \pm 0.18) \times 10^1$
0.625	$(2.28 \pm 0.07) \times 10^1$	$(3.10 \pm 0.10) \times 10^1$	$(3.84 \pm 0.14) \times 10^1$	$(4.66 \pm 0.14) \times 10^1$
0.675	$(1.77 \pm 0.04) \times 10^1$	$(2.47 \pm 0.06) \times 10^1$	$(2.85 \pm 0.09) \times 10^1$	$(3.76 \pm 0.04) \times 10^1$

TABLE XXVII. Identified π^+ invariant transverse momentum spectra at midrapidity ($|y| < 0.1$) in Au + Au collisions at 130 GeV: $d^2N/(2\pi p_{\perp} dp_{\perp} dy)$ [(GeV/c) $^{-2}$] vs p_{\perp} (GeV/c). Errors are the quadratic sum of statistical errors and point-to-point systematic errors. See Sec. V A for other systematic uncertainties.

p_{\perp}	58–85%	45–58%	34–45%	26–34%
0.225	$(2.31 \pm 0.07) \times 10^1$	$(5.96 \pm 0.18) \times 10^1$	$(9.82 \pm 0.27) \times 10^1$	$(1.44 \pm 0.04) \times 10^2$
0.275	$(1.75 \pm 0.05) \times 10^1$	$(4.43 \pm 0.12) \times 10^1$	$(7.60 \pm 0.18) \times 10^1$	$(1.05 \pm 0.03) \times 10^2$
0.325	$(1.29 \pm 0.03) \times 10^1$	$(3.35 \pm 0.06) \times 10^1$	$(5.66 \pm 0.10) \times 10^1$	$(7.82 \pm 0.14) \times 10^1$
0.375	9.76 ± 0.22	$(2.60 \pm 0.05) \times 10^1$	$(4.21 \pm 0.08) \times 10^1$	$(6.06 \pm 0.11) \times 10^1$
0.425	6.97 ± 0.17	$(1.85 \pm 0.04) \times 10^1$	$(3.14 \pm 0.06) \times 10^1$	$(4.57 \pm 0.09) \times 10^1$
0.475	5.01 ± 0.14	$(1.39 \pm 0.03) \times 10^1$	$(2.40 \pm 0.05) \times 10^1$	$(3.68 \pm 0.07) \times 10^1$
0.525	4.04 ± 0.12	$(1.07 \pm 0.03) \times 10^1$	$(1.92 \pm 0.05) \times 10^1$	$(2.68 \pm 0.06) \times 10^1$
0.575	2.86 ± 0.11	8.37 ± 0.28	$(1.47 \pm 0.05) \times 10^1$	$(2.15 \pm 0.07) \times 10^1$
0.625	2.39 ± 0.09	6.38 ± 0.23	$(1.12 \pm 0.04) \times 10^1$	$(1.65 \pm 0.06) \times 10^1$
0.675	1.88 ± 0.07	4.87 ± 0.18	8.82 ± 0.23	$(1.29 \pm 0.04) \times 10^1$
p_{\perp}	18–26%	11–18%	6–11%	0–6%
0.225	$(1.85 \pm 0.05) \times 10^2$	$(2.49 \pm 0.06) \times 10^2$	$(3.01 \pm 0.09) \times 10^2$	$(3.63 \pm 0.08) \times 10^2$
0.275	$(1.43 \pm 0.03) \times 10^2$	$(1.86 \pm 0.04) \times 10^2$	$(2.27 \pm 0.06) \times 10^2$	$(2.75 \pm 0.06) \times 10^2$
0.325	$(1.08 \pm 0.02) \times 10^2$	$(1.41 \pm 0.02) \times 10^2$	$(1.80 \pm 0.03) \times 10^2$	$(2.10 \pm 0.02) \times 10^2$
0.375	$(8.25 \pm 0.14) \times 10^1$	$(1.11 \pm 0.02) \times 10^2$	$(1.31 \pm 0.03) \times 10^2$	$(1.60 \pm 0.02) \times 10^2$
0.425	$(6.26 \pm 0.11) \times 10^1$	$(8.31 \pm 0.15) \times 10^1$	$(9.76 \pm 0.23) \times 10^1$	$(1.25 \pm 0.01) \times 10^2$
0.475	$(4.89 \pm 0.09) \times 10^1$	$(6.39 \pm 0.11) \times 10^1$	$(7.94 \pm 0.16) \times 10^1$	$(9.70 \pm 0.11) \times 10^1$
0.525	$(3.71 \pm 0.09) \times 10^1$	$(5.03 \pm 0.11) \times 10^1$	$(6.29 \pm 0.17) \times 10^1$	$(7.67 \pm 0.15) \times 10^1$
0.575	$(2.90 \pm 0.09) \times 10^1$	$(3.90 \pm 0.12) \times 10^1$	$(4.71 \pm 0.17) \times 10^1$	$(5.94 \pm 0.18) \times 10^1$
0.625	$(2.29 \pm 0.08) \times 10^1$	$(3.14 \pm 0.10) \times 10^1$	$(3.83 \pm 0.14) \times 10^1$	$(4.71 \pm 0.14) \times 10^1$
0.675	$(1.77 \pm 0.05) \times 10^1$	$(2.44 \pm 0.06) \times 10^1$	$(2.98 \pm 0.11) \times 10^1$	$(3.69 \pm 0.04) \times 10^1$

TABLE XXVIII. Identified K^- invariant transverse momentum spectra at midrapidity ($|y| < 0.1$) in Au + Au collisions at 130 GeV: $d^2N/(2\pi p_{\perp} dp_{\perp} dy)$ [(GeV/c) $^{-2}$] vs p_{\perp} (GeV/c). Errors are the quadratic sum of statistical errors and point-to-point systematic errors. See Sec. V A for other systematic uncertainties. Data were published in Ref. [18].

p_{\perp}	58–85%	45–58%	34–45%	26–34%
0.175	1.93 ± 0.25	3.78 ± 0.50	7.13 ± 0.79	$(1.12 \pm 0.13) \times 10^1$
0.225	2.03 ± 0.18	4.24 ± 0.56	7.42 ± 0.61	$(1.08 \pm 0.09) \times 10^1$
0.275	1.45 ± 0.13	4.09 ± 0.33	6.52 ± 0.50	9.93 ± 0.71
0.325	1.48 ± 0.12	3.91 ± 0.30	6.09 ± 0.42	7.85 ± 0.54
0.375	1.30 ± 0.10	3.26 ± 0.23	5.46 ± 0.36	7.61 ± 0.51
0.425	1.09 ± 0.09	2.89 ± 0.21	4.58 ± 0.32	6.34 ± 0.43

TABLE XXVIII. (*Continued.*)

p_{\perp}	58–85%	45–58%	34–45%	26–34%
0.475	$(8.70 \pm 0.69) \times 10^{-1}$	2.42 ± 0.18	4.49 ± 0.32	6.40 ± 0.42
0.525	$(7.72 \pm 0.91) \times 10^{-1}$	1.98 ± 0.26	3.64 ± 0.54	5.32 ± 0.58
0.575	$(6.83 \pm 0.81) \times 10^{-1}$	2.24 ± 0.29	3.38 ± 0.38	4.58 ± 0.51
0.625	$(6.56 \pm 0.80) \times 10^{-1}$	1.77 ± 0.24	2.72 ± 0.32	4.08 ± 0.47
0.675	$(5.28 \pm 0.73) \times 10^{-1}$	1.17 ± 0.18	2.74 ± 0.35	3.08 ± 0.43
0.725	$(4.64 \pm 1.08) \times 10^{-1}$	1.34 ± 0.20	1.93 ± 0.37	2.78 ± 0.43
0.775	$(2.95 \pm 1.45) \times 10^{-1}$	$(6.56 \pm 2.20) \times 10^{-1}$	$(9.90 \pm 3.54) \times 10^{-1}$	2.32 ± 0.52
p_{\perp}	18–26%	11–18%	6–11%	0–6%
0.175	$(1.17 \pm 0.13) \times 10^1$	$(1.61 \pm 0.17) \times 10^1$	$(2.27 \pm 0.14) \times 10^1$	$(2.68 \pm 0.16) \times 10^1$
0.225	$(1.23 \pm 0.10) \times 10^1$	$(1.70 \pm 0.13) \times 10^1$	$(2.25 \pm 0.13) \times 10^1$	$(2.75 \pm 0.15) \times 10^1$
0.275	$(1.26 \pm 0.09) \times 10^1$	$(1.55 \pm 0.11) \times 10^1$	$(1.91 \pm 0.11) \times 10^1$	$(2.37 \pm 0.13) \times 10^1$
0.325	$(1.07 \pm 0.07) \times 10^1$	$(1.42 \pm 0.09) \times 10^1$	$(1.71 \pm 0.09) \times 10^1$	$(2.20 \pm 0.12) \times 10^1$
0.375	$(1.03 \pm 0.07) \times 10^1$	$(1.31 \pm 0.09) \times 10^1$	$(1.60 \pm 0.09) \times 10^1$	$(2.01 \pm 0.10) \times 10^1$
0.425	9.22 ± 0.62	$(1.12 \pm 0.07) \times 10^1$	$(1.50 \pm 0.08) \times 10^1$	$(1.85 \pm 0.10) \times 10^1$
0.475	8.28 ± 0.56	$(1.04 \pm 0.07) \times 10^1$	$(1.39 \pm 0.07) \times 10^1$	$(1.69 \pm 0.09) \times 10^1$
0.525	6.93 ± 0.63	8.65 ± 0.94	$(1.19 \pm 0.14) \times 10^1$	$(1.48 \pm 0.15) \times 10^1$
0.575	6.78 ± 1.06	8.52 ± 1.33	9.81 ± 1.51	$(1.30 \pm 0.13) \times 10^1$
0.625	6.00 ± 0.95	8.13 ± 1.29	8.89 ± 0.92	$(1.10 \pm 0.11) \times 10^1$
0.675	5.29 ± 0.89	5.77 ± 0.98	8.00 ± 0.86	8.86 ± 0.93
0.725	3.74 ± 0.57	5.69 ± 0.98	6.83 ± 0.79	8.30 ± 0.93
0.775	3.51 ± 0.68	4.43 ± 0.77	4.36 ± 1.03	6.78 ± 0.90

TABLE XXIX. Identified K^+ invariant transverse momentum spectra at midrapidity ($|y| < 0.1$) in Au + Au collisions at 130 GeV: $d^2N/(2\pi p_{\perp} dp_{\perp} dy) [(GeV/c)^{-2}]$ vs p_{\perp} (GeV/c). Errors are the quadratic sum of statistical errors and point-to-point systematic errors. See Sec. V A for other systematic uncertainties. Data were published in Ref. [18].

p_{\perp}	58–85%	45–58%	34–45%	26–34%
0.175	1.58 ± 0.22	6.26 ± 0.70	7.02 ± 0.79	$(1.19 \pm 0.12) \times 10^1$
0.225	2.14 ± 0.20	5.56 ± 0.46	8.18 ± 0.63	9.21 ± 0.74
0.275	1.90 ± 0.15	4.91 ± 0.37	7.00 ± 0.49	9.27 ± 0.69
0.325	1.38 ± 0.11	3.82 ± 0.28	6.37 ± 0.42	9.31 ± 0.62
0.375	1.32 ± 0.10	3.69 ± 0.26	5.70 ± 0.38	8.65 ± 0.55
0.425	1.06 ± 0.09	3.23 ± 0.22	5.47 ± 0.37	6.99 ± 0.46
0.475	$(9.09 \pm 0.72) \times 10^{-1}$	2.88 ± 0.22	4.55 ± 0.33	6.13 ± 0.40
0.525	$(9.23 \pm 1.06) \times 10^{-1}$	2.49 ± 0.28	3.77 ± 0.41	5.61 ± 0.61
0.575	$(7.45 \pm 0.88) \times 10^{-1}$	2.29 ± 0.26	3.91 ± 0.43	5.51 ± 0.60
0.625	$(5.90 \pm 0.79) \times 10^{-1}$	1.98 ± 0.24	3.23 ± 0.36	4.73 ± 0.54
0.675	$(6.55 \pm 0.90) \times 10^{-1}$	1.80 ± 0.28	3.09 ± 0.38	4.97 ± 0.81
0.725	$(4.52 \pm 0.87) \times 10^{-1}$	1.23 ± 0.31	2.03 ± 0.31	3.45 ± 0.57
0.775	$(2.83 \pm 0.92) \times 10^{-1}$	$(8.81 \pm 2.61) \times 10^{-1}$	2.15 ± 0.40	2.55 ± 0.54
p_{\perp}	18–26%	11–18%	6–11%	0–6%
0.175	$(1.47 \pm 0.14) \times 10^1$	$(1.82 \pm 0.18) \times 10^1$	$(2.26 \pm 0.14) \times 10^1$	$(2.99 \pm 0.17) \times 10^1$
0.225	$(1.60 \pm 0.12) \times 10^1$	$(1.89 \pm 0.14) \times 10^1$	$(2.36 \pm 0.13) \times 10^1$	$(3.02 \pm 0.16) \times 10^1$
0.275	$(1.27 \pm 0.09) \times 10^1$	$(1.74 \pm 0.12) \times 10^1$	$(2.16 \pm 0.12) \times 10^1$	$(2.58 \pm 0.14) \times 10^1$
0.325	$(1.27 \pm 0.08) \times 10^1$	$(1.51 \pm 0.10) \times 10^1$	$(1.92 \pm 0.10) \times 10^1$	$(2.45 \pm 0.13) \times 10^1$
0.375	$(1.03 \pm 0.07) \times 10^1$	$(1.37 \pm 0.09) \times 10^1$	$(1.76 \pm 0.09) \times 10^1$	$(2.19 \pm 0.11) \times 10^1$
0.425	$(1.01 \pm 0.06) \times 10^1$	$(1.34 \pm 0.09) \times 10^1$	$(1.56 \pm 0.08) \times 10^1$	$(1.99 \pm 0.10) \times 10^1$
0.475	8.13 ± 0.53	$(1.14 \pm 0.07) \times 10^1$	$(1.38 \pm 0.07) \times 10^1$	$(1.78 \pm 0.09) \times 10^1$
0.525	7.36 ± 0.79	$(1.04 \pm 0.11) \times 10^1$	$(1.22 \pm 0.12) \times 10^1$	$(1.57 \pm 0.16) \times 10^1$
0.575	7.34 ± 0.80	8.15 ± 0.89	$(1.06 \pm 0.16) \times 10^1$	$(1.43 \pm 0.14) \times 10^1$
0.625	6.17 ± 0.71	8.13 ± 0.91	9.93 ± 1.02	$(1.23 \pm 0.13) \times 10^1$
0.675	6.05 ± 0.76	7.18 ± 0.94	8.74 ± 0.94	9.78 ± 1.02
0.725	5.06 ± 0.84	5.43 ± 0.82	7.61 ± 0.87	9.10 ± 1.01
0.775	2.59 ± 0.92	4.60 ± 1.14	5.48 ± 0.79	6.28 ± 0.84

TABLE XXX. Identified \bar{p} invariant transverse momentum spectra at midrapidity ($|y| < 0.1$) in Au + Au collisions at 130 GeV: $d^2N/(2\pi p_\perp dp_\perp dy)$ [(GeV/c) $^{-2}$] vs p_\perp (GeV/c). Errors are the quadratic sum of statistical errors and point-to-point systematic errors. See Sec. V A for other systematic uncertainties. Data were published in Ref. [20].

p_\perp	58–85%	45–58%	34–45%	26–34%
0.375	$(5.05 \pm 0.29) \times 10^{-1}$	1.14 ± 0.06	1.62 ± 0.09	2.01 ± 0.11
0.425	$(4.84 \pm 0.20) \times 10^{-1}$	1.02 ± 0.04	1.56 ± 0.06	1.99 ± 0.07
0.475	$(4.37 \pm 0.13) \times 10^{-1}$	1.00 ± 0.03	1.53 ± 0.04	1.98 ± 0.05
0.525	$(4.02 \pm 0.12) \times 10^{-1}$	$(9.70 \pm 0.26) \times 10^{-1}$	1.42 ± 0.04	1.93 ± 0.05
0.575	$(3.61 \pm 0.11) \times 10^{-1}$	$(8.84 \pm 0.23) \times 10^{-1}$	1.32 ± 0.03	1.77 ± 0.04
0.625	$(3.37 \pm 0.10) \times 10^{-1}$	$(8.13 \pm 0.22) \times 10^{-1}$	1.24 ± 0.03	1.72 ± 0.04
0.675	$(3.24 \pm 0.09) \times 10^{-1}$	$(7.62 \pm 0.20) \times 10^{-1}$	1.18 ± 0.03	1.64 ± 0.04
0.725	$(2.71 \pm 0.08) \times 10^{-1}$	$(6.52 \pm 0.17) \times 10^{-1}$	1.10 ± 0.03	1.49 ± 0.03
0.775	$(2.36 \pm 0.07) \times 10^{-1}$	$(6.37 \pm 0.17) \times 10^{-1}$	1.02 ± 0.02	1.36 ± 0.03
0.825	$(2.12 \pm 0.07) \times 10^{-1}$	$(5.93 \pm 0.16) \times 10^{-1}$	$(9.12 \pm 0.22) \times 10^{-1}$	1.29 ± 0.03
0.875	$(1.95 \pm 0.06) \times 10^{-1}$	$(5.08 \pm 0.14) \times 10^{-1}$	$(8.02 \pm 0.20) \times 10^{-1}$	1.21 ± 0.03
0.925	$(1.61 \pm 0.05) \times 10^{-1}$	$(4.36 \pm 0.12) \times 10^{-1}$	$(7.40 \pm 0.19) \times 10^{-1}$	1.13 ± 0.03
0.975	$(1.45 \pm 0.05) \times 10^{-1}$	$(3.92 \pm 0.11) \times 10^{-1}$	$(6.69 \pm 0.17) \times 10^{-1}$	$(9.31 \pm 0.23) \times 10^{-1}$
<hr/>				
p_\perp	18–26%	11–18%	6–11%	0–6%
0.375	2.56 ± 0.13	3.05 ± 0.15	3.54 ± 0.12	4.24 ± 0.13
0.425	2.62 ± 0.09	3.06 ± 0.11	3.49 ± 0.07	4.25 ± 0.08
0.475	2.41 ± 0.06	2.94 ± 0.07	3.45 ± 0.04	4.14 ± 0.04
0.525	2.49 ± 0.06	2.88 ± 0.06	3.37 ± 0.03	4.08 ± 0.03
0.575	2.39 ± 0.05	2.78 ± 0.06	3.29 ± 0.03	3.92 ± 0.03
0.625	2.12 ± 0.05	2.74 ± 0.06	3.16 ± 0.03	3.84 ± 0.03
0.675	2.05 ± 0.05	2.56 ± 0.05	3.04 ± 0.03	3.67 ± 0.03
0.725	1.92 ± 0.04	2.42 ± 0.05	2.88 ± 0.03	3.49 ± 0.03
0.775	1.78 ± 0.04	2.17 ± 0.05	2.76 ± 0.03	3.31 ± 0.03
0.825	1.63 ± 0.04	2.07 ± 0.04	2.54 ± 0.03	3.09 ± 0.03
0.875	1.50 ± 0.03	1.85 ± 0.04	2.31 ± 0.02	2.89 ± 0.02
0.925	1.38 ± 0.03	1.77 ± 0.04	2.15 ± 0.02	2.72 ± 0.02
0.975	1.33 ± 0.03	1.60 ± 0.04	2.00 ± 0.02	2.50 ± 0.02

TABLE XXXI. Identified proton invariant transverse momentum spectra at midrapidity ($|y| < 0.1$) in Au + Au collisions at 130 GeV: $d^2N/(2\pi p_\perp dp_\perp dy)$ [(GeV/c) $^{-2}$] vs p_\perp (GeV/c). Errors are the quadratic sum of statistical errors, point-to-point systematic errors, and systematic uncertainties due to proton background subtraction. See Sec. V A for other systematic uncertainties. Data were published in Ref. [20].

p_\perp	58–85%	45–58%	34–45%	26–34%
0.375	$(6.40 \pm 0.66) \times 10^{-1}$	1.46 ± 0.15	2.19 ± 0.22	2.78 ± 0.28
0.425	$(5.99 \pm 0.47) \times 10^{-1}$	1.45 ± 0.11	2.07 ± 0.16	2.74 ± 0.21
0.475	$(5.54 \pm 0.32) \times 10^{-1}$	1.34 ± 0.07	1.81 ± 0.10	2.59 ± 0.14
0.525	$(5.12 \pm 0.24) \times 10^{-1}$	1.25 ± 0.05	1.87 ± 0.08	2.54 ± 0.10
0.575	$(4.50 \pm 0.21) \times 10^{-1}$	1.19 ± 0.05	1.82 ± 0.07	2.44 ± 0.10
0.625	$(4.61 \pm 0.16) \times 10^{-1}$	1.05 ± 0.03	1.65 ± 0.05	2.27 ± 0.07
0.675	$(3.72 \pm 0.13) \times 10^{-1}$	$(9.52 \pm 0.31) \times 10^{-1}$	1.57 ± 0.05	2.24 ± 0.06
0.725	$(3.51 \pm 0.12) \times 10^{-1}$	$(9.17 \pm 0.30) \times 10^{-1}$	1.47 ± 0.04	2.03 ± 0.06
0.775	$(3.09 \pm 0.08) \times 10^{-1}$	$(8.34 \pm 0.19) \times 10^{-1}$	1.38 ± 0.03	1.90 ± 0.04
0.825	$(2.79 \pm 0.08) \times 10^{-1}$	$(7.48 \pm 0.17) \times 10^{-1}$	1.23 ± 0.03	1.73 ± 0.03
0.875	$(2.43 \pm 0.07) \times 10^{-1}$	$(6.65 \pm 0.16) \times 10^{-1}$	1.10 ± 0.02	1.64 ± 0.03
0.925	$(2.02 \pm 0.06) \times 10^{-1}$	$(5.84 \pm 0.14) \times 10^{-1}$	$(9.43 \pm 0.21) \times 10^{-1}$	1.51 ± 0.03
0.975	$(1.77 \pm 0.05) \times 10^{-1}$	$(5.13 \pm 0.13) \times 10^{-1}$	$(9.62 \pm 0.21) \times 10^{-1}$	1.36 ± 0.03
<hr/>				
p_\perp	18–26%	11–18%	6–11%	0–6%
0.375	3.54 ± 0.34	4.29 ± 0.42	4.95 ± 0.41	6.01 ± 0.49
0.425	3.50 ± 0.26	4.25 ± 0.31	4.75 ± 0.28	5.73 ± 0.33
0.475	3.25 ± 0.17	4.16 ± 0.21	4.80 ± 0.19	5.69 ± 0.21

TABLE XXXI. (*Continued.*)

p_{\perp}	58–85%	45–58%	34–45%	26–34%
0.525	3.22 ± 0.13	3.96 ± 0.16	4.66 ± 0.13	5.67 ± 0.15
0.575	3.09 ± 0.12	3.89 ± 0.15	4.62 ± 0.13	5.62 ± 0.15
0.625	3.04 ± 0.09	3.70 ± 0.10	4.44 ± 0.08	5.39 ± 0.09
0.675	2.96 ± 0.08	3.53 ± 0.10	4.29 ± 0.08	5.18 ± 0.09
0.725	2.64 ± 0.08	3.28 ± 0.09	4.03 ± 0.07	4.96 ± 0.08
0.775	2.49 ± 0.05	3.11 ± 0.05	3.74 ± 0.03	4.73 ± 0.03
0.825	2.26 ± 0.04	2.96 ± 0.05	3.52 ± 0.03	4.36 ± 0.03
0.875	2.12 ± 0.04	2.62 ± 0.05	3.27 ± 0.03	4.08 ± 0.03
0.925	1.91 ± 0.04	2.41 ± 0.04	3.11 ± 0.03	3.87 ± 0.03
0.975	1.78 ± 0.04	2.32 ± 0.04	2.81 ± 0.02	3.52 ± 0.03

TABLE XXXII. Identified π^{-} invariant transverse momentum spectra at midrapidity ($|y| < 0.1$) in Au + Au collisions at 200 GeV: $d^2N/(2\pi p_{\perp} dp_{\perp} dy)$ [(GeV/c) $^{-2}$] vs p_{\perp} (GeV/c). Errors are the quadratic sum of statistical errors and point-to-point systematic errors. See Sec. V A for other systematic uncertainties. Data were published in Ref. [17].

p_{\perp}	70–80%	60–70%	50–60%	40–50%	
0.225	$(1.61 \pm 0.05) \times 10^1$	$(3.06 \pm 0.09) \times 10^1$	$(5.09 \pm 0.15) \times 10^1$	$(7.86 \pm 0.24) \times 10^1$	
0.275	$(1.16 \pm 0.02) \times 10^1$	$(2.21 \pm 0.04) \times 10^1$	$(3.69 \pm 0.07) \times 10^1$	$(5.90 \pm 0.12) \times 10^1$	
0.325	8.56 ± 0.18	$(1.63 \pm 0.03) \times 10^1$	$(2.79 \pm 0.06) \times 10^1$	$(4.48 \pm 0.09) \times 10^1$	
0.375	6.46 ± 0.08	$(1.25 \pm 0.01) \times 10^1$	$(2.12 \pm 0.02) \times 10^1$	$(3.45 \pm 0.04) \times 10^1$	
0.425	4.82 ± 0.06	9.41 ± 0.10	$(1.62 \pm 0.02) \times 10^1$	$(2.63 \pm 0.03) \times 10^1$	
0.475	3.69 ± 0.05	7.17 ± 0.08	$(1.25 \pm 0.01) \times 10^1$	$(2.05 \pm 0.02) \times 10^1$	
0.525	2.73 ± 0.04	5.56 ± 0.06	9.75 ± 0.11	$(1.59 \pm 0.02) \times 10^1$	
0.575	2.13 ± 0.03	4.31 ± 0.06	7.63 ± 0.11	$(1.24 \pm 0.02) \times 10^1$	
0.625	1.65 ± 0.04	3.38 ± 0.08	5.96 ± 0.14	9.69 ± 0.24	
0.675	1.27 ± 0.03	2.63 ± 0.06	4.64 ± 0.11	7.61 ± 0.19	
0.725	$(9.77 \pm 0.33) \times 10^{-1}$	2.04 ± 0.07	3.65 ± 0.12	6.02 ± 0.21	
0.775	$(7.85 \pm 0.29) \times 10^{-1}$	1.57 ± 0.06	2.86 ± 0.10	4.81 ± 0.17	
p_{\perp}	30–40%	20–30%	10–20%	5–10%	0–5%
0.225	$(1.24 \pm 0.04) \times 10^2$	$(1.74 \pm 0.05) \times 10^2$	$(2.46 \pm 0.07) \times 10^2$	$(3.27 \pm 0.10) \times 10^2$	$(4.10 \pm 0.12) \times 10^2$
0.275	$(8.93 \pm 0.18) \times 10^1$	$(1.32 \pm 0.03) \times 10^2$	$(1.86 \pm 0.04) \times 10^2$	$(2.46 \pm 0.05) \times 10^2$	$(3.05 \pm 0.06) \times 10^2$
0.325	$(6.77 \pm 0.14) \times 10^1$	$(1.02 \pm 0.02) \times 10^2$	$(1.45 \pm 0.03) \times 10^2$	$(1.92 \pm 0.04) \times 10^2$	$(2.39 \pm 0.05) \times 10^2$
0.375	$(5.18 \pm 0.05) \times 10^1$	$(7.91 \pm 0.08) \times 10^1$	$(1.13 \pm 0.01) \times 10^2$	$(1.50 \pm 0.01) \times 10^2$	$(1.88 \pm 0.02) \times 10^2$
0.425	$(4.01 \pm 0.04) \times 10^1$	$(6.13 \pm 0.06) \times 10^1$	$(8.84 \pm 0.09) \times 10^1$	$(1.18 \pm 0.01) \times 10^2$	$(1.47 \pm 0.01) \times 10^2$
0.475	$(3.13 \pm 0.03) \times 10^1$	$(4.76 \pm 0.05) \times 10^1$	$(6.90 \pm 0.07) \times 10^1$	$(9.18 \pm 0.09) \times 10^1$	$(1.15 \pm 0.01) \times 10^2$
0.525	$(2.45 \pm 0.03) \times 10^1$	$(3.72 \pm 0.04) \times 10^1$	$(5.41 \pm 0.06) \times 10^1$	$(7.22 \pm 0.07) \times 10^1$	$(9.07 \pm 0.09) \times 10^1$
0.575	$(1.91 \pm 0.03) \times 10^1$	$(2.94 \pm 0.05) \times 10^1$	$(4.27 \pm 0.07) \times 10^1$	$(5.68 \pm 0.10) \times 10^1$	$(7.20 \pm 0.14) \times 10^1$
0.625	$(1.50 \pm 0.04) \times 10^1$	$(2.32 \pm 0.06) \times 10^1$	$(3.37 \pm 0.09) \times 10^1$	$(4.50 \pm 0.13) \times 10^1$	$(5.67 \pm 0.17) \times 10^1$
0.675	$(1.19 \pm 0.03) \times 10^1$	$(1.82 \pm 0.05) \times 10^1$	$(2.67 \pm 0.07) \times 10^1$	$(3.55 \pm 0.10) \times 10^1$	$(4.48 \pm 0.13) \times 10^1$
0.725	9.55 ± 0.34	$(1.45 \pm 0.05) \times 10^1$	$(2.13 \pm 0.08) \times 10^1$	$(2.83 \pm 0.11) \times 10^1$	$(3.57 \pm 0.14) \times 10^1$
0.775	7.58 ± 0.27	$(1.16 \pm 0.04) \times 10^1$			

TABLE XXXIII. Identified π^{+} invariant transverse momentum spectra at midrapidity ($|y| < 0.1$) in Au + Au collisions at 200 GeV: $d^2N/(2\pi p_{\perp} dp_{\perp} dy)$ [(GeV/c) $^{-2}$] vs p_{\perp} (GeV/c). Errors are the quadratic sum of statistical errors and point-to-point systematic errors. See Sec. V A for other systematic uncertainties. Data were published in Ref. [17].

p_{\perp}	70–80%	60–70%	50–60%	40–50%
0.225	$(1.62 \pm 0.05) \times 10^1$	$(3.05 \pm 0.09) \times 10^1$	$(5.05 \pm 0.15) \times 10^1$	$(7.85 \pm 0.24) \times 10^1$
0.275	$(1.15 \pm 0.02) \times 10^1$	$(2.20 \pm 0.04) \times 10^1$	$(3.69 \pm 0.07) \times 10^1$	$(5.85 \pm 0.12) \times 10^1$
0.325	8.57 ± 0.18	$(1.64 \pm 0.03) \times 10^1$	$(2.78 \pm 0.06) \times 10^1$	$(4.45 \pm 0.09) \times 10^1$
0.375	6.38 ± 0.08	$(1.23 \pm 0.01) \times 10^1$	$(2.12 \pm 0.02) \times 10^1$	$(3.44 \pm 0.04) \times 10^1$
0.425	4.80 ± 0.06	9.45 ± 0.10	$(1.63 \pm 0.02) \times 10^1$	$(2.63 \pm 0.03) \times 10^1$
0.475	3.66 ± 0.05	7.22 ± 0.08	$(1.25 \pm 0.01) \times 10^1$	$(2.03 \pm 0.02) \times 10^1$

TABLE XXXIII. (*Continued.*)

p_{\perp}	70–80%	60–70%	50–60%	40–50%	
0.525	2.81 ± 0.04	5.52 ± 0.06	9.66 ± 0.10	$(1.59 \pm 0.02) \times 10^1$	
0.575	2.15 ± 0.03	4.30 ± 0.06	7.57 ± 0.10	$(1.24 \pm 0.02) \times 10^1$	
0.625	1.66 ± 0.04	3.29 ± 0.08	5.95 ± 0.14	9.73 ± 0.24	
0.675	1.29 ± 0.03	2.58 ± 0.06	4.66 ± 0.11	7.65 ± 0.19	
0.725	$(9.97 \pm 0.34) \times 10^{-1}$	2.09 ± 0.07	3.62 ± 0.12	6.03 ± 0.21	
0.775	$(7.84 \pm 0.29) \times 10^{-1}$	1.61 ± 0.06	2.91 ± 0.10	4.76 ± 0.17	
p_{\perp}	30–40%	20–30%	10–20%	5–10%	0–5%
0.225	$(1.24 \pm 0.04) \times 10^2$	$(1.74 \pm 0.05) \times 10^2$	$(2.42 \pm 0.07) \times 10^2$	$(3.24 \pm 0.10) \times 10^2$	$(4.03 \pm 0.12) \times 10^2$
0.275	$(8.84 \pm 0.18) \times 10^1$	$(1.30 \pm 0.03) \times 10^2$	$(1.82 \pm 0.04) \times 10^2$	$(2.41 \pm 0.05) \times 10^2$	$(2.98 \pm 0.06) \times 10^2$
0.325	$(6.67 \pm 0.13) \times 10^1$	$(1.00 \pm 0.02) \times 10^2$	$(1.42 \pm 0.03) \times 10^2$	$(1.88 \pm 0.04) \times 10^2$	$(2.33 \pm 0.05) \times 10^2$
0.375	$(5.15 \pm 0.05) \times 10^1$	$(7.80 \pm 0.08) \times 10^1$	$(1.11 \pm 0.01) \times 10^2$	$(1.47 \pm 0.01) \times 10^2$	$(1.84 \pm 0.02) \times 10^2$
0.425	$(4.00 \pm 0.04) \times 10^1$	$(6.08 \pm 0.06) \times 10^1$	$(8.71 \pm 0.09) \times 10^1$	$(1.16 \pm 0.01) \times 10^2$	$(1.45 \pm 0.01) \times 10^2$
0.475	$(3.12 \pm 0.03) \times 10^1$	$(4.73 \pm 0.05) \times 10^1$	$(6.84 \pm 0.07) \times 10^1$	$(9.05 \pm 0.09) \times 10^1$	$(1.14 \pm 0.01) \times 10^2$
0.525	$(2.44 \pm 0.03) \times 10^1$	$(3.71 \pm 0.04) \times 10^1$	$(5.38 \pm 0.06) \times 10^1$	$(7.16 \pm 0.07) \times 10^1$	$(9.00 \pm 0.09) \times 10^1$
0.575	$(1.92 \pm 0.03) \times 10^1$	$(2.92 \pm 0.05) \times 10^1$	$(4.25 \pm 0.07) \times 10^1$	$(5.63 \pm 0.10) \times 10^1$	$(7.11 \pm 0.14) \times 10^1$
0.625	$(1.51 \pm 0.04) \times 10^1$	$(2.30 \pm 0.06) \times 10^1$	$(3.34 \pm 0.09) \times 10^1$	$(4.46 \pm 0.13) \times 10^1$	$(5.61 \pm 0.16) \times 10^1$
0.675	$(1.19 \pm 0.03) \times 10^1$	$(1.81 \pm 0.05) \times 10^1$	$(2.65 \pm 0.07) \times 10^1$	$(3.50 \pm 0.10) \times 10^1$	$(4.43 \pm 0.13) \times 10^1$
0.725	9.44 ± 0.33	$(1.44 \pm 0.05) \times 10^1$	$(2.13 \pm 0.08) \times 10^1$	$(2.81 \pm 0.11) \times 10^1$	$(3.58 \pm 0.14) \times 10^1$
0.775	7.62 ± 0.27	$(1.16 \pm 0.04) \times 10^1$			

TABLE XXXIV. Identified K^- invariant transverse momentum spectra at midrapidity ($|y| < 0.1$) in Au + Au collisions at 200 GeV: $d^2N/(2\pi p_{\perp} dp_{\perp} dy)$ [(GeV/c) $^{-2}$] vs p_{\perp} (GeV/c). Errors are the quadratic sum of statistical errors and point-to-point systematic errors. See Sec. V A for other systematic uncertainties. Data were published in Ref. [17].

p_{\perp}	70–80%	60–70%	50–60%	40–50%	
0.225	1.35 ± 0.11	2.34 ± 0.17	3.77 ± 0.27	6.47 ± 0.47	
0.275	1.14 ± 0.05	2.18 ± 0.08	3.49 ± 0.12	5.66 ± 0.18	
0.325	$(9.22 \pm 0.25) \times 10^{-1}$	1.89 ± 0.04	3.05 ± 0.06	4.79 ± 0.09	
0.375	$(7.44 \pm 0.24) \times 10^{-1}$	1.61 ± 0.04	2.83 ± 0.07	4.31 ± 0.11	
0.425	$(6.63 \pm 0.27) \times 10^{-1}$	1.37 ± 0.05	2.38 ± 0.09	3.66 ± 0.15	
0.475	$(5.57 \pm 0.59) \times 10^{-1}$	1.14 ± 0.12	2.11 ± 0.23	3.26 ± 0.35	
0.525	$(4.78 \pm 0.50) \times 10^{-1}$	$(9.60 \pm 1.00) \times 10^{-1}$	1.81 ± 0.19	2.80 ± 0.30	
0.575	$(4.35 \pm 0.46) \times 10^{-1}$	$(8.78 \pm 0.93) \times 10^{-1}$	1.55 ± 0.17	2.54 ± 0.28	
0.625	$(3.61 \pm 0.28) \times 10^{-1}$	$(7.16 \pm 0.54) \times 10^{-1}$	1.34 ± 0.10	2.17 ± 0.16	
0.675	$(2.81 \pm 0.23) \times 10^{-1}$	$(5.63 \pm 0.46) \times 10^{-1}$	1.13 ± 0.09	1.86 ± 0.16	
0.725	$(2.41 \pm 0.28) \times 10^{-1}$	$(4.73 \pm 0.53) \times 10^{-1}$	$(9.60 \pm 1.10) \times 10^{-1}$	1.58 ± 0.18	
p_{\perp}	30–40%	20–30%	10–20%	5–10%	0–5%
0.225	9.54 ± 0.68	$(1.16 \pm 0.08) \times 10^1$	$(1.68 \pm 0.12) \times 10^1$	$(2.20 \pm 0.16) \times 10^1$	$(2.63 \pm 0.19) \times 10^1$
0.275	8.01 ± 0.25	$(1.09 \pm 0.03) \times 10^1$	$(1.56 \pm 0.05) \times 10^1$	$(2.06 \pm 0.06) \times 10^1$	$(2.47 \pm 0.08) \times 10^1$
0.325	7.03 ± 0.12	$(1.02 \pm 0.02) \times 10^1$	$(1.44 \pm 0.03) \times 10^1$	$(1.92 \pm 0.04) \times 10^1$	$(2.27 \pm 0.05) \times 10^1$
0.375	6.38 ± 0.17	9.31 ± 0.25	$(1.32 \pm 0.04) \times 10^1$	$(1.77 \pm 0.05) \times 10^1$	$(2.11 \pm 0.06) \times 10^1$
0.425	5.80 ± 0.24	8.42 ± 0.36	$(1.22 \pm 0.05) \times 10^1$	$(1.59 \pm 0.07) \times 10^1$	$(1.98 \pm 0.10) \times 10^1$
0.475	5.23 ± 0.58	7.53 ± 0.85	$(1.09 \pm 0.12) \times 10^1$	$(1.44 \pm 0.17) \times 10^1$	$(1.77 \pm 0.21) \times 10^1$
0.525	4.55 ± 0.50	6.73 ± 0.76	9.80 ± 1.10	$(1.31 \pm 0.15) \times 10^1$	$(1.58 \pm 0.19) \times 10^1$
0.575	4.14 ± 0.46	6.03 ± 0.68	8.80 ± 1.00	$(1.18 \pm 0.14) \times 10^1$	$(1.47 \pm 0.17) \times 10^1$
0.625	3.42 ± 0.27	5.35 ± 0.41	7.91 ± 0.61	$(1.06 \pm 0.08) \times 10^1$	$(1.27 \pm 0.10) \times 10^1$
0.675	2.93 ± 0.25	4.68 ± 0.42	6.45 ± 0.59	8.58 ± 0.82	$(1.08 \pm 0.11) \times 10^1$
0.725	2.50 ± 0.28	3.65 ± 0.42	5.21 ± 0.61		

TABLE XXXV. Identified K^+ invariant transverse momentum spectra at midrapidity ($|y| < 0.1$) in Au + Au collisions at 200 GeV: $d^2N/(2\pi p_\perp dp_\perp dy)$ [(GeV/c) $^{-2}$] vs p_\perp (GeV/c). Errors are the quadratic sum of statistical errors and point-to-point systematic errors. See Sec. V A for other systematic uncertainties. Data were published in Ref. [17].

p_\perp	70–80%	60–70%	50–60%	40–50%	
0.225	1.31 ± 0.10	2.43 ± 0.18	3.95 ± 0.29	6.69 ± 0.48	
0.275	1.08 ± 0.04	2.22 ± 0.08	3.65 ± 0.12	5.79 ± 0.19	
0.325	$(9.40 \pm 0.25) \times 10^{-1}$	1.90 ± 0.04	3.17 ± 0.06	5.02 ± 0.09	
0.375	$(7.82 \pm 0.24) \times 10^{-1}$	1.66 ± 0.05	2.94 ± 0.08	4.39 ± 0.11	
0.425	$(6.79 \pm 0.27) \times 10^{-1}$	1.43 ± 0.05	2.56 ± 0.10	3.85 ± 0.15	
0.475	$(5.78 \pm 0.61) \times 10^{-1}$	1.19 ± 0.13	2.20 ± 0.24	3.46 ± 0.38	
0.525	$(4.80 \pm 0.51) \times 10^{-1}$	1.04 ± 0.11	1.91 ± 0.20	2.98 ± 0.32	
0.575	$(4.27 \pm 0.45) \times 10^{-1}$	$(8.66 \pm 0.91) \times 10^{-1}$	1.64 ± 0.18	2.65 ± 0.29	
0.625	$(3.80 \pm 0.29) \times 10^{-1}$	$(7.26 \pm 0.54) \times 10^{-1}$	1.41 ± 0.10	2.25 ± 0.17	
0.675	$(3.24 \pm 0.26) \times 10^{-1}$	$(6.11 \pm 0.49) \times 10^{-1}$	1.11 ± 0.09	1.93 ± 0.16	
0.725	$(2.49 \pm 0.29) \times 10^{-1}$	$(4.88 \pm 0.55) \times 10^{-1}$	$(9.50 \pm 1.10) \times 10^{-1}$	1.56 ± 0.17	
p_\perp	30–40%	20–30%	10–20%	5–10%	0–5%
0.225	9.84 ± 0.70	$(1.21 \pm 0.09) \times 10^1$	$(1.72 \pm 0.12) \times 10^1$	$(2.31 \pm 0.16) \times 10^1$	$(2.73 \pm 0.19) \times 10^1$
0.275	8.11 ± 0.26	$(1.15 \pm 0.04) \times 10^1$	$(1.65 \pm 0.05) \times 10^1$	$(2.09 \pm 0.06) \times 10^1$	$(2.54 \pm 0.08) \times 10^1$
0.325	7.27 ± 0.13	$(1.06 \pm 0.02) \times 10^1$	$(1.50 \pm 0.03) \times 10^1$	$(1.97 \pm 0.04) \times 10^1$	$(2.39 \pm 0.05) \times 10^1$
0.375	6.71 ± 0.18	9.70 ± 0.26	$(1.38 \pm 0.04) \times 10^1$	$(1.80 \pm 0.05) \times 10^1$	$(2.22 \pm 0.07) \times 10^1$
0.425	5.91 ± 0.24	8.73 ± 0.37	$(1.27 \pm 0.06) \times 10^1$	$(1.68 \pm 0.08) \times 10^1$	$(2.05 \pm 0.10) \times 10^1$
0.475	5.46 ± 0.60	7.97 ± 0.89	$(1.14 \pm 0.13) \times 10^1$	$(1.49 \pm 0.17) \times 10^1$	$(1.81 \pm 0.21) \times 10^1$
0.525	4.75 ± 0.52	7.05 ± 0.79	$(1.01 \pm 0.11) \times 10^1$	$(1.34 \pm 0.16) \times 10^1$	$(1.65 \pm 0.20) \times 10^1$
0.575	4.20 ± 0.46	6.29 ± 0.71	9.20 ± 1.00	$(1.22 \pm 0.14) \times 10^1$	$(1.48 \pm 0.18) \times 10^1$
0.625	3.42 ± 0.27	5.55 ± 0.42	8.14 ± 0.63	$(1.05 \pm 0.08) \times 10^1$	$(1.31 \pm 0.10) \times 10^1$
0.675	3.10 ± 0.27	4.71 ± 0.42	6.77 ± 0.62	8.91 ± 0.85	$(1.08 \pm 0.11) \times 10^1$
0.725	2.61 ± 0.29	3.79 ± 0.43	5.39 ± 0.63		

TABLE XXXVI. Identified \bar{p} invariant transverse momentum spectra at midrapidity ($|y| < 0.1$) in Au + Au collisions at 200 GeV: $d^2N/(2\pi p_\perp dp_\perp dy)$ [(GeV/c) $^{-2}$] vs p_\perp (GeV/c). Errors are the quadratic sum of statistical errors and point-to-point systematic errors. See Sec. V A for other systematic uncertainties. Data were published in Ref. [17].

p_\perp	70–80%	60–70%	50–60%	40–50%	
0.375	$(3.63 \pm 0.12) \times 10^{-1}$	$(6.68 \pm 0.19) \times 10^{-1}$	$(9.92 \pm 0.26) \times 10^{-1}$	1.48 ± 0.04	
0.425	$(3.42 \pm 0.10) \times 10^{-1}$	$(6.23 \pm 0.14) \times 10^{-1}$	$(9.31 \pm 0.18) \times 10^{-1}$	1.37 ± 0.02	
0.476	$(3.27 \pm 0.09) \times 10^{-1}$	$(5.72 \pm 0.12) \times 10^{-1}$	$(8.74 \pm 0.16) \times 10^{-1}$	1.31 ± 0.02	
0.525	$(2.86 \pm 0.08) \times 10^{-1}$	$(5.19 \pm 0.11) \times 10^{-1}$	$(8.32 \pm 0.15) \times 10^{-1}$	1.21 ± 0.02	
0.574	$(2.61 \pm 0.07) \times 10^{-1}$	$(4.80 \pm 0.10) \times 10^{-1}$	$(7.95 \pm 0.14) \times 10^{-1}$	1.16 ± 0.02	
0.624	$(2.27 \pm 0.07) \times 10^{-1}$	$(4.27 \pm 0.09) \times 10^{-1}$	$(7.22 \pm 0.13) \times 10^{-1}$	1.06 ± 0.02	
0.675	$(2.09 \pm 0.06) \times 10^{-1}$	$(3.73 \pm 0.09) \times 10^{-1}$	$(6.43 \pm 0.13) \times 10^{-1}$	$(9.95 \pm 0.19) \times 10^{-1}$	
0.725	$(1.79 \pm 0.06) \times 10^{-1}$	$(3.48 \pm 0.10) \times 10^{-1}$	$(5.97 \pm 0.15) \times 10^{-1}$	$(9.36 \pm 0.22) \times 10^{-1}$	
0.775	$(1.52 \pm 0.05) \times 10^{-1}$	$(3.03 \pm 0.09) \times 10^{-1}$	$(5.37 \pm 0.14) \times 10^{-1}$	$(8.47 \pm 0.20) \times 10^{-1}$	
0.824	$(1.39 \pm 0.05) \times 10^{-1}$	$(2.64 \pm 0.08) \times 10^{-1}$	$(4.83 \pm 0.12) \times 10^{-1}$	$(7.72 \pm 0.18) \times 10^{-1}$	
0.875	$(1.12 \pm 0.04) \times 10^{-1}$	$(2.44 \pm 0.07) \times 10^{-1}$	$(4.35 \pm 0.11) \times 10^{-1}$	$(6.91 \pm 0.17) \times 10^{-1}$	
0.924	$(1.08 \pm 0.04) \times 10^{-1}$	$(2.16 \pm 0.07) \times 10^{-1}$	$(3.92 \pm 0.11) \times 10^{-1}$	$(6.14 \pm 0.17) \times 10^{-1}$	
0.975	$(9.16 \pm 0.37) \times 10^{-2}$	$(1.84 \pm 0.06) \times 10^{-1}$	$(3.42 \pm 0.10) \times 10^{-1}$	$(5.67 \pm 0.16) \times 10^{-1}$	
1.025	$(7.49 \pm 0.34) \times 10^{-2}$	$(1.64 \pm 0.06) \times 10^{-1}$	$(3.15 \pm 0.11) \times 10^{-1}$	$(5.12 \pm 0.17) \times 10^{-1}$	
1.075	$(6.92 \pm 0.34) \times 10^{-2}$	$(1.39 \pm 0.06) \times 10^{-1}$	$(2.69 \pm 0.10) \times 10^{-1}$	$(4.62 \pm 0.16) \times 10^{-1}$	
1.125	$(5.74 \pm 0.32) \times 10^{-2}$	$(1.24 \pm 0.06) \times 10^{-1}$	$(2.39 \pm 0.10) \times 10^{-1}$	$(4.00 \pm 0.16) \times 10^{-1}$	
1.175	$(5.10 \pm 0.39) \times 10^{-2}$	$(1.11 \pm 0.06) \times 10^{-1}$	$(2.17 \pm 0.11) \times 10^{-1}$	$(3.53 \pm 0.17) \times 10^{-1}$	
p_\perp	30–40%	20–30%	10–20%	5–10%	0–5%
0.375	1.95 ± 0.05	2.69 ± 0.06	3.44 ± 0.08	4.41 ± 0.10	5.08 ± 0.12
0.425	1.83 ± 0.03	2.54 ± 0.04	3.31 ± 0.04	4.17 ± 0.06	4.88 ± 0.07
0.476	1.81 ± 0.03	2.45 ± 0.03	3.23 ± 0.04	4.04 ± 0.06	4.84 ± 0.07

TABLE XXXVI. (*Continued.*)

p_{\perp}	70–80%	60–70%	50–60%	40–50%	
0.525	1.76 ± 0.03	2.34 ± 0.03	3.15 ± 0.04	3.95 ± 0.05	4.68 ± 0.06
0.574	1.63 ± 0.02	2.27 ± 0.03	3.06 ± 0.04	3.79 ± 0.05	4.61 ± 0.06
0.624	1.54 ± 0.02	2.15 ± 0.03	2.93 ± 0.04	3.77 ± 0.05	4.37 ± 0.06
0.675	1.47 ± 0.03	2.06 ± 0.04	2.80 ± 0.05	3.60 ± 0.07	4.29 ± 0.09
0.725	1.36 ± 0.03	1.91 ± 0.04	2.65 ± 0.06	3.35 ± 0.07	4.01 ± 0.09
0.775	1.22 ± 0.03	1.79 ± 0.04	2.50 ± 0.05	3.16 ± 0.07	3.82 ± 0.08
0.824	1.15 ± 0.03	1.67 ± 0.04	2.30 ± 0.05	3.06 ± 0.07	3.66 ± 0.08
0.875	1.04 ± 0.02	1.56 ± 0.03	2.18 ± 0.05	2.88 ± 0.06	3.50 ± 0.08
0.924	$(9.70 \pm 0.27) \times 10^{-1}$	1.41 ± 0.04	2.00 ± 0.06	2.60 ± 0.08	3.17 ± 0.10
0.975	$(8.81 \pm 0.24) \times 10^{-1}$	1.32 ± 0.04	1.85 ± 0.05	2.42 ± 0.07	2.99 ± 0.09
1.025	$(7.86 \pm 0.25) \times 10^{-1}$	1.21 ± 0.04	1.72 ± 0.05	2.28 ± 0.07	2.81 ± 0.09
1.075	$(7.07 \pm 0.23) \times 10^{-1}$	1.10 ± 0.04	1.58 ± 0.05	2.09 ± 0.07	2.60 ± 0.09
1.125	$(6.50 \pm 0.25) \times 10^{-1}$	1.01 ± 0.04	1.48 ± 0.06	1.91 ± 0.08	2.43 ± 0.11
1.175	$(6.06 \pm 0.28) \times 10^{-1}$	$(9.05 \pm 0.41) \times 10^{-1}$	1.39 ± 0.06	1.78 ± 0.09	2.22 ± 0.12

TABLE XXXVII. Identified proton invariant transverse momentum spectra at midrapidity ($|y| < 0.1$) in Au + Au collisions at 200 GeV: $d^2N/(2\pi p_{\perp} dp_{\perp} dy)$ $[(\text{GeV}/c)^{-2}]$ vs p_{\perp} (GeV/c). Errors are the quadratic sum of statistical errors, point-to-point systematic errors, and systematic uncertainties due to proton background subtraction. See Sec. V A for other systematic uncertainties. Data were published in Ref. [17].

p_{\perp}	70–80%	60–70%	50–60%	40–50%	
0.425	$(3.87 \pm 0.20) \times 10^{-1}$	$(7.12 \pm 0.36) \times 10^{-1}$	1.17 ± 0.06	1.65 ± 0.08	
0.476	$(3.62 \pm 0.16) \times 10^{-1}$	$(6.65 \pm 0.27) \times 10^{-1}$	1.11 ± 0.04	1.61 ± 0.06	
0.525	$(3.43 \pm 0.13) \times 10^{-1}$	$(6.31 \pm 0.22) \times 10^{-1}$	1.01 ± 0.03	1.54 ± 0.05	
0.574	$(3.08 \pm 0.10) \times 10^{-1}$	$(5.56 \pm 0.16) \times 10^{-1}$	$(9.46 \pm 0.26) \times 10^{-1}$	1.46 ± 0.04	
0.624	$(2.64 \pm 0.08) \times 10^{-1}$	$(5.10 \pm 0.13) \times 10^{-1}$	$(8.50 \pm 0.20) \times 10^{-1}$	1.34 ± 0.03	
0.675	$(2.37 \pm 0.07) \times 10^{-1}$	$(4.46 \pm 0.11) \times 10^{-1}$	$(7.85 \pm 0.18) \times 10^{-1}$	1.25 ± 0.03	
0.725	$(2.15 \pm 0.07) \times 10^{-1}$	$(4.03 \pm 0.11) \times 10^{-1}$	$(7.11 \pm 0.18) \times 10^{-1}$	1.13 ± 0.03	
0.775	$(1.87 \pm 0.06) \times 10^{-1}$	$(3.71 \pm 0.10) \times 10^{-1}$	$(6.34 \pm 0.16) \times 10^{-1}$	1.03 ± 0.02	
0.824	$(1.63 \pm 0.05) \times 10^{-1}$	$(3.17 \pm 0.09) \times 10^{-1}$	$(5.79 \pm 0.14) \times 10^{-1}$	$(9.62 \pm 0.22) \times 10^{-1}$	
0.875	$(1.46 \pm 0.05) \times 10^{-1}$	$(2.84 \pm 0.08) \times 10^{-1}$	$(5.28 \pm 0.13) \times 10^{-1}$	$(8.71 \pm 0.20) \times 10^{-1}$	
0.924	$(1.26 \pm 0.04) \times 10^{-1}$	$(2.56 \pm 0.08) \times 10^{-1}$	$(4.93 \pm 0.13) \times 10^{-1}$	$(7.86 \pm 0.21) \times 10^{-1}$	
0.975	$(1.07 \pm 0.04) \times 10^{-1}$	$(2.29 \pm 0.07) \times 10^{-1}$	$(4.28 \pm 0.12) \times 10^{-1}$	$(7.12 \pm 0.19) \times 10^{-1}$	
1.025	$(9.88 \pm 0.43) \times 10^{-2}$	$(2.14 \pm 0.08) \times 10^{-1}$	$(3.89 \pm 0.13) \times 10^{-1}$	$(6.53 \pm 0.21) \times 10^{-1}$	
1.075	$(8.37 \pm 0.38) \times 10^{-2}$	$(1.76 \pm 0.07) \times 10^{-1}$	$(3.38 \pm 0.12) \times 10^{-1}$	$(5.81 \pm 0.19) \times 10^{-1}$	
1.125	$(7.00 \pm 0.36) \times 10^{-2}$	$(1.60 \pm 0.07) \times 10^{-1}$	$(3.14 \pm 0.12) \times 10^{-1}$	$(5.24 \pm 0.20) \times 10^{-1}$	
1.175	$(6.18 \pm 0.40) \times 10^{-2}$	$(1.38 \pm 0.07) \times 10^{-1}$	$(2.82 \pm 0.14) \times 10^{-1}$	$(4.76 \pm 0.21) \times 10^{-1}$	
p_{\perp}	30–40%	20–30%	10–20%	5–10%	0–5%
0.425	2.33 ± 0.11	3.34 ± 0.16	4.21 ± 0.20	5.70 ± 0.28	6.42 ± 0.31
0.476	2.31 ± 0.09	3.26 ± 0.13	4.28 ± 0.17	5.62 ± 0.22	6.45 ± 0.25
0.525	2.17 ± 0.07	3.13 ± 0.10	4.12 ± 0.13	5.38 ± 0.17	6.18 ± 0.20
0.574	2.07 ± 0.05	2.99 ± 0.08	3.97 ± 0.10	5.09 ± 0.13	5.96 ± 0.16
0.624	1.91 ± 0.04	2.79 ± 0.06	3.77 ± 0.08	4.89 ± 0.11	5.75 ± 0.13
0.675	1.78 ± 0.04	2.63 ± 0.06	3.58 ± 0.08	4.56 ± 0.11	5.44 ± 0.13
0.725	1.67 ± 0.04	2.42 ± 0.06	3.32 ± 0.08	4.30 ± 0.10	5.07 ± 0.12
0.775	1.54 ± 0.04	2.23 ± 0.05	3.13 ± 0.07	4.09 ± 0.09	4.89 ± 0.11
0.824	1.40 ± 0.03	2.11 ± 0.05	2.93 ± 0.06	3.83 ± 0.08	4.67 ± 0.10
0.875	1.30 ± 0.03	1.94 ± 0.04	2.78 ± 0.06	3.66 ± 0.08	4.44 ± 0.09
0.924	1.18 ± 0.03	1.82 ± 0.05	2.59 ± 0.07	3.42 ± 0.10	4.16 ± 0.13
0.975	1.09 ± 0.03	1.66 ± 0.05	2.37 ± 0.07	3.17 ± 0.09	3.95 ± 0.12
1.025	$(9.97 \pm 0.32) \times 10^{-1}$	1.53 ± 0.05	2.21 ± 0.07	2.95 ± 0.09	3.68 ± 0.12
1.075	$(8.82 \pm 0.28) \times 10^{-1}$	1.38 ± 0.04	2.06 ± 0.06	2.71 ± 0.09	3.36 ± 0.11
1.125	$(8.21 \pm 0.31) \times 10^{-1}$	1.27 ± 0.05	1.85 ± 0.07	2.57 ± 0.10	3.24 ± 0.14
1.175	$(7.36 \pm 0.32) \times 10^{-1}$	1.16 ± 0.05	1.70 ± 0.07	2.34 ± 0.11	2.89 ± 0.14

- [1] E. V. Shuryak, Phys. Lett. **B78**, 150 (1978); Sov. J. Nucl. Phys. **28**, 408 (1978); Yad. Fiz. **28**, 796 (1978).
- [2] J. D. Bjorken, Phys. Rev. D **27**, 140 (1983).
- [3] F. Karsch, Nucl. Phys. **A698**, 199c (2002).
- [4] S. A. Bass *et al.*, Nucl. Phys. **A661**, 205 (1999).
- [5] L. Molnar, Ph.D. thesis (Purdue University, 2006), arXiv:0805.3086.
- [6] J. Adams *et al.* (STAR Collaboration), Nucl. Phys. **A757**, 102 (2005).
- [7] K. H. Ackermann *et al.* (STAR Collaboration), Nucl. Instrum. Methods A **499**, 624 (2003).
- [8] K. H. Ackermann *et al.* (STAR Collaboration), Nucl. Phys. **A661**, 681 (1999).
- [9] M. Anderson *et al.*, Nucl. Instrum. Methods A **499**, 659 (2003).
- [10] C. Adler *et al.*, Nucl. Instrum. Methods A **470**, 488 (2001).
- [11] J. Adams *et al.* (STAR Collaboration), Phys. Rev. Lett. **92**, 171801 (2004).
- [12] F. S. Bieser *et al.* (STAR Collaboration), Nucl. Instrum. Methods A **499**, 766 (2003).
- [13] J. Adams *et al.* (STAR Collaboration), Phys. Rev. Lett. **91**, 172302 (2003).
- [14] M. Anderson *et al.*, Nucl. Instrum. Methods A **499**, 679 (2003).
- [15] F. Bergsma *et al.* (STAR Collaboration), Nucl. Instrum. Methods A **499**, 633 (2003).
- [16] J. Adams *et al.* (STAR Collaboration), Phys. Lett. **B637**, 161 (2006).
- [17] J. Adams *et al.* (STAR Collaboration), Phys. Rev. Lett. **92**, 112301 (2004).
- [18] C. Adler *et al.* (STAR Collaboration), Phys. Lett. **B595**, 143 (2004).
- [19] C. Adler *et al.* (STAR Collaboration), Phys. Rev. Lett. **87**, 262302 (2001).
- [20] J. Adams *et al.* (STAR Collaboration), Phys. Rev. C **70**, 041901 (2004).
- [21] K. H. Ackermann *et al.*, Nucl. Instrum. Methods A **499**, 713 (2003).
- [22] J. Adams *et al.* (STAR Collaboration), Phys. Rev. C **70**, 064907 (2004).
- [23] C. Adler *et al.* (STAR Collaboration), Phys. Rev. Lett. **87**, 112303 (2001).
- [24] B. I. Abelev *et al.* (STAR Collaboration), arXiv:nucl-ex/0703016.
- [25] M. Calderón de la Barca Sánchez, Ph.D. thesis (Yale University, 2001), arXiv:nucl-ex/0111004.
- [26] W. R. Chen and R. C. Hwa, Phys. Rev. D **39**, 179 (1989).
- [27] X.-N. Wang, Phys. Rev. D **43**, 104 (1991).
- [28] V. Topor Pop *et al.*, Phys. Rev. C **68**, 054902 (2003).
- [29] D. Kharzeev and M. Nardi, Phys. Lett. **B507**, 121 (2001).
- [30] D. Kharzeev, E. Levin, and L. McLerran, Phys. Lett. **B561**, 93 (2003).
- [31] L. McLerran and J. Schaffner-Bielich, Phys. Lett. **B514**, 29 (2001).
- [32] J. Schaffner-Bielich, D. Kharzeev, L. D. McLerran, and R. Venugopalan, Nucl. Phys. **A705**, 494 (2002).
- [33] S.-y. Li and X.-N. Wang, Phys. Lett. **B527**, 85 (2002).
- [34] R. J. Glauber, *Lectures in Theoretical Physics* (Interscience, New York, 1958), Vol. I, p. 315.
- [35] T. Adachi and T. Kotani, Prog. Theor. Phys. **39**, 430 (1968); **39**, 785 (1968).
- [36] B. Bonner *et al.*, Nucl. Instrum. Methods A **508**, 181 (2003).
- [37] M. Shao *et al.*, Nucl. Instrum. Methods A **492**, 344 (2002).
- [38] W. M. Yao *et al.* (Particle Data Group), J. Phys. G **33**, 1 (2006).
- [39] H. Bichsel, Nucl. Instrum. Methods A **562**, 154 (2006).
- [40] M. Aguilar-Benitez *et al.*, Z. Phys. C **50**, 405 (1991).
- [41] L. Arnold *et al.*, Nucl. Instrum. Methods A **499**, 652 (2003).
- [42] M. Gyulassy and X.-N. Wang, Comput. Phys. Commun. **83**, 307 (1994).
- [43] D. Ashery and J. P. Schiffer, Annu. Rev. Nucl. Part. Sci. **36**, 207 (1986).
- [44] C. Adler *et al.* (STAR Collaboration), Phys. Rev. Lett. **89**, 092301 (2002).
- [45] C. Adler *et al.* (STAR Collaboration), Phys. Rev. Lett. **86**, 4778 (2001); **90**, 119903(E) (2003).
- [46] C. Adler *et al.* (STAR Collaboration), Phys. Lett. **B616**, 8 (2005).
- [47] B. I. Abelev *et al.* (STAR Collaboration), Phys. Lett. **B655**, 104 (2007).
- [48] C. Adler *et al.* (STAR Collaboration), Phys. Rev. C **66**, 061901 (2002).
- [49] J. Adams *et al.* (STAR Collaboration), Phys. Lett. **B567**, 167 (2003).
- [50] J. Adams *et al.* (STAR Collaboration), Phys. Rev. Lett. **92**, 182301 (2004).
- [51] J. Adams *et al.* (STAR Collaboration), Phys. Rev. C **71**, 064902 (2005).
- [52] B. I. Abelev *et al.* (STAR Collaboration), Phys. Rev. C **75**, 064901 (2007).
- [53] B. I. Abelev *et al.* (STAR Collaboration), Phys. Rev. Lett. **97**, 132301 (2006).
- [54] J. Adams *et al.* (STAR Collaboration), Phys. Rev. D **74**, 032006 (2006).
- [55] Z. Chajeki and M. Lisa, arXiv:0807.3569.
- [56] A. Leonidov, M. Nardi, and H. Satz, Z. Phys. C **74**, 535 (1997).
- [57] X.-N. Wang and M. Gyulassy, Phys. Rev. Lett. **86**, 3496 (2001).
- [58] K. J. Eskola, K. Kajantie, P. V. Ruuskanen, and K. Tuominen, Nucl. Phys. **B570**, 379 (2000).
- [59] L. McLerran, Nucl. Phys. **A702**, 49 (2002).
- [60] L. McLerran, Nucl. Phys. **A699**, 73 (2002).
- [61] X.-N. Wang and M. Gyulassy, Phys. Rev. D **44**, 3501 (1991).
- [62] G. J. Alner *et al.* (UA5 Collaboration), Z. Phys. C **33**, 1 (1986).
- [63] G. J. Alner *et al.* (UA5 Collaboration), Phys. Lett. **B115**, 71 (1982).
- [64] G. J. Alner *et al.* (UA5 Collaboration), Phys. Rep. **154**, 247 (1987).
- [65] F. Abe *et al.* (CDF Collaboration), Phys. Rev. D **41**, 2330 (1990).
- [66] C. Albajar *et al.* (UA1 Collaboration), Nucl. Phys. **B335**, 261 (1990).
- [67] J. Adams *et al.* (STAR Collaboration), Phys. Rev. Lett. **95**, 152301 (2005).
- [68] M. L. Miller *et al.*, Annu. Rev. Nucl. Part. Sci. **57**, 205 (2007).
- [69] K. Adcox *et al.* (PHENIX Collaboration), Phys. Rev. Lett. **88**, 192302 (2002).
- [70] T. Alber *et al.* (NA49 Collaboration), Phys. Rev. Lett. **75**, 3814 (1995).
- [71] S. A. Bass and A. Dumitru, Phys. Rev. C **61**, 064909 (2000).
- [72] E. Wang and X.-N. Wang, Phys. Rev. Lett. **89**, 162301 (2002).
- [73] K. J. Eskola, P. V. Ruuskanen, S. S. Rasanen, and K. Tuominen, Nucl. Phys. **A696**, 715 (2001).
- [74] I. G. Bearden *et al.* (BRAHMS Collaboration), Phys. Rev. Lett. **87**, 112305 (2001).

- [75] L. Ahle *et al.* (E802 Collaboration), Phys. Rev. Lett. **81**, 2650 (1998).
- [76] L. Ahle *et al.* (E802 Collaboration), Phys. Rev. C **60**, 044904 (1999).
- [77] S. V. Afanasiev *et al.* (NA49 Collaboration), Phys. Rev. C **66**, 054902 (2002).
- [78] M. van Leeuwen *et al.* (NA49 Collaboration), Nucl. Phys. **A715**, 161 (2003).
- [79] I. G. Bearden *et al.* (NA44 Collaboration), Phys. Rev. C **66**, 044907 (2002).
- [80] F. Videbaek and O. Hansen, Phys. Rev. C **52**, 2684 (1995).
- [81] F. Wang, J. Phys. G: Nucl. Part. Phys. **27**, 283 (2001).
- [82] R. Rapp and E. Shuryak, Phys. Rev. Lett. **86**, 2980 (2001).
- [83] W. Busza and R. Ledoux, Annu. Rev. Nucl. Part. Sci. **38**, 119 (1988).
- [84] D. Kharzeev, Phys. Lett. **B378**, 238 (1996).
- [85] S. E. Vance, M. Gyulassy, and X.-N. Wang, Phys. Lett. **B443**, 45 (1998).
- [86] L. Ahle *et al.* (E802 Collaboration), Phys. Rev. C **60**, 064901 (1999).
- [87] H. Appelshauser *et al.* (NA49 Collaboration), Phys. Rev. Lett. **82**, 2471 (1999).
- [88] T. Anticic *et al.* (NA49 Collaboration), Phys. Rev. C **69**, 024902 (2004).
- [89] C. Alt *et al.* (NA49 Collaboration), Phys. Rev. C **73**, 044910 (2006).
- [90] I. G. Bearden *et al.* (BRAHMS Collaboration), Phys. Rev. Lett. **93**, 102301 (2004).
- [91] J. Rafelski and B. Muller, Phys. Rev. Lett. **48**, 1066 (1982); **56**, 2334(E) (1986).
- [92] J. Rafelski, Phys. Rep. **88**, 331 (1982).
- [93] P. Koch, B. Muller, and J. Rafelski, Phys. Rep. **142**, 167 (1986).
- [94] H. Sorge, R. Mattiello, A. Jahns, H. Stoecker, and W. Greiner, Phys. Lett. **B271**, 37 (1991).
- [95] H. Sorge, Phys. Rev. C **52**, 3291 (1995).
- [96] L. Ahle *et al.* (E802 Collaboration), Phys. Rev. C **58**, 3523 (1998).
- [97] L. Ahle *et al.* (E866 Collaboration) and B. B. Back *et al.* (E917 Collaboration), Phys. Lett. **B476**, 1 (2000).
- [98] L. Ahle *et al.* (E866 Collaboration) and B. B. Back *et al.* (E917 Collaboration), Phys. Lett. **B490**, 53 (2000).
- [99] J. Bartke *et al.* (NA35 Collaboration), Z. Phys. C **48**, 191 (1990).
- [100] T. Alber *et al.* (NA35 Collaboration), Eur. Phys. J. C **2**, 643 (1998).
- [101] F. Sikler (NA49 Collaboration), Nucl. Phys. **A661**, 45c (1999).
- [102] I. G. Bearden *et al.* (NA44 Collaboration), Phys. Lett. **B471**, 6 (1999).
- [103] H. Boggild *et al.* (NA44 Collaboration), Phys. Rev. C **59**, 328 (1999).
- [104] C. Alt *et al.* (NA49 Collaboration), Phys. Rev. C **77**, 024903 (2008).
- [105] C. Alt *et al.* (NA49 Collaboration), Phys. Rev. Lett. **94**, 052301 (2005).
- [106] A. M. Rossi, G. Vannini, A. Bussiere, E. Albini, D. D'Alessandro, and G. Giacomelli, Nucl. Phys. **B84**, 269 (1975).
- [107] J. L. Bailly *et al.* (EHS-RCBC Collaboration), Phys. Lett. **B195**, 609 (1987).
- [108] T. Alexopoulos *et al.* (E735 Collaboration), Phys. Rev. D **48**, 984 (1993).
- [109] Bocquet *et al.* (UA1 Collaboration), Phys. Lett. **B366**, 441 (1996).
- [110] K. Adcox *et al.* (PHENIX Collaboration), Phys. Rev. Lett. **88**, 242301 (2002).
- [111] F. Wang, Phys. Lett. **B489**, 273 (2000).
- [112] F. Wang *et al.*, Phys. Rev. C **61**, 064904 (2000).
- [113] P. Braun-Munzinger *et al.*, Nucl. Phys. **A697**, 902 (2002).
- [114] J. Cleymans, K. Redlich, and E. Suhonen, Z. Phys. C **51**, 137 (1991).
- [115] S. Hamieh, K. Redlich, and A. Tounsi, Phys. Lett. **B486**, 61 (2000).
- [116] A. Tounsi and K. Redlich, arXiv:hep-ph/0111159.
- [117] A. Tounsi, A. Mischke, and K. Redlich, Nucl. Phys. **A715**, 565 (2003).
- [118] D. Kharzeev and E. Levin, Phys. Lett. **B523**, 79 (2001).
- [119] D. Kharzeev, E. Levin, and M. Nardi, Phys. Rev. C **71**, 054903 (2005) and references therein.
- [120] P. Braun-Munzinger, J. Stachel, J. P. Wessels, and N. Xu, Phys. Lett. **B344**, 43 (1995).
- [121] P. Braun-Munzinger, J. Stachel, J. P. Wessels, and N. Xu, Phys. Lett. **B365**, 1 (1996).
- [122] P. Braun-Munzinger, I. Heppe, and J. Stachel, Phys. Lett. **B465**, 15 (1999).
- [123] N. Xu and M. Kaneta, Nucl. Phys. **A698**, 306 (2002).
- [124] L. A. Stiles and M. Murray, arXiv:nucl-ex/0601039.
- [125] F. Karsch, Prog. Theor. Phys. Suppl. **153**, 106 (2004).
- [126] F. Becattini and G. Pettini, Phys. Rev. C **67**, 015205 (2003).
- [127] E. Schnedermann, J. Sollfrank, and U. Heinz, Phys. Rev. C **48**, 2462 (1993).
- [128] D. Teaney, J. Lauret, and E. V. Shuryak, nucl-th/0110037.
- [129] D. Teaney, J. Lauret, and E. V. Shuryak, Phys. Rev. Lett. **86**, 4783 (2001).
- [130] P. Kolb *et al.*, Nucl. Phys. **A696**, 197 (2001).
- [131] P. Huovinen *et al.*, Phys. Lett. **B503**, 58 (2001).
- [132] U. Heinz and P. Kolb, Nucl. Phys. **A702**, 269 (2002).
- [133] F. Retiere and M. A. Lisa, Phys. Rev. C **70**, 044907 (2004).
- [134] G. Wilk and Z. Włodarczyk, Phys. Rev. Lett. **84**, 2770 (2000).
- [135] J. Adams *et al.* (STAR Collaboration), Phys. Rev. C **73**, 064907 (2006).
- [136] J. Adams *et al.* (STAR Collaboration), J. Phys. G **32**, L37 (2006).
- [137] G. Torrieri and J. Rafelski, Phys. Lett. **B509**, 239 (2001).
- [138] M. Bleicher and J. Aichelin, Phys. Lett. **B530**, 81 (2002).
- [139] W. Schmitz *et al.*, J. Phys. G **28**, 1861 (2002).
- [140] J. Cleymans, H. Oeschler, and K. Redlich, J. Phys. G **25**, 281 (1999).
- [141] J. Cleymans *et al.*, Phys. Rev. C **57**, 3319 (1998).
- [142] F. Becattini, J. Cleymans, A. Keranen, E. Suhonen, and K. Redlich, Phys. Rev. C **64**, 024901 (2001).
- [143] J. Cleymans *et al.*, Phys. Rev. C **73**, 034905 (2006).
- [144] A. Andronic, P. Braun-Munzinger, and J. Stachel, Nucl. Phys. **A772**, 167 (2006).
- [145] W. Reisdorf *et al.*, Nucl. Phys. **A612**, 493 (1997).
- [146] M. A. Lisa *et al.*, Phys. Rev. Lett. **75**, 2662 (1995).
- [147] C. Muntz, arXiv:nucl-ex/9806002.
- [148] H. Appelshauser *et al.*, Eur. Phys. J. C **2**, 661 (1998).
- [149] B. I. Abelev *et al.* (STAR Collaboration), Phys. Rev. Lett. **99**, 112301 (2007).
- [150] P. Braun-Munzinger, K. Redlich, and J. Stachel, in *Quark-Gluon Plasma 3*, edited by R. C. Hwa and X.-N. Wang (World Scientific, Singapore, 2004).

- [151] J. Stachel, Nucl. Phys. **A654**, 119c (1999).
- [152] C. Y. Wong, *Introduction to High-Energy Heavy-Ion Collisions* (World Scientific, Singapore, 1994).
- [153] A. J. Baltz, C. Chasman, and S. N. White, Nucl. Instrum. Methods A **417**, 1 (1998).
- [154] F. Antinori *et al.* (WA97 Collaboration), Eur. Phys. J. C **18**, 57 (2000) and references therein.
- [155] C. Adler *et al.* (STAR Collaboration), Phys. Rev. Lett. **89**, 202301 (2002).
- [156] K. Adcox *et al.* (PHENIX Collaboration), Phys. Lett. **B561**, 82 (2003).
- [157] I. G. Bearden *et al.* (BRAHMS Collaboration), Phys. Lett. **B523**, 227 (2001).
- [158] B. B. Back *et al.* (PHOBOS Collaboration), Phys. Rev. C **65**, 031901 (2002).
- [159] B. B. Back *et al.* (PHOBOS Collaboration), Phys. Lett. **B578**, 297 (2004).
- [160] C. W. De Jager, H. De Vries, and C. De Vries, At. Data Nucl. Data Tables **14**, 479 (1974).
- [161] C. W. De Jager, H. De Vries, and C. De Vries, At. Data Nucl. Data Tables **36**, 495 (1987).
- [162] J. Adams *et al.* (STAR Collaboration), Phys. Rev. Lett. **95**, 062301 (2005).
- [163] J. Adams *et al.* (STAR Collaboration), Phys. Rev. Lett. **91**, 072304 (2003).
- [164] U. A. Wiedemann and U. W. Heinz, Phys. Rev. C **56**, 3265 (1997).
- [165] B. I. Abelev *et al.* (STAR Collaboration), Phys. Rev. C **77**, 044908 (2008).
- [166] W. Broniowski and W. Florkowski, Phys. Rev. Lett. **87**, 272302 (2001).
- [167] W. Broniowski and W. Florkowski, Phys. Rev. C **65**, 064905 (2002).
- [168] W. Broniowski, A. Baran, and W. Florkowski, Acta Phys. Pol. B **33**, 4235 (2002).